Characterisation of Cytochrome *c* MtoD from the Iron-Oxidising Autotroph *Sideroxydans lithotrophicus* ES-1.

Christopher Robert Beckwith

PhD Thesis

University of East Anglia

School of Biological Sciences

Norwich

September 2015

Abstract

Despite the discovery of iron-oxidising microorganisms as early as 1836 by Ehrenberg, as described by Harder in 1919, iron-oxidising lithotrophs and their respiratory pathways remain poorly understood. The neutrophilic iron-oxidiser *Sideroxydans lithotrophicus* ES-1 contains a conserved *mtoDAB* gene cluster. MtoAB, consisting of a decaheme *c*-type cytochrome (MtoA) and β-barrel porin (MtoB), is implicated in Fe(II) oxidation at the outer membrane, performing a similar electron transfer function to the well-studied MtrCAB complex from iron-reducing bacterium *Shewanella oneidensis*, albeit in reverse. MtoD is predicted to be a monoheme class I cytochrome *c* that is proposed to transfer electrons from MtoA to the predicted inner membrane quinone reductase $CymA_{ES-1}$ (Shi *et al.* 2012). Very little is understood about the electron transfer pathways in *S. lithotrophicus* and the current model (Shi *et al.* 2012) does not propose a mechanism that would allow NADH and ATP to be generated for the fixation of CO_2. To probe the potential electron transfer pathways in *S. lithotrophicus*, MtoD was overexpressed in *S. oneidensis,* purified and characterised using biophysical, structural and spectroelectrochemical methods. The primary structure of MtoD contains a single CXXCH *c*-type heme binding motif, but the mature protein sequence lacks methionine, which is the distal ligand to the heme iron in almost all class I cytochromes *c*. Biophysical characterisation using AUC and SAXS indicated MtoD behaved as a monomer in solution with an approximate molecular weight of 11.5 kDa and the molecular envelope fitted well to previously characterised monoheme cytochromes *c*. The X-ray crystal structure of MtoD was determined to a resolution of 1.47 Å and revealed a protein fold typical of a class I cytochrome *c*. Unlike many other class I cytochromes *c*, MtoD contains a bis-His ligated heme which is solvent exposed on two sides. Redox characterisation of MtoD revealed a midpoint potential of +150 mV vs. SHE for MtoDs *c*-type heme, which shifted to more negative potentials when adsorbed to SnO_2 electrodes, potentially as a result of interaction-induced conformational changes. These redox changes in addition to the atypical structure around the highly exposed heme cofactor make it possible that MtoD could be capable of interacting with multiple redox partners, allowing electron transfer to quinone reductases and cytochrome *c* oxidase at the inner membrane of *S. lithotrophicus*. Based on the characterisation of MtoD and an analysis of the *c*-type cytochromes present in the *S. lithotrophicus* genome, a new model for electron transfer during aerobic iron lithotrophy is proposed.

Table of Contents   Page

List of tables   Page

List of figures   Page

List of Abbreviations

ADP	Adenosine diphosphate
APS	Ammonium persulfate
ATP	Adenosine triphosphate
AUC	Analytical ultracentrifugation
BIF	Banded iron formations
BLAST	Basic Local Alignment Search Tool
CCO	Cytochrome c oxidase
CV	Cyclic voltammetry
DLS	Dynamic light scattering
DMSO	Dimethyl sulfoxide
E_m	Midpoint potential
FeOB	Iron-oxidising bacteria
FeRB	Iron-reducing bacteria
GOE	Great oxygenation event
HEPES	4-(2-hydroxyethyl)-1-piperazineethanesulfonic acid
IM	Inner membrane
IMAC	Immobilised metal affinity chromatography
ITO	Indium-doped tin oxide
LB	Luria broth
MAD	Multiple-wavelength anomalous dispersion
MALDI-MS	Matrix-assisted laser desorption/ionization mass spectrometry
MME	Monomethyl ether
MR	Molecular replacement
MWCO	Molecular weight cut-off
MWMM	Modified Wolfe's mineral medium
NAD^+	Oxidised nicotinamide adenine dinucleotide
NADH	Reduced nicotinamide adenine dinucleotide
NCS	Non-crystallographic symmetry
NFR	Non-Faradaic response
OM	Outer membrane
OMC/Omc	Outer membrane cytochrome
PAGE	Polyacrylamide gel electrophoresis
PAL	Present atmospheric levels
PCR	Polymerase chain reaction
PDB	Protein databank
PFV	Protein film voltammetry
PMF	Proton motive force
PVDF	polyvinylidene difluoride
r.m.s.	root-mean-square
RMSD	Root-mean-square deviation
RO water	Reverse osmosis-treated water
SAD	Single-wavelength anomalous dispersion

SAM	Self-assembled monolayers
SAXS	Small angle X-ray scattering
SDS	Sodium dodecyl sulfate
SHE	Standard hydrogen electroded
TEMED	Tetramethylethylenediamine
TM	Trans-membrane
TMBD	3,3',5,5'-tetramethylbenzidine dihydrochloride hydrate

Acknowledgements

Firstly, I would like to thank my supervisor Professor David Richardson for giving me the opportunity to pursue the research presented here. I would also like to thank Professor Julea Butt for being so generous in offering her insight and guidance while writing this thesis. In particular, I owe a tremendous debt of gratitude to Dr Marcus Edwards, whose supervision and support from the day I began my research to the day I finished writing has been unwavering and truly inspirational.

I feel genuinely privileged to have had the opportunity to study alongside such great friends. In particular, I would like to thank (soon to be Drs.) Matt Lawes, John Munnoch and Hannah Wells for their kindness, patience and friendship during this journey and for sharing the highs and the lows of life and research while understanding or at least coping with my terrible sense of humour.

I would also like to thank my family for their endless love and support throughout my studies.

Chapter 1

General Introduction

1.1 The importance of biogeochemical cycles and metals for life

1.1.1 Geochemical cycling of alkali elements

Biogeochemical cycling of elements is essential to all life on Earth. The carbon, nitrogen and oxygen cycles are fundamental to the composition of all genetic material, proteins, carbohydrates and lipids, each of which are requirements for the survival and reproduction of life. Sulfur, as a constituent of the amino acids methionine and cysteine, and phosphorus, as a constituent of DNA should also be included in this group of essential core elements. Oxygen (47.2%), carbon (0.2%), sulfur (0.07%) and nitrogen (0.006%) are among the most abundant elements in the Earth's continental crust (table 1.1) [1,2], with oxygen (21%) [3] and nitrogen (78%) [4] also being abundant in the Earth's atmosphere as gasses. It should not be surprising therefore that these elements are involved in complex biogeochemical cycles and are important elemental constituents that have enabled life to grow and evolve on Earth.

However, numerous other elements including the alkali elements calcium, potassium and sodium and the transition elements iron, copper, manganese, molybdenum and zinc play essential roles in a wide range of cellular functions.

Rank	Element	Abundance in continental crust (%)	Rank	Element	Abundance in continental crust (%)
1	Oxygen	47.2	12	Manganese	0.072
2	Silicon	28.8	13	Sulfur	0.070
3	Aluminium	7.96	16	Chlorine	0.047
4	Iron	4.32	18	Zirconium	0.020
5	Calcium	3.85	19	Chromium	0.012
6	Sodium	2.36	20	Vanadium	0.0098
7	Magnesium	2.20	22	Zinc	0.0078
8	Potassium	2.14	23	Nitrogen	0.0060
9	Titanium	0.40	28	Copper	0.0025
10	Carbon	0.20	29	Cobalt	0.0024
11	Phosphorus	0.076	53	Molybdenum	0.0001

Table 1.1 Most abundant elements in the Earth's continental crust. Adapted from Wedepohl KH (1995) The Composition of the Continental-Crust. *Geochimica et Cosmochimica Acta* 59(7): 1217–1232.

The biogeochemical cycles of the alkali metals and alkali earth metals are relatively simple. The monovalent ions of sodium (Na^+) and potassium (K^+) in addition to the divalent ion of magnesium (Mg^{2+}) are highly soluble and major contributors to the salinity of seawater in their chloride salt forms (NaCl, KCl and $MgCl_2$ respectively). The high solubility of these elements causes them to be readily leached from ores and soils in the lithosphere where they are washed through groundwater into lakes and seawater (figure 1.1) [5]. Environmental calcium is commonly found in granites in continental crusts and as basalts in oceanic crusts [6]. Calcium liberated from minerals by weathering leaches into the hydrosphere where it is available for uptake by plants and microorganisms as Ca^{2+} (figure 1.1) [6,7].
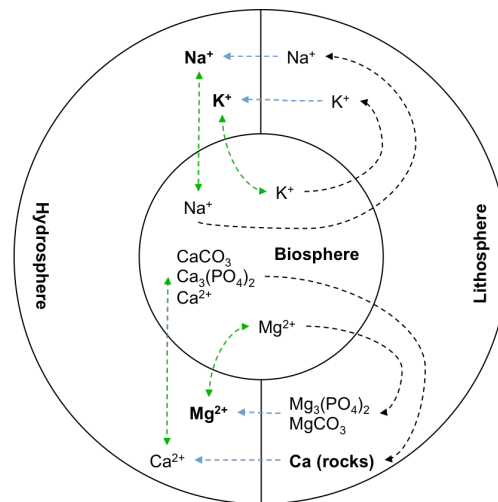
Figure 1.1 Biogeochemical cycling of Na^+, K^+, Mg^{2+} and Ca^{2+}. Alkali elements are cycled between the lithosphere, hydrosphere and the biosphere. The high solubility of Na^+, K^+ and Mg^{2+} makes these elements abundant in the hydrosphere since they are readily leached from rocks and soils. Calcium is less soluble and enters the hydrosphere after weathering of rocks such as calcite and aragonite ($CaCO_3$ minerals). These elements are either excreted or released by decomposition from living organisms in the biosphere where they may return to the hydrosphere or lithosphere. Lithosphere → hydrosphere (blue arrows); Hydrosphere ↔ biosphere (green arrows); Biosphere → lithosphere (black arrows).

The distribution of these monovalent and divalent alkali elements is crucial for maintaining environmental salinity and osmotic stability in living organisms. Sodium and potassium are involved in molecular transport mechanisms such as passive and active transport of ions and organic molecules across biological membranes. Magnesium is an essential ion present in the green pigment chlorophyll,

produced by photosynthetic cyanobacteria, algae and plants [8]. Divalent calcium is the most common signal transduction element in bacteria and eukaryotes [9], but readily precipitates phosphates in the cytosol, which has lethal consequences [10]. As a result, both prokaryotic and eukaryotic organisms have developed mechanisms to sequester Ca^{2+} in the cell using a mixture of chelating molecules, compartmentalisation in the endoplasmic reticulum and mitochondria of eukaryotic organisms and tightly controlled calcium channels that regulate the influx and efflux of Ca^{2+} in the cell [9]. Calcium is implicated in a variety of prokaryotic cell functions such as cell differentiation, transport, motility, gene expression, metabolism, cell cycle and pathogenesis [10–14].

1.1.2. Biogeochemical cycling of transition elements

Compared to the cycling of the alkali metals and alkali earth elements the biogeochemical cycles of the transition metals are complex. One of the main reasons for the additional complexity is the occurrence of many transition elements in more than one oxidation state. For example, iron, which is the fourth most abundant element in the Earth's continental crust (table 1.1), is found environmentally in the +2 (ferrous) and +3 (ferric) oxidation states. Manganese on the other hand, which ranks twelfth in continental crust abundance, is most commonly stable in the +2, +4 and +7 oxidation states, although the biogenic oxidation of Mn(II) by manganese oxidising bacteria produce Mn(III) and Mn(IV) minerals [15]. As a result, iron, manganese and other transition elements are able to form a broader range of stable compounds and mineral complexes compared to the alkali metals and alkali earth elements, leading to more complex elemental cycling. The oxidation state of the transition elements can be rapidly interconverted depending on the prevailing environmental conditions, such as pH and redox potential. This adds to the complexity of the transition element cycling by introducing redox cycling. The geochemical and biological redox cycling of transition elements is absolutely fundamental to life on Earth and the origins and evolution of ancient microbial metabolisms. The biogeochemical cycles and the biological importance of some transition elements will be summarised in the following section, focussing on iron.

After iron, manganese and titanium the abundance of transition elements in the Earth's crust is relatively low, with chromium (0.0126%), vanadium (0.0098%), zinc (0.007%), copper (0.0025%), cobalt (0.0024%) and molybdenum (0.0001%) the next most common (table 1.1). Iron, zinc and copper are the most abundant transition metals in biological systems [16].

Zinc is a constituent in a range of metalloenzymes, including carbonic anhydrase, dehydrogenases and peptidases [17,18] and is an essential trace element in microbes, being present in a number of DNA and RNA polymerases, alkaline phosphatase and members of the 'Fur' family of iron/zinc uptake regulators [19,20]. Zinc-containing proteins coordinate zinc in the +2 oxidation state (Zn(II)); Zn is not found in any other stable oxidation states, making it redox inactive [16].

Copper on the other hand is stable in the +1 (cuprous) and +2 (cupric) oxidation states (Cu(I) and Cu(II) respectively). Copper in the lithosphere is present in a range of mineral forms including chalcopyrite ($CuFeS_2$), chalcocite (Cu_2S) and covellite (CuS), each of which can be utilised for the anthropogenic purification of copper by bioleaching [19,21]. Copper bioleaching is an environmentally important process for solubilising copper from minerals. Bioleaching of insoluble copper sulphides generates copper sulphates, which are available for uptake by plants and microorganisms into the biosphere [21]. Similar to the biogeochemical cycle of calcium, copper in the lithosphere is also liberated by weathering of rocks and the resulting sediment is mobilised by freshwater or seawater [22]. Determining marine copper concentrations is complex; concentrations of copper in oceans are greatest around landmasses due to weathering and leaching of copper from terrestrial rocks and sediments. Seawater copper concentrations also increase with depth [22]. However, Rauch and Graedel (2007) have estimated a mean ocean copper concentration of 145 parts per trillion (~2.3 nM), which compares to an estimated average global freshwater copper concentration of 768 parts per trillion (~12 nM) [22].

As an essential trace element, bacteria, plants and higher kingdoms of life require copper. Copper in prokaryotic and eukaryotic organisms is present in metalloproteins and enzymes that function in small molecule processing, production/scavenging of reactive oxygen species' (ROS) and electron transfer [23]. Perhaps one of the best-known and most important copper-containing enzymes for cell survival is the copper-zinc superoxide dismutase (Cu-Zn SOD), which catalyses the disproportionation of the highly reactive and deleterious radical superoxide (O_2^-),

which can form during the incomplete reduction of O_2 during respiration, to O_2 and H_2O_2. The ubiquity of SOD enzymes demonstrates their importance for protecting the cell from catastrophic damage by ROS.

Examples of copper in electron transfer proteins include plastocyanin [24], azurin [25] and a range of copper oxidases, including mononuclear copper oxidases, multi-copper oxidases and heme-copper oxidases [23]. The copper oxidases are involved in essential functions in prokaryotic and eukaryotic organisms from metabolism of primary amines (copper amine oxidases) and alcohols (galactose oxidase) to aerobic respiration (cytochrome *c* oxidases and quinol oxidases) [23]. Quinol oxidases (primarily found in bacteria) and cytochrome *c* oxidases are membrane-associated protein complexes that contain both copper and iron sites, which are involved in the respiratory reduction of O_2 to H_2O. The redox properties of copper and iron are essential to the function of these enzymes.

Iron, like copper, is a redox active transition element and exists environmentally in the +2 and +3 oxidation states [26]. Iron is essential to cellular function in numerous enzymes and electron transfer proteins where it is commonly found in iron-sulfur and heme cofactors. Iron-sulfur centres, such as 2Fe-2S, 3Fe-4S and 4Fe-4S, are among the most ancient biological structures and the most common form of non-heme iron in living organisms [27,28]. These centres are important for a range of cellular functions including electron transfer (e.g. Rieske protein), transcriptional regulation (e.g. SoxR), structural stability (e.g. endonuclease) and catalysis (e.g. aconitase) [27].

The majority of cellular iron in living organisms is associated with the heme prosthetic group, which is composed of protoporphyrin IX and a single iron atom. The heme cofactor exists in either an oxidised or reduced state owing to the presence of iron, which is found either as Fe^{3+} or Fe^{2+} in the oxidised and reduced states respectively.

There are numerous types of heme cofactor including heme *a*, heme *b*, heme *c*, heme *d*, heme *o* and siroheme [29]. Two of the most common types that will become relevant to later results and discussion presented in this thesis are heme *b* and heme *c* (figure 1.2). Hemes *b* and *c* are structurally similar; heme *b* is associated with proteins through axial ligation of the heme iron by methionine, histidine or lysine residues. Heme *c* is associated with proteins through both axial heme ligation and the formation of covalent thioether bonds between protoporphyrin IX and cysteine

residues (figure 1.2) that are typically found in the canonical CXXCH motif, where the histidine residue forms the proximal ligand to the heme iron in the axial orientation.

Heme *B*　　　　　　　Heme *C*
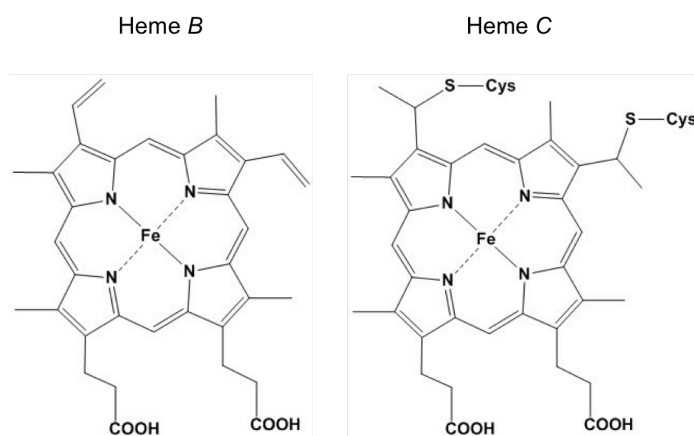
Figure 1.2 Structure of *b*-type and *c*-type heme cofactors. In reduced heme, the iron atom is present as Fe(II), whereas iron is present as Fe(III) in oxidised heme. Four nitrogen atoms from the protoporphyrin IX molecule form the equatorial ligands to the heme iron in both heme structures. Diagrams were produced in ChemDraw.

Hemes *b* and *c* are present in *b*-type and *c*-type cytochromes respectively, which are ubiquitous among respiratory electron transfer chains [30,31]. Examples include cytochrome bc_1, which oxidises quinol to generate a proton motive force and class I cytochromes *c*, which transfers electrons from quinol oxidases to terminal oxidases in the periplasm of bacteria or the intermembrane space of mitochondria. The cytochrome terminal oxidases vary depending on the organism in question and the type of respiration being performed. Cytochrome *c* oxidases that couple the oxidation of class I cytochrome *c* to the reduction of O_2 to H_2O include aa_3, ba_3, baa_3, caa_3, cbb_3, cao and *co*-type cytochrome *c* oxidases [29], which contain *a*, *b*, *c* and *o*-type hemes [30]. There are a numerous types of terminal heme-containing oxidases that are associated with anaerobic respiration in bacteria, with common examples being in nitrate/nitrite respiration (NAR, NAP, NIR and NRF), and thiosulfate, sulfite and polysulfide respiration (PHS, SIR and PSR) [29,32,33].

The majority of cytochromes contain hemes that are ligated by two axial ligands (hexacoordinate iron), since the function of these proteins often relies only on the redox transformation of heme iron between the ferric and ferrous state. However, there are a number of cytochromes that are ligated in the axial orientation by only a single protein ligand (pentacoordinate iron); these hemes tend to be

involved in catalysis. For example, nitrite reductase NrfA is a multiheme cytochrome containing five *c*-type hemes, four of which are hexacoordinate and one of which is pentacoordinate. Each of the hexacoordinated heme cofactors is involved in electron transfer to drive the catalytic reduction of nitrite to ammonia [34]. It is the pentacoordinate *c*-type heme (axially ligated by the less common lysine ligand) that is found at the active site of the enzyme and allows substrate binding and catalysis [34].

Iron can be as dangerous to the cell as it is useful; iron is capable of generating ROS and organic radicals, which rapidly react with and cause damage to cellular macromolecules including proteins and DNA, leading to protein oxidation, deleterious DNA modification and eventually cell death [27]. Unsurprisingly, one of the most widespread iron-containing proteins from bacteria through to higher life organisms is ferritin, which plays a crucial sequestration role in iron homeostasis [27]. In order for living organisms to make use of iron, they must interact with the iron biogeochemical cycle. This cycle is both important for the survival and function in biology, but is also implicated in evolution of life on Earth [26]. The biogeochemical cycle of iron will be described in the following sections.

1.1.3. Biogeochemical cycling of iron

Despite its abundance in the Earth's crust (table 1.1), very little iron is present in the Earth's oceans (<1 nM) [26] due to the insoluble nature of ferric Fe^{3+} species (approximately 10^{-17} M) [35] which are formed under the aerobic conditions that prevail in the Earth's oceans and terrestrial waters [26,36]. In the presence of O_2, ferrous iron (Fe(II)) is oxidised to ferric iron (Fe(III)), which then reacts rapidly with water at circumneutral pH to precipitate ferric oxyhydroxides (equation 1.1) [37]:

Equation 1.1 $\qquad O_2(aq) + 4Fe^{2+} + 6H_2O \leftrightarrow 4FeOOH(s) + 8H^+$

Examples of common ferric iron-containing minerals found in sediments include, hematite (α-Fe_2O_3), ferrihydrite ($5Fe_2O_3 \bullet 9H_2O$), magnetite (Fe_3O_4) and goethite (α-FeOOH) [19,35,38], all of which are poorly soluble. The concentration of iron in solution, the distribution of iron and the rate at which abiotic oxidation of

Fe^{2+} by molecular oxygen occurs in marine and sedimentary environments depend greatly on oxygen concentrations, pH and temperature (equation 1.2):

Equation 1.2
$$\frac{\Delta[\text{Fe(II)}]}{\Delta t} = -k[\text{Fe}^{2+}][O_2][OH^-]^2$$

Where k is the temperature-dependent constant 8.0 x 10^{13} $L^2.mol^{-2}.atm^{-1}$ (25°C) [39,40].

Ferrous iron species' are most abundant under acidic and/or microaerobic/anaerobic conditions, while ferric iron species' are prevalent in oxic environments at circumneutral pH [35]. Ferrous iron may be oxidised under acidic or low-oxygen conditions by acidophilic iron-oxidising bacteria (FeOB) or neutrophillic FeOB capable of anaerobic or microaerobic growth [19]. FeOB and iron-reducing bacteria (FeRB) play a substantial role in iron redox cycling.

The three environmentally dominant forms of iron shown in figure 1.3 include Fe^{2+}, which is stable in solution in the absence of sulphides and oxygen, Fe^{3+}, which is only stable in solution under acidic conditions and Fe(III) minerals, which rapidly form in the presence of oxygen and water at circumneutral pH [26]. Chemical oxidation of iron from the ferrous to the ferric oxidation state at circumneutral pH in oxic environments is rapid, causing this process to be almost exclusively abiotic (figure 1.3 A). However, under microaerobic conditions ($[O_2]$ < 50 µM), neutrophillic FeOB are able to compete with rates of abiotic iron oxidation to utilise Fe^{2+} as an energy source for lithotrophic growth [40] (figure 1.3 B). Microaerophilic FeOB in this group of neutrophiles are able to couple Fe^{2+} oxidation to the reduction of O_2, although some neutrophilic FeOB can also couple the oxidation of Fe^{2+} to the reduction of nitrate under anaerobic conditions (figure 1.3 C) [41,42]. Photoferrotrophic FeOB are able to oxidise Fe^{2+} to drive the photosynthetic fixation of carbon dioxide (figure 1.3 D). Instead of oxidising H_2O and generating O_2, as is the case in oxygenic photosynthesis, these FeOB oxidise Fe^{2+} to Fe^{3+} under anaerobic conditions (equation 1.3) [26,43]:

Equation 1.3 $4Fe^{2+} + CO_2 + 11H_2O + \text{light} \rightarrow 4Fe(OH)_3 + CH_2O + 8H^+$
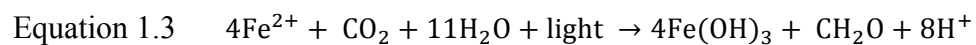
The biogenic precipitation of ferric oxyhydroxides by neutrophillic FeOB produces iron deposits with unique structures that have altered surface areas and reactivity compared to chemically oxidised iron deposits [44,45]. These biogenically-produced ferric oxyhydroxides have been shown to be excellent substrates for iron-reducing bacteria found in freshwater and marine environments, as well as the rhizosphere [46]. The coexistence of iron oxidising bacteria and iron reducing bacteria theoretically provides mutually beneficial outcomes. The biogenic oxidation of iron provides a reactive terminal electron acceptor for FeRB, which in turn reduce the ferric iron precipitates, mitigating encapsulation of FeOB by solid iron deposits while recycling the supply of ferrous iron for FeOB (figure 1.3 B – F). Evidence of FeOB and FeRB coexistence has been observed in microbial communities dominated by FeOB and FeRB discovered in a groundwater iron seep at circumneutral pH in Indiana [47]. Roden *et al.* (2012) concluded the activities of lithotrophic FeOB and dissimilatory FeRB on mm-to-cm scale redox gradients in this environment provided the energetic driving force for a 'microbial ferrous wheel', which supported growth of this iron cycling microbial community.
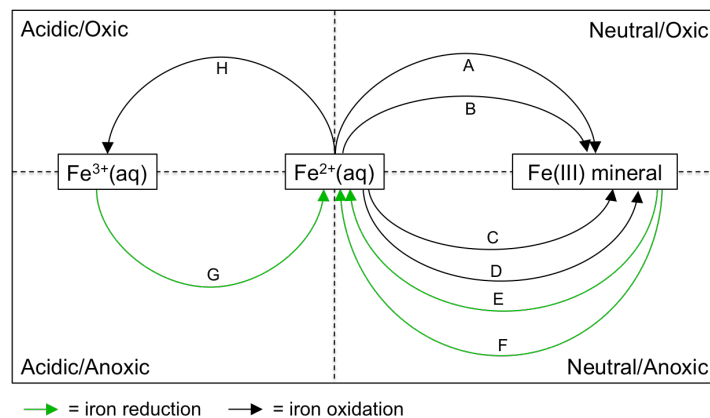
Figure 1.3 Redox cycling of ferric and ferrous iron varies with differences in pH and availability of O_2. At circumneutral pH, Fe^{2+} is rapidly oxidised by O_2, allowing abiotic processes to dominate Fe^{2+} oxidation **(A)**. However, under microaerobic conditions ($[O_2] < 50$ µM) neutrophillic FeOB are able to utilise Fe^{2+} for lithotrophic growth **(B)**. Under anoxic conditions, nitrate-reducing chemoautotrophic **(C)** and photoferrotrophic **(D)** FeOB are able to utilise Fe^{2+} as an energy source. Ferric minerals are known substrates for dissimilatory iron reducing bacteria (FeRB), which can perform iron reduction via direct contact **(E)** or at large distances by electron shuttling or using electrically conductive nanowires **(F)**. Acidophilic FeRB are capable of performing the dissimilatory reduction of soluble species' of ferric iron **(G)**. Slow rates of Fe^{2+} oxidation by O_2 under acidic conditions allow acidophilic iron-oxidising bacteria (FeOB) to dominate Fe^{2+} oxidation for lithotrophic growth under aerobic conditions **(H)**.

Dissimilatory reduction of iron minerals occurs by one of several mechanisms: FeRB can form direct contacts between the cell surface and ferric minerals, allowing outer membrane iron reductases to transfer electrons directly to the mineral (figure 1.3 E) [48,49]. There is also evidence for electron shuttles and electrically conductive biological nanowires providing alternate mechanisms for FeRB to reduce iron minerals that are distant from the cell [50–52] (figure 1.3 F). Current evidence indicates electron shuttling allows the FeRB *Shewanella oneidensis* to transfer electrons across distances greater than 50 μm [50,51]. Proposed electron shuttles include riboflavin and flavin mononucleotide (FMN), which is supported by evidence indicating these molecules are secreted by *Shewanella oneidensis* [50]. *S. oneidensis* has also been observed to produce extracellular electrically conductive nanowires in response to electron acceptor-limited conditions [52]. Images taken of *S. oneidensis* grown under these conditions using scanning electron microscopy have shown the electrically conductive nanowires can extend micrometer distances [52]. Similarly, electrically conductive pili have been shown to be essential for dissimilatory mineral reduction in the FeRB *Geobacter sulfurreducens* [53]. Electrically conductive nanowires similar to those observed in *S. oneidensis* and *G. sulfurreducens* have also been observed in non-metal reducing bacteria including phototrophic cyanobacterium *Synechocystis* PCC6803 and the thermophilic, fermentative bacterium *Pelotomaculum thermopropionicum* [52]. The presence of conductive extracellular appendages beyond bacteria involved in mineral reduction indicates these structures provide a broader function than simply transferring electrons to minerals. These conductive cellular appendages might provide a mechanism to facilitate inter-cellular and even inter-species electron transfer in complex microbial communities and biofilms as well as long-distance mineral reduction [52,54]. For example, species' of *Geobacter* have been shown to be capable of utilising acetate as an energy source during syntrophic growth with nitrate or fumarate-reducing microorganisms, including rumen-associated bacterium *Wolinella succinogenes* [55,56].

The redox potential of the Fe(III)/Fe(II) couple varies significantly depending on pH and ligands [35]. Under acidic conditions (pH 1-3) the potential of the Fe(III)/Fe(II) redox couple ranges from +0.77 V to +0.697 V (table 1.2) [35], which is oxidising enough to provide an alternative to aerobic respiration for bacteria capable of extracellular electron transfer (figure 1.3 G) [57–59]. Slow rates of abiotic iron

oxidation at acidic pH allows ferrous iron to pool, which acidophilic iron-oxidising bacteria can utilise as a source of energy [57] (figure 1.3 H). The high redox potential of the Fe^{2+}/Fe^{3+} couple under acidic conditions makes Fe^{2+} a poor energy source due to the small potential energy difference between the electron source and anaerobic electron sinks (e.g. NO_3^-/NO_2^- E = +0.42 V). Respiration in FeOB under acidic conditions is aerobic since only the redox potential of the O_2/H_2O couple (+1.12 V at pH 2) is positive enough to generate sufficient energy for growth [35,57]. However, at circumneutral pH the lower redox potentials associated with a variety of ferrous/ferric redox couples (table 1.2) make anaerobic respiration possible. Nitrate respiration is the most common anaerobic form of respiration among the neutrophilic iron-oxidising bacteria. Aerobic respiration by iron-oxidising bacteria under neutrophilic conditions presents the greatest theoretical source of energy for growth, but this is compromised by autoxidation of ferrous iron by oxygen. The redox cycling of iron is a dynamic process and has changed considerably during the development of Earth through the geological eras. Major developments to the iron redox cycle with respect to microbial growth and survival will be described in the following section.

Redox couple	pH	Redox potential (V)
$Fe(SO_4)_2^-/Fe^{2+}$	1	+0.697
O_2/H_2O	2	+1.12
Fe^{3+}/Fe^{2+}	2	+0.77
$Fe(SO_4)_2^-/Fe^{2+}$	3	+0.72
O_2/H_2O	7	+0.8
NO_3^-/NO_2^-	7	+0.42
$Fe(OH)_3/Fe(II)_{aq}$	7	+0.014
$\alpha\text{-}FeOOH_{(goethite)}/Fe(II)_{aq}$	7	-0.274
$\alpha\text{-}Fe_2O_{3(hematite)}/Fe(II)_{aq}$	7	-0.287
$Fe_3O_{4(magnetite)}/Fe(II)_{aq}$	7	-0.314

Table 1.2 Redox potentials of iron couples at acidic and circumneutral pH. O_2/H_2O and NO_3^-/NO_2^- redox couples have been included as these are relevant for respiration of iron-oxidising bacteria. Adapted from Ilbert & Bonnefoy, *Insight into evolution of the iron oxidation pathways*, (2013).

1.2 Iron cycling through the geological eras

The importance of biogeochemical cycling for the growth and survival of microorganisms cannot be underestimated since minerals and trace elements are essential for all life on Earth, as summarised in previous sections [60]. Interaction of microbes with the redox cycling of transition elements and their minerals enables microbial chemoautotrophic growth, through oxidising processes, and anaerobic respiration through dissimilatory reduction of minerals. Iron-containing compounds are prominent in both of these processes, in part due to the abundance of iron on Earth, as well as the broad range of redox potentials associated with the oxidation and reduction of iron species' (table 1.2) [35].

The relationship between microbes and redox cycling is bi-directional. In fact the impact of biological activity can have massive effects on the Earth's geological cycles. A particularly important example involves the phototrophic cyanobacteria and a theory that these microorganisms made a dramatic impact to the chemistry of Earth's climate and by extension the redox cycling of both terrestrial and marine metals during the Great Oxygenation Event (GOE) approximately 2.4 billion years ago [46,61]. Photoautotrophs acquire energy for growth from sunlight, which is used for the reductive fixation of CO_2 during photosynthesis (equation 1.4).

Equation 1.4: $$CO_2 + 2H_2A + light \rightarrow CH_2O + H_2O + 2A$$

The identity of 'A' varies depending on the reductant present. For example, utilisation of the reductant H_2O results in the formation of O_2 (oxygenic photosynthesis). It is oxygenic photosynthesis by ancient cyanobacteria that are implicated in oxygenating the Earth's atmosphere during the first GOE [26,62].

The sudden and large increase in estimated atmospheric O_2 concentrations from <0.1% of present atmospheric levels (PAL) to ~5-18% PAL is proposed to have fundamentally altered the geochemical cycling of iron due to chemical oxidation of ferrous iron by atmospheric and dissolved molecular oxygen [61]. Evidence for the first GOE is provided by the observation of superior-type banded iron formations (BIFs) in marine environments [63] (figure 1.4). The superior-type BIFs, which are not associated with volcanic formations, contain iron oxides, silicon

dioxide, iron carbonates, and iron silicates [63]. Superior-type BIFs are almost exclusively limited to the late Archaean and early Proterozoic era (3 to 2 billion years) sedimentary formations indicating a massive iron deposition event during this period [63]. A second major oxygenation event is believed to have occurred during the late Neoproterozoic era (~500 million years ago), as supported by carbon isotope analysis of sedimentary organic carbon and carbonates [64]. This second oxygenation event brought O_2 concentrations in the Earth's atmosphere to their current levels [9]. Figure 1.4 summarises the proposed changes to atmospheric O_2 concentrations during the great oxygenation events and the impact of these changes on the redox state of ocean water.
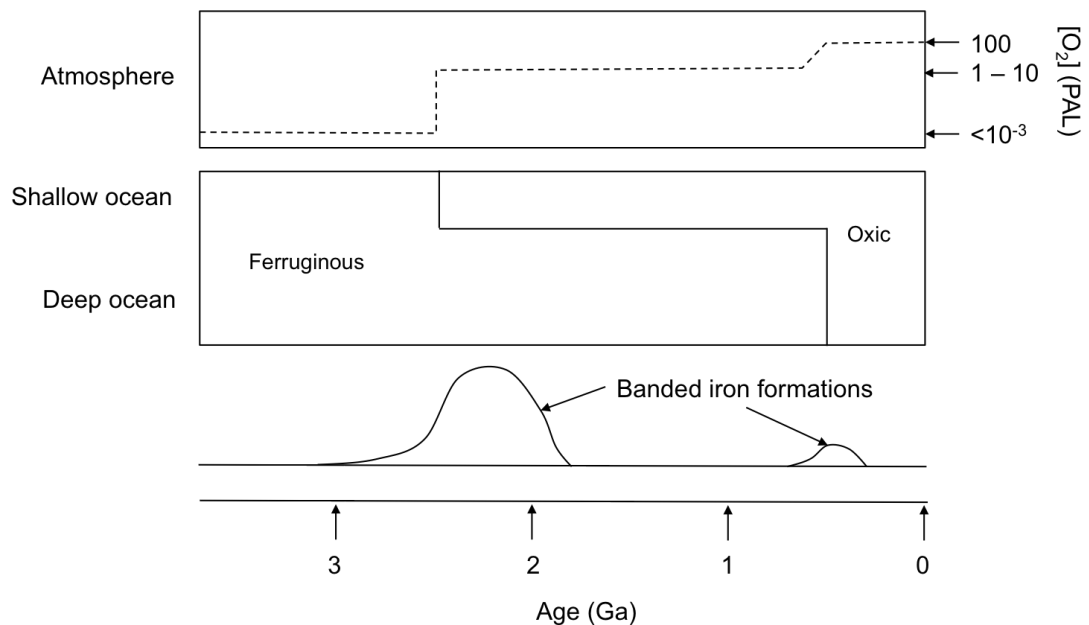
Figure 1.4 Proposed changes to atmospheric O_2 concentrations and ocean redox conditions over time. Increase in atmospheric O_2 concentrations caused Fe^{2+}-rich (ferruginous) oceans to become oxygenated, affecting shallow ocean depths during the first oxygenation event approximately 2-3 Ga (giga-annum). A second global atmospheric oxygenation event increased atmospheric O_2 concentrations to present levels. The resulting increase in ocean oxygenation extended to the deep ocean. These great oxygenation events have been linked to the sedimentation of ferric iron minerals as banded iron formations in oceanic crust. O_2 concentrations are given as a percentage of present atmospheric O_2 concentrations (PAL). This figure has been adapted from Kendall *et al.* (2012) and Ilbert & Bonnefoy (2013).

The Fe^{2+}-rich (ferruginous) state of ancient oceans in the early Achaean era would have provided an abundant source of electrons for marine microorgnisms capable of autotrophic growth using Fe^{2+} as an energy source. Precipitation of ferric

iron species' during the first GOE (figure 1.4) would have caused iron concentrations in the oceans to decrease, relegating obligate iron-oxidising bacteria (FeOB) to deeper ocean waters to anaerobic and microaerophilic conditions where ferruginous conditions remained. Further oxygenation of the Earth's atmosphere during the second great oxygenation event approximately 0.5 billion years ago (figure 1.4) has led to FeOB becoming extremely isolated in marine environments. Iron-oxidising bacteria are still found in marine habitats where hydrothermal venting occurs either at seamounts or crustal spreading centres [65]. The estimated flux of Fe^{2+} through hydrothermal venting is estimated to be approximately $3x10^{11}$ mol.yr^{-1}, which provides a localised energy source for FeOB in marine environments [65,66]. Microbial mats containing FeOB have been observed around hydrothermal venting regions, for example *Mariprofundus ferrooxydans* strains PV-1 and JV-1 were isolated from iron mats associated with the Loihi seamount [65].

Iron-oxidation is believed to be an ancient form of metabolism that developed during the Archaean and early Proterozoic eras while atmospheric oxygen concentrations were low [67]. The morphological unity of FeOB despite their phylogenetic diversity hints at evolutionary divergence consistent with such an ancient metabolism [46,67].

1.3 Utilising the iron redox cycle: lithotrophic iron oxidation and dissimilatory iron reduction by microbes

Iron-oxidising bacteria (FeOB) acquire energy for growth by coupling the oxidation of ferrous iron to the reduction of a range of terminal electron acceptors (TEAs), the two most common being molecular oxygen and nitrate (figure 1.3 B & C) [68].

The susceptibility of ferrous iron to oxidation by molecular oxygen and the half-life ($t^{1/2}$) of this process is dependent on pH, temperature and oxygen concentrations. The importance of oxygen concentrations for FeOB was demonstrated in equation 1.2. The oxygenated atmosphere, oceans and terrestrial waters of present-day Earth have confined obligate aerobic FeOB to redox-interfacial environments where opposing gradients of ferrous iron and oxygen create a habitable niche for FeOB.

These conditions have been found in range of freshwater and marine environments in which many of the presently studied FeOB were discovered [46]. For example, fresh water bacteria *Sideroxydans lithotrophicus* (ES-1) and *Gallionella capsiferriformans* (ES-2) were both isolated from iron-rich groundwaters in Michigan [46,69]; *Gallionella ferruginea* has been discovered in numerous iron-rich groundwaters [70–73]; betaproteobacterial strain designated TW-2 was discovered in iron-rich sediments in Alabama [46], while *Ferritrophicum radicicola* was isolated from the rhizosphere of *Juncus effuses* [46]. The majority of known marine FeOB have been isolated from hydrothermal vents, oceanic crust and iron-rich mats, as exemplified by the well-studied zetaproteobacteria *Mariprofundus ferrooxydans* [46,74–76].

In addition to competing with O_2 for sources of Fe^{2+}, iron-oxidising bacteria face the additional challenge of acquiring sufficient energy from the oxidation of ferrous iron to support lithotrophic growth. The $Fe^{2+} \rightarrow Fe^{3+} + e^-$ oxidation half reaction yields only 29 kJ.mol^{-1} of energy [46,68]. The oxidation of ferrous iron produces ferric iron, which at circumneutral pH rapidly reacts with water to precipitate ferric hydroxides (e.g. $Fe(OH)_3$, FeO_2H, Fe_2O_3) [77,78]. This is reported to produce an energetic yield of 109 kJ.mol^{-1} [46,78]. This is small compared to the estimated free energy associated with the oxidation of organic substrates such as glucose (-2883 kJ.mol^{-1}), lactate (-1,333 kJ.mol^{-1}) and acetate (-847 kJ.mol^{-1}) [79]. This places further emphasis on the importance of pH and oxygen concentrations for the growth of FeOB because in order to acquire the necessary energy to generate ATP from ADP (30.5 kJ.mol^{-1}) [80] and produce reducing equivalents such as NADH from NAD^+ (220 kJ.mol^{-1}) [81] a steady, high flux of ferrous iron is required [46], which would be significantly diminished by autoxidation of iron under aerobic conditions.

Measured rates of biotic vs. abiotic iron oxidation using cultures of the neutrophilic bacterium *Sideroxydans lithotrophicus* ES-1 have shown that biotic iron oxidation contributes a significant proportion of the total iron oxidation at oxygen concentrations <50 μM [40]. This indicates FeOB can successfully compete for ferrous iron at neutral pH, although microaerobic conditions are required. Nevertheless, the challenges of cultivating neutrophilic iron oxidising bacteria such as strains ES-1 and ES-2 *in vitro* has significantly hindered efforts to probe the biochemical mechanisms that enable these bacteria to acquire metabolic energy from iron.

At present, the best understanding of electron transfer between microbes and iron in aqueous and mineral forms comes from the iron-reducing bacteria. A significant effort to probe the mechanisms of electron transfer in the iron reducing bacteria *Shewanella oneidensis* MR-1 and *Geobacter sulfurreducens* has revealed networks of multi-heme cytochromes that allow electrons to traverse the periplasm and the outer membrane of these organisms [49,82–85]. Outer membrane cytochromes enable these organisms to carry out the direct and indirect extracellular reduction of minerals, including ferric iron minerals such as goethite and hematite [86,87]. A model of the electron transfer pathway for *Shewanella oneidensis* MR-1 during iron respiration is shown in figure 1.6 A (page 22).

Tetraheme quinol dehydrogenase CymA, which is anchored at the periplasmic face of the inner membrane acts as an electron transfer hub [88,89]. Electrons are proposed to be transferred from CymA to soluble periplasmic cytochromes such as small tetraheme cytochrome (STC) and flavocytochrome c fumarate reductase (FccA), which shuttle electrons to decaheme cytochrome MtrA at the periplasmic face of the outer membrane [90]. MtrA is part of the trans-outer membrane heterocomplex MtrCAB in which MtrA and MtrC are believed to form a conductive biological wire composed of closely associated heme cofactors and MtrB is a β-porin, which acts as an insulating sheath that holds the complex in the outer membrane [82]. This network of cytochromes allows *S. oneidensis* to rapidly transfer electrons across the periplasmic space and the outer membrane where outer membrane cytochromes, including MtrC, MtrF and OmcA, interact with and facilitate the reduction of ferric mineral substrates [87,90,91].

The respiratory cytochromes of *S. oneidensis* MR-1, in particular the *mtrCAB* gene cluster, are highly conserved across the *Shewanellaceae* (figure 1.5) [92]. Some of the *Shewanellaceae* also encode a number of other multiheme outer membrane cytochromes including decaheme cytochrome OmcA or endecaheme cytochrome UndA, while some *Shewanellaceae*, in addition to the *mtrCAB* gene cluster, also include an *mtrDEF* gene cluster, where *mtrD, mtrE* and *mtrF* are homologous to *mtrA, mtrB* and *mtrC* respectively [92].
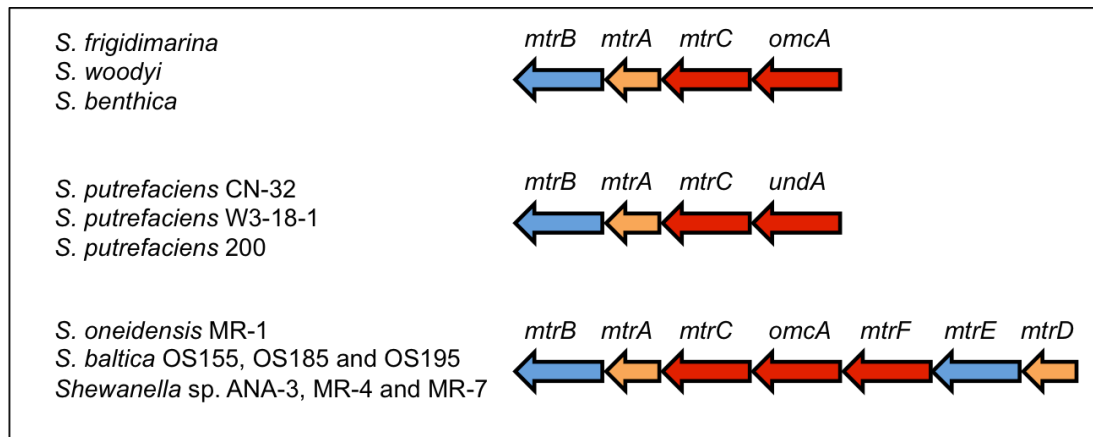
Figure 1.5 Occurrence of the three most common types of *mtr* gene cluster observed in the genomes of *Shewanellaceae*. Predicted outer membrane porins are coloured blue, outer membrane cytochromes are coloured red and cytochromes located at the periplasmic face of the outer membrane are coloured orange.

Shewanella pealeana and *Shewanella halifaxensis* encode outer membrane cytochromes *undB* and two variants of *omcA* (*omcA1* and *omcA2*) while *Shewanella loihica* PV4 encodes *mtrG*, all of which are additional outer membrane cytochromes compared to most *Shewanellaceae*. The three most common types of *mtr* gene clusters observed in species' of *Shewanella* are shown in figure 1.5.

The electron transfer pathways of *G. sulfurreducens* during iron respiration are less clear compared to *S. oneidensis*. A genomic analysis of six *Geobacter* species (*G. sulfurreducens, G. metallireducens, G.* sp. FRC-32*, G. Lovleyi, G. uraniumreducens* and *G. bemidjiensis*) revealed these organisms contained an average of 79 predicted *c*-type cytochromes, most of which are predicted to be multiheme cytochromes with an average of 7.7 hemes per predicted cytochrome [84]. This compares to 44 predicted cytochromes in *S. oneidensis* MR-1 and 7 in *E. coli*. Despite the abundance of multiheme cytochromes in these *Geobacter* species, few cytochromes were found to be conserved across all of the species [84]. The outer membrane cytochromes OmcE, OmcF, OmcS, OmcT, OmcX, OmcZ and predicted inner membrane cytochrome MacA have all been shown to be important to iron reduction in *G. sulfurreducens*, but these proteins are not well conserved [84]. Butler *et al.* (2010) suggested that unlike the *Shewanellaceae* there might not be a conserved electron transfer pathway that allows the *Geobacteraceae* to perform dissimilatory mineral reduction. A greater mechanistic diversity of iron-respiration in *Geobacter* species' certainly seems likely. However, homologs of the periplasmic cytochrome

PpcA and potential orthologs of the outer membrane multiheme cytochrome OmcB were identified in each of the six *G. sulfurreducens* genomes mentioned previously [84,85], making it possible these proteins are involved in a conserved electron transfer pathway. Liu *et al.* (2014) proposed a model for electron transfer across the outer membrane of *G. sulfurreducens* through a trans-outer membrane heterocomplex containing multiheme cytochromes OmaB and OmcB, which are held in the outer membrane of *G. sulfurreducens* by membrane protein OmbB (figure 1.6 B) [85]. The presence of a predicted multiheme cytochrome downstream of *omaB* is a conserved feature in these *Geobacter* species, although the encoded protein (OmcB) is not well conserved in terms of its sequence. Conceptually, this complex could function in a similar way to MtrCAB from *Shewanella oneidensis*.

There are a broad range of proposed electron transfer mechanisms in iron oxidising bacteria, some of which share similarity with previously studied iron reducing bacteria [35].

The most well characterised electron transfer chain thus far among the iron-oxidising bacteria is from *Acidothiobacillus ferroxydans*, which contains an outer membrane cytochrome iron oxidase and a network of periplasmic cytochromes that transfer electrons to the inner membrane. Elbehti *et al.* (2000) first proposed an intriguing respiratory electron transfer pathway for *A. ferroxydans,* which showed electron transfer to quinone reductase cytochrome bc_1 and directly to cytochrome *c* oxidase (figure 1.6 C). Further research has provided substantial advances in the understanding of the biochemistry and physiology of this acidophilic bacterium [57]. The model for electron transfer in *A. ferroxydans* has two pathways: an energetically favourable 'downhill' pathway to cytochrome *c* oxidase (shown as green lines in figure 1.6 C) and an energetically unfavourable 'uphill' pathway to cytochrome bc_1 and NADH dehydrogenase with both proteins functioning in reverse to produce NADH [57,93].

The outer membrane monoheme cytochrome Cyc 2 is utilised as an iron oxidase and translocates electrons from ferrous iron to the periplasm of *A. ferroxydans*. Omp40, a proposed 16-stranded β-barrel porin [94], which is localised to the outer membrane, is believed to play an important role in adhesion of *A. ferroxydans* to minerals such as pyrite (FeS_2) [94,95]. As an outer membrane porin, it is possible Omp40 forms an outer membrane complex with Cyc 2, similar to MtrAB from the *Shewanellaceae* (figure 1.6 A). The copper protein rustacyanin (RcY)

accepts electrons from Cyc 2 and is instrumental in connecting the two alternate electron transfer pathways. The low redox potentials of the UQ/UQH_2 (+100 mV) and $NAD^+/NADH$ (-320) couples makes the transfer of electrons from iron to these couples unfavourable under acidic conditions (E = +697 mV to +770 mV – table 1.2). However, this energetically unfavourable electron transfer pathway is essential for the generation of NADH, which is required by lithotrophic microorganisms to fix CO_2 [96]. Elbehti *et al* (2000) proposed the energy to drive this process is derived from the energetically favourable 'downhill' electron transfer pathway. Cytochrome *c* oxidase produces a proton motive force (PMF) of $4H^+$ per molecule of di-oxygen reduced to water [97], which could be supplemented by ATP hydrolysis (figure 1.6 C) to provide the energetic driving force necessary to reduce quinone by a reverse-functioning cytochrome bc_1, which in turn reduces NAD^+ to NADH.

It is clear this pathway bears a number of differences to the electron transfer pathway in the iron reducing bacterium *S. oneidensis* MR-1 (figure 1.6 A), although the possible formation of a Cyc 2/Omp40 outer membrane complex would be similar to the MtrAB component of the MtrCAB complex from the *Shewanellaceae*. The respiratory pathway in *A. ferroxydans* is also quite dissimilar to other acidophilic iron-oxidising bacteria, which have a wide-ranging variety of iron oxidases and mechanisms for transferring electrons to inner membrane redox proteins [35]. Despite this variety, the overall direction of electron transfer changes little, with respiratory pathways predominantly terminating at aa_3-type and bb_3-type cytochrome *c* oxidases with a secondary electron transfer pathway dedicated to supplying quinones with the reducing power to generate NADH [35]. The unusual *A. ferroxydans* electron transfer pathway could provide valuable insight into the respiratory pathways of other chemolithotrophic iron oxidising bacteria, since these bacteria must generate sufficient energy to drive the energetically unfavourable reduction of NAD^+ from Fe(II)/Fe(III) couples, all of which have higher redox potentials than $NAD^+/NADH$ (-320 mV) (table 1.2).

The electron transfer pathways of neutrophilic iron oxidising bacteria are of particular interest, not only because the physiology of these organisms is poorly understood, but also because there are potentially biotechnological applications for iron oxidising bacteria. For example, *A. ferroxydans* is a key bacterium in the industrial extraction of copper and uranium from ores [93,98], while more recent

research has focussed on the development of lithotrophic microbial fuel cells containing neutrophilic iron-oxidising bacteria [99].

At circumneutral pH aerobic iron oxidising bacteria must compete with aerobic autoxidation of ferrous iron, which has relegated these organisms to microaerobic niches. The two prime factors that contribute to the difficulty in working with neutrophilic iron oxidising bacteria in the laboratory are the need to grow them under microaerobic conditions and providing a steady flux of ferrous iron. The development of methods that satisfy these conditions to grow neutrophilic iron oxidising bacteria *in vitro* has been important in the current microbiological understanding of neutrophilic iron oxidising bacteria. Underpinning these methods is the use of opposing Fe^{2+}/O_2 gradients, which allow iron oxidising bacteria to grow microaerobically in the redox boundary formed at the interface between these two gradients [69,100]. The practical aspects of culturing neutrophilic iron oxidising bacteria using this technique will be described in further detail in chapter 5.

The current cultivation methods have shown that the neutrophilic iron oxidising bacteria *Sideroxydans lithotrophicus* ES-1 and *Galionella capsiferriformans* ES-2 are incapable of utilising organic substrates as a source of energy for growth in the absence of iron, nor has cell growth been stimulated by supplementing iron-containing media with acetate [69]. While the supplemented growth test is not extensive, the current evidence indicates both strains ES-1 and ES-2 are obligate chemolithotrophic organisms.

The current models of electron transfer in these organisms during lithotrophic growth on iron, presented previously by Shi *et al* (2012), are shown in figure 1.6 E and F. Both *S. lithotrophicus* (Figure 1.6 E) and *G. capsiferriformans* (figure 1.6 F) contain the outer membrane iron oxidase complex MtoAB, which is comprised of a trans-outer membrane porin MtoB and decaheme cytochrome MtoA. As the name suggests, MtoAB and MtrAB from the MtrCAB complex in *S. oneidensis* MR-1 perform similar functions (figure 1.6 A); MtoA is an iron oxidase whereas MtrA functions as part of an iron reductase complex [86]. MtoA was shown to be 42-44% identical to MtrA sequences from a range of *Shewanella* species' and 39% identical to the outer membrane iron oxidase PioA from the phototrophic iron oxidiser *Rhodopseudomonas palustris* TIE-1 (figure 1.6 D) [101]. In the same study, MtoB was shown to be 19-21% identical to MtrB from *Shewanella* species' and 17% identical to PioB, a predicted outer membrane porin from *R. palustris* [101]. The combination of

a multiheme cytochrome embedded in an outer membrane porin appears to be conserved in numerous iron oxidising and iron reducing bacteria (figure 1.6). [35].

The examples of iron reducing and iron oxidising electron transfer pathways shown in figure 1.6 demonstrate an intriguing diversity, which is reflected in the range of proteobacteria represented. The facultative anaerobic iron reducing bacteria *S. oneidensis* and the acidophilic iron oxidising bacterium *Acidothiobacillus ferroxydans* are both members of the gammaproteobacteria, which is perhaps not surprising given the gammaproteobacteria are one of the largest and most diverse classes of microorganisms, containing ~250 genera including *Escherichia*, *Salmonella*, *Pseudomonas, Acinetobacter* and *Yersinia* [102]. Extensive research over the last decade has led to a good understanding of the biochemistry and physiology of the electron transfer pathways of gammaproteobacteria *S. oneidensis* and *A. ferroxydans*, as can be seen from the detailed electron transfer models shown in figure 1.6 (A and D). Unlike *Shewanella*, the iron-reducing organism *G. sulfurreducens* is an obligate anaerobic member of the deltaproteobacteria, which contain many of the known sulfate and sulphur reducing bacteria as well as iron reducing bacteria [103]. The phylogenetic distance between *S. oneidensis* and *G. sulfurreducens* is accompanied by differences in the proteins believed to be involved in extracellular electron transfer in these organisms (figure 1.6 B) [49]. Despite this, both organisms have developed conceptually similar solutions to performing extracellular iron reduction. The same can be noted of *R. palustris*, a photoferrotrophic iron oxidising bacterium that belongs to the class alphaproteobacteria [68]. The phototrophic growth of *R. palustris* makes this bacterium distinct from the other organisms represented in figure 1.6, but the presence of the PioAB outer membrane protein complex bears similarity to the outer membrane complexes MtrAB, OmaB/OmbB and Cyc 2/Omp40 (figure 1.6 A-D). The sequence similarity between the *pio* and *mtr* gene clusters encoding outer membrane associated electron transfer proteins potentially supports common ancestry of these genes. The MtrAB proteins from *S. lithotrophicus* and *G. capsiferriformans* bear similarity to both the MtrAB and PioAB proteins.

The iron oxidising bacteria *S. lithotrophicus* ES-1 and *G. capsiferriformans* ES-2 are both members of the betaproteobacteria, a class closely related to the gammaproteobacteria [104] and contain numerous species' capable of lithotrophic growth under aerobic or nitrate-reducing conditions [105–107].
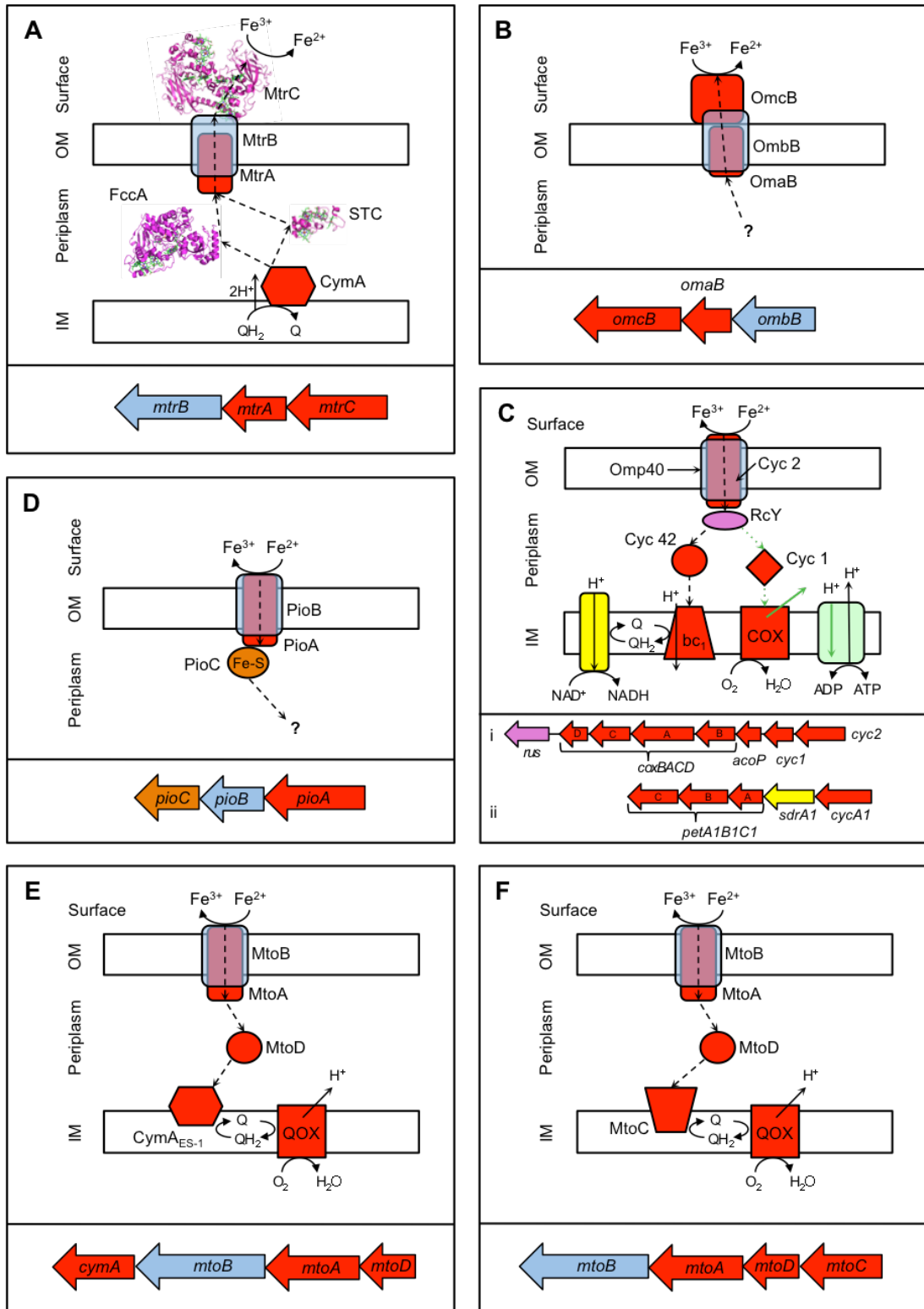
Figure 1.6 Current models of trans-membrane electron transfer in iron reducing and iron oxidising bacteria accompanied by gene clusters encoding their pathways. Iron reducing bacteria: *Shewanella oneidensis* MR-1 (**A**) and *Geobacter sulfurreducens* (**B**). Iron oxidising bacteria: *Rhodopseudomonas palustris* TIE-1 (**C**), *Acidothiobacillus ferroxydans* (**D**), *Sideroxydans lithotrophicus* ES-1 (**E**) and *Galionella capsiferriformans* ES-2 (**F**).

Thus far, investigations of the neutrophilic iron oxidising betaproteobacteria have been mostly limited to a number of microbiological studies and the current electron transfer models shown in figure 1.6 E and F are based primarily on bioinformatics approaches [41,42,74,100,101]. Current evidence indicates strains ES-1 and ES-2 are obligate lithotrophs and are incapable of coupling growth on Fe(II) to the reduction of nitrate [108].

The current models show electrons acquired from iron oxidation being transferred from MtoA to MtoD, a predicted monoheme class I cytochrome *c*, which is proposed to reduce predicted quinone reductases $CymA_{ES-1}$ (*S. lithotrophicus*) or MtoC (*G. capsiferriformans*). The close proximity (112 bp) of the *cymA_{ES-1}* gene to the *mtoDAB* gene cluster suggests $CymA_{ES-1}$ could be involved in electron transfer in the same pathway as MtoAB and MtoD. The *cymA_{ES-1}* gene is not conserved in *G. capsiferriformans* and instead multiheme cytochrome MtoC is encoded 51 bp upstream of *mtoD*. Shi *et al* (2012) proposed electrons from the quinol pool in *S. lithotrophicus* and *G. capsiferriformans* reduce a terminal oxidase that facilitates the reduction of O_2 to H_2O and generates a PMF (figure 1.6 E and F). An ATPase is not shown in the Shi (2012) model, but it is assumed the PMF generated at the terminal oxidase is used to generate ATP. The terminal quinol oxidase is not identified in either model and a mechanism for generating NADH for CO_2 fixation is not suggested. These points will be addressed in a more comprehensive model of electron transfer in the discussion of this thesis.

As a predicted class I cytochrome *c*, MtoD would be expected to have a redox potential more positive than quinone/quinol redox couples. The menaquinone/menaquinol (MQ/MQH_2) and ubiquinone/ubiquinol (UQ/UQH_2) redox couples for example have midpoint potentials at pH 7 of -70 mV and $+100$ mV respectively [107]. The redox potentials of class I cytochromes *c* are typically in the region of $+250$ mV [109,110]. Class I cytochromes *c* contain a single *c*-type heme cofactor that is normally axially ligated by a histidine and a methionine. His/Met-ligated hemes are known to produce higher redox potentials compared to heme cofactors with bis-histidinyl ligation [110]. In many organoheterotrophic organisms the high potential of the class I cytochrome *c* allows the oxidation of quinol dehydrogenase enzymes at the inner membrane and transfer of electrons to a terminal oxidase [29].

MtoD is an unusual class I cytochrome *c* because it is predicted to contain a bis-histidinyl ligated *c*-type heme cofactor. Few monoheme cytochromes *c* with bis-

His heme ligation have been characterised [31], however the redox potentials reported for these proteins have been as low as -250 to -280 mV [111]. Such a low redox potential would theoretically make electron transfer from MtoD to the Q-pool via CymA$_{ES-1}$ an energetically favourable process and would allow the generation of a PMF via a quinol oxidase (figure 1.6 E). However, if the redox potential of the MtoD heme were as low as -250 mV it would be nearly the same as that of ferrous iron couples at circumneutral pH (table 1.2), surely offering a weak drawing power to move electrons into the cell.

Alternatively, if the redox potential of the MtoD heme were as positive as the majority of previously characterised class I cytochromes c [31,110,112], electron transfer to the Q- pool via CymA$_{ES-1}$ would become energetically unfavourable, but the transfer of electrons from ferrous iron to MtoD would be much more favourable and might offer a greater energetic driving force to draw electrons into the cell than if MtoD were a low potential cytochrome. Given the requirement for high iron (II) flux for growth of neutrophilic iron oxidising bacteria [100], a high potential periplasmic cytochrome c might allow *S. lithotrophicus* and *G. capsiferriformans* to rapidly oxidise Fe(II) and compete with aerobic autoxidation of Fe(II). These organisms might utilise the PMF to drive the then energetically unfavourable reduction of the Q-pool as has been reported for electron transfer from Cyc 42 to the Q-pool via cytochrome bc_1 in *A. ferroxydans* (figure 1.6 C) [57].

Further analysis of the *S. lithotrophicus* and *G. capsiferriformans* genomes is required to search for other soluble cytochromes that might also be involved in electron shuttling. However, the abundance of genes encoding predicted cytochromes in iron-oxidising and iron-reducing bacteria makes such analyses challenging; experimental evidence of protein expression and localisation is required to identify periplasmic cytochromes.

Some of the present ambiguity surrounding electron transfer in *S. lithotrophicus* and *G. capsiferriformans* resides in the fact very little is known about MtoD and precisely what its role is during lithotrophic growth. This ambiguity extends to other iron-oxidising bacteria that contain the *mtoDAB* gene cluster. Knowledge of the redox properties of MtoD could provide further insight into the energetics associated with electron transfer from MtoA to the Q-pool and whether the redox potential of the MtoD heme is low enough to allow favourable electron transfer to the Q-pool via CymA$_{ES-1}$.

A structural and biophysical characterisation of MtoD is required to inform on the similarities between MtoD and other previously characterised class I cytochromes *c*. Equally interesting though are the potential structural differences, since MtoD is not expected to form His/Met axial heme ligation, which is unusual for a class I cytochrome *c*.

Organism name	E-value	
S. lith ES-1	–	------------MTRQAYSSMLLSTAAALTLAFSLNASAAVDVDAAKSLA 38
G. capsiferi	5e-32	----------------MKKQLAASIAFVLVTGLFSSAHAAIDEPAAKSLA 34
R. gelatinos	3e-31	--------------------MLITGLGLAAPAFAL------DEGAAEALV 24
A. toluclast	1e-29	-------------MQFRLNRMSLLVAATAA-IFASSSAFAVDADAAKSLA 36
D. aromatica	9e-29	-------------MKFGFARSALIAASAAAFLFTTAASAAVDEDAAKALA 37
B. JOSHI_001	2e-25	MPLRAPPLLKDAMSTLTHRHLFPTLAALLSAGLLALPAQAIDVDAAKALH 50
A. ferriredu	3e-25	--------------MFKSTLTIVSASLMLAFASVAPAHAAVDADAAQALF 36
Pol. Sp EUR3	6e-25	-------------------MVVLCG-----FMAGSIAHAQVDADAAKALL 26
S. hydrogeni	6e-25	--------------MKIHTTLVLTGSLVVALAGIAPAHAQVDEAAAQALA 36
		* **:**:*
S. lith ES-1	–	RENN**CFKCH**GVDKEKDGPSYKKVAEKYRGK-ADAEAKLIHHVTSGEKAKF 87
G. capsiferi	5e-32	KKND**CFKCH**AVDKTKKGPSYKKIAIKYKGK-ADAEVSLIKQITTGPKVKM 83
R. gelatinos	3e-32	RRNN**CLKCH**GVDKDKDGPSFQKTAKKYRGK-AGAVDRVVEHLTSGEKAKF 73
A. toluclast	1e-29	KEND**CFKCH**AIDKTKKGPSYKKIADKYKGKEAEGFEKIRKNITTGPKVKL 86
D. aromatica	9e-29	KKND**CFKCH**AIDKTKKGPAYKKIAAKYKGKEAEGEQKMIKNITTGPKVKL 87
B. JOSHI_001	2e-25	KKND**CAKCH**ATDKDKKGPSLKKIADKYRGK-PDGEEKAIKNMTTGPKVKL 99
A. ferriredu	3e-25	KKND**CTKCH**SVDKTKKGPSLKKIAAKYKGK-ADGQEKVIKNITTGPKVKL 85
Pol. Sp EUR3	6e-25	KKSG**CMKCH**AIDKKKEGPPYQEVAKKYKGK-ADAQEKLFTHITTGPKIKI 75
S. hydrogeni	6e-25	KKND**CFKCH**AVDKTKKGPSYKKIAAKYKEK-KLGEKEAIKQMTTSPKVKL 85
		:...* ***. ** *.**. :: * **: * . ::*:. * *:
S. lith ES-1	–	PDGHEEE**H**KNINGKASPEAIKNLVDWILSL 117
G. capsiferi	5e-32	EDGTEEN**H**KIIE-TKDQSEIKNLVGWILSL 112
R. gelatinos	3e-32	PDGHEED**H**KIVR--AERADLENLAQWILSR 101
A. toluclast	1e-29	EDGTEED**H**KIIN-TKDEAQIKNLMQWILSQ 115
D. aromatica	9e-29	EDGTEED**H**KIID-TKDQAEIKNLVHWILSL 116
B. JOSHI_001	2e-25	DDGTEEE**H**KIIK-TNDPAELKNLAQWILSH 128
A. ferriredu	3e-25	DDGSEEE**H**KIID-SKDPAALKNVADWILSQ 114
Pol. Sp EUR3	6e-25	D-GKEEE**H**TIIK-SKDKAEITNAIQWILSL 103
S. hydrogeni	6e-25	EDGTEED**H**KNIE-TRDPKELSNLAQWILSR 114
		* **:*. : . : * ****

Figure 1.7 Alignment of the full MtoD polypeptide sequence with similar protein sequences determined by BTAST analysis [113] **revealed numerous predicted class I cytochromes *c* with potentially important conserved regions.** The conserved CXXCH heme-binding motif is shown in bold, conserved lysine residues are shown in blue and the conserved histidine residue is shown in green. Organism names: *Sideroxydans lithotrophicus* ES-1; *Galionella capsiferriformans* ES-2; *Rubrivivax gelatinosus*; *Azoarcus toluclasticus*; *Dechloromonas aromatic*; *Burkholderiales bacterium* JOSHI_001; *Albidiferax ferrireducens*; *Polaromonas* sp. EUR3 1.2.1; *Sulfuritalea hydrogenivorans*.

A preliminary sequence alignment of the full MtoD polypeptide sequence against all other non-redundant protein sequences using ClustalO [114] revealed a number of conserved regions (figure 1.7). The CXXCH motif, which is associated with covalent attachment of *c*-type heme cofactors, was conserved in all sequences as 'CXKCH'. Numerous lysine residues are also conserved in homologues of MtoD. Given lysine residues are important to the formation of electrostatic interactions

between class I cytochromes *c* and cytochrome *c* oxidase, it is possible this conserved arrangement of lysine residues could give MtoD a conserved binding site, or perhaps binding sites if MtoD is capable of interacting with several redox partners. A single histidine residue (H95) is conserved in all of the homologous MtoD sequences near the C-terminal end of the polypeptides where the distal methionine heme ligand is located in class I cytochromes *c* [31], making this residue the most likely distal heme ligand.

Sequence alignment of MtoD with cytochrome *c* from horse heart (Appendix figure X1) demonstrates the conservation of the *c*-type heme-binding motif in class I cytochromes *c* and highlights a number of conserved lysine residues. In addition to the role lysine residues play in the formation of electrostatic interactions between cytochrome *c* and cytochrome *c* oxidase, there is also evidence for lysine residues playing a role in conformational rearrangements under alkaline conditions [112]. It is possible lysine conservation in MtoD could be important for both functions.

1.4   Aims of the project

Work in this thesis presents the expression and purification of His-tagged (MtoD-His) and Strep II-tagged (MtoD-Strep) MtoD from *S. lithotrophicus* ES-1 followed by the biochemical, spectroscopic, biophysical, structural and redox characterisations. This work aimed to probe the structure and redox properties of MtoD in order to validate its proposed function as a periplasmic electron shuttle capable of accepting electrons from MtoA and supplying these electrons to respiratory cytochromes at the inner membrane of *S. lithotrophicus* and *G. capsiferriformans*. Greater cultivation yields of iron oxidising bacteria, compared to previously published results [69] are required to experimentally probe the cytochrome content of *S. lithotrophicus*, which could potentially provide the first insights towards validating the current model of electron transfer during lithotrophic growth.

1.5   References

1.   Brimblecombe, P. *The Global Sulfur Cycle. Treatise Geochemistry Second Ed.* **10,** (Elsevier Ltd., 2013).

2.   Wedepohl, K. H. Composition of the Continental Crust. *Geochemica Cosmochim. Acta* **59,** 1217–1232 (1995).

3.   Kump, L. R. The rise of atmospheric oxygen. *Nature* **451,** 277–278 (2008).

4.   Galloway, J. N. *et al. Nitrogen Cycles: Past, Present, and Future. Biogeochemistry* (2004). doi:10.1007/s10533-004-0370-0

5.   Ochiai, E. I. *General Principles of Biochemistry of the Elements.* (Springer US, 2012). at <https://books.google.co.uk/books?id=kzzjBwAAQBAJ>

6.   Fahey, T. J. *et al.* The biogeochemistry of calcium at Hubbard Brook. **41,** 89–173 (2014).

7.   Edwards, H. G. M., Villar, S. E. J., Jehlicka, J. & Munshi, T. FT-Raman spectroscopic study of calcium-rich and magnesium-rich carbonate minerals. *Spectrochim. Acta - Part A Mol. Biomol. Spectrosc.* **61,** 2273–2280 (2005).

8.   Jahnen-Dechent, W. & Ketteler, M. Magnesium basics. *CKJ Clin. Kidney J.* **5,** (2012).

9.   Clapham, D. E. Calcium signaling. *Cell* **80,** 259–268 (1995).

10.   Clapham, D. E. Calcium Signaling. *Cell* **131,** 1047–1058 (2007).

11.   Pettersson, J. *et al.* Modulation of virulence factor expression by pathogen target cell contact. *Science* **273,** 1231–1233 (1996).

12.   Sanders, D., Brownlee, C. & Harper, J. Communicating with calcium. *Plant Cell* **11,** 691–706 (1999).

13.   Whitaker, M. Calcium and mitosis. *Prog. Cell Cycle Res.* **3,** 261–269 (1997).

14.   Ikura, M., Osawa, M. & Ames, J. B. The role of calcium-binding proteins in the control of transcription: structure to function. *Bioessays* **24,** 625–636 (2002).

15.   Tebo, B. M., Johnson, H. a., McCarthy, J. K. & Templeton, A. S. Geomicrobiology of manganese(II) oxidation. *Trends Microbiol.* **13,** 421–428 (2005).

16.   Lawrance, G. A. *Introduction to Coordination Chemistry.* (Wiley, 2013). at <https://books.google.co.uk/books?id=40NWXyI7DskC>

17.   Keilin, D. & Mann, T. Activity of Purified Carbonic Anhydrase. *Nature* **153,** (1944).

18.   Vallee, B. L. Biochemistry, Physiology and Pathology of Zinc. *Physiol Rev* **39,** 443–490 (1959).

19.   Zajic, J. *Microbial Biogeochemistry.* (Academic Press, 1969).

20.   Hantke, K. Iron and metal regulation in bacteria. *Curr. Opin. Microbiol.* **4,** 172–177 (2001).

21.   Gadd, G. M. Metals, minerals and microbes: Geomicrobiology and bioremediation. *Microbiology* **156,** 609–643 (2010).

22. Rauch, J. N. & Graedel, T. E. Earth's anthrobiogeochemical copper cycle. *Global Biogeochem. Cycles* **21,** 1–13 (2007).

23. Peterson, R. L., Kim, S. & Karlin, K. D. *Copper Enzymes. Compr. Inorg. Chem. II (Second Ed. From Elem. to Appl.* **3,** (Elsevier Ltd., 2013).

24. Guss, J. M., Bartunik, H. D. & Freeman, H. C. Accuracy and precision in protein structure analysis: restrained least-squares refinement of the structure of poplar plastocyanin at 1.33 A resolution. *Acta Crystallogr. B.* **48,** (1992).

25. Baker, E. N. Structure of azurin from Alcaligenes denitrificans refinement at 1.8 A resolution and comparison of the two crystallographically independent molecules. *J. Mol. Biol.* **203,** 1071–1095 (1988).

26. Kendall, B., Anbar, A. D., Kappler, A. & Konhauser, K. O. The Global Iron Cycle. *Fundam. Geobiol.* 65–92 (2012). doi:10.1002/9781118280874.ch6

27. Papanikolaou, G. & Pantopoulos, K. Iron metabolism and toxicity. *Toxicol. Appl. Pharmacol.* **202,** 199–211 (2005).

28. Beinert, H., Holm, R. H. & Mu, E. Iron-Sulfur Clusters : Nature ' s Modular , Multipurpose Structures. **277,** (1997).

29. Thöny-Meyer, L. Biogenesis of respiratory cytochromes in bacteria. *Microbiol. Mol. Biol. Rev.* **61,** 337–76 (1997).

30. Pettigrew, G. W. & Moore, G. R. *Cytochromes c: Biological Aspects.* (1987).

31. Moore, G. & Pettigrew, G. *Cytochromes c: Evolutionary, Structural and Physicochemical Aspects.* (Springer-Verlag, 1990).

32. Kern, M. & Simon, J. Electron transport chains and bioenergetics of respiratory nitrogen metabolism in Wolinella succinogenes and other Epsilonproteobacteria. *Biochim. Biophys. Acta* **1787,** 646–56 (2009).

33. Shirodkar, S., Reed, S., Romine, M. & Saffarini, D. The octahaem SirA catalyses dissimilatory sulfite reduction in Shewanella oneidensis MR-1. *Environ. Microbiol.* **13,** 108–15 (2011).

34. Clarke, T. a *et al.* Escherichia coli cytochrome c nitrite reductase NrfA. *Methods Enzymol.* **437,** 63–77 (2008).

35. Ilbert, M. & Bonnefoy, V. Insight into the evolution of the iron oxidation pathways. *Biochim. Biophys. Acta - Bioenerg.* **1827,** 161–175 (2013).

36. Boyd, P. W. & Ellwood, M. J. The biogeochemical cycle of iron in the ocean. *Nat. Geosci.* **3,** 675–682 (2010).

37. Al, A., Meriç, G., Akkurt, F. & Olcay, Ş. Air Oxidation of Ferrous Iron in Water. *J. Int. Environ. Appl. Sci.* **3,** 409–414 (2008).

38. Michel, F. M. *et al.* Ordered ferrimagnetic form of ferrihydrite reveals links among structure, composition, and magnetism. *Proc. Natl. Acad. Sci. U. S. A.* **107,** 2787–2792 (2010).

39. Singer, P. C. & Stumm, W. Acidic mine drainage: the rate-determining step. *Science* **167,** 1121–1123 (1970).

40. Druschel, G. K., Emerson, D., Sutka, R., Suchecki, P. & Luther, G. W. Low-oxygen and chemical kinetic constraints on the geochemical niche of neutrophilic iron(II) oxidizing microorganisms. *Geochim. Cosmochim. Acta* **72,** 3358–3370 (2008).

41. Benz, M., Brune, A. & Schink, B. Anaerobic and aerobic oxidation of ferrous iron at neutral pH by chemoheterotrophic nitrate-reducing bacteria. *Arch. Microbiol.* **169,** 159–165 (1998).

42. Blöthe, M. & Roden, E. E. Composition and activity of an autotrophic Fe(II)-oxidizing, nitrate-reducing enrichment culture. *Appl. Environ. Microbiol.* **75,** 6937–40 (2009).

43. Jiao, Y. & Newman, D. K. The pio operon is essential for phototrophic Fe(II) oxidation in Rhodopseudomonas palustris TIE-1. *J. Bacteriol.* **189,** 1765–1773 (2007).

44. Chan, C. S. *et al.* Microbial Polysaccharides Template Assembly of Nanocrystal Fibers. *Science (80-.).* **303,** 1656–1658 (2004).

45. Mikutta, C. *et al.* Synthetic coprecipitates of exopolysaccharides and ferrihydrite. Part I: Characterization. *Geochim. Cosmochim. Acta* **72,** 1111–1127 (2008).

46. Emerson, D., Fleming, E. J. & McBeth, J. M. Iron-oxidizing bacteria: an environmental and genomic perspective. *Annu. Rev. Microbiol.* **64,** 561–583 (2010).

47. Roden, E. E. *et al.* The microbial ferrous wheel in a neutral pH groundwater seep. *Front. Microbiol.* **3,** 1–18 (2012).

48. Ross, D. E., Brantley, S. L. & Tien, M. Kinetic characterization of OmcA and MtrC, terminal reductases involved in respiratory electron transfer for dissimilatory iron reduction in Shewanella oneidensis MR-1. *Appl. Environ. Microbiol.* **75,** 5218–26 (2009).

49. Shi, L. *et al.* The roles of outer membrane cytochromes of Shewanella and Geobacter in extracellular electron transfer. *Environ. Microbiol. Rep.* **1,** 220–227 (2009).

50. Marsili, E. *et al.* Shewanella secretes flavins that mediate extracellular electron transfer. *Proc. Natl. Acad. Sci. U. S. A.* **105,** 3968–73 (2008).

51. Lies, D. P. *et al.* Shewanella oneidensis MR-1 Uses Overlapping Pathways for Iron Reduction at a Distance and by Direct Contact under Conditions Relevant for Biofilms Shewanella oneidensis MR-1 Uses Overlapping Pathways for Iron Reduction at a Distance and by Direct Contact. *Appl. Environ. Microbiol.* **71,** 4414–4426 (2005).

52. Gorby, Y. a *et al.* Electrically conductive bacterial nanowires produced by Shewanella oneidensis strain MR-1 and other microorganisms. *Proc. Natl. Acad. Sci. U. S. A.* **103,** 11358–63 (2006).

53. Reguera, G. *et al.* Extracellular electron transfer via microbial nanowires. *Nature* **435,** 1098–1101 (2005).

54. Malvankar, N. S. & Lovley, D. R. Microbial Nanowires: A New Paradigm for Biological Electron Transfer and Bioelectronics. *ChemSusChem* **5,** 1039–1046 (2012).

55. Lovley, D. R. & Coates, J. D. Novel forms of anaerobic respiration of environmental relevance. *Curr. Opin. Microbiol.* **3,** 252–6 (2000).

56. Galushko, A. S. & Schink, B. Oxidation of acetate through reactions of the citric acid cycle by Geobacter sulfurreducens in pure culture and in syntrophic

coculture. *Arch. Microbiol.* **174,** 314–321 (2000).

57. Roger, M. *et al.* Mineral respiration under extreme acidic conditions: from a supramolecular organization to a molecular adaptation in Acidithiobacillus ferrooxidans. *Biochem. Soc. Trans.* **40,** 1324–9 (2012).

58. Johnson, D. B. & McGinness, S. Ferric iron reduction by acidophilic heterotrophic bacteria. *Appl. Environ. Microbiol.* **57,** 207–211 (1991).

59. Baker, B. J. & Banfield, J. F. Microbial communities in acid mine drainage. *FEMS Microbiol. Ecol.* **44,** 139–152 (2003).

60. Borch, T. *et al.* Biogeochemical redox processes and their impact on contaminant dynamics. *Environ. Sci. Technol.* **44,** 15–23 (2010).

61. Sessions, A. L., Doughty, D. M., Welander, P. V., Summons, R. E. & Newman, D. K. The Continuing Puzzle of the Great Oxidation Event. *Curr. Biol.* **19,** R567–R574 (2009).

62. Olson, J. M. Photosynthesis in the Archean era. *Photosynth. Res.* **88,** 109–117 (2006).

63. Farquhar, J., Zerkle, A. L. & Bekker, A. Geological constraints on the origin of oxygenic photosynthesis. *Photosynth. Res.* **107,** 11–36 (2011).

64. Des Marais, D. J., Strauss, H., Summons, R. E. & Hayes, J. M. Carbon isotope evidence for the stepwise oxidation of the Proterozoic environment. *Nature* **359,** 605–609 (1992).

65. Emerson, D. *et al.* A novel lineage of proteobacteria involved in formation of marine Fe-oxidizing microbial mat communities. *PLoS One* **2,** (2007).

66. Holland, H. D., Lazar, B. & McCaffrey, M. Evolution of the atmosphere and oceans. *Nature* **320,** 27–33 (1986).

67. Emerson, D. Biogeochemistry and microbiology of microaerobic Fe(II) oxidation. *Biochem. Soc. Trans.* **40,** 1211–6 (2012).

68. Hedrich, S., Schlömann, M. & Johnson, D. B. The iron-oxidizing proteobacteria. *Microbiology* **157,** 1551–64 (2011).

69. Emerson, D. & Moyer, C. Isolation and characterization of novel iron-oxidizing bacteria that grow at circumneutral pH. *Appl. Environ. Microbiol.* **63,** 4784–4792 (1997).

70. Hallbeck, L. & Pedersen, K. Culture parameters regulating stalk formation and growth rate of Gallionella ferruginea. *J. Gen. Microbiol.* **136,** 1675–1680 (1990).

71. Wheatley, R. E. Ochre deposits and associated bacteria in some field drains in Scotland. *J. Soil Sci.* **39,** 253–264 (1988).

72. Barbic, F. F., Bracilovic, D. M. & Djindjic, M. V. Iron and manganese bacteria in Ranney wells. *Water Res.* **8,** 895–898 (1974).

73. Cullimore, D. & McCann, A. in *Aquat. Microbiol.* (Skinner, F. & Shewan, J.) 219–261 (London: Academic Press, 1978).

74. Emerson, D. & Moyer, C. L. Neutrophilic Fe-oxidizing bacteria are abundant at the Loihi Seamount hydrothermal vents and play a major role in Fe oxide deposition. *Appl. Environ. Microbiol.* **68,** 3085–3093 (2002).

75. Singer, E. *et al.* Mariprofundus ferrooxydans PV-1 the first genome of a marine Fe(II) oxidizing Zetaproteobacterium. *PLoS One* **6,** (2011).

76. Chan, C. S., Emerson, D. & Edwards, K. J. Biomineralogy and Morphology of the Marine Iron-oxidizing Bacterium Mariprofundus ferrooxydans. *Am. Geophys. Union, Fall Meet. 2006, Abstr. #V31E-07* (2006).

77. Summers, Z. M., Gralnick, J. A. & Bond, D. R. Cultivation of an Obligate Fe (II)-Oxidizing Lithoautotrophic Bacterium Using Electrodes. *MBio* **4,** (2013).

78. Roden, E. E., Sobolev, D., Glazer, B. & Luther, G. W. Potential for Microscale Bacterial Fe Redox Cycling at the Aerobic-Anaerobic Interface. *Geomicrobiol. J.* **21,** 379–391 (2004).

79. Roden, E. E. & Jin, Q. Thermodynamics of microbial growth coupled to metabolism of glucose, ethanol, short-chain organic acids, and hydrogen. *Appl. Environ. Microbiol.* **77,** 1907–1909 (2011).

80. Berg, J. M., Tymoczko, J. L. & Stryer, L. *Biochemistry*. (W H Freeman, 2002).

81. Nicholls, D. G. & Ferguson, S. J. *Bioenergetics*. (Academic Press, 2002).

82. Hartshorne, R. S. *et al.* Characterization of an electron conduit between bacteria and the extracellular environment. *Proc. Natl. Acad. Sci. U. S. A.* **106,** 22169–74 (2009).

83. Ross, D. E. *et al.* Characterization of protein-protein interactions involved in iron reduction by Shewanella oneidensis MR-1. *Appl. Environ. Microbiol.* **73,** 5797–808 (2007).

84. Butler, J. E., Young, N. D. & Lovley, D. R. Evolution of electron transfer out of the cell: comparative genomics of six Geobacter genomes. *BMC Genomics* **11,** 40 (2010).

85. Liu, Y. *et al.* A trans-outer membrane porin-cytochrome protein complex for extracellular electron transfer by   G   eobacter sulfurreducens PCA. *Environ. Microbiol. Rep.* **6,** 776–785 (2014).

86. White, G. F. *et al.* Rapid electron exchange between surface-exposed bacterial cytochromes and Fe(III) minerals. *Proc. Natl. Acad. Sci. U. S. A.* **110,** 6346–51 (2013).

87. Hartshorne, R. S. *et al.* Characterization of Shewanella oneidensis MtrC: a cell-surface decaheme cytochrome involved in respiratory electron transport to extracellular electron acceptors. *J. Biol. Inorg. Chem.* **12,** 1083–94 (2007).

88. Marritt, S. J. *et al.* A functional description of CymA, an electron-transfer hub supporting anaerobic respiratory flexibility in Shewanella. *Biochem. J.* **444,** 465–74 (2012).

89. Myers, J. M. & Myers, C. R. Role of the Tetraheme Cytochrome CymA in Anaerobic Electron Transport in Cells of Shewanella putrefaciens MR-1 with Normal Levels of Menaquinone Role of the Tetraheme Cytochrome CymA in Anaerobic Electron Transport in Cells of Shewanella putrefaciens MR-1. (2000). doi:10.1128/JB.182.1.67-75.2000.Updated

90. Shi, L. *et al.* Molecular Underpinnings of Fe(III) Oxide Reduction by Shewanella Oneidensis MR-1. *Front. Microbiol.* **3,** 50 (2012).

91. Edwards, M. J. *et al.* The X-ray crystal structure of Shewanella oneidensis OmcA reveals new insight at the microbe-mineral interface. *FEBS Lett.* **588,** 1886–1890 (2014).

92. Fredrickson, J. K. *et al.* Towards environmental systems biology of Shewanella. *Nat. Rev. Microbiol.* **6,** 592–603 (2008).

93. Elbehti, A., Brasseur, G. & Lemesle-Meunier, D. First Evidence for Existence of an Uphill Electron Transfer through the bc1 and NADH-Q Oxidoreductase Complexes of the Acidophilic Obligate Chemolithotrophic Ferrous Ion-Oxidizing Bacterium Thiobacillus ferrooxidans. *J. Bacteriol.* **182,** 3602–3606 (2000).

94. Guiliani, N. & Jerez, C. a. Molecular cloning, sequencing, and expression of omp-40, the gene coding for the major outer membrane protein from the acidophilic bacterium Thiobacillus ferrooxidans. *Appl. Environ. Microbiol.* **66,** 2318–2324 (2000).

95. Arredondo, R., Garcia, a. & Jerez, C. a. Partial removal of lipopolysaccharide from Thiobacillus ferrooxidans affects its adhesion to solids. *Appl. Environ. Microbiol.* **60,** 2846–2851 (1994).

96. Shively, J. M., van Keulen, G. & Meijer, W. G. Something from almost nothing: carbon dioxide fixation in chemoautotrophs. *Annu. Rev. Microbiol.* **52,** 191–230 (1998).

97. Rauhamaki, V., Bloch, D. a. & Wikstrom, M. Mechanistic stoichiometry of proton translocation by cytochrome cbb3. *Proc. Natl. Acad. Sci.* **109,** 7286–7291 (2012).

98. Meurant, G. *Advances In Organic Chemistry*. (Elsevier Science, 1991).

99. Nguyen, T. T. *et al.* A lithotrophic microbial fuel cell operated with pseudomonads-dominated iron-oxidizing bacteria enriched at the anode. *Microb. Biotechnol.* n/a–n/a (2015). doi:10.1111/1751-7915.12267

100. Emerson, D. & Floyd, M. M. Enrichment and isolation of iron-oxidizing bacteria at neutral pH. *Methods Enzymol.* **397,** 112–23 (2005).

101. Liu, J. *et al.* Identification and Characterization of MtoA: A Decaheme c-Type Cytochrome of the Neutrophilic Fe(II)-Oxidizing Bacterium Sideroxydans lithotrophicus ES-1. *Front. Microbiol.* **3,** 37 (2012).

102. Williams, K. P. *et al.* Phylogeny of Gammaproteobacteria. *J. Bacteriol.* **192,** 2305–2314 (2010).

103. Mussmann, M., Ishii, K., Rabus, R. & Amann, R. Diversity and vertical distribution of cultured and uncultured Deltaproteobacteria in an intertidal mud flat of the Wadden Sea. *Environ. Microbiol.* **7,** 405–418 (2005).

104. Dworkin, M., Falkow, S., Rosenberg, E., Schleifer, K. H. & Stackebrandt, E. *The Prokaryotes: Vol. 5: Proteobacteria: Alpha and Beta Subclasses*. (Springer New York, 2006). at <https://books.google.co.uk/books?id=sTsC65kCJbUC>

105. Straub, K. L. *et al.* Anaerobic, Nitrate-Dependent Microbial Oxidation of Ferrous Iron. **62,** (1996).

106. Ghosh, W. & Dam, B. Biochemistry and molecular biology of lithotrophic sulfur oxidation by taxonomically and ecologically diverse bacteria and

archaea. *FEMS Microbiol. Rev.* **33,** 999–1043 (2009).

107. Beckwith, C. R. *et al.* Characterization of MtoD from Sideroxydans lithotrophicus: a cytochrome c electron shuttle used in lithoautotrophic growth. *Front. Microbiol.* **6,** (2015).

108. Emerson, D. *et al.* Comparative genomics of freshwater Fe-oxidizing bacteria: implications for physiology, ecology, and systematics. *Front. Microbiol.* **4,** 254 (2013).

109. Dolla, a, Blanchard, L., Guerlesquin, F. & Bruschi, M. The protein moiety modulates the redox potential in cytochromes c. *Biochimie* **76,** 471–479 (1994).

110. Zheng, Z. & Gunner, M. R. Analysis of the electrochemistry of hemes with E(m)s spanning 800 mV. *Proteins* **75,** 719–34 (2009).

111. Kerfeld, C. a. *et al.* Structural and EPR characterization of the soluble form of cytochrome c-550 and of the psbV2 gene product from the cyanobacterium Thermosynechococcus elongatus. *Plant Cell Physiol.* **44,** 697–706 (2003).

112. Barker, P. D. & Ma, A. G. pH-Linked Conformational Regulation of a Metalloprotein Oxidation-Reduction Equilibrium : Electrochemical Analysis of the Alkaline Form of Cytochrome c. *J. Am. Chem. Soc.* **114,** 3619–3624 (1992).

113. Madden, T. The BLAST sequence analysis tool. *BLAST Seq. Anal. Tool* 1–17 (2013). at <http://www.ncbi.nlm.nih.gov/books/NBK153387/>

114. Sievers, F. *et al.* Fast, scalable generation of high-quality protein multiple sequence alignments using Clustal Omega. *Mol. Syst. Biol.* **7,** (2011).

Chapter 2

Design of MtoD expression constructs, expression, purification and initial characterisation of MtoD in *Shewanella oneidensis* MR-1.

Work presented in this chapter has been published in the following paper:

Beckwith CR, Edwards MJ, Lawes M, Shi L, Butt JN, Richardson DJ and Clarke TA (2015) **Characterization of MtoD from *Sideroxydans lithotrophicus*: a cytochrome *c* electron shuttle used in lithoautotrophic growth**. Front. Microbiol. 6:332. doi: 10.3389/fmicb.2015.00332

2.1 Abstract

Sideroxydans lithotrophicus ES-1 acquires the energy necessary for growth by coupling the oxidation of extracellular ferrous iron to the reduction of oxygen to water at the inner membrane under microaerophilic conditions. Work to gain insight into the electron transfer pathway that enables this process resulted in the discovery of a homologue of the well studied outer membrane decaheme cytochrome/porin complex MtrAB from *Shewanella oneidensis* MR-1 [1,2,3,4,5]. The homologues *mtoA* and *mtoB* are located in a gene cluster with a predicted homologue of the quinol dehydrogenase CymA from *Shewanella* as well as a gene encoding a predicted monoheme cytochrome *c*, designated *mtoD*. The primary structure of MtoD contains a single CXXCH *c*-type heme-binding motif and, unusually for a class I cytochrome *c*, was predicted to have bis-His axial heme ligation, rather than the common His/Met ligation. To probe the nature of the role MtoD plays in the electron transfer network of *S. lithotrophicus,* the MtoD protein was expressed, purified and comprehensively characterised. Chapter 2 describes the production of plasmid-based genetic constructs for the expression of His-tagged MtoD and Strep II-tagged MtoD (MtoD-His and MtoD-Strep) in *Shewanella oneidensis* MR-1, in addition to the purification and initial characterisation of MtoD to validate some of the predicted features of the protein. Purified MtoD produced UV-visible spectra typical of a *c*-type cytochrome containing low-spin heme iron lacking methionine ligation. Pyridine hemochrome analysis coupled with total protein assays showed an approximate 1:1 ratio of heme/protein, confirming MtoD as a monoheme cytochrome. Mass spectrometry and N-terminal sequencing results corroborated and confirmed the cleavage of a 27-residue signal peptide, producing a mature *c*-type cytochrome 90 residues in length containing a single heme.

2.2   Introduction

The gene encoding MtoD (locus *Slit_2498*) from *Sideroxydans lithotrophicus* ES-1 resides in a gene cluster, designated the '*mto* gene cluster', which is implicated in the process of generating metabolic energy from the oxidation of extracellular ferrous iron [6,1]. The discovery of this gene cluster came about as the result of a genome-wide search for open reading frames (ORFs) that produced similar peptide products to the protein complexes MtrAB and PioAB [1]. MtrAB forms the transmembrane component of the outer membrane protein complex MtrCAB, which has been extensively studied in the iron-reducing bacteria *Shewanella oneidensis* MR-1, although homologues are present in other species' of *Shewanella* and related organisms including *Rhodoferax ferrireducens*, *Aeromonas hydrophila* and *Femeniasia balearica*, as demonstrated in figure 2.1 [7]. MtrAB is required to allow electrons to traverse the outer membrane during dissimilatory mineral reduction, with MtrA being a decaheme cytochrome capable of rapid electron transfer and MtrB being a transmembrane β-barrel porin, which holds MtrA at the periplasmic face of the outer membrane [2,8,4]. PioAB, a homologue of MtrAB, has been shown to be a critical component of the iron-oxidising pathway in the phototrophic iron oxidising bacterium *Rhodopseudomonas palustris* TIE-1 [9].

The *mto* gene cluster encodes four predicted proteins: a predicted monoheme cytochrome *c* with bis-His heme ligation (MtoD – primary structure shown in figure 2.2), a decaheme cytochrome of the MtrA family (MtoA), a predicted decaheme-associated outer membrane porin of the MtrB/PioB family (MtoB) and a predicted tetraheme *c*-type cytochrome of the NapC/NirT family (CymA$_{ES-1}$) [1,7]. The protein products MtoA, MtoB and CymA$_{ES-1}$ are believed to perform homologous roles to MtrA, MtrB and CymA from *Shewanella oneidensis*, albeit with electron transfer occurring in the opposite direction.

mtoD homologues are absent from the *mtr* gene cluster of *Shewanella* and the *pio* gene cluster of *Rhodopseudomonas. Shewanella*, and other related organisms with the ability to perform dissimilatory mineral reduction, contain one or several genes encoding outer membrane cytochromes (OMCs) in place of *mtoD*.
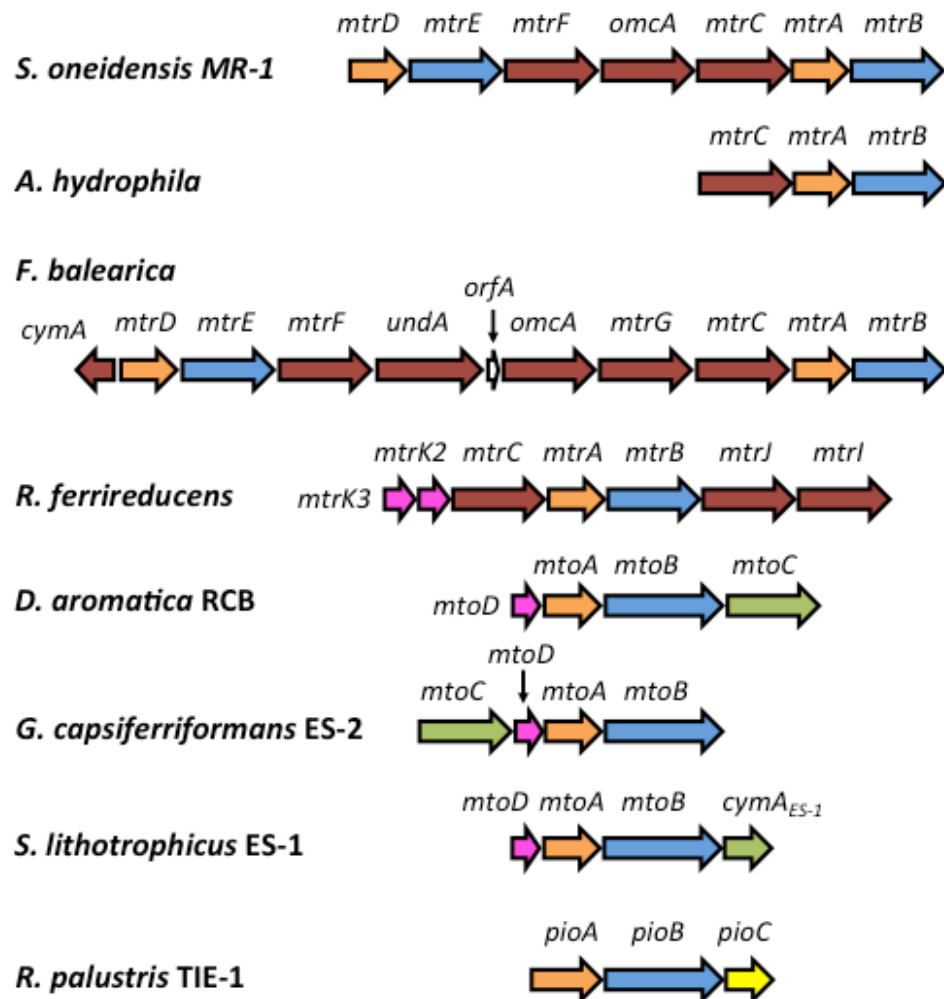
Figure 2.1 Adapted from Shi *et al.* (2012) – the genetic organisation of *mtr* and *mto* gene clusters from iron reducing and iron oxidising bacteria respectively, showing relative positions and sizes of genes. Colouring indicates protein function as follows: red – predicted outer membrane cytochromes; blue – predicted trans-outer membrane porins; orange – periplasm/porin-associated cytochromes; magenta – predicted monoheme cytochromes; green – predicted inner membrane-associated quinone reductases; *pioC*, coloured yellow, is a predicted FeS protein.

In *Shewanella oneidensis* MR-1 these Omcs are encoded by *mtrF, omcA* and *mtrC* and their respective proteins (MtrF, OmcA and MtrC) have been extensively studied and have available crystal structures in the protein databank (PDB) [10–12]. However, the presence of the *mtoD* gene is a common feature among some neutrophilic iron oxidising lithotrophs, such as *Sideroxydans lithotrophicus* ES-1, *Gallionella capsiferriformans* ES-2 and *Dechloromonas aromatica* RCB [7]. In addition to the *mtoD* genes previously discovered by Liu *et al* (2012), a BLAST search using the pre-MtoD polypeptide sequence to identify ORFs with similar structure to MtoD from *S. lithotrophicus* revealed a number of cytochrome *c*

homologues from other proteobacteria [1]. These organisms included the iron reducing bacterium Albidiferax ferrireducens, although homologues of *mtoD* were also observed in bacteria not implicated in iron cycling, including *A. toluclasticus*, which obtains energy by oxidising aromatic compounds and the facultative photoheterotroph *Rubrivivax gelatinosus*. Homologues of the *mtoD* gene encode class I cytochromes *c* with predicted bis-His axial heme ligation, however the exact function(s) MtoD performs in the cell is somewhat ambiguous. Liu *et al* (2012) proposed MtoD could play a shuttling role in the periplasm, transferring electrons from the outer membrane-associated decaheme cytochrome/porin complex MtoAB to the inner membrane predicted tetraheme quinone reductase $CymA_{ES-1}$, although as yet there has been no experimental evidence to support this role for MtoD.

In order to facilitate a greater understanding of the role MtoD plays in the electron transfer pathway of *Sideroxydans lithotrophicus,* and potentially a number of other organisms with homologous proteins, work began to construct a recombinant expression system that could produce large quantities of MtoD to be purified and comprehensively characterised. The *mtoD* gene, as shown with the polypeptide product in figure 2.1, was synthesised (GenScript) and addition of a topo-cloning site and ribosome binding sequence to *mtoD* for cloning with the pBAD202/D-TOPO expression system in addition to tagging for protein purification was performed on the synthesised gene. In order to produce large quantities of MtoD for characterisation, *Shewanella oneidensis* MR-1 was elected as the expression host due to its vastly greater growth rates compared to *S. lithotrophicus* and its well established use for over-expressing recombinant *c*-type cytochromes [13,14,15].

```
ATGACTCGTCAAGCTTATTCCTCAATGTTGCTCAGTACCGCCGCCGCCCTTACTTTAGCC

  M   T   R   Q   A   Y   S   S   M   L   L   S   T   A   A   A   L   T   L   A

TTCTCACTCAATGCCTCCGCCGCTGTCGATGTCGACGCTGCGAAATCGCTGGCGCGAGAA

  F   S   L   N   A   S   A   A   V   D   V   D   A   A   K   S   L   A   R   E

AACAATTGCTTCAAGTGCCACGGCGTCGACAAGGAAAAAGACGGCCCTTCCTACAAGAAA

  N   N   C   F   K   C   H   G   V   D   K   E   K   D   G   P   S   Y   K   K

GTCGCCGAAAAATACCGTGGCAAGGCCGATGCCGAAGCCAAGCTGATCCACCATGTCACG

  V   A   E   K   Y   R   G   K   A   D   A   E   A   K   L   I   H   H   V   T

TCTGGTGAAAAGGCCAAGTTCCCCGATGGTCATGAAGAAGAGCACAAGAACATCAACGGC

  S   G   E   K   A   K   F   P   D   G   H   E   E   E   H   K   N   I   N   G

AAAGCCTCACCTGAAGCCATCAAGAACCTGGTGGACTGGATCCTTTCGCTCTAG

  K   A   S   P   E   A   I   K   N   L   V   D   W   I   L   S   L   -
```

Figure 2.2 The 354 base pair *mtoD* gene translates to a 117-residue polypeptide sequence (shown in bold) containing a single CXXCH heme binding motif. Cys43 and Cys46, which are predicted to form thioether bonds to a single heme cofactor are coloured green. His47 from the CXXCH heme binding motif and His95 which was predicted to form an axial ligand to the heme iron based on sequence conservation evidence are coloured blue. Residues Met1 – Ala27, coloured grey, make up the predicted signal peptide based on SignalP analysis.

2.3   Methods

2.3.1 General methods

2.3.1.1 Agarose gel electrophoresis

1% agarose gels were made by adding 1 g of agarose to 100 mL of 1xTAE (Tris-acetate-EDTA) buffer. The mixture was heated in a microwave oven until the agarose was in solution. The agarose solution was cooled to approximately $60^{o}C$ before adding 5 μL of 10 mg.mL^{-1} ethidium bromide solution. This solution was mixed then poured into a casting tray to set for 20 minutes. Samples to be run on agarose gels were prepared by mixing 5:1 with 6x purple gel loading dye (NEB). Electrophoresis was performed at a constant potential of 90 V for 90 minutes. Results of Agarose gel electrophoresis were visualised by imaging using a UV transilluminator.

2.3.1.2 SDS PAGE

Polyacrylamide gels for SDS PAGE were typically made up with final polyacrylamide concentrations of 12%, 15% or 17% each using a 5% polyacrylamide stacking gel. Gels and running buffers were prepared using standard methods [16]. 2x SDS PAGE loading buffer contained 0.125 M Tris pH 6.8, 4% (wt/vol) SDS, 20% (vol/vol) glycerol, 5 M urea and 0.005% (wt/vol) bromophenol blue. Gels were run using a BioRad mini-gel system at a potential of 150 V. Duration of electrophoresis typically ranged from 60-90 minutes or until the loading dye reached the end of the gel.

	Resolving gel			Stacking gel
	12%	15%	17%	5%
	Volume (mLs)			
Acrylamide (30%)	7.5	9.47	10.7	1.67
H_2O	4.2	2.23	1.0	7.0
1 M Tris/HCl pH 6.8	-			1.25
1 M Tris/HCl pH 8.8	7.0			-
APS (10%)	0.125			0.050
SDS (20%)	0.094			0.050
TEMED	0.025			0.010

Table 2.1 Gels with 12-17% acrylamide concentrations for SDS PAGE were prepared using the above volumes of reagents. Volumes of Tris/HCl buffer (pH 8.8), APS (ammonium persulphate), SDS (sodium dodecyl sulphate) and TEMED (*N,N,N',N'*-Tetramethylethylenediamine) were constant for all preparation of resolving gels. Stacking gels were prepared using Tris/HCl buffer at pH 6.8.

2.3.1.3 Heme-linked peroxidase staining of SDS PAGE gels

Gels to be heme-stained were washed with analytical-grade water and placed in an ethanol-cleaned gel tray then incubated at room temperature with 45 mL 0.25 M sodium acetate pH 5.0 for 10 minutes. 15 mL 1 mg.mL^{-1} 3,3',5,5'-tetramethylbenzidine dihydrochloride hydrate (TMBD) solution was made in methanol and added to the gel tray. The gel was incubated for a further 10 minutes in the dark before adding 200 µL 30% hydrogen peroxide to stain. Gels were incubated in the dark for 15 minutes.

2.3.1.4 Western blotting

Immediately after performing SDS PAGE, gels were washed briefly in analytical-grade water (Fisher) before submerging in cathode buffer (25 mM Tris base and 40 mM glycine in 10% methanol) for 15 minutes. PVDF membrane was activated by washing with 100% methanol for 20 seconds before washing with analytical-grade water for 2 minutes. The membrane was then washed in anode buffer II (25 mM Tris-base in 10% methanol) for 5 minutes. 6 sheets of blotting paper were incubated in cathode buffer, 2 sheets incubated in anode buffer II and 4 sheets incubated in anode buffer I (300 mM Tris-base in 10% methanol) until the blotting paper was saturated. The transfer stack was arranged with filter paper soaked in anode buffer I at the anodic surface, followed by filter paper soaked with anode buffer II. The PVDF membrane was placed on top of this filter paper then the gel was placed on the membrane. Filter paper soaked in cathode buffer was placed on top of the stack at the surface of the cathode plate. During the stacking, bubbles were gently removed to ensure the transfer covered the entire gel. A semi-dry transfer system (Scie-Plas) was used to perform the transfer at a constant current of 95 mA (~10 V) for 60 minutes.

2.3.2 Synthesis, cloning and subcloning of *mtoD* into expression vector pBAD202

The 345 base pair gene encoding *mtoD* (gene locus: Slit_2498) was synthesised and cloned into a pUC57 cloning vector by GenScript using restriction digestion by EcoRV and blunt end ligation.

2.3.2.1 Subcloning *mtoD* for expression of MtoD-His

PCR amplification and His-tagging of *mtoD* from the pUC57 vector was performed using primers *mtoD*_1_F and *mtoD*_R_6His (details given in Appendix table X1) with Phusion® polymerase. 10 µL of high fidelity buffer for Phusion® polymerase, 4 µL of 2.5 mM dNTP mixture, 5 µL of 0.2 µg.µL^{-1} pUC57-*mtoD*,1 µL of each primer mixture and 1 µL of Phusion® polymerase made up the core PCR

mixture. This mixture was made up to 50 µL by addition of 28 µL of H_2O, or in DMSO-containing samples 25.5 µL H_2O was added with 2.5 µL DMSO, giving 0% and 5% DMSO reaction mixtures (table 2.2). 30 cycles of PCR were performed with a 15 second denaturing step at 98^oC, 30 second annealing step at 65^oC followed by a 15 second extension step at 72^oC. Initial denaturing of the template was performed by heating to 98^oC for 3 minutes and a final extension was performed by heating the samples to 72^oC for 10 minutes (program shown in figure 2.3 A).

A second PCR was performed using primers *mtoD_2_F* and *mtoD_R_6His* to add a 5' 'CACC' overhang which would allow cloning with the pBAD202 vector and a ribosome binding sequence (details given in Appendix table X1) The same reaction conditions were used for the initial reaction apart from the annealing temperature, which was increased to 70^oC (figure 2.3 B).

Component	Volume (µL)
Phusion buffer HF	10
dNTP mixture (2.5 mM)	4
pUC57-*mtoD* (0.2 µg/µL)	5
Primer *mtoD_1_F*/*mtoD_2_F*	1
Primer *mtoD_R_6His*	1
Phusion polymerase	1
DMSO	0/2.5
H_2O	28/25.5
Total volume:	50

Table 2.2 Reaction components for the PCR amplification and cloning of *mtoD* from pUC57 in PCR 1 (*mtoD_1_F*) and PCR 2 (*mtoD_2_F*).

A

Initial denaturation, 98°C
(3 minutes)

$\downarrow$

30x | - 98°C (15 seconds)
     - 65°C/70°C (30 seconds)
     - 72°C (15 seconds)

$\downarrow$

Final extension, 72°C
(10 minutes)

B

Initial denaturation, 98°C
(3 minutes)

$\downarrow$

30x | - 98°C (15 seconds)
     - 70°C (30 seconds)
     - 72°C (210 seconds)

$\downarrow$

Final extension, 72°C
(10 minutes)
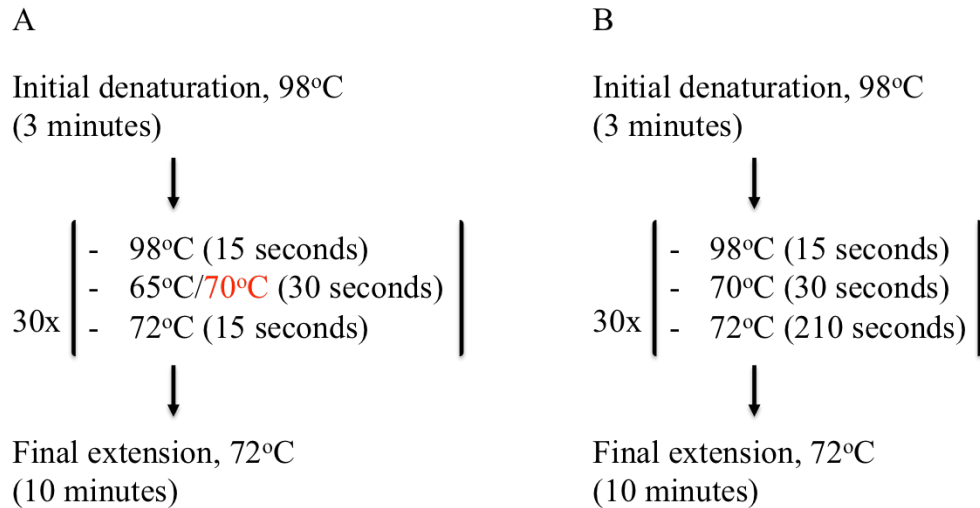
Figure 2.3 PCR programs used to create His-tagged and Strep II-tagged *mtoD*.
A. His-tagged *mtoD* was generated using two reactions: PCR 1 and PCR 2, which
performed 30 cycles of denaturation (90°C), annealing at 65°C for PCR 1 and 70°C
for PCR 2 followed by extension (72°C). **B.** Strep II-tagged *mtoD* was made by
substituting sequence coding for a 6xHis tag with sequence for a Strep II tag
contained in two primers. The reaction amplified the entire vector, necessitating a
much longer primer extension (210 seconds) time than previously.

2.3.2.2 PCR-based substitution of 6xHis tag with a Strep II tag.

Recombinant *Shewanella oneidensis* MR-1 containing pBAD202-*mtoD*-His
was transferred from a glycerol stock to a 10 mL LB/Kan culture and grown
overnight at 30°C, shaking at 220 rpm. Cells from 5 mL of this culture were
harvested by centrifugation and a miniprep kit was used to isolate plasmid DNA, as
described in 2.3.3.3. PCR was performed using 1 µL pBAD202-*mtoD*-His plasmid
DNA, 1 µL of each primer *mtoD*_SII_F and *mtoD*_SII_R (details in Appendix table
X1), 1 µL Phusion® polymerase, 10 µL HF buffer for Phusion® polymerase, 4 µL
2.5 mM dNTPs and 32 µL H_2O (table 2.3). The PCR reaction was performed as
described in 2.3.2.1, but the annealing temperature was changed to 70°C and the
extension time was increased to 210 seconds to allow for the extension of the 4,826
base pair pBAD202 vector and tagged *mtoD*. A *Dpn*I digestion was performed on
the PCR product to fragment the template DNA. 10 µL PCR product, 1 µL *Dpn*I
enzyme (NEB), 5 µL 10x *Dpn*I reaction buffer and 34 µL H_2O were mixed in a 1.5
mL microcentrifuge tube and incubated in a water bath at 37°C for 2 hours. PCR

purification was performed as described in 2.3.2.2 and the eluted product was quantified using nanodrop spectral analysis.

Component	Volume (μL)
Phusion buffer HF	10
dNTP mixture (2.5 mM)	4
pBAD202-*mtoD*-His	1
Primer *mtoD*_SII_F	1
Primer *mtoD*_SII_R	1
Phusion polymerase	1
H_2O	32
Total volume:	50

Table 2.3 Reaction components for the PCR-based exchange of the *mtoD* 6x His tag with a Strep II tag.

The pure, linear PCR product was circularised by performing a phosphorylation reaction using T4 polynucleotide kinase to phosphorylate the 5' end of the product. The phosphorylated product was then circularised by blunt-end ligation using T4 DNA ligase. Two methods were used to complete this process:

1. Sequential phosphorylation and ligation was performed by adding 1 μL T4 PNK, 2 μL reaction buffer for DNA ligase (includes ATP), 12.5 μL 160 ng.μL^{-1} pure PCR product and 4.5 μL H_2O to a PCR tube and incubating at 37°C for 5 minutes, after which 1 μL T4 DNA ligase was immediately added. This reaction mixture was left overnight at room temperature.

2. Separate phosphorylation and ligation reactions were performed as follows: 1 μL T4 PNK, 2 μL 10x reaction buffer A for T4 PNK, 2 μL 10 mM ATP, 12.5 μL 160 ng.μL^{-1} pure PCR product and 2.5 μL H_2O were mixed in a PCR tube and incubated for 20 minutes at 37°C. The mixture was incubated at 75°C for 10 minutes to deactivate the PNK. PCR purification was carried out as described previously prior to incubation with T4 DNA ligase. 10 μL 95 ng.μL^{-1} PCR-purified, phosphorylated DNA was mixed with 1 μL T4 DNA ligase, 2 μL 10x ligase buffer and 7 μL H_2O. This mixture was incubated overnight at room temperature.

2.3.2.3 Directional TOPO cloning *mtoD*-His into expression vector pBAD202

PCR product was purified using a QIAquick PCR purification kit, following the user guidelines supplied. Purified PCR product was diluted to a concentration of 2 ng.µL^{-1}, confirmed by UV nanodrop quantification. The TOPO cloning reaction mixture was composed of 1 µL salt solution, 3 µL sterile water and 1 µL pBAD202/D-TOPO$^{®}$ vector, which were supplied with the cloning kit (Invitrogen™), in addition to 1 µL of *mtoD* PCR product. The reaction tube was mixed gently and incubated at 22°C for 5 minutes after which the reaction mixture was held at ice-cool temperature.

2.3.2.4 Preparation of chemically competent *E. coli*.

E. coli TOP10 cells from a glycerol stock were streaked onto an LB agar plate and incubated overnight at 37°C. A single colony was picked after 24 hours using a sterile pipette tip and used to inoculate a sterile 10 mL overnight culture. This culture was incubated at 37°C while shaking at 220 rpm overnight. 1 mL of the overnight culture was used to inoculate 100 mL LB in a 250 mL conical flask. This culture was incubated at 37°C, shaking at 220 rpm until an OD$_{600}$ of 0.45-0.6 was achieved. The culture was incubated on ice for 10 minutes prior to harvesting cells by centrifugation at 3,500 x *g* for 5 minutes. Pelleted TOP10 cells were resuspended in 20 mL ice-cold, sterile 100 mM CaCl$_2$ then incubated on ice for 20 minutes. The cells were harvested again by centrifugation at 3,500 x *g* for 5 minutes then resuspended in 2.4 mL 100 mM CaCl$_2$ + 20% glycerol. The competent TOP10 cells were divided into 50 µL aliquots and vitrified by submerging in liquid nitrogen, then stored at -80°C.

2.3.2.5 Transformation of competent TOP10 cells

3 µL of pBAD202-*mtoD*-His TOPO cloning product or 10 µL (9 µg) circularised pBAD202-*mtoD*-SII was added to a 50 µL aliquot of chemically competent TOP10 cells in a 2 mL screw cap tube and mixed gently before incubating on ice for 15 minutes. Heat shock was performed by incubating this sample at 42°C in a water bath for 30 seconds; the mixture was then immediately

transferred to ice. 250 µL of sterile S.O.C. medium was added to the sample tube which was then incubated at 37°C, shaking horizontally at 220 rpm for 60 minutes. 200 µL of the transformation sample was pipetted onto the centre of a LB agar plate containing 50 µg.mL^{-1} kanamycin. 50 µL from the same transformation sample was pipetted onto the centre of a second, identical LB agar plate. Both plates were sealed with parafilm and incubated at 37°C overnight. Colonies were picked using a sterile pipette tip and re-plated onto a gridded LB agar 'master' plate containing 50 µg.mL^{-1} kanamycin so each colony had a numeric identifier. This plate was incubated at 37°C overnight.

2.3.2.6 Rapid Colony screening for plasmids with inserts

Methods were based on work by Law & Crickmore, 1997. Cells from a master LB agar plate were transferred to separate 30 µL aliquots of 1x lysis buffer pre-warmed to 37°C. Lysis buffer was composed of 20% sucrose, 200 mM NaOH, 120 mM KCl, 10 mM EDTA, 0.5% SDS and 0.1% bromophenol blue. Samples were incubated at 41°C for 5 minutes then placed on ice for a further 5 minutes. Cell lysate was isolated by centrifugation at 13,000 rpm in a bench top centrifuge for 10 minutes. 15 µL of the supernatant from each sample was loaded onto a 0.5% agarose gel (figure 2.5 and figure 2.7) and run as described in 2.3.1.1 to determine a molecular weight shift consistent with successful insertion of *mtoD*.

2.3.3 Conjugating pBAD202-*mtoD* into *Shewanella oneidensis* MR-1
2.3.3.1 Preparation and cultivation of the bacterial conjugation mixture

Glycerol stocks of TOP10-*mtoD* (containing either pBAD202-*mtoD*-His or pBAD202-*mtoD*-Strep), *E. coli* DH5α (pRK2013) and *Shewanella oneidensis* MR-1 were used to inoculate separate 10 mL LB cultures. The culture containing *E. coli* TOP10 was grown with 30 µg.mL^{-1} kanamycin and the *Shewanella* culture was grown with 100 µg.mL^{-1} carbenicillin. Cultures were incubated overnight, shaking at 220 rpm. The *E. coli* cultures were grown at 37°C and *Shewanella* grown at 30°C. 1.5 mL of each of these cultures was transferred to a separate 2 mL screw-cap tube and cells were pelleted by centrifugation at 5,000 rpm. The supernatant was

discarded and the cell pellets were resuspended in 1 mL sterile LB to wash remaining antibiotics from the samples. The DH5α sample was pelleted as before and the supernatant was discarded and replaced the 1 mL *Shewanella* sample. This was centrifuged again to pellet the cells and the supernatant was discarded and replaced with the 1 mL TOP10 sample (a negative control was also prepared without adding the TOP10). This sample was centrifuged again and the supernatant was removed and replaced with 150 µL sterile LB. The cells were thoroughly resuspended and mixed. The entire 150 µL volume was pipetted onto the centre of a LB agar plate and incubated at room temperature for 8 hours before being transferred to 30°C to incubate for 48 hours.

The bacterial conjugate mixture was scraped from the surface of the LB agar plate using a flame-sterilised loop and resuspended in 10 mL LB. Six serial 10-fold dilutions of this cell suspension were performed in LB. This was repeated for the negative control conjugate mixture. 100 µL of each dilution was spread onto separate LB agar plates containing 30 µg.mL^{-1} kanamycin and 100 µg.mL^{-1} carbenicillin. These plates were incubated at 30°C overnight, then at room temperature (~22°C) for 24 hours. 6 single colonies were selected from plates that produced them and were used to inoculate separate 10 mL LB cultures containing required antibiotics, as before, and incubated at 30°C, shaking at 220 rpm overnight. 1 mL of each of these cultures was mixed 1:1 with sterile glycerol and vitrified in liquid nitrogen before storing at -80°C.

2.3.3.2 *Nde*I-digestion of pBAD202-*mtoD*-His

Plasmid DNA was extracted from overnight cultures using a QIAprep spin miniprep kit (Qiagen) and procedures advised in the user guide. The plasmid DNA was linearised using restriction enzyme *Nde*I to allow molecular weight determination of the linear plasmid vector containing *mtoD* by gel electrophoresis. 1 µL 10x *Nde*I reaction buffer, 0.5 µL *Nde*I (NEB), 2 µL plasmid DNA and 6.5 µL H$_2$O were mixed gently in a PCR tube and incubated in a water bath at 37°C for 60 minutes. Samples were run on 1% agarose gels as described in 2.3.1.2.

2.3.3.3 Confirming the presence and correct insertion of *mtoD*-His/Strep into pBAD202.

Sequence analysis of each plasmid DNA sample was performed by Eurofins MWG Operon using the primer MJE_PBAD_F, (details given in Appendix table X1).

2.3.4 Expression trials of MtoD-His in *Shewanella oneidensis* MR-1.
2.3.4.1 Cultivation of *Shewanella oneidensis* and arabinose-induced expression of MtoD-His.

Recombinant *Shewanella oneidensis* MR-1 containing pBAD202-*mtoD*-His (designated *Shewanella_mtoD*-His), stored as glycerol stocks was used to inoculate a 10 mL LB culture containing 30 μg.mL^{-1} kanamycin (LB/Kan). This culture was grown overnight at 30°C, shaking at 220 rpm. This culture was used to inoculate a 6x 50 mL LB/Kan cultures which were incubated at 30°C, shaking at 220 rpm until OD$_{600}$=0.5-0.6 was achieved. Cultures were induced by addition arabinose to final concentrations of 2% $\rightarrow$ 2x10^{-5}% with increments of an order of magnitude. Cultures were incubated at 30°C, shaking at 220 rpm. 3 hours after addition of arabinose, 15 mL of each induced culture was transferred to separate sample tubes and cells were harvested by centrifugation at 5000 x *g* for 8 minutes. The supernatant was discarded and cell pellets were stored at -20°C overnight. After 18 hours under arabinose-inducing conditions a further 15 mL of culture was collected and cells harvested for each sample.

2.3.4.2 Lysis of *Shewanella* cultures by sonication.

Shewanella cell pellets were resuspended in 8 mL His Mag sepharose™ binding buffer (500 mM NaCl, 20 mM imidazol and 20 mM sodium phosphate, pH 7.4). Each sample received 5x 30-second bursts of sonication while held on ice with 30-second intervals. 2 mL of each sample were transferred to screw cap microcentrifuge tubes and unbroken cells were pelleted by centrifugation at 13,000 rpm. The supernatant was retained for His Mag-purification of His-tagged MtoD.

2.3.4.3 His Mag Sepharose™ purification of MtoD-His.

His Mag Sepharose™ beads were used according to the supplied guidelines (GE Healthcare). 2 tubes of supplied His Mag beads (~2 mL) were washed thoroughly and resuspended in 1.2 mL binding buffer, then 12x 100 µL aliquots of the beads were made – one for each sample of cell lysate. The His Mag beads were collected using a magnetic sample holder, the binding buffer discarded and replaced with 1.8 mL cell lysate then incubated, shaking at 4°C for 30 minutes. The supernatant was removed and 3x binding buffer washes were performed as described in the user guideline. Elution was performed using 50 µL elution buffer (binding buffer + 500 mM imidazole). Each sample was vortexed before the beads were collected and the elution samples were transferred to fresh sample tubes and prepared for SDS PAGE.

2.3.5 Purification of pure MtoD-His and MtoD-Strep

2.3.5.1 Growth of recombinant *Shewanella oneidensis* MR-1 and cell lysis for preparation of pure tagged MtoD.

A glycerol stock of the relevant *Shewanella-mtoD* (His or Strep) was used to inoculate 2 x 10 ml LB/Kan cultures, grown overnight at 30°C, shaking at 220 rpm. These cultures were used to inoculate 10x 1 L LB in 2.5 L baffled conical flasks. These cultures were incubated at 30°C, shaking at 180 rpm until an OD_{600}=0.6 was achieved. Induction was performed with 2 mM arabinose and incubation under the same conditions for 5 hours. Cells were harvested by centrifugation at 6,000 x *g* for 12 minutes. Cell pellet from 10 L of culture were resuspended in 50 mL 20 mM HEPES pH 7.6. Lysis of *Shewanella-mtoD* cell suspensions was performed at ice-cold temperature by two passes of French Press treatment at 1,000 psi (6.9 MPa). 5 $\mu g.mL^{-1}$ deoxyribonuclease I from bovine pancreas (Sigma Aldrich) was added to the cell suspension prior to lysis to decrease the viscosity of the cell lysate during the treatment. Unbroken cells and debris were pelleted by centrifugation at 15,000 x *g* for 15 minutes.

2.3.5.2 Purification of MtoD-His from recombinant *S. oneidensis* MR-1

The soluble cell fraction of *Shewanella-mtoD*-His lysate was isolated by ultracentrifugation (Beckman Optima XL100K/rotor Ti45). Samples were centrifuged at 42,000 rpm (205,000 x *g*) for 2 hours; supernatant was applied to a pre-charged 5 mL HisTrap cartridge pre-equilibrated with a solution of 20 mM HEPES pH 7.6, 20 mM imidazole and 500 mM NaCl at a flow rate of 2 mL.min^{-1} using a ÅKTA Prime liquid chromatography system. MtoD-His was eluted by increasing imidazole concentrations to 500 mM in 50 mM increments. 5 mL elution fractions were collected and SDS PAGE was performed as described previously to determine the MtoD-containing fractions using coomassie-based stain InstantBlue (Expedeon) and heme-stain visualisation. MtoD-containing fractions were pooled and concentrated to a final volume of 1 mL using centrifugal concentration with a 3 kDa MWCO membrane (Amicon). The concentrate was applied to a Superdex 75 16/60 gel filtration column pre-equilibrated with 20 mM HEPES pH 7.6, 150 mM NaCl at a flow rate of 0.5 mL.min^{-1}. 1 mL elution fractions were collected and analysed by SDS-PAGE and coomassie-based staining to assess the purity of MtoD-containing fractions.

2.3.5.3 Purification of MtoD-Strep from recombinant *S. oneidensis* MR-1

The soluble cell fraction of *Shewanella-mtoD*-Strep, prepared as above, was applied at a flow rate of 2 mL.min^{-1} using a ÅKTA Prime liquid chromatography system to a 5 mL StrepTactin cartridge (IBA) pre-equilibrated with 20 mM HEPES, pH 7.5 + 150 mM NaCl (Buffer A). The column was washed with 50 mL of buffer A prior to a one-step elution using the equilibration buffer + 2.5 mM d-Desthiobiotin (Buffer B). The StrepTactin cartridge was regenerated using a solution of buffer A + 1 mM HABA (4'-hydroxyazobenzene-2-carboxylic acid) and re-loaded with soluble cell fraction. Four cycles of this purification process were used to isolate MtoD-Strep from *Shewanella-mtoD*-Strep soluble cell fraction. 5 mL elution fractions were collected and SDS PAGE was performed with InstantBlue and heme-stain gel visualisation to locate and determine the purity of MtoD-containing samples. Size exclusion chromatography was performed as described in 2.3.5.2 using a Superdex 75 16/60 gel filtration column and assessed by SDS-PAGE.

2.3.6 Initial characterisation of MtoD

2.3.6.1 Spectroscopic characterisation of MtoD

UV-Visible spectra were collected using a 250 – 700 nm wavelength range on oxidised and reduced samples of MtoD-His and MtoD-Strep diluted in 20 mM HEPES pH 7.6, 100 mM NaCl. 498 µL buffer was prepared in a reduced-volume quartz cuvette and stoppered with a Suba-Seal® septa before the headspace of the cuvette was purged with nitrogen gas. UV-Vis spectroscopy performed on the buffer sample was used to baseline all protein measurements. 2 µL MtoD stock solution was added to the cuvette using a Hamilton syringe and the sample was mixed thoroughly before measuring a wavelength scan to record an oxidised spectrum. Reduced spectra of MtoD were recorded after injecting 2 µL sodium dithionite from a 100 mg.mL^{-1} solution prepared by dissolving dithionite in anaerobic water in a glovebox with a nitrogen atmosphere. An additional injection of dithionite was made after the initial measurement to ensure full protein reduction was achieved. All reduced spectra were adjusted for change in volume attributed to dithionite additions.

2.3.6.2 Intact MALDI-MS analysis of MtoD-His

SDS PAGE was performed using a pure solution of MtoD-His; 5 µg of protein was loaded and electrophoresis was performed as previously described. The gel was stained with InstantBlue to check the purity and homogeneity of the sample. 20 µl of 1 µg.mL^{-1} MtoD in 20 mM HEPES pH 7.6 was transferred to a 1.5 mL microcentrifuge tube, MALDI-MS and analyses were performed by the John Innes Centre Proteomics Facility.

2.3.6.3 N-terminal sequencing of MtoD-His

SDS PAGE was performed using a pure solution containing 15 µg MtoD-His. Electrophoresis was performed as previously described and the gel was washed with analytical grade water (Fisher) before performing a Western blot to transfer MtoD to a PVDF membrane as described in 2.3.1.4. A clean scalpel was used to cut around the MtoD band on the PVDF membrane, which could be seen due to its red colour,

then placed in a 1.5 mL microcentrifuge tube for shipment. N-terminal sequencing was performed by CambridgePeptides.

2.3.6.4 Quantifying MtoD protein concentration

A protein assay kit (BioRad) was used to quantify protein concentration in pure samples of MtoD-His. The assay is based on the Bradford method for quantifying proteins and similarly uses absorption at 595 nm. A standard curve was produced using the microassay method for bovine serum albumin (BSA) ranging from 1 μg to 10 μg, following the manufacturers recommended protocol. 1 μL of pure MtoD was made up to 1 mL using 200 μL assay reagent and 799 μL 20 mM HEPES pH 7.0. The sample was incubated at room temperature for 5 minutes prior to optical measurement at 595 nm.

2.3.6.5 Pyridine hemochrome analysis

The pyridine hemochrome method was used to establish the concentration of heme in a pure solution of MtoD-His with a known protein concentration in order to calculate a heme/protein ratio. Pyridine derivatives of MtoD and cytochrome c from horse heart were prepared by adding pure protein to solutions containing 20 mM HEPES pH 7, 100 mM NaCl, 6 mM pyridine and 75 mM NaOH. These solutions were mixed well and left to incubate at room temperature for 10 minutes. Pyridine derivatives of MtoD and horse heart cytochrome c were each divided into two 1 mL aliquots. One aliquot was oxidised by addition of 1 mM potassium ferricyanide and the other was reduced by addition of 2 mM anaerobically prepared sodium dithionite. The concentration of cytochrome c was quantified based on its known extinction coefficient ε_{410}=406,100 $M^{-1}.cm^{-1}$ [18]. $\Delta\varepsilon_{550-535}$ was calculated for the reduced-oxidised pyridine derivative spectrum for horse heart cytochrome c and used as a standard difference extinction coefficient for a known concentration of heme. The same method was used to produce a $\Delta A_{550-535}$ for the MtoD reduced-oxidised pyridine hemochrome derivative spectrum. The concentration of heme in the MtoD sample was calculated using Beer-Lambert law and $\Delta\varepsilon_{550-53}$ from horse heart cytochrome c:

$$\text{Equation. 2.1} \qquad A = \varepsilon.c.l$$

The Beer-Lambert law, shown in equation 2.1, can be modified to calculate concentration based on difference absorbance and a difference extinction coefficient as shown in equation 2.2:

$$\text{Equation. 2.2} \qquad c = \frac{\Delta A}{\Delta \varepsilon.l}$$

Equation 2.2 was used to quantify the heme concentration in the pyridine hemochrome derivative sample containing MtoD.

2.4   Results

2.4.1 Constructing an inducible *mtoD*-His construct in recombinant *Shewanella oneidensis* MR-1.

The 354 bp *mtoD* gene was subcloned from the pUC57 cloning vector using two sequential PCRs; the first reaction was performed with primers *mtoD*_1_F and *mtoD*_R_His, which amplified *mtoD* and added 3' sequence coding for a 6x His tag followed by a stop codon. The second reaction was performed as before using PCR product from the first reaction as template, but with primers *mtoD*_R_His and *mtoD*_2_F, which added 5' sequence coding for the CACC overhang, required for cloning with the pBAD202 D-TOPO system, and ribosome binding sequence required for the expression of recombinant *mtoD* in *Shewanella oneidensis* MR-1. Reaction 1 (PCR 1) produced gel electrophoresis results consistent with amplification of the 354 base pair sequence encoding *mtoD* and the addition of a 21 base pair sequence coding for the His tag followed by a TAG 'stop' codon (figure 2.4 A). The second reaction (PCR 2) should have added an additional 25 base pairs of sequence to the 5' end of *mtoD*. Gel electrophoresis performed on the products of the second PCR showed very similar results to the first reaction (figure 2.4 B); a slight increase in DNA size was observed and so it was assumed the reaction had been successful.
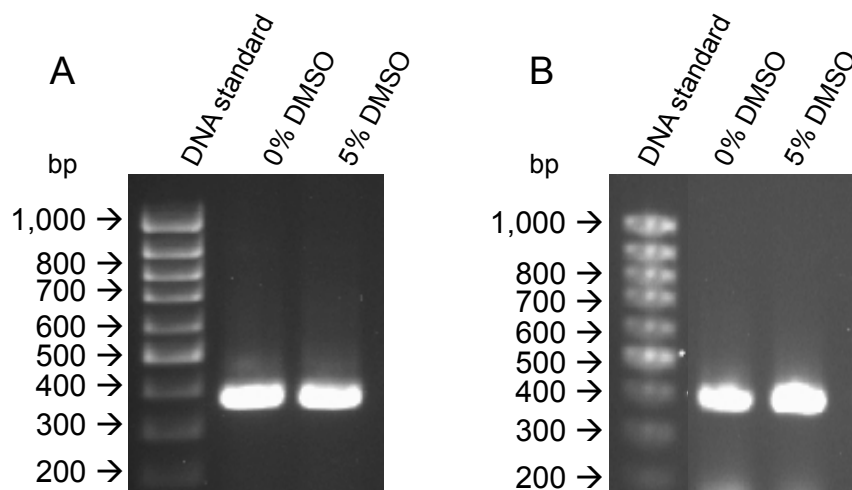
Figure 2.4 Agarose gel electrophoresis results of PCR-based amplification and tagging of *mtoD*. A. PCR-based amplification and addition of a 6x His tag to *mtoD* from the pUC57 cloning vector with 0% DMSO and 5% DMSO yielded the same result – the amplification of a ~370 base pair DNA sequence. **B.** A second PCR amplification was performed to add a 5' CACC 'overhang' that would enable TOPO cloning into pBAD202 and a ribosome binding sequence. Performing PCR with 0% and 5% DMSO produced similar results to the first reaction with marginally increased product size.

PCR product from the second reaction was used as insert for a TOPO cloning reaction using the expression vector pBAD202/D-TOPO. pBAD202-*mtoD*-His cloning product was used to transform TOP10 *E.coli*. 28 colonies of transformant TOP10 cells were observed on LB agar plates grown with kanamycin. These colonies were screened using gel electrophoresis to assess the probability the pBAD202 vector contained a *mtoD*-His insert. Based on the relative shift in size of DNA fragments in adjacent lanes, eight samples were selected as promising candidates (figure 2.5) and their respective colonies were grown overnight in LB with kanamycin.
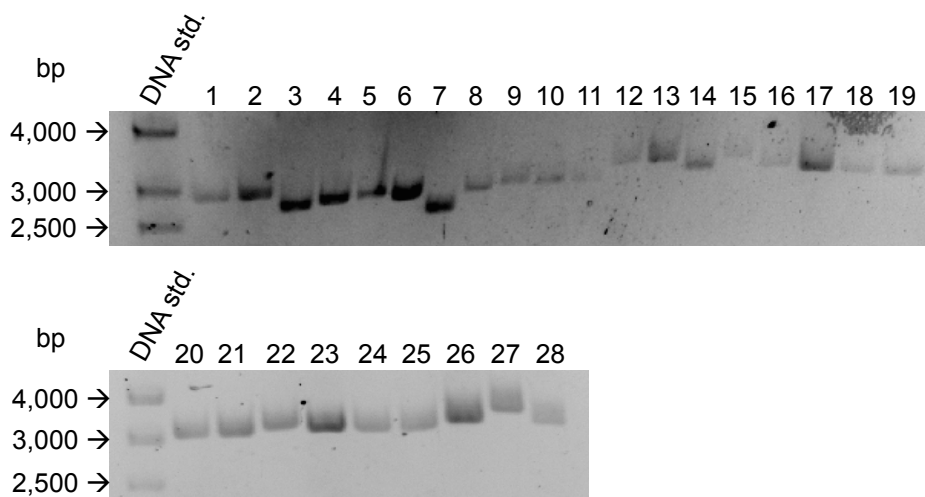
Figure 2.5 Rapid screening for plasmids with *mtoD*-His inserts. A shift in the size of supercoiled vector DNA in adjacent wells was used to assess the likelihood of the pBAD202 plasmid containing an *mtoD* insert. Colonies 1, 2, 12, 13, 15, 26, 27 and 28 were selected as promising candidates.

Plasmid DNA from these overnight cultures was isolated and DNA sequencing using primer MJE_PBAD_F (Appendix table X1) confirmed all selected samples except 26 and 28 (figure 2.5) sequenced to be the correct construct containing *mtoD* with a preceding ribosome binding site and 3' sequence coding for a 6x His tag, followed by a stop codon. Tri-parental conjugation was used to transfer plasmid DNA from *E.coli mtoD*-1 to *Shewanella oneidensis* MR-1 via the helper strain DH5α (PRK2013). Serial dilution of the conjugate cell mixture and growth on LB agar with kanamycin and carbenicillin (Kan/Carb) produced single colonies on two of the plates: 10^{-2} and 10^{-3}. Six single colonies, which had a faint red colour consistent with *Shewanella* colonies, were picked (designated MR-1 *mtoD*-1→6) and grown in LB Kan/Carb overnight. Glycerol stocks were made and minipreps were performed to isolate plasmid DNA from each of the cultures. To confirm the conjugation had been successful, the pBAD202 vector was linearized in each of the samples by *Nde*I digestion and agarose gel electrophoresis was performed. The linear vector migrated at approximately 5,000 base pairs which was comparable to the linearized pBAD202-*mtoD*-His from transformant *E. coli* TOP10 (figure 2.6). No plasmid DNA was observed in sample 'MR-1 *mtoD*-4', suggesting conjugation or isolation of plasmid DNA may have been ineffective for this sample. Plasmid DNA from samples MR-1 *mtoD*-1, 5 and 6 were sequenced to confirm the correct construct had been transferred into *Shewanella oneidensis* MR-1.
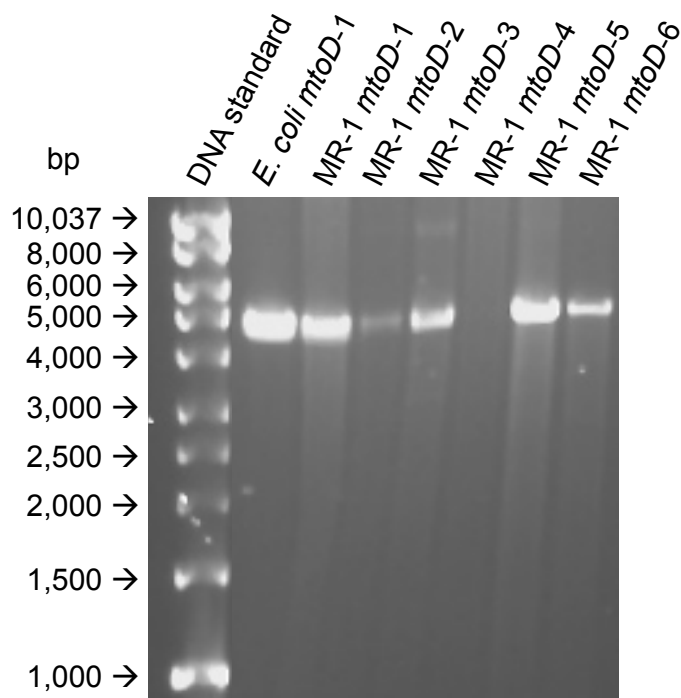
Figure 2.6 Confirming successful conjugation of *Shewanella oneidensis* with pBAD202-*mtoD*-His by gel electrophoresis. Plasmid DNA isolated from cultures of recombinant *Shewanella oneidensis* MR-1 (labelled MR-1 *mtoD*-1→6) was linearized by *Nde*I-digestion and electrophoresis was performed in parallel with linearized pBAD202-*mtoD*-His DNA isolated from TOP10-*mtoD*-1. Plasmid DNA from *E. coli* and *Shewanella* cultures appeared to migrate identically, with an approximate size of 5,000 base pairs. DNA was not observed in sample 'MR-1 *mtoD*-4' probably due to ineffective conjugation or isolation of DNA during miniprep.

2.4.2 Re-tagging MtoD-His as MtoD-Strep

In order to avoid advantageous metal binding to the C-terminal His-tag, which may potentially affect electrochemical experiments, the 6xHis tag at the C-terminus of MtoD-His was replaced with a Strep II tag. Plasmid DNA was isolated from recombinant *Shewanella* containing pBAD202-*mtoD*-His and PCR was used to replace nucleotides at the 3' end of *mtoD* coding for a 6xHis tag with nucleotides coding for a Strep II tag (amino acid sequence: WSHPQFEK). The linear PCR product was phosphorylated and blunt-end ligated before transformation into *E. coli* TOP10 cells. Conjugation was performed as before to transfer the vector into *Shewanella oneidensis* (named *Shewanella-mtoD*-Strep). The rapid screening for plasmids with inserts method was used to screen recombinant *Shewanella* colonies

for the best candidates for sequence analysis. Little difference in the migration of bands in adjacent wells was observed, however some lanes did not contain DNA of the correct size to be supercoiled pBAD202 (figure 2.7). Samples 2 → 6 were selected for sequence analysis; DNA in these samples migrated at a similar size, comparable to the size of bands that gave positive results during the rapid screening experiment for pBAD202-*mtoD*-His. DNA sequencing (Eurofins MWG Operon) confirmed the His tag sequence had been successfully replaced with sequence encoding the 8 amino acid Strep II tag.
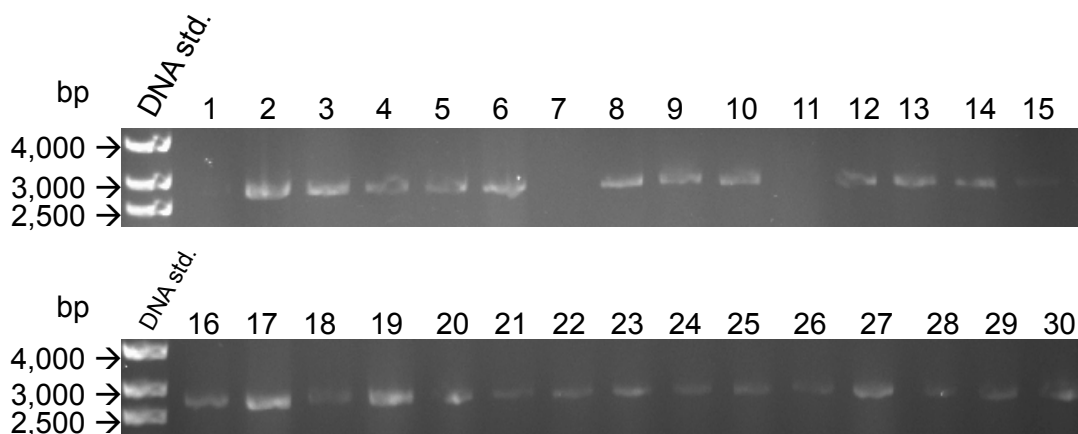
Figure 2.7 Rapid screening for plasmids with *mtoD*-Strep inserts. DNA prepared using the rapid screening approach was run on a 0.5% agarose gel. Supercoiled pBAD202 ran, as previously observed, at ~3,000 base pairs. There was not an obvious shift in the size of DNA bands in adjacent wells, however some samples appeared to be lacking DNA of the correct size. Samples 2, 3, 4, 5 and 6 were selected for sequence analysis.

2.4.3 Expression and purification of MtoD-His

Small-scale expression trials of His-tagged MtoD (MtoD-His) in recombinant *Shewanella oneidensis* MR-1 were performed using 50 mL LB cultures in 250 mL conical flasks incubated at 30°C, shaking at 220 rpm, induced using a range of arabinose concentrations. Cells were harvested after 3 hours and 18 hours after induction. Cells were harvested by centrifugation and lysis was achieved by sonication. His Mag Sepharose® beads were used to perform a rapid, small-scale purification of MtoD-His from the cell lysate of each sample. The relative levels of MtoD expression were determined by performing SDS PAGE on the eluted protein and results visualised by heme staining. A faint band was observed after inducing with 0.2% arabinose and harvesting after 3 hours. More prominent signal was

observed for 0.2% and 2% arabinose-induced cultures harvested after 18 hours (figure 2.8).
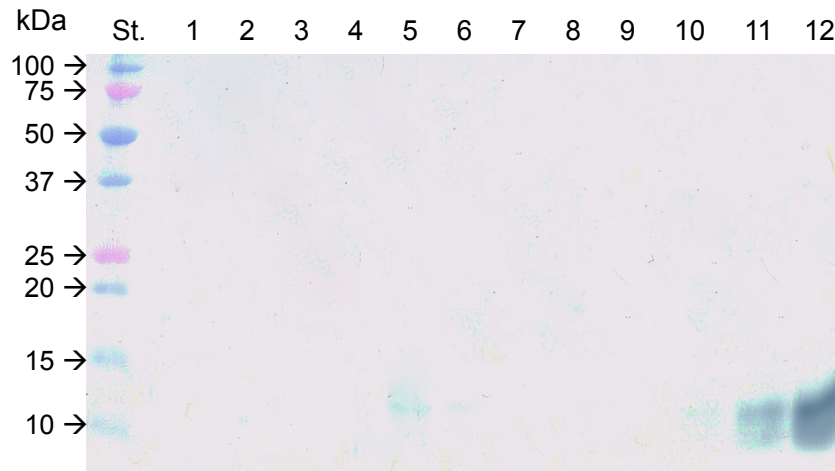
Figure 2.8 Expression trial of MtoD-His in *Shewanella oneidensis* MR-1. SDS PAGE performed on His Mag-treated protein samples from cultures of recombinant *Shewanella* expressing MtoD-His. Lanes 1-6 contain samples induced with $2x10^{-5}$% → 2% arabinose with increments of an order of magnitude induced for 3 hours. Lanes 7 → 12 contain the same arabinose gradient but were induced for 18 hours. Heme staining shows one faint band in lane 5 (0.2% arabinose) and bands in lanes 10, 11 and 12 all of which migrated at an approximate molecular weight of 12 kDa.

Large-scale culture of recombinant *Shewanella oneidensis* and expression of MtoD-His was performed using 10 x 1 L cultures in 2.5 L baffled conical flasks, shaking at 180 rpm, incubated at 30°C. Induction performed using 2 mM arabinose was carried out over a 15-hour period to maximise protein expression. However, SDS PAGE results after purification by HisTrap immobilised metal affinity chromatography (IMAC) followed by size exclusion chromatography revealed MtoD migrated as a smeared protein band which appeared to be consistent with severe protein degradation (figure 2.9 A).
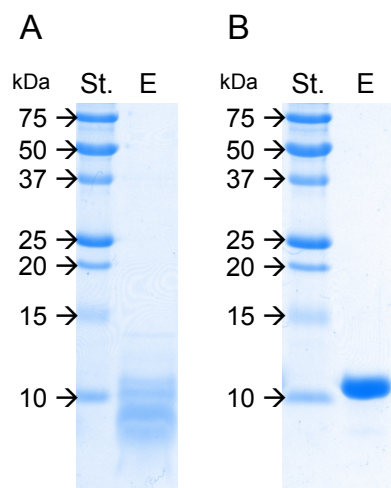
Figure 2.9 SDS PAGE revealed 15-hour inductions produced MtoD-His samples with severe degradation. A. MtoD-His, from cultures of *Shewanella oneidensis* which had been arabinose-induced for 15 hours, after size exclusion chromatography could be seen as smeared bands on 15% acrylamide gels. **B.** MtoD-His, prepared using the same methods, but expressed in *Shewanella oneidensis* incubated under inducing conditions for only 5 hours produced high quality pure protein. Gels were visualised using InstantBlue; St.=M_W standard, E=elution.

As a precaution, the large-scale preparation of MtoD-His was repeated using a 5-hour induction phase using the same concentration of arabinose as previously. MtoD-His eluted from 5 mL HisTrap cartridges (GE Healthcare) at an imidazole concentration of 100 mM, which was consistent with the previous attempt, however SDS PAGE analysis after size exclusion chromatography revealed MtoD-His migrated as a single, concise protein band lacking the previously observed smearing effect (figure 2.9 B). It was assumed the prolonged incubation of MtoD-His in *Shewanella oneidensis* led to significantly increased levels of protein degradation. As a result of this observation, all further preparations of His-tagged and Strep II-tagged MtoD were performed using 5-hour inductions. Extensive optimisation experiments to test the possible longevity of inductions to produce the greatest yield of MtoD were not performed. Preparation of MtoD-His from 10 L of *Shewanella oneidensis* culture after 5-hour induction yielded 5-10 mg pure protein, which was sufficient to perform initial characterisation and electrochemical experiments. Yields were later increased using larger volumes cell culture.

2.4.4 Expression and purification of MtoD-Strep

Strep II-tagged MtoD was expressed using the same conditions as His-tagged MtoD, using 20x1 L cultures. After harvesting cell cultures lysis was performed by French press treatment and the soluble cell fraction was isolated by ultracentrifugation. Four cycles of protein loading, washing and elution were performed to isolate 1 mg MtoD-Strep per litre of culture from the soluble cell fraction due to the significantly lower theoretical column binding capacity (~3 mg MtoD-Strep) compared to the HisTrap columns previously used (~200 mg MtoD-His). However, the highly specific StrepTactin purification method produced pure samples of MtoD-Strep after a single purification as confirmed by SDS PAGE analysis with coomassie staining (figure 2.10 A). To remove the eluent d-Desthiobiotin from the MtoD-Strep fractions and to ensure the final protein sample was homogenous, size exclusion chromatography was performed. SDS PAGE analysis revealed each of the fractions collected after size exclusion contained pure, homogenous MtoD, which migrated at an approximate molecular weight of 12 kDa (figure 2.10 B).
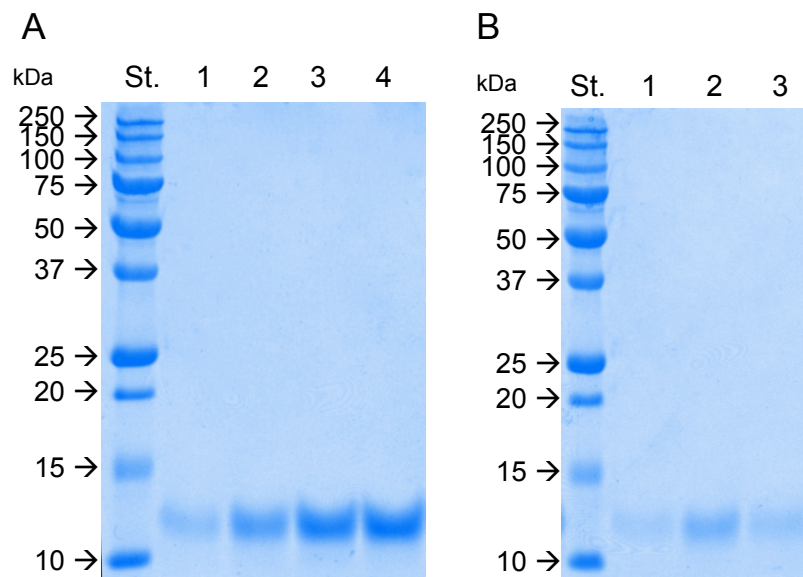
Figure 2.10 SDS PAGE analysis of StrepTactin and size exclusion chromatography. A. Elutions 1→4 from the StrepTactin purification indicating protein eluted from the column after each purification cycle contained pure MtoD-Strep. **B.** Elution fractions from size exclusion chromatography: MtoD-Strep migrated as a single band approximately 12 kDa in size.

2.4.5 Initial characterisation of MtoD-His

As a predicted class I cytochrome *c* with unusual bis-His axial heme ligation, the initial interest was MtoD's spectroscopic properties and how they compared to previously studied cytochromes *c* with bis-His ligated *c*-type hemes. UV-Visible spectroscopy was performed with oxidised and reduced samples of MtoD-His. Additions of the oxidant potassium ferricyanide (E_{m7} = +430 mV vs. SHE) made to aerobic samples of MtoD had no effect on the peak positions of absorption maxima. Aerobically prepared MtoD could therefore be used as oxidised samples. Oxidised and reduced spectra of MtoD-His in the visible region were typical of a *c*-type cytochrome with characteristic absorption features for $\pi \rightarrow \pi^*$ electronic transitions associated with a heme ligand [19]. Reduction with sodium dithionite shifted the absorption peak maximum of the Soret band from 406 nm to 416 nm and caused the appearance of the characteristic α/β peaks at 549 nm and 520 nm respectively (figure 2.11).
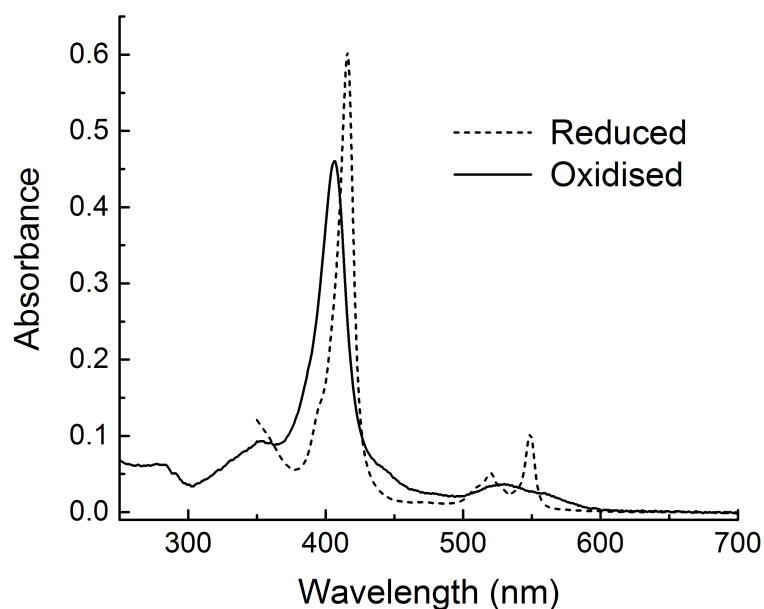
Figure 2.11 UV-visible spectroscopy of oxidised and reduced MtoD-His. Oxidised MtoD-His (solid line) produced a UV-vis spectrum characteristic of a c-type cytochrome containing low-spin ferric heme. The 280/410 nm absorption ratio was 0.147. Reduction of MtoD with dithionite shifted the Soret maximum from 406 nm to 416 nm and caused the appearance of α and β absorption bands at 549 nm and 520 nm respectively (dotted line). An electronic transition above 600 nm, often associated with His/Met ligation in cytochromes *c*, was absent. Reduced spectra are presented to 350 nm rather than 250 nm because dithionite absorbs in this region.

No detectable electronic transitions occurred above 600 nm; absorption in this region of the visible spectrum is associated with ligand-to-metal charge transfers and is present in cytochromes *c* with His/Met ligation. The lack of such absorption is consistent with MtoD containing low-spin heme iron with bis-His or His/Lys ligation. The observed ratio of absorption at 280/410 nm, sometimes used as a measure of purity for cytochromes, was 0.147.

Intact MALDI-MS was performed on MtoD-His to more accurately establish the protein's molecular weight and provide insight into the primary structure of mature MtoD by comparing the theoretical molecular weight of MtoD-His to that recorded by MALDI-MS. A pure homogenous solution MtoD-His, as confirmed by SDS PAGE analysis, containing 20 μg protein was prepared. Intact MALDI-MS and analyses performed by the JIC Proteomics Facility revealed MtoD-His had a molecular weight of 11,365 Da. Assuming MtoD-His contained a single heme, as predicted, a signal peptide of 27 amino acids must be cleaved and the N-terminus of mature MtoD should begin at position 28 in the peptide sequence. The signal-cleavage prediction tool SignalP 4.0 [20] was used to plot the most likely point of signal cleavage in the MtoD polypeptide sequence. SignalP predicted the presence of a 27 amino acid signal peptide and mature MtoD's N-terminal amino acid as ALA28 (figure 2.12), consistent with the MALDI-MS result. N-terminal sequencing was performed to confirm whether this predicted structure of mature MtoD was correct. SDS PAGE was performed on a pure sample of MtoD-His and Western blotting used to transfer this protein to a PVDF membrane. N-terminal sequencing, performed by Cambridge Peptides, revealed the 5-amino acid sequence ALA-VAL-ASP-VAL-ASP. This amino acid sequence aligned perfectly with the MtoD polypeptide sequence between positions 28-32. This result confirms the primary structure of MtoD begins at residue ALA28 and based on the intact mass should contain a total of 90 residues (not including the His tag) and contain a single heme cofactor.
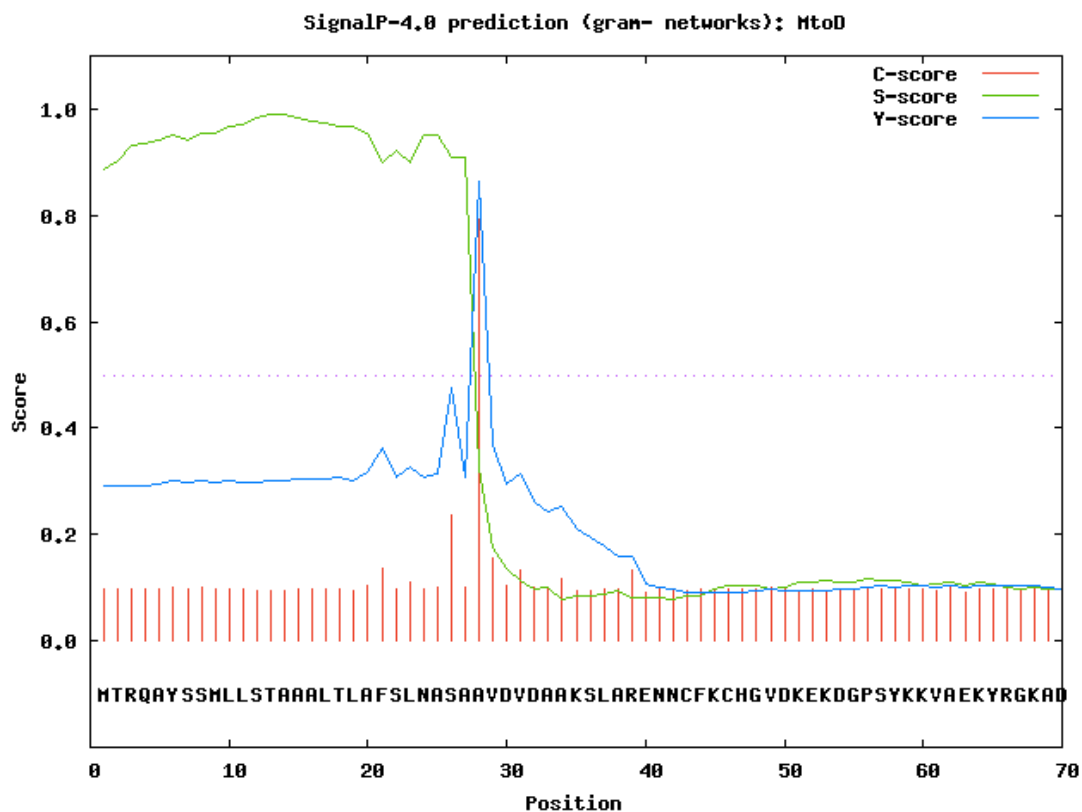
Figure 2.12 SignalP [20] prediction of presence and location of signal peptide cleavage sites in MtoD. SignalP-4.0 predicted MtoD contained a signal peptide cleavage site between residues Ala27 and Ala28 as shown by the magnitude of the C-score (cleavage site score) and corresponding decrease of the S-score (signal sequence score); the Y-score (derivative of the C-score and S-score) maximum was also consistent with signal cleavage between residues Ala27 and Ala28.

2.4.6 Initial characterisation of MtoD-Strep

UV-Vis spectroscopy was performed on MtoD-Strep as was carried out previously with MtoD-His. The main features of the fully oxidised and reduced spectra were identical to MtoD-His, with protein reduction leading to a shift in the Soret band from 406 nm to 416 nm and appearance of α/β bands at 549 nm and 520 nm respectively (figure 2.13 A). The most apparent difference between the oxidised spectra of MtoD-His and MtoD-Strep was the difference in absorbance at 280 nm for the pure protein samples. The 280/410 nm absorbance ratio for MtoD-Strep was 0.195, compared to 0.147 for MtoD-His. Some difference in this region of the spectrum was expected due to the addition of a tryptophan and a phenylalanine residue to the protein sequence in the Strep II tag. The predicted increase to the molar extinction coefficient at 280 nm as a result of this change was 5,700 $M^{-1}.cm^{-1}$.

This was determined using methods described by Gill & Hippel (1989) with Protein Calculator v3.4, developed by Chris Putnam at the Scripps Research Institute (www.scripps.edu/~cdputnam/protcalc). To determine how much the additional aromatic residues from the tag contributed to the difference in absorbance at 280 nm, the absorption difference at this region of the normalised spectrum (figure 2.13 B) was used to calculate the difference in the molar extinction coefficient using the theoretical concentration of MtoD from the normalised spectra with the experimentally determined extinction coefficient at 406 nm (the determination of which is detailed in the next section). At 4,130 $M^{-1}.cm^{-1}$, the observed increase in extinction coefficient was smaller than that predicted using Protein Calculator v3.4. It is possible additional protein impurities in the MtoD-His sample relative to the MtoD-Strep sample could have caused the $\Delta\varepsilon$ to be smaller than predicted. However, the closeness between the predicted $\Delta\varepsilon$ at 280 nm and that observed suggests that for future experiments with MtoD-His and MtoD-Strep, the different observed 280/410 nm absorbance ratios for the two tagged proteins could be used for the purposes of assessing sample purity.

To confirm the presence of a single c-heme cofactor in MtoD, a pure solution of MtoD-Strep was analysed using the pyridine hemochrome method to quantify the concentration of heme and a protein assay kit was used to estimate the protein concentration. Cytochrome c from horse heart was used as a standard for the pyridine hemochrome experiment; UV-Vis spectroscopy was performed (figure 2.14 A) and the literature value for ε_{410} of 406,100 $M^{-1}.cm^{-1}$ [18] was used to quantify the concentration of protein and heme in the sample since cytochrome c from horse heart has a single heme per protein molecule [22]. The pyridine hemochrome method was performed on pyridine derivatives of oxidised and reduced cytochrome c to produce a difference extinction coefficient in the reduced minus oxidised spectrum between 550 nm and 535 nm ($\Delta\varepsilon_{550-535}$) for a known concentration of heme (figure 2.14 B). Pyridine derivatives of oxidised and reduced MtoD-Strep were produced and difference in absorbance between 535 nm and 550 nm ($\Delta A_{550-535}$) was used with $\Delta\varepsilon_{550-535}$ for the known concentration of heme in the horse heart cytochrome c sample to calculate a concentration for heme in the stock MtoD-Strep sample of 550 μM (figure 2.14 C). The reduced pyridine derivative of MtoD produced a visible spectrum characteristic of a c-type heme cofactor (Appendix, figure X4).
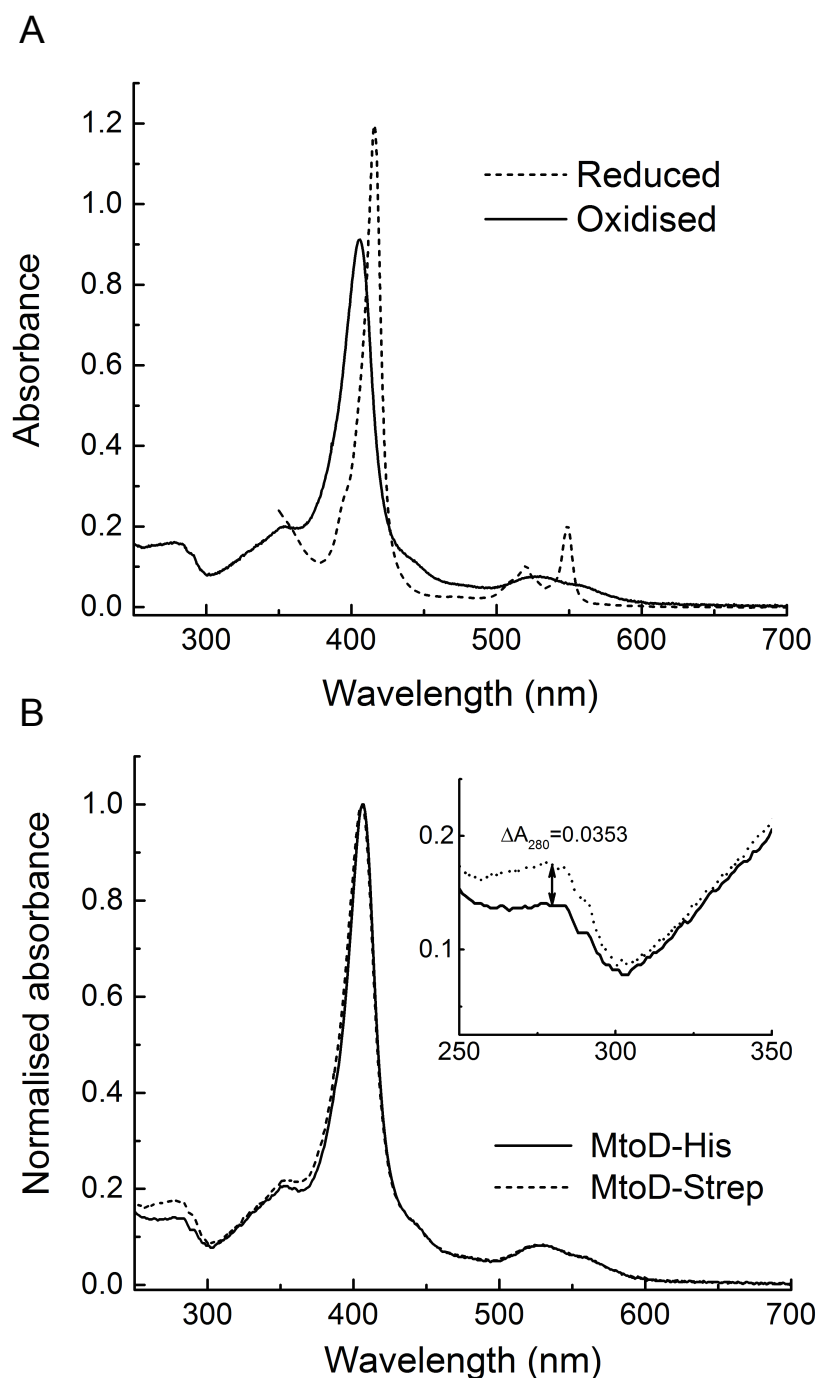
Figure 2.13 Spectroscopic analysis of Strep-tagged MtoD. A. The main features of the oxidised and reduced spectra for Strep II-tagged MtoD were almost identical to His-tagged MtoD. Upon reduction the Soret-band maximum shifted from 406 nm to 416 nm and α/β absorption bands appeared at 549 nm and 520 nm respectively. **B.** Overlaid and normalised oxidised spectra of pure MtoD-Strep and MtoD-His show MtoD-Strep had greater 280 nm absorption, leading to a greater 280/410 nm absorbance ratio. The difference in absorption at 280 nm (ΔA_{280}) was converted to a difference molar extinction coefficient ($\Delta \varepsilon$) using the experimentally determined ε_{406}=117,000 for MtoD. $\Delta \varepsilon$ observed (4,130 $M^{-1}.cm^{-1}$) accounted for the predicted $\Delta \varepsilon$ (5,700 $M^{-1}.cm^{-1}$) determined for changing the His tag to a Strep II tag using Protein Calculator v3.4.
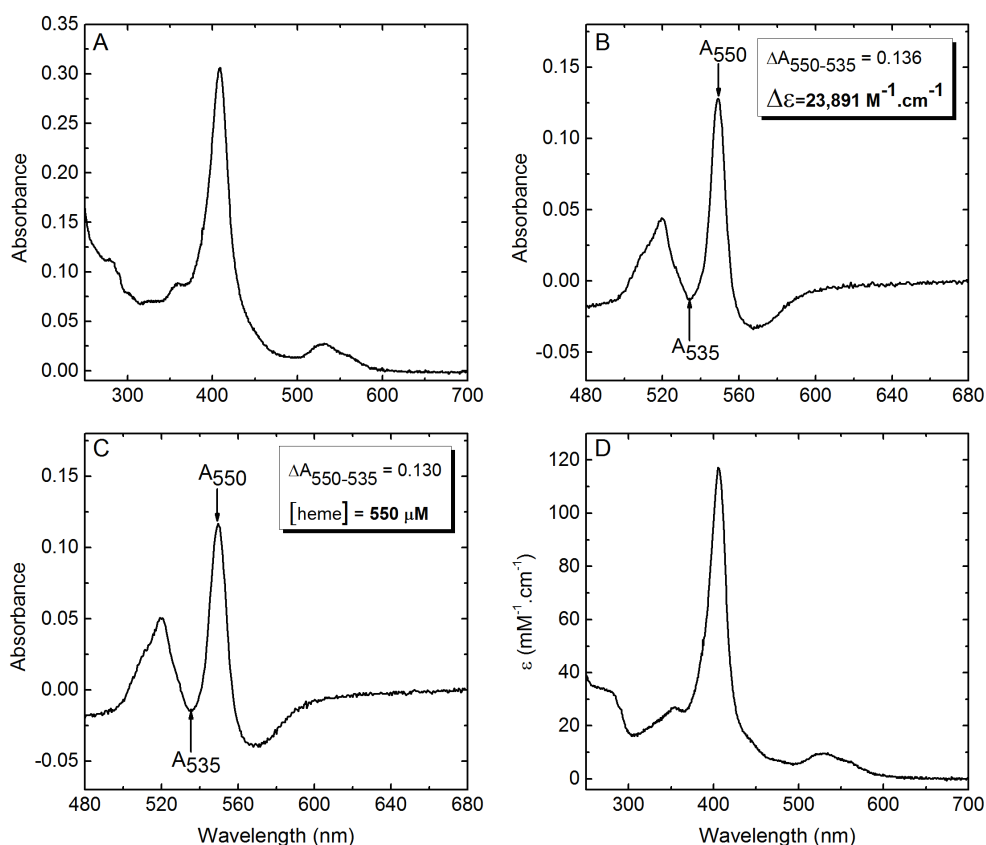
Figure 2.14 Pyridine hemochrome analysis to quantify heme in MtoD. A. UV-Vis spectrum of oxidised cytochrome c from horse heart. The literature ε_{410}=106,100 $M^{-1}.cm^{-1}$ was used to quantify the concentration of the cytochrome c sample. **B.** Reduced-oxidised spectrum of the pyridine derivative of cytochrome c from horse heart. The known concentration of heme in the cytochrome c sample was used to calculate $\Delta\varepsilon_{550-535}$ 23,891 $M^{-1}.cm^{-1}$ from $\Delta A_{550-535}$. **C.** Reduced-oxidised spectrum of the pyridine derivative of MtoD. $\Delta\varepsilon_{550-535}$=23,891 $M^{-1}.cm^{-1}$ for a known concentration of heme from horse heart cytochrome c was used with $\Delta A_{550-535}$ for the MtoD pyridine derivative sample to calculate the heme concentration as shown in equation 2.2. **D.** Concentration of heme in the MtoD sample was used to calculate millmolar extinction coefficients for the full UV-Vis spectrum of MtoD.

The total protein concentration of the pure MtoD-Strep sample was estimated using a BioRad protein assay kit with a BSA standard from 1-10 μg. The BSA standard produced a linear increase in absorption at 595 nm over the selected range (Appendix, figure X3) and MtoD-Strep, prepared identically to the standards, produced 595 nm absorption, which indicated the sample's protein concentration was 7.4 mg.mL^{-1} (638 μM). Given the relatively large errors associated with using a protein assay kit and the possibility that the MtoD-Strep sample was not 100% pure, a heme/protein ratio of 0.86 is consistent with a 1:1 ratio of heme to protein in

MtoD. Using the knowledge [heme]=[MtoD] the 550 µM concentration determined for MtoD-Strep using the pyridine hemochrome method was used to calculate extinction coefficients for MtoD's UV-visible spectrum (figure 2.14 D). For the purposes of accurately quantifying the concentration of MtoD, the extinction coefficient for the Soret maximum at 406 nm (117,000 $M^{-1}.cm^{-1}$) was used.

2.5 Discussion

The work detailed in this chapter provides a method for rapidly purifying milligram quantities of MtoD-His and MtoD-Strep protein, validates the predicted signal cleavage point to determine the proteins size, provides an initial spectroscopic fingerprint for MtoD and confirms the predicted 'monoheme cytochrome' designation of MtoD.

As was outlined in the introduction to this chapter, the ability to isolate MtoD for characterisation is critical to understanding its role in the process of dissimilatory iron oxidation. A more detailed investigation into the predicted cytochromes *c* in the genome of *Sideroxydans lithotrophicus* is presented in chapter 5. However, what makes *mtoD* of particular interest is its location in the *mto* gene cluster, which is implicated in the process of dissimilatory iron oxidation [1,6]. Furthermore, the primary structure of MtoD did not contain methionine in the predicted mature protein sequence but histidine and lysine residues were abundant (figure 2.2), leading to the possibility of MtoD being an unusual bis-His or His/Lys axially ligated cytochrome *c*.

The abundance of lysine is not surprising, since lysine residues are important for the formation of an electrostatic protein-protein interaction between cytochrome *c* and cytochrome c oxidase (CCO) binding sites, allowing rapid electron transfer from cytochrome *c* to the oxidase [23,24]. Based on BLAST analysis and sequence alignments, as shown in chapter 1 (figure 1.10), two histidine residues are conserved in homologues of MtoD, His47 located in the CXXCH motif and His95, which is located in the conserved sequence motif 'GXEEE/DH'. This histidine pair was predicted to provide axial ligands to the heme iron.

Overexpression of His-tagged MtoD in *Shewanella oneidensis* MR-1 and purification after 15-hour arabinose inductions gave poor quality results compared to

overexpression using 5-hour inductions. This issue has not been encountered during overexpression of outer membrane cytochromes in *Shewanella oneidensis* [10,25] due to the extracellular location of these proteins. Overexpression of MtrA and CymA, both of which are exposed to the periplasm in *Shewanella oneidensis*, using similar methods also did not show obvious degradation effects on the overexpressed protein [13,26], although CymA was overexpressed at 23°C. MtoD was purified from the soluble cell fraction of *Shewanella oneidensis* cultures and was predicted to be localised to the periplasm. It is possible incubations of the foreign MtoD protein in the periplasm of the *Shewanella* host resulted in MtoD being quickly proteolysed, resulting in degraded quality of purified protein, since similar methods have not had the same deleterious effects on purified MtrA and CymA, which are native to *Shewanella oneidensis*. While extensive optimisation of the overexpression method for MtoD was not performed, on reflection reducing the incubation temperature during the induction phase could have potentially improved the quality of purified protein by slowing proteolysis. The stability of MtoD at 30°C, which is beneficial for achieving cell mass, was not known and could have lead to increased rates of protein degradation. Previous overexpression of CymA in *Shewanella oneidensis* at 23°C yielded 0.5 mg pure protein per litre of culture [26], which is comparable to the 0.5-1.0 mg yield of pure MtoD per litre of culture grown at 30°C, suggesting it should be possible to produce sufficient yields of MtoD at lower induction temperatures for further characterisation studies.

A poly-Histidine tag and HisTrap purification method were initially chosen for the purification of MtoD due to the ability of this purification system to rapidly isolate large quantities of protein. MtoD purified using the HisTrap method required size exclusion chromatography to remove some higher molecular weight protein impurities from the sample that were co-eluted from the HisTrap column. However, it was possible to produce protein samples with ≥ 95% purity based on SDS PAGE analysis with InstantBlue staining. The rationale for selecting a His tag was reconsidered after the results of electrochemical characterisation of the His-tagged MtoD appeared peculiar for a monoheme cytochrome *c*, as detailed in chapter 4. The decision was made to switch to the Strep II tag and StrepTactin purification system due to the small tag size, low reported incidence of bioactivity changes in the Strep tag user guide (Genosys Biotechnologies Inc.) and the previous success of characterising Strep II-tagged redox proteins, including *Geobacter sulfurreducens*

cytochrome c_6 and OmcF [27–29]. Using the StrepTactin purification system, it was possible to rapidly produce high purity samples of ($\geq$ 95%) pure MtoD in a single step; size exclusion chromatography was still used, but as a means of removing the eluent d-Desthiobiotin from the purified protein samples and ensuring sample homogeneity rather than to perform further purification. There was a noticeable difference in the yield of pure protein isolated per purification using the StrepTactin system compared to the HisTrap system. While the affinity of the Strep II tag-StrepTactin interaction is strong (K_d = 1 μM [30,31]), the significantly lower reported theoretical protein binding capacity of the StrepTactin matrix relative to the more conventional IMAC method utilised in the HisTrap system (~3 mg MtoD-Strep vs. ~200 mg MtoD-His per purification) meant several cycles of StrepTactin purification were required to isolate sufficient protein yields for characterisation and particularly for crystallisation trials.

Initial UV-Vis spectroscopic characterisation of His-tagged and Strep II-tagged MtoD revealed the pure protein solutions had near identical oxidised and reduced spectra, both of which were typical of *c*-type cytochromes containing low-spin heme iron, and the addition of aromatic residues to MtoD in the Strep II tag accounted for the difference in 280 nm absorption between the oxidised spectra. Pyridine hemochrome analysis and assaying for total protein concentration confirmed MtoD is a monoheme cytochrome. Based on the primary structure of MtoD containing a single CXXCH *c*-type heme-binding motif, it was proposed the heme was covalently attached to MtoD via thioether bonds with Cys43 and Cys46 and axial ligation of the heme iron occurred via His47 and a His95.

Mass spectrometry and N-terminal sequencing confirmed the predicted position of signal peptide cleavage from MtoD occurred after residue Ala27, making MtoD 90 amino acids in length with a single *c*-type heme cofactor.

2.6 References

1. Liu, J. *et al.* Identification and Characterization of MtoA: A Decaheme c-Type Cytochrome of the Neutrophilic Fe(II)-Oxidizing Bacterium Sideroxydans lithotrophicus ES-1. *Front. Microbiol.* **3,** 37 (2012).

2. Hartshorne, R. S. *et al.* Characterization of an electron conduit between bacteria and the extracellular environment. *Proc. Natl. Acad. Sci. U. S. A.* **106,** 22169–74 (2009).

3. Shi, L. *et al.* Molecular Underpinnings of Fe(III) Oxide Reduction by Shewanella Oneidensis MR-1. *Front. Microbiol.* **3,** 50 (2012).

4. Pitts, K. E. *et al.* Characterization of the Shewanella oneidensis MR-1 decaheme cytochrome MtrA: expression in Escherichia coli confers the ability to reduce soluble Fe(III) chelates. *J. Biol. Chem.* **278,** 27758–65 (2003).

5. Firer-Sherwood, M. a, Ando, N., Drennan, C. L. & Elliott, S. J. Solution-based structural analysis of the decaheme cytochrome, MtrA, by small-angle X-ray scattering and analytical ultracentrifugation. *J. Phys. Chem. B* **115,** 11208–14 (2011).

6. Emerson, D. *et al.* Comparative genomics of freshwater Fe-oxidizing bacteria: implications for physiology, ecology, and systematics. *Front. Microbiol.* **4,** 254 (2013).

7. Shi, L., Rosso, K. M., Zachara, J. M. & Fredrickson, J. K. Mtr extracellular electron-transfer pathways in Fe(III)-reducing or Fe(II)-oxidizing bacteria: a genomic perspective. *Biochem. Soc. Trans.* **40,** 1261–7 (2012).

8. Ross, D. E. *et al.* Characterization of protein-protein interactions involved in iron reduction by Shewanella oneidensis MR-1. *Appl. Environ. Microbiol.* **73,** 5797–808 (2007).

9. Jiao, Y. & Newman, D. K. The pio operon is essential for phototrophic Fe(II) oxidation in Rhodopseudomonas palustris TIE-1. *J. Bacteriol.* **189,** 1765–1773 (2007).

10. Clarke, T. a *et al.* Structure of a bacterial cell surface decaheme electron conduit. *Proc. Natl. Acad. Sci. U. S. A.* **108,** 9384–9 (2011).

11. Edwards, M. J. *et al.* The crystal structure of the extracellular 11-heme cytochrome UndA reveals a conserved 10-heme motif and defined binding site for soluble iron chelates. *Structure* **20,** 1275–1284 (2012).

12. Edwards, M. J. *et al.* Redox Linked Flavin Sites in Extracellular Decaheme Proteins Involved in Microbe-Mineral Electron Transfer. *Sci. Rep.* **5,** 11677 (2015).

13. Shi, L., Lin, J. T., Markillie, L. M., Squier, T. C. & Hooker, B. S. Overexpression of multi-heme C-type cytochromes. *Biotechniques* **38,** 297–299 (2005).

14. Shi, L. *et al.* Isolation of a high-affinity functional protein complex between OmcA and MtrC: Two outer membrane decaheme c-type cytochromes of Shewanella oneidensis MR-1. *J. Bacteriol.* **188,** 4705–14 (2006).

15. Edwards, M. J. *et al.* The X-ray crystal structure of Shewanella oneidensis OmcA reveals new insight at the microbe-mineral interface. *FEBS Lett.* **588,**

1886–1890 (2014).

16.   Laemmli, U. K. Cleavage of structural proteins during the assembly of the head of bacteriophage T4. *Nature* **227,** 680–685 (1970).

17.   Law, D. & Crickmore, N. Use of a simplified rapid size screen protocol for the detection of recombinant plasmids. *Tech. Tips Online* **2,** 136–137 (1997).

18.   Margoliash, E. & Frohwirt, N. Spectrum of horse-heart cytochrome c. *Biochem. J.* **71,** 570–2 (1959).

19.   Moore, G. & Pettigrew, G. *Cytochromes c: Evolutionary, Structural and Physicochemical Aspects.* (Springer-Verlag, 1990).

20.   Petersen, T. N., Brunak, S., von Heijne, G. & Nielsen, H. SignalP 4.0: discriminating signal peptides from transmembrane regions. *Nat. Methods* **8,** 785–786 (2011).

21.   Gill, S. & Hippel, P. Von. Calculation of protein extinction coefficients from amino acid sequence data. *Anal. Biochem.* **182,** 319–26 (1989).

22.   Banci, L. *et al.* Solution structure of oxidized horse heart cytochrome c. *Biochemistry* **36,** 9867–9877 (1997).

23.   Döpner, S. *et al.* The structural and functional role of lysine residues in the binding domain of cytochrome c in the electron transfer to cytochrome c oxidase. *Eur. J. Biochem.* **261,** 379–91 (1999).

24.   Sampson, V. & Alleyne, T. Cytochrome c/cytochrome c oxidase interaction. Direct structural evidence for conformational changes during enzyme turnover. *Eur. J. Biochem.* **268,** 6534–6544 (2001).

25.   Hartshorne, R. S. *et al.* Characterization of Shewanella oneidensis MtrC: a cell-surface decaheme cytochrome involved in respiratory electron transport to extracellular electron acceptors. *J. Biol. Inorg. Chem.* **12,** 1083–94 (2007).

26.   Schwalb, C., Chapman, S. K. & Reid, G. a. The tetraheme cytochrome CymA is required for anaerobic respiration with dimethyl sulfoxide and nitrite in Shewanella oneidensis. *Biochemistry* **42,** 9491–7 (2003).

27.   Roberts, S. a. *et al.* A labile regulatory copper ion lies near the T1 copper site in the multicopper oxidase CueO. *J. Biol. Chem.* **278,** 31958–31963 (2003).

28.   Kern, M., Klotz, M. G. & Simon, J. The Wolinella succinogenes mcc gene cluster encodes an unconventional respiratory sulphite reduction system. *Mol. Microbiol.* **82,** 1515–30 (2011).

29.   Lukat, P., Hoffmann, M. & Einsle, O. Crystal packing of the c6-type cytochrome OmcF from Geobacter sulfurreducens is mediated by an N-terminal Strep-tag II. *Acta Crystallogr. Sect. D Biol. Crystallogr.* **64,** 919–926 (2008).

30.   Voss, S. & Skerra, a. Mutagenesis of a flexible loop in streptavidin leads to higher affinity for the Strep-tag II peptide and improved performance in recombinant protein purification. *Protein Eng.* **10,** 975–982 (1997).

31.   Schmidt, T. G. M. & Skerra, A. The Strep-tag system for one-step purification and high-affinity detection or capturing of proteins. *Nat. Protoc.* **2,** 1528–1535 (2007).

Chapter 3

Biophysical and structural characterisation of MtoD.

Work presented in this chapter has been published in the following paper:

Beckwith CR, Edwards MJ, Lawes M, Shi L, Butt JN, Richardson DJ and Clarke TA (2015) **Characterization of MtoD from *Sideroxydans lithotrophicus*: a cytochrome *c* electron shuttle used in lithoautotrophic growth**. Front. Microbiol. 6:332. doi: 10.3389/fmicb.2015.00332

3.1 Abstract

The structural characterisation of class I cytochromes *c* from numerous prokaryotic and eukaryotic organisms has led to an understanding that this type of cytochrome is highly conserved in terms of its polypeptide folding and redox properties [1–3]. Class I cytochromes *c* are typically monomeric, soluble, low-molecular weight proteins (9-15 kDa) that contain a single covalently bound *c*-type heme cofactor [1,3]. In the mitochondria of eukaryotes, class I cytochromes *c* function in the transfer of electrons from quinol dehydrogenase cytochrome bc_1 to cytochrome *c* oxidase (CCO), which reduces molecular di-oxygen to water [2,4]. This electron transfer also happens in prokaryotes, although the respiratory flexibility among many prokaryotic organisms means electrons may be transferred to several types of terminal oxidase under anaerobic conditions. The structures of class I cytochrome *c* are highly-conserved around the heme cofactor, where the heme iron is typically axially ligated by a histidine and a methionine residue and lysine residues are conserved around the thiolated heme edge, where the cytochrome *c*:CCO electrostatic interaction occurs [3,5]. Analytical ultracentrifugation (AUC) and small-angle X-ray scattering (SAXS) were used to probe the biophysical properties of MtoD-Strep while X-ray crystallography was used to determine the atomic structure. Results of AUC and SAXS were typical for a class I cytochrome *c*; MtoD-Strep behaved as a monomer in solution and its surface structure was similar to a number of previously characterised bacterial small monoheme cytochromes *c*. The atomic structure of MtoD-Strep, determined by X-ray crystallography, revealed the *c*-type heme cofactor was axially ligated by two histidine residues, which is uncommon for class I cytochromes *c*. Structure superpositions showed MtoD retains the conserved cytochrome *c* protein fold, but forms an atypical β-hairpin motif around the heme, which results in the heme cofactor being solvent-exposed not only from the thiolated heme edge, but also from the propionate heme edge. The unusually high solvent exposure of the MtoD heme and the presence of lysine residues around both sites could potentially make MtoD capable of interacting with multiple redox partners in *S. lithotrophicus*.

3.2   Introduction

3.2.1   Structure of class I cytochromes *c*

The structure of cytochromes *c* have been the subject of intense study for many decades now and a great deal of work and debate around the subject of classifying them has led to an extensive understanding of these proteins with spectroscopic data and structural evidence to support the function and classification of each newly discovered cytochrome. Structurally, class I cytochromes *c* can be viewed as relatively simple proteins. Many of them consist of short polypeptide sequences in the range of 80-120 residues (9-15 kDa), much of which forms a secondary structure composed of α-helices folded into a globular shape connected by short loops, resulting in the formation of a conserved, hydrophobic pocket, which contains a covalently-bound heme cofactor. The structure of class I cytochromes *c* are typified by the well-studied mitochondrial cytochrome *c* from horse heart (figure 3.1) [6,7]; 45% of the residues in this cytochrome *c* are contained in α-helices and the folding of the protein is dominated by type II and type III β-turns [6]. The structure of cytochrome *c*550 from the nitrate-reducing bacterium *Paracoccus denitrificans* is remarkably similar to mitochondrial cytochrome *c* from horse heart and tuna (36% and 37% sequence identity respectively). This similarity has been demonstrated by quantitatively comparing *c*550 from *P. denitrificans* with mitochrondrial cytochrome *c* from tuna using a main-chain superposition method and measuring the divergent distances of atoms between the two structures [8]. On average a 1.14 Å divergence in the chemically equivalent main-chain atoms and an overall difference of 1.3 Å was observed, with the greatest differences observed where the bacterial cytochrome contained additional loops of polypeptide. This small difference in protein structure after an evolutionary divergence which extends to at least 1.6 billion years [8] underlines the importance of the role class I cytochromes *c* play in respiratory chains in many vastly different forms of life. Figure 3.1 shows a main-chain superposition of mitochondrial cytochrome *c* from horse heart (PDB ID: 1HRC) with cytochrome *c*550 from *Paracoccus denitrificans* (PDB ID: 155C), highlighting the similarity between eukaryotic and bacterial cytochromes *c*. Both proteins contain a single heme cofactor ligated by histidine and methionine and covalently linked to the polypeptide chain by two cysteine residues. Clustal Omega [9] alignment of the primary structures

indicated sequence identity of 36%. Nevertheless, the α-helical structures and the folding of the proteins around the heme cofactor are very similar, despite the additional 2.5 kDa of polypeptide chain contained in 155C.
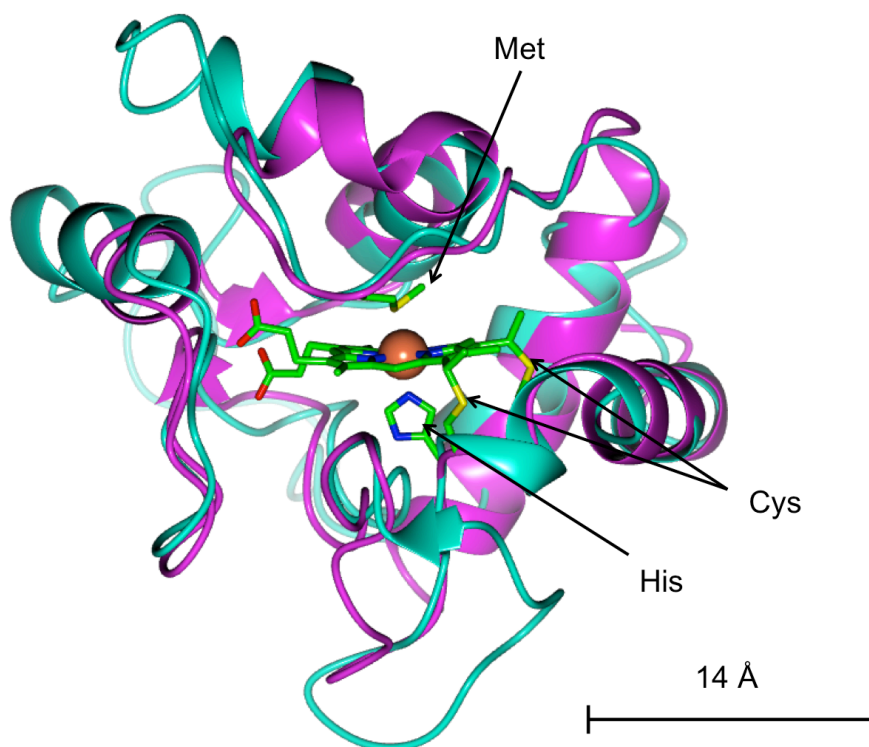
Figure 3.1 Main-chain superposition of mitochondrial cytochrome c from horse heart, 1HRC (magenta) and cytochrome *c*550 from *Paracoccus denitrificans*, 155C (cyan).

The function of cytochromes *c* hinges on their ability to exist in either an oxidised or reduced state, allowing them to behave as electron shuttles in the respiratory chain, transferring electrons from quinol dehydrogenase (complex III) to cytochrome *c* oxidase (complex IV), which completes the terminal reduction of molecular oxygen to water. Overall, the bioenergetics of this process require the transfer of electrons to occur down an electrochemical potential gradient to incrementally more oxidising potentials with the terminal oxidoreductase containing redox centres with the most oxidising (positive) electrochemical potentials. There are multiple factors that determine whether or not an electron transfer event between two redox-active heme cofactors is biologically viable and notably two of these can be directly related to the structure of the proteins involved: the magnitude of the

potential difference between redox centres and the physical distance between these centres, with distances of ≤14 Å giving rise to biologically relevant electron transfer rates according to Marcus theory [10]. While class I cytochromes c are small and contain a single heme cofactor, as a protein class they exhibit redox potentials over a broad range, with examples of redox potentials as negative as -0.260 V and as positive as +0.358 V (vs. SHE) [11]. This considerable breadth of redox potentials arises largely as a result of a relatively small range of structural differences. The most obvious of these differences include the ligation of the heme cofactor by amino acid residues from the polypeptide chain. Axial ligation of the heme iron in class I cytochromes c is commonly in the form of a histidine residue contained in the canonical CXXCH heme-binding motif and a methionine residue, the location of which varies depending on type of cytochrome c [12].

As was discussed in chapter 1 and confirmed in chapter 2, methionine is absent from the mature MtoD polypeptide sequence and the initial spectroscopic characterisation indicated the protein contained a low-spin heme iron, leading to the hypothesis that the second ligand to the heme iron came from one of the histidine residues close to the C-terminus of the protein. X-ray diffraction studies on MtoD crystals were performed to establish the ligation state and protein structure around the heme cofactor in order to obtain a structural insight into the potential redox properties of the protein.

The solvent exposure of the heme cofactor was of particular interest, since this is a critical factor in determining the relative stability of neutral Fe(II)-heme vs. the cationic Fe(III)-heme, which influences the redox potential of the heme cofactor [13]. Although the determinants of the redox potentials of heme cofactors tend to be complex, the current literature indicates a negative correlation between solvent exposure of the heme cofactor in c-type cytochromes and increasingly positive redox potentials, leading to the summation that more exposed heme cofactors generally have lower redox potentials [13].

Cytochromes c tend to be relatively small monomeric globular proteins and it was predicted MtoD would fit into this category. To confirm this, a thorough biophysical characterisation of MtoD was performed using sedimentation velocity analytical ultracentrifugation (AUC) and small angle X-ray scattering (SAXS) to determine the oligomeric state, shape and size of MtoD in free solution.

Chapter 3 provides a comprehensive biophysical and structural characterisation of MtoD from *Sideroxydans lithotrophicus* using AUC, SAXS and X-ray crystallography, which are introduced in the following sections.

3.2.2 Introduction to Sedimentation Velocity

Analytical ultracentrifugation (AUC) is a powerful biophysical technique employed for the characterisation of macromolecules in free solution. It is commonly used for the characterisation of proteins and protein complexes. AUC is capable of performing rigorous and accurate measurements of the molecular weight, hydrodynamic and thermodynamic properties of proteins and their complexes based on the unique sedimenting properties of the proteins as a result of their differing density, shapes, and molecular weights.

The principle of sedimentation velocity experiments, in their simplest form is to measure the rate at which boundaries of macromolecules redistribute in a known gravitational field generated by centrifugation [14]. However, the experiment is complicated by the number of opposing forces constantly acting on proteins in solution. The gravitational force experienced by a protein molecule in solution relates to the mass of the molecule as well as the gravitational field it experiences (equation 3.1):

$$\text{Equation 3.1:} \qquad F_s = M_p\omega^2 r$$

F_s (gravitational/sedimenting force) is equal to the particle mass (M_p) multiplied by the square of the angular velocity (ω) and the distance of the particle from the axis of rotation (r). Opposing this is the buoyant force of the protein molecule (F_b) – (equation 3.2):

$$\text{Equation 3.2:} \qquad F_b = M_s\omega^2 r$$

M_s is the mass of solvent displaced by the protein in solution; solvent mass is determined by multiplying the particle mass by the partial specific volume (υ) and the solvent density (p) – (equation 3.3):

Equation 3.3: $\qquad M_s = M_p.\upsilon.p.$

In addition to these forces, a protein molecule moving through solution experiences a frictional force (F_f), which opposes the gravitational force and greatly depends on the size and shape of the molecule. The frictional force felt by a protein molecule is demonstrated in equation 3.4:

Equation 3.4: $\qquad F_f = \textit{-fu}$

f is the frictional coefficient of the protein molecule and u is the velocity, which becomes greater with decreasing distance from the axis of rotation. By collecting and combining the terms from each of the equations for these contributing forces it is possible to produce the Svedberg equation (equation 3.5) [14,15]:

Equation 3.5: $\qquad S \equiv \dfrac{\upsilon}{\omega^2 r} = \dfrac{M_p(1-\upsilon p)}{f} = \dfrac{M_b}{f}$

Where M_b is the buoyant molar mass. A complete understanding of the system parameters, including properties specific to the solvent and the centrifugal field makes it is possible to determine the sedimentation coefficient (s) which is given Svedberg units, S (10^{-13} sec) and the frictional coefficient (f). These coefficients contain valuable information regarding the size and the shape of sedimenting protein molecules. The sedimentation velocity experiments presented in chapter 3 provide an accurate measurement of the solution molecular weight, the size and shape of MtoD based on the resulting sedimentation and frictional coefficients.

3.2.3 Introduction to Small Angle X-ray Scattering (SAXS)

Biological small angle X-ray scattering (BioSAXS) is a rapidly developing technique, which provides structural information of biological macromolecules in solution, with the solution of low-resolution protein structures becoming increasingly frequent [16]. The strengths of the SAXS technique lie in the ability to determine the low-resolution structure of proteins that are resistant to crystallisation,

such as proteins containing intrinsically flexible domains. SAXS makes it possible to study these flexible structures and can be readily used alongside X-ray crystallography and nuclear magnetic resonance (NMR) as a means of validating protein structures in solution.

Similar to the well-established X-ray crystallography technique (which will be introduced in the next section), SAXS uses the elastic scattering of incident X-rays to obtain a 2-dimensional interference (scattering) pattern, which contains information about the averaged electronic distribution of molecules in the X-ray beam. A basic schematic of the experimental set-up is shown in figure 3.2. A monochromatic incident X-ray beam is passed through the sample and diffracted X-rays are measured at the detector.
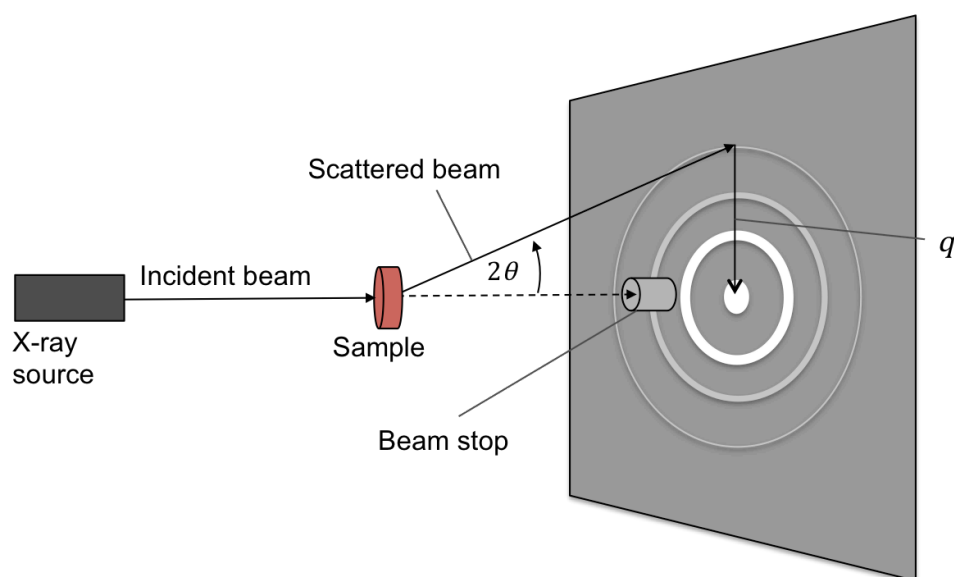
Figure 3.2 Schematic of a typical SAXS experiment. Monochromatic incident X-rays are scattered by the sample and collected on a detector, producing a 2 dimensional scattering pattern. The intensity of the diffracted X-rays is recorded as a function of their momentum transfer (q), which is derived from the scattering angle (2θ) and the wavelength of the incident X-ray radiation (λ).

A beam stop is used to prevent damage to the detector and to limit noise around the centre of the detector as a result of the intensity of the incident beam. The intensity of the diffracted X-rays is measured as a function of their momentum transfer (q), which has units of inverse length (nm^{-1}). A momentum transfer (q) is used rather than the scattering angle (2θ) so that measurements of intensity become independent of the wavelength used for the incident beam. Equation 3.6

demonstrates how the momentum transfer is derived from the wavelength of the applied radiation (λ) and the half scattering angle (θ).

$$\text{Equation 3.6:} \qquad q = \frac{4\pi}{\lambda} . sin\,(\theta)$$

By subtracting data recorded on the sample holder alone and the sample holder containing only solvent from samples at multiple concentrations contained in the same solvent, it is possible to reveal the signal intensities resulting from the biological sample of interest at a range of concentrations. By normalising these intensities to the flux density of the incident beam and the exposed sample volume it is possible to present these data as absolute intensities [17]. Primary data reduction can be performed on the interference patterns by radially averaging the recorded intensities as a function of momentum transfer to produce a 1-dimensional plot of absolute intensity as a function of momentum transfer (I/q). Normally this is plotted as $\ln(I)/q$ (figure 3.3A).

Subsequent analyses of the data are able to reveal important information about the size and shape of the protein in solution. A simple method of determining whether inter-particle attraction or repulsion affects samples of different concentrations is to compare the shape of the scattering curve at low q between each sample concentration prepared. Inter-particle attraction tends to result in an increase in intensity at small q whereas inter-particle repulsion tends to result in decreased scattering intensity at small q (figure 3.3B). Since inter-particle effects become more apparent with higher concentrations, it is possible to observe these characteristics by changes in the shape of the scattering curve of higher concentrations relative to lower concentrations. A solution to this problem is to merge low q data from low concentrations, where the inter-particle effects are much smaller, with high concentration data for the remainder of the scattering curve [17].

By producing a plot of $\ln(I)/q^2$ (Guinier plot) and fitting a line to a linear 'Guiner region' it is possible to calculate the radius of gyration (R_g) from the extrapolated zero angle intensity (I_0) and the slope of the linear region [16,17] (figure 3.3C), which provides model-independent information about the size of the scattering particles (not to be confused with the molecular weight). Producing Kratky plots of q^2I/q is a useful method of determining tertiary structure features in

protein molecules; globular proteins tend to produce a prominent peak at low q, whereas unfolded or flexible protein structures tend to produce a gradually increasing q^2I with increasing q [16] (figure 3.3D).
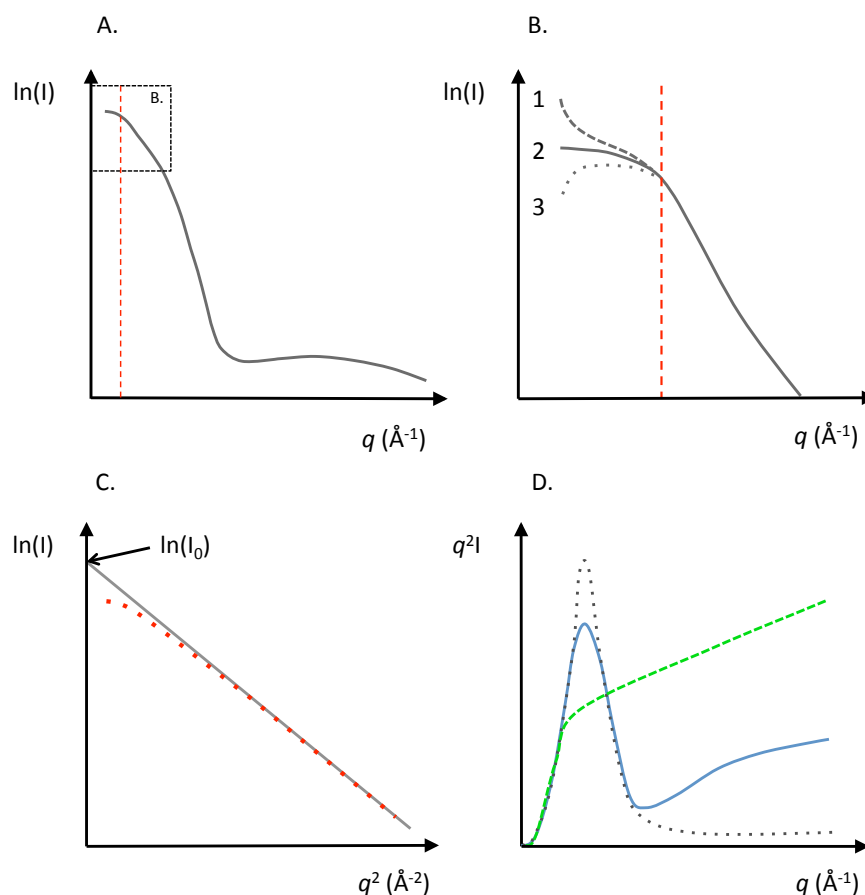
Figure 3.3 Interpretation of radially averaged scattering intensity data from SAXS. A. Typical 1-dimensional scattering profile of SAXS data with scattering intensity decaying at greater scattering angles. Boxed area = panel B. **B.** Inter-particle attractions (aggregation effects) cause increases in intensity at small q (**1**), while inter-particle repulsion causes the opposite effect (**3**), **2** shows no interparticle effects. A common procedure to overcome these effects is to merge low concentration data at small q with high concentration data from the point the scaled intensities converge (red dashed line). **C.** Guinier plot with a linear fit (grey line) to the small angle 'Guinier region' (red dotted line). The slope of the fit and the intercept with the y-axis can be used to estimate R_g. **D.** Kratky plots reveal important information about the folding and flexibility of structures. Grey dotted line = globular protein. Dotted green line = unfolded/flexible protein. Blue line = typical protein with mixed globular/flexible features.

By performing an inverse Fourier transform of the scattering intensities as a function of their momentum transfer it is possible to obtain a real space pair-distance distribution function: $p(r)$, which provides further information about the shape of the scattering molecule [18,19]. The process used to calculate $p(r)$ in the program GNOM [20]

is to estimate $p(r)$ that produces a reciprocal-space intensity profile ($I(q)$) that closely matches the experimental data and iteratively repeat the process to yield a $p(r)$ that produces the closest match to the experimentally observed intensity profile as determined by the magnitude of χ^2 between the estimated intensities calculated from the $p(r)$ and the experimental intensities [19,20].

It is possible to calculate R_g and to observe structural properties of the protein from the shape of the pair-distance distribution. For example, globular proteins yield a bell-shaped curve, whereas proteins with an elongated prolate shape produce a sharp feature at low r, which gradually decays to zero (figure 3.4). The pure features observed for categorical shapes can be mixed in $p(r)$ curves for real protein structures because proteins may have mixtures of structural features in their tertiary and/or quaternary structures. It is therefore possible to make predictions about the overall features present in protein structures from the $p(r)$ distribution.
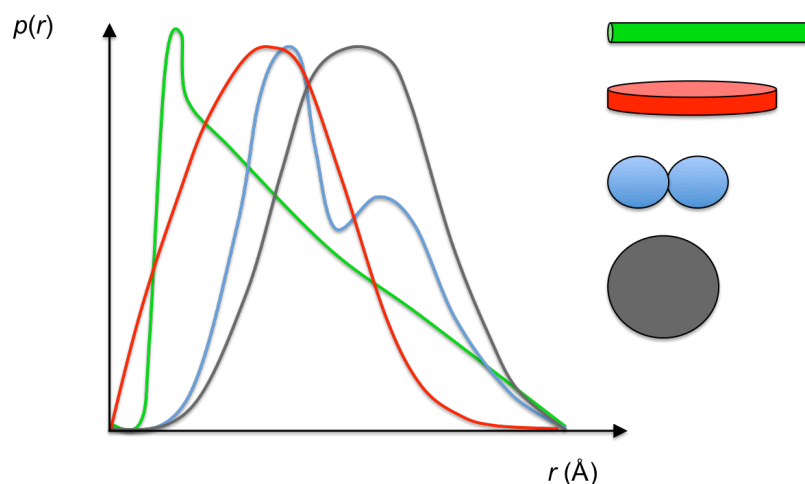
Figure 3.4 Real space pair-distance distribution function $p(r)$ for four theoretical protein shapes. The $p(r)$ curve for a prolate shape (green) features a sharp peak at low r before gradually decaying to zero, while an oblate shape produces a prominent, broad peak which tails off at small r (red). Multi-domain shapes (blue) produce a $p(r)$ curve with multiple peaks and globular proteins with a single domain (grey) produces a bell-shaped $p(r)$ curve.

Using the $p(r)$ distribution it is possible to produce an *ab initio* bead model of the protein structure with a maximum diameter, defined by the experimentally determined D_{max}, by performing dummy atom model minimisation (DAMMIN) analysis [16,21]. Normally this procedure is repeated, normally producing 10-20 independent bead models, which can be averaged and filtered to produce a model in

which low-occupancy atoms are removed according to a given experimentally determined cut-off volume and a bead model structure of the most probable distribution of atoms is produced.

3.2.4 Introduction to macromolecular X-ray crystallography

In order to perform an X-ray crystallography experiment, one must first be able to grow high-quality protein crystals. This is by no means a trivial task and can often take months or occasionally years to perform successfully. Protein crystallisation occurs as a result of many weak surface interactions occurring between protein molecules in solution, including hydrogen bonding, electrostatic interactions and hydrophobic interactions. Protein crystals can only form if these interactions occur in a consistently ordered fashion, leading to the formation of a lattice of protein molecules, which contain faultless repetitions of the same interactions throughout. Therefore, it is critical during the preparation of protein for crystallisation that protein solutions be as near homogenous as possible, both in terms of the purity of the protein sample and the polydispersity of the protein solution. High-concentration protein solutions are required to facilitate frequent inter-particle interactions and the process of regular, specific protein aggregation leading to the formation of crystal nuclei. Crystal nuclei are formed under conditions of supersaturation in the protein solution (figure 3.5B). Such conditions are made possible by the use of precipitants and vapour diffusion techniques (figure 3.5A) to grow crystals of sufficient size to perform macromolecular X-ray crystallography, which is normally in the region of 0.1-1.0 mm.

In a typical vapour diffusion experiment, protein solution is mixed with a crystallisation solution containing a precipitant and placed in a sealed environment with a reservoir solution containing the same crystallisation solution (figure 3.5A). The concentration difference of precipitant in the protein drop compared to the reservoir solution, as a result of being diluted by the protein solution causes solvent vapour from the protein drop to diffuse to the reservoir, increasing the concentration of protein and precipitant in the protein drop. Ideally, this concentration effect gradually increases the frequency of specific contacts formed between protein molecules and allows the formation of crystal nuclei (figure 3.5B). Due to the complex nature of the specific contacts required for proteins to crystallise, often

specific precipitants, protein concentrations and incubation temperatures are required for the successful crystallisation of proteins. For this reason, sparse-matrix screening and grid screening are regularly used to search for potential conditions under which a given protein will crystallise.
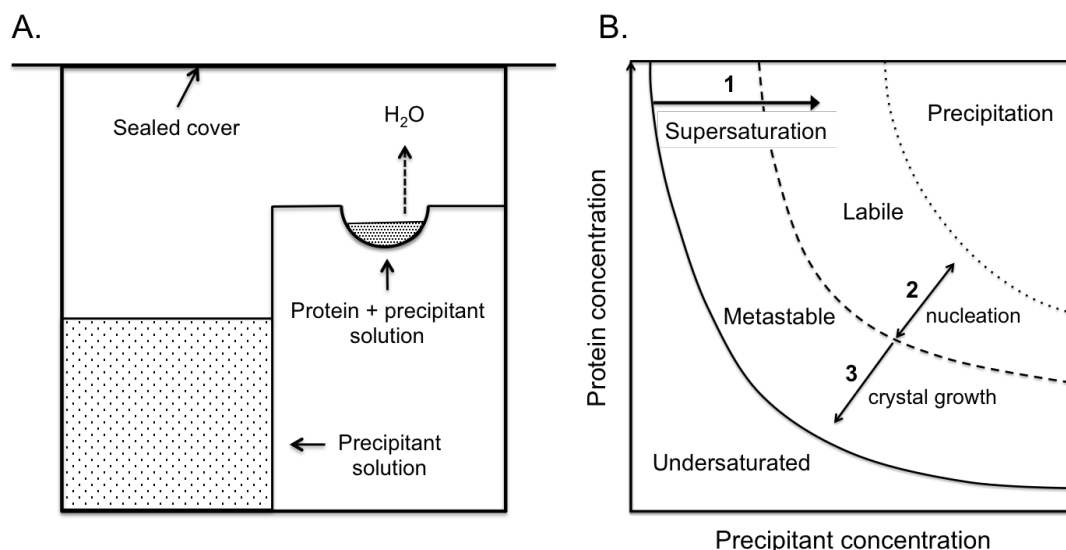
Figure 3.5 Vapour diffusion experiments enable the crystallisation of proteins with a precipitant by creating a supersaturated protein solution. A. Sitting drop vapour diffusion uses a sealed environment in which solvent moves from the protein solution to the precipitant/reservoir solution equilibrate the concentrations of precipitant in the protein drop compared to the reservoir solution. **B.** Typically during sparse-matrix screening of protein crystallisation conditions, protein solutions are prepared at high concentrations and a range of precipitant types and concentrations are tested to bring proteins to a supersaturated state (**1**). Occasionally, when protein solutions enter the 'labile zone' specific aggregates form and begin crystal nucleation (**2**). Under optimum conditions this leads to crystal growth (**3**). Many crystallisation conditions are either unable to initiate nucleation, or supersaturate protein solutions to the point of non-specific aggregation and precipitation.

X-ray diffraction experiments are routinely performed on protein crystals under cryogenic conditions using a nitrogen cryostream to minimise the damaging effects X-ray radiation-induced radical formation causes the protein crystal. As a result, a further challenge during the preparation of an X-ray diffraction experiment is the vitrification of protein crystals. Protein crystals must be cooled to liquid nitrogen temperatures rapidly in order to prevent the formation of ice crystals from the solvent water in and around the crystal. The negative effects of water crystallisation are two-fold; the formation of ice causes the protein crystal solvent to expand – damaging the crystal packing, and ice produces an intense diffraction

pattern that interferes with the signal from the protein crystal. Cryoprotectants are used during the vitrification process to further prevent ice formation.

Somewhat similar to SAXS, X-ray crystallography uses monochromatic X-ray radiation generated by a synchrotron, such as the Diamond Light Source, where the data presented in this chapter was collected. Synchrotron radiation is generated at the Diamond Light Source using particle accelerators, which utilise magnetic arrays to channel particles around a booster ring and then into an outer storage ring, with electrons moving at energy of 3 GeV. The Diamond Light Source storage ring is a polygonal shape; electrons are accelerated in straight lines around the storage ring with bending magnets at each angle in the ring diverting electrons. Each diversion causes electrons to lose energy in the form of intense X-ray radiation, which is channelled to individual beamlines. The X-ray diffraction experiment is performed using single crystals, which are rotated in a monochromatic X-ray beam and the diffracted X-ray radiation is collected and recorded using a detector (e.g. Pilatus [22]) as shown in figure 3.6.
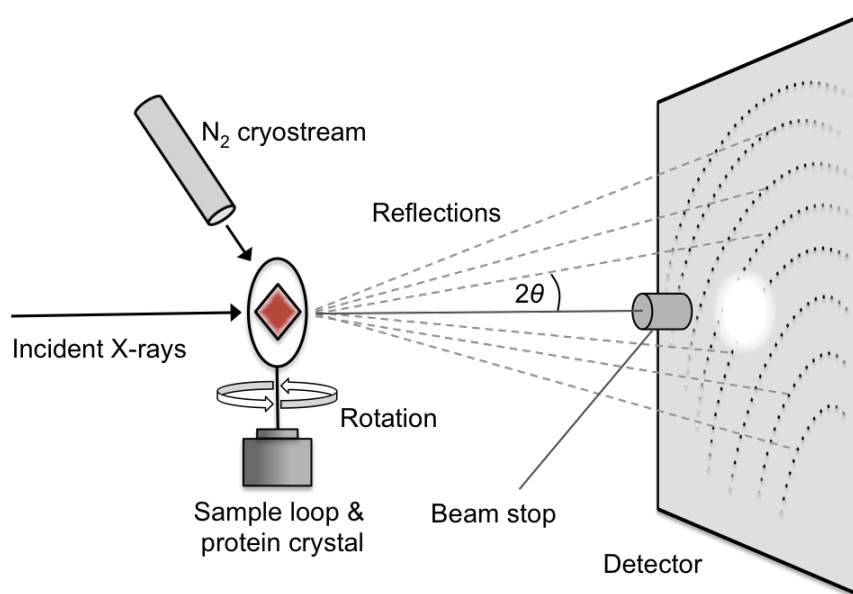
Figure 3.6 Performing the X-ray diffraction experiment. A protein crystal mounted in a sample loop is brought into the path of a nitrogen cryostream, which maintains cryogenic temperatures throughout the experiment. The crystal is aligned and centred in the direction X-ray beam manually using goniometric controls. Incident monochromatic X-ray radiation is scattered by the crystal; the intensities and positions of reflections are recorded at the detector, with the positions of Bragg spots giving the deviation angle of the reflection from the direction of the incident X-rays (2θ). Depending on the symmetry of the crystal lattice, varying degrees of crystal rotation may be required to record a complete dataset.

Beamline I03, the beamline used to collect X-ray diffraction data on MtoD crystals, provides X-ray radiation in the energy range 5.2-21.0 keV, which corresponds to an X-ray wavelength range of 0.6-2.3 Å. The tuneable X-ray wavelengths provided by beamline I03 were ideal for collection of X-ray diffraction data in native and anomalous scattering experiments. The presence of iron in the MtoD heme allowed anomalous data to be collected using Fe-edge SAD, which will be described later.

As previously discussed, SAXS provides useful low-resolution structural information based on the averaged intensities of X-rays diffracted by proteins tumbling in solution. For the determination of a high-resolution structure, X-ray crystallography has the advantage of molecules being oriented and organised in a crystal lattice as determined by the space group of the crystal. So while the resulting intensities from X-rays scattered by a crystal contain information on all scattering molecules held in the beam the molecules in a crystal are ordered by a specific crystallographic symmetry, therefore if one knows the internal symmetry of the crystal lattice and can provide phase information for the scattered X-rays, it is possible to produce a detailed real space electronic distribution for the molecules in the crystal.

Protein crystals grow within crystallographic symmetry constraints and are categorised and reported by their space-group. The space-group of a crystal provides the smallest symmetry operations required to translate the unit cell from one position to all other positions throughout the crystal lattice. The 65 unique space-groups for a chiral molecule such as a protein originate from 7 crystal systems, each of which has their own symmetry requirements and constraints. The notation for space groups using international notation contains information about the lattice type, the point-group and the required translations in the form XY_Z, where 'X' is a letter denoting the lattice type, 'Y' gives the point-group and $_Z$ provides the required translation through glide plane or screw axis symmetry operations. Symmetry operators may be listed one after another, for example the common space-group $P2_12_12_1$ is a primitive lattice (denoted by 'P') and contains three separate symmetry components, each with two-fold screw axes where the unit cell must be rotated by 180° around the screw axis and translated ½ of the repeat distance to complete a translation. A comprehensive index of the properties of all crystal space-groups is available in

International Tables for Crystallography, Volume A: Space-group symmetry [23]. Determination of a crystal's symmetry elements is crucial to reduction and processing of X-ray diffraction data and space-group determination becomes crucial to the final solution of a crystal structure. Determination of crystal symmetry is now often a relatively straightforward process due to the availability of programs that can use the point-group based on the 2-dimensional diffraction pattern to infer the crystal's space group.

The critical pieces of information, which must be obtained to solve the crystal structure of a protein using X-ray crystallography, are the angles, amplitudes and phases of X-ray reflections that contribute to the scattering pattern.

The positions of diffracted X-rays measured at the detector, given by their scattering angle or deviation from the incident beam (figure 3.6), provide important information about the crystal's lattice planes through Bragg's Law (equation 3.8) and about the symmetry within the crystal.

$$\text{Equation 3.8:} \qquad \lambda = 2d_{hkl}sin\theta$$

Equation 3.8 shows the wavelength of the incident X-ray radiation (λ) is equal to the lattice inter-planar distance (*d*) with lattice indices *h,k and l* multiplied by *sinθ*, where *θ* is the 'glancing angle' at which X-rays are reflected by lattice planes given by Miller indices *hkl*.

Atoms in a crystal scatter incident X-rays in all directions. The wavelength and phase of the incoming X-rays are identical and only reflected X-rays that remain in phase contribute to the recorded scattering pattern, since destructive interference by out of phase diffracted X-rays cancel each other. In order for diffracted X-rays to remain 'in phase' and contribute to the formation of Bragg spots on the detector, the distance between lattice planes must be equal to *nλ,* where n is an integer. Under these conditions, X-rays which are reflected in a given direction by the same plane travel the same distance to the wavefront and so remain in phase and X-rays that are reflected by other parallel lattice planes are also in phase; the additional distance the X-rays travel at planes further away is given by *2dsinθ* (figure 3.7). The coherent scattering of 'in phase' X-rays constructively interfere to produce Bragg spots.
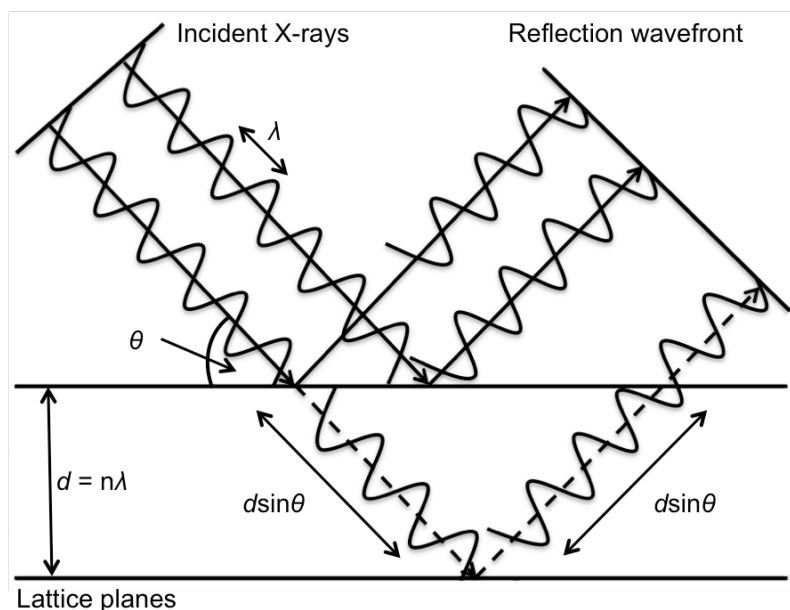
Figure 3.7 Diffraction of X-rays by lattice planes. Incident X-rays are monochromatic and 'in phase'. Scattering of X-rays by atoms occurs in all directions leading to a mixture of phases, which destructively interfere with one another. The scattering of X-rays by atoms in a lattice plane results in the formation of a wavefront due to reflected X-rays having travelled equal distances. Parallel lattice planes also produce in phase reflections if the distance between the planes is equal to an integer multiple of the X-ray wavelength ($d = n\lambda$). In this case $2d\sin\theta$ accounts for the extra distance travelled by X-rays; θ is half the total deviation angle for reflected X-rays relative to the direction of the incoming beam. The in phase reflected X-rays result in constructive interference, which produces coherent scattering and Bragg spots at the detector.

The lattice (Miller) indices *h,k and l* give the fractional spacing of lattice planes along the unit cell relative to the unit cell origin, where the unit cell is the smallest repeating volume that can be related to the rest of the crystal lattice through translational symmetry. Protein crystals contain many lattice planes, each with their own Miller indices and discrete d_{hkl}. Since the wavelength of X-ray radiation is constant during an X-ray diffraction experiment, d_{hkl} associated with discrete lattice planes relate to θ through Bragg's Law. The total divergence of the reflected X-ray from the incoming beam is given by 2θ. Therefore, knowing the wavelength of the incident X-ray radiation and the deviation angle of reflections provided by the positions of Bragg spots (figure 3.6) it is possible to provide information about the lattice geometry. As can be seen in equation 3.8, large values of θ correspond to small distances between lattice planes (*d*). Since lattice planes in close proximity contain finer detail of the crystal lattice, reflections scattered further from the angle

of the incident beam provide higher resolution information while reflections from lattice planes spaced further apart, which scatter to smaller angles provide lower resolution information.

The position of Bragg spots also provides useful information about the internal symmetry and space group of the crystal. Data reduction and processing by programs such as XDS [24] and POINTLESS [25,26] attempt to predict the space group of the crystal by first determining the Laue group (point-group symmetry) from the scattering symmetry then: select the space group that explains the observed intensities with the greatest lattice symmetry within tolerable multiplicity-weighted R-factors [24] (XDS) or by sequentially scoring potential rotational symmetry elements then searching for systematically absent reflections (POINTLESS) [26]. The space group determination is a hypothesis until structure solution due to the difficulty distinguishing between the precise crystallographic symmetry and approximate non-crystallographic symmetry [26]. However, the best prediction is useful for the subsequent interpretation of data and the point group is required during the scaling of intensities.

Scaling recorded intensities aims to introduce internal consistency to the diffraction data to make symmetry-related and duplicate measurements equal throughout the dataset by modelling the diffraction experiment [26]. This process is necessary due to divergence in the in the intensities of equivalent reflections throughout the dataset as a result of errors associated with the incident X-ray beam, such as intensity variance, crystal diffraction and the detector. The automated data reduction package XIA2 inputs indexed diffraction data from XDS into XSCALE (in 3d and 3dii mode), which assesses the completeness and quality of the data, then combines symmetry-related measurements and determines correction factors associated with radiation damage, X-ray absorption effects and detector imperfections [24]. The output is a scaled and merged dataset. Measures of internal consistency, such as R factors and correlation coefficients are normally used to provide information about the quality of the scaled data.

Once the data have been reduced and scaled, phasing the reflections can be attempted by a number of different methods; the X-ray diffraction experiment is approached knowing which phasing method is going to be used, since protein crystals must be prepared before the experiment for each method. The two main branches of phasing are experimental phasing and molecular replacement, where

experimental phasing techniques aim to determine the phases of reflections using isomorphous replacement, single/multi-wavelength anomalous dispersion or combinations of the two.

Isomorphous replacement relies on the differential scattering intensity of one (Single Isomorphous Replacement – SIR) or more (Multiple Isomorphous Replacement – MIR) heavy atom-containing crystals compared to crystals containing no heavy atoms. So long as the symmetry and forms of the crystals are consistent (isomorphous), the heavy atom diffraction of X-rays can be used to solve the proteins substructure and facilitate the solution of phases for the remaining non-heavy atom scatterers.

Phasing by anomalous scattering methods makes use of the differential scattering of atoms with electronic transitions close to the energy of the incident X-ray radiation compared to other atoms in the crystal. Friedel's law states that a pair of reflections (e.g. *h, k, l* and *–h, -k, -l*) must have the same amplitude but phases of opposite sign. This is the case for most scattering by atoms but changes when there are atoms that scatter anomalously. Anomalous scattering is the result of the excitation of electrons in an atom by incident radiation that results in some absorption of energy (*f''*) if the energy of the incident X-rays is close to a transition energy for the atom. This absorption causes the total coherent scattering (*f'*) to be reduced and there is a phase shift in the diffracted X-rays. The reason for the phase shift is due to changes of the total structure factors of Friedel pairs. The normal scattering components from protein and anomalous scatterers adhere to Friedel's law and are related as complex conjugates, however the anomalous components from the anomalously scattering atoms cause the overall structure factors to deviate, changing the resulting wave amplitude and phase (figure 3.8), creating a Bijvoet pair of reflections with an amplitude difference of $F^+_{total} - F^-_{total}$ (figure 3.8). This breach of Friedel's law has an observable effect, since the phase shift results in a change to the intensities of reflections, and can be used to position the anomalous scatterers in the substructure of the protein using programs such as HySS and SHELXD. These programs utilise direct methods or direct space/reciprocal space Patterson interpretation to find the sites of anomalously scattering atoms [27,28].
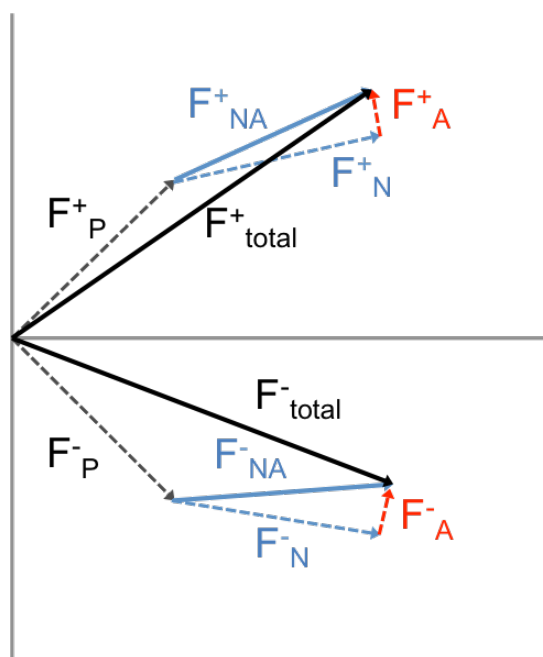
Figure 3.8 Argand diagram representation of wave phases and amplitudes in vector form. X-rays scattered by protein atoms in a lattice plane on opposite sides (e.g. with Miller indices *h, k, l* and *–h, -k, -l*) produce in phase structure factors with the same amplitude but opposite sign (F_P). Atoms that produce significant anomalous scattering at a given wavelength have a normal dispersive component (F_N) and an anomalous component (F_A). The normal dispersive components obey Friedel's law but the anomalous components do not. As a result, the total structure factor associated with the anomalous scatterer changes in breach of Friedel's law. The overall effect is a change to the total structure factor for all components (F_{total}), giving the Bijvoet pair different phases and amplitudes for the reflections.

Solving the substructure of a protein crystal by molecular replacement (MR) requires the rigid-body positioning (rotation and translation) of a molecular model that has a similar structure to the target protein rather than the positioning of anomalous scatterers. While it is possible for proteins with moderate sequence similarity, but high structural similarity to be used for molecular replacement, more commonly proteins of high sequence similarity are used since without prior knowledge of the target's structure finding such a model is challenging. However, the development of automated model search pipelines such as MrBUMP [29] are making model discovery quicker. Using sequence similarity is often the most effective method for finding a suitable model for MR when attempting to solve a new structure, although if no models of suitably similar protein structures are available *ab initio* methods of model building, using programs such as Rosetta [30] can be employed to provide a model. Models with high sequence identity tend to

produce lowest r.m.s. differences between the search model and the target. Low r.m.s. differences produce greater signal/noise ratios and improve the likelihood of a structure solution. Either Patterson methods or maximum likelihood methods can be used to apply 3-dimensional rotation and translation functions to position the postulated model based on the calculated amplitudes. As described by Evans & McCoy (2007) the maximum likelihood approach, as used in PHASER, is the more robust approach since it accounts for experimental and model errors, whereas the Patterson approach assumes no errors [31].

Substructure phases and amplitudes calculated by SAD and MR provide initial electron density maps in which to begin building a model. The phase information from these experiments provides sufficient phase information and an estimate of the electron density map to be modified and refined. The phasing solution can be improved significantly using additional phase information from anomalous data collected at other wavelengths (MAD) or by performing density modification. For experimental data collected to low resolutions (typically >3 Å), additional experimental data is normally required to provide accurate phase improvements. However, for high resolution data (typically <3 Å), a range of density modification techniques can be used to improve phase angles including solvent flattening, non-crystallographic symmetry (NCS) averaging, phase extension, molecular replacement and iterative model building [32]. The method of density modification employed by the PHENIX AutoBuild wizard uses experimentally determined structure factor amplitudes and prior phase/model information to perform iterative model building and structure refinement followed by model-based density modification. The program RESOLVE [33] performs density modification using NCS averaging, histogram matching, solvent flattening and local density pattern identification before initiating model building and scoring. For experimentally determined phases, model building is performed by iteratively fitting models into the available electron density and performing refinements using phenix.refine [34]. The models are initially scored based on the number of residues built (N_{built}), the number of residues assigned to the input polypeptide sequence (N_{placed}) and the number of chains in the model (N_{chains}): $Q = N_{built} + N_{placed} - 2 \times N_{chains}$. Model building and refinement are performed iteratively to achieve greater scores (Q). Further model-based density modification is performed using the refined model and scoring is repeated. Final scoring and evaluation of the model is performed using R-factors [33].

3.2.5 Cryoradiolytic reduction of hemes

Radiation damage to biological crystals is rapid and arises as a result of the ionising effects of X-ray radiation, which causes free radical formation in the irradiated sample. Cryo-cooling crystals to temperatures of approximately 100 K slows the diffusion of free radicals and enables significantly more high-quality diffraction data to be collected from biological crystals. The ionising effects of X-ray radiation are of particular importance to redox-active biomolecules such as oxidoreductase enzymes and cytochromes, which become reduced as a result of the X-ray induced electron generation in the crystal [35]. It is possible to monitor the reducing effects of X-ray irradiation using spectroscopic techniques with enzymes that produce a spectral change upon transition from the oxidised to the reduced state and the routine use of *in situ* UV-Vis spectroscopy during X-ray diffraction experiments is becoming increasingly common [36–38]. Current evidence indicates that photoreduction of redox-active proteins is rapid enough using 3rd generation synchrotron radiation sources that structures of almost all cytochromes represent the reduced state [35]. By contrast, 3D protein structures produced using NMR spectroscopy are not photoreduced and as a result it is possible to resolve structures at user-defined redox potentials, allowing oxidised and reduced forms of proteins to be captured.

3.3 Methods

3.3.1 Analytical ultracentrifugation (AUC)

A stock solution of 5 mg.mL^{-1} (430 µM) MtoD-Strep was prepared for sedimentation velocity experiments by dialysis against a buffer solution containing 20 mM HEPES pH 7.0 and 100 mM NaCl. The protein solution was transferred to a 1.5 mL microcentrifuge tube and centrifugation at 13,000 rpm in a bench-top centrifuge was performed to pellet any protein aggregates of particulates in the solution. MtoD-Strep was prepared at three concentrations: 11.5 µM, 6.2 µM and 3.5 µM, based on absorption at 406 nm, using the experimentally determined ε_{406}=117 mM^{-1}.cm^{-1} (as described in chapter 2). 410 µL of each MtoD-Strep sample was transferred into sample chambers of a double sector cell, quartz window cell

assembly (Beckman) and 420 µL 20 mM HEPES pH 7, 100 mM NaCl was measured into the reference chambers. A Beckman Optima XL-A analytical ultracentrifuge and AN-50 Ti rotor were used to optically measure sedimentation, monitoring absorbance at 406 nm with a rotational speed of 42,000 rpm. 300 radial scans were performed over a 20-hour period at a constant temperature of 20°C.

Buffer density and viscosity parameters (1.0039 g.mL^{-1} and 1.0264x10^{-2} ρ respectively) in addition to predicted v-bar for MtoD-Strep containing a single heme (0.7282 mL.g^{-1}), were estimated using the program SEDNTERP [39] and included in the $c(s)$ model during data processing in ULTRASCAN II [40]. Sedimentation velocity absorbance data were loaded into ULTRASCAN II [40] and edited to correct the baseline and remove any large spikes in the data. Spikes in absorbance data are often a result of electrical noise, failed lamp flashes and scratches in the cell windows (please refer to the UltraScan II manual at http://www.ultrascan2.uthscsa.edu) [40]. The edited data were analysed using the $c(s)$ distribution analysis tool using the above parameters to give estimates for the sedimentation coefficient, the frictional coefficient and the corresponding molecular weight of proteins in each of the samples. The input parameters and resulting sedimentation and frictional coefficients were used to reproduce the same data and fit SEDFIT [15] in order to produce plots of the data, fit and residuals as well as the $c(s)$ distribution in the graphing tool GUSSI.

3.3.2 Small Angle X-ray Scattering (SAXS)

Samples of MtoD-Strep were prepared for SAXS experiments as previously described for sedimentation velocity (section 3.3.1). A solution of MtoD-Strep was concentrated to 500 µM (~6 mg.mL^{-1}) by centrifugal concentration with a 3 kDa MWCO membrane and dynamic light scattering (DLS) experiments were performed to determine the degree of polydispersity in the concentrated protein solution. DLS was performed using a DynaPro-LSR. 15 µL of buffer prepared for the SAXS experiment and 15 µL of the concentrated MtoD-Strep sample in the same buffer were separately measured into a reduced-volume quartz cuvette; DLS was performed with 824 nm incident light at 20°C and intensity of scattered light was measured (in counts/second) over a period of 80 seconds to determine the polydispersity of the solutions.

Primary data reduction to perform buffer subtractions and normalisation of the SAXS scattering data was performed at the B21 beam line at the Diamond Light Source. These data for three MtoD-Strep concentrations were processed further using the ATSAS 2.6.0. suite of programs [41]. Scaling of the datasets was performed in PRIMUS and the initial calculation of R_g was performed using the program AUTORG [41], which applies the Guinier approximation to estimate R_g and I_0 by extrapolation of scattering intensities to zero-angle. Inspection of the low q data for each concentration was performed for the subtracted scattering profiles and Guinier plots to identify concentration-dependent inter-particle interaction effects. An indirect Fourier transform method was used to produce a real space electron pair-distance distribution $p(r)$ using the program GNOM [20]. *Ab initio* model building was performed using DAMMIF [42], which was run in 'slow' mode without imposing symmetry constraints. 10 batches of bead modelling were performed, producing 10 discrete models, which were then aligned by SUPCOMB [43] and averaged using the program suite DAMAVER [44]. Further refinement and filtering of the averaged model was performed automatically by the DAMAVER suite using programs DAMMIN [21] and DAMFILT respectively.

3.3.3 X-ray crystallography

Pure MtoD-Strep was concentrated by centrifugal concentration to 30 mg.mL^{-1} (2.55 mM) as quantified spectroscopically and centrifuged as previously described for sample preparation during AUC to pellet particulates in the solution. Sparse matrix screening was performed using the sitting drop crystallisation method with two drops per condition at 1:1 and 2:1 ratios of mother liquor/protein. JCSG-plus HT-96 (Molecular Dimensions) and Classics II (Qiagen) sparse matrix screening solutions were used to provide mother liquor for the crystallisation trials. Crystallisation experiments were dispensed in 1 μL drops using Douglas Instruments Oryx robotics and crystallisation trays were incubated at 16°C. Crystals formed in conditions containing 30% PEG 2000 MME + 0.1 M potassium thiocyanate (KCN) or 28% PEG 2000 MME + 0.1 M Bis-Tris pH 6.5. Conditions were optimised by producing a PEG 2000 MME gradient of 24-34% in 2% increments and producing a

second gradient for KCN and Bis-Tris from 50-400 mM. Optimisation experiments were also incubated at 16°C.

A total of six cryoprotectants were tested with the optimised mother liquor solutions that produced protein crystals: ethylene glycol, hexylene glycol (MPD), glycerol, PEG 550 MME, PEG 300, DMSO and trehalose. Each was made up at incrementally decreasing concentrations with mother liquor, starting at 20% (v/v) then vitrified in liquid nitrogen. 50 µL test cryogenic solutions that appeared opaque – showing signs of freezing were discarded and those that remained translucent – indicating successful vitrification were kept and lower cryoprotectant concentrations were tested. Final cryogenic solutions used included: 10% ethylene glycol, 10% DMSO, 12% MPD, 12% glycerol, 12% PEG 550 MME and 15% PEG 300.

MtoD crystals were harvested at 16°C using 0.1-0.2 mm mounted litholoops (Molecular Dimensions) then incubated for 5-20 seconds in cryogenic solution before vitrifying by plunging in liquid nitrogen (77 K).

X-ray diffraction data were collected from MtoD crystals held in a gaseous nitrogen cryostream (100 K) at beamline I03 at the Diamond Light Source, which is capable of supplying X-ray radiation with wavelengths ranging from 0.6-2.3 Å (corresponding energy: 5.2-21.0 keV). SAD and native X-ray diffraction by MtoD crystals was tested using respective X-ray wavelengths of 1.72 Å and 0.97 Å with an unattenuated 20 x 20 µm aperture beam. Three 0.05-second exposures were performed on the crystals using 0.2^o Ω oscillations and Ω overlap of -44.8^o.

Single-wavelength Anomalous Diffraction (SAD) experiments were performed using X-ray radiation with a wavelength of 1.72 Å. The theoretical absorption peak for anomalous scattering by iron was experimentally determined as 1.74 Å (7,134 eV) using an X-ray fluorescence scan. An X-ray wavelength of 1.72 Å (7,208 eV) was selected to maximise dispersive and anomalous scattering during the SAD experiment. 360° of diffraction data were collected to a resolution of 2.50 Å at the detector edge using 0.2^o Ω oscillations and 0.05 seconds exposures to an unattenuated 20 x 20 µm beam. The SAD experiment successfully used to phase the X-ray diffraction data was performed on an MtoD crystal grown in 24% PEG 2000 MME, 50 mM KCN and cryoprotected with 12% glycerol.

The wavelength of the X-ray beam was reduced to 0.97 Å to record a native dataset using the same crystal as was used during the SAD experiment. 180° of diffraction data were collected to a resolution of 1.50 Å at the detector edge using

0.2° Ω oscillations and 0.1 second exposures using the same X-ray beam parameters as previously.

Data reduction, including integration, indexing, and scaling of the SAD dataset and the native dataset was performed to the maximum resolutions recorded using XIA2 in 3dii mode, which uses XDS and XSCALE to index and scale peaks from all images [45,46]. Phasing and structure solution of the SAD dataset was performed using the Phenix automated structure solution wizard AutoSol [47]. Specifically, phasing of the anomalous data was performed with PHASER and automated density modification and model building were performed by RESOLVE [48,49], using the inputted reduced data and polypeptide sequence of mature Strep II-tagged MtoD. One cycle of model refinement was performed by phenix.refine to produce a partial structure solution.

Automated model building and refinement were performed using AutoBuild [33]. AutoBuild used the Phenix programs RESOLVE, phenix.xtriage [50] and phenix.refine [34,51] to perform iterative cycles of model building and refinement with model-based density modification. The fragmented model produced from this low-resolution structure solution from SAD-phasing was used to provide phase information to attempt a structure solution for the 1.47 Å resolution native dataset by molecular replacement. Molecular replacement was performed using PHASER [52] in the CCP4 suite and the partial structure solution were used as an input for a second AutoBuild run which produced a complete structure solution. Further cycles of model building and refinement was performed manually using COOT [53] and REFMAC5 [54] in the CCP4 program suite.

3.4 Results

3.4.1 Sedimentation velocity

To determine the biophysical properties of MtoD-Strep in solution, sedimentation velocity was performed on 3.5, 6.2 and 11.5 µM MtoD-Strep dialysed against 20 mM HEPES pH 7.0, 100 mM NaCl as described in methods. The strong Soret-band absorption at 406 nm ($\varepsilon = 117,000$ M^{-1}.cm^{-1}) allowed the migration of MtoD-Strep in the centrifugal field to be monitored optically at this wavelength. Simultaneous measurement of boundary migration for each of the three concentrations of MtoD over 20 hours allowed a direct comparison of the data to inspect for concentration-dependent attraction or repulsion effects on MtoD-Strep. Absorbance data for each MtoD concentration was processed in UltraScan II and $c(s)$ analysis was performed individually using buffer parameters and predicted partial specific volume (υ) for MtoD estimated in SEDNTERP [39]. Lamm equation solutions fitted to absorbance data using the c(s) distribution model for each MtoD-Strep concentration produced fits to the absorbance data with residuals no greater than ± 0.05 absorbance units (figure 3.9 A, C & F) and revealed a sedimentation coefficient of 1.465 S ± 0.024 S and a corresponding molecular weight of 11,894 Da ± 286 Da. This molecular weight compares very well with the estimated molecular weight of MtoD-Strep containing a single heme (11,584 Da). The molecular weight derived from $c(s)$ analysis confirmed Strep II-tagged MtoD behaved as a monomer in solution. Aggregation effects were not observed, as can be seen in the plot of $c(s)$ at each concentration, which produced single, sharp distributions of sedimentation coefficients characteristic of a homogenous sample (figure 3.9 B, D & F). An average f/f_0 coefficient of 1.32 ± 0.03 was determined for MtoD, which is consistent with MtoD-Strep being a globular protein, elongated slightly in either a prolate or oblate manner.
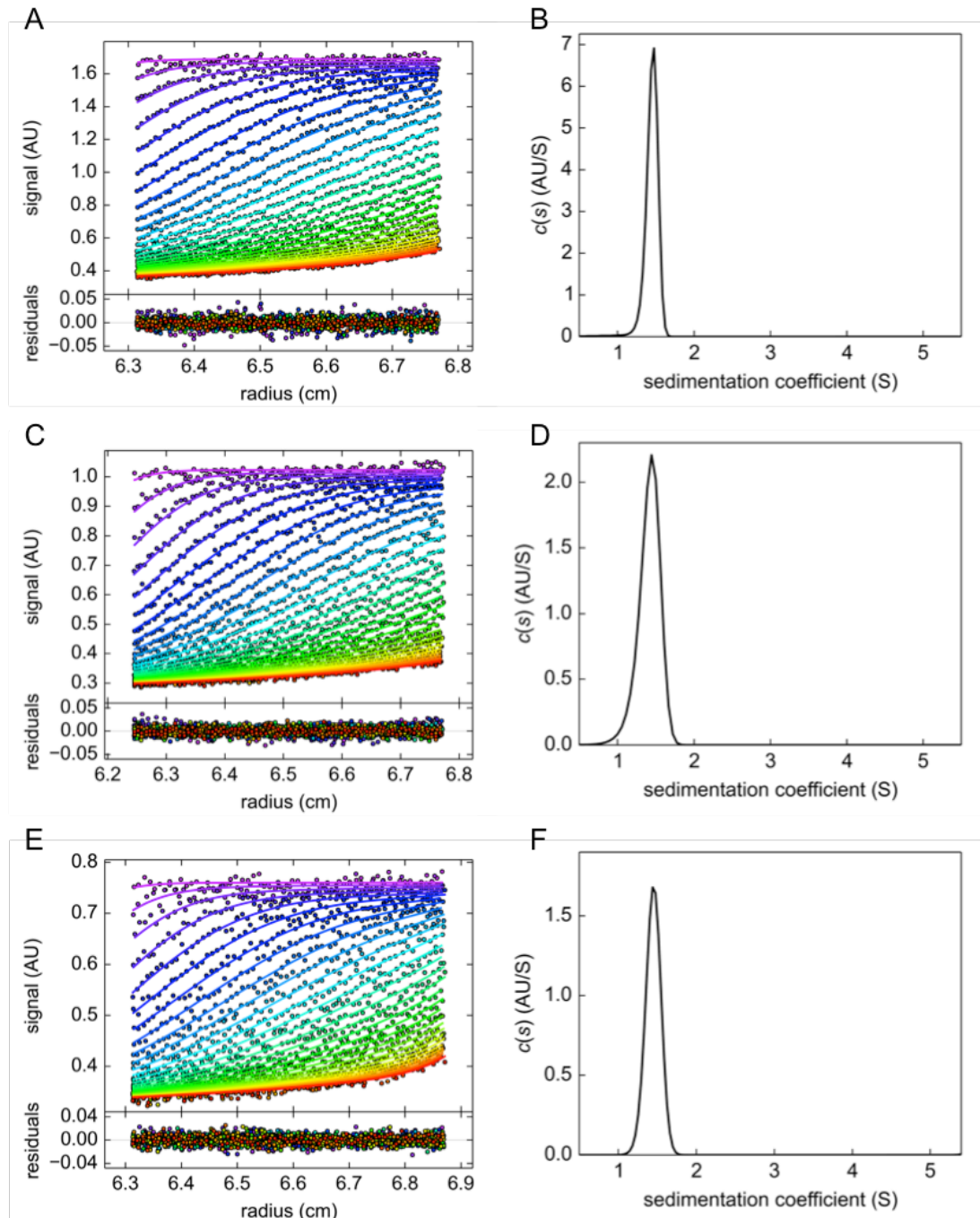
Figure 3.9 Sedimentation velocity analyses of 11.5 µM, 6.2µM and 3.5 µM Strep II-tagged MtoD. A, **C** & **E**: Lamm equation solutions fitted to absorbance data using the $c(s)$ model for boundary migration during sedimentation velocity of Strep II-tagged MtoD at 11.5 µM, 6.2 µM and 3.5 µM concentrations respectively. Residual absorption from the fitted data is shown below each panel. **B**, **D** & **F**: $c(s)$ distribution analysis of 11.5 µM, 6.2 µM and 3.5 µM MtoD. $c(s)$ analysis produced an average sedimentation coefficient of 1.465 S ± 0.024, a corresponding molecular weight of 11,894 Da ± 286 and an f/f_0 ratio of 1.32 ± 0.03. The single, sharp peaks present in each of the $c(s)$ distributions are characteristic of homogenous samples indicating MtoD is monomeric in solution.

3.4.2. Small Angle X-ray Scattering

Preliminary analysis by dynamic light scattering (DLS) was used to assess the quality of MtoD-Strep samples destined for SAXS experiments. The results, as shown in Appendix table X2, indicated 6 mg.mL^{-1} MtoD-Strep solutions were homogenous with sample polydispersity of 17% ± 3.4% and the protein was likely to be monomeric, with a hydrodynamic radius of 19.4 Å ± 1.9 Å and an estimated molecular weight of 16.3 kDa ± 3.8 kDa.

Small angle X-ray scattering experiments were performed on 6 mg.mL^{-1} MtoD-Strep as prepared for DLS in addition to two dilutions with MtoD-Strep concentrations of 3 mg.mL^{-1} and 1.6 mg.mL^{-1}. Collection and initial reduction of scattering data were performed at beamline B21 at the Diamond Light Source and the resulting buffer-subtracted 1-dimensional scattering data were further processed using programs from the ATSAS suite [41]. Presentation of the subtracted data on a plot of log intensity vs. momentum transfer (q) at small scattering angles (figure 3.10 A) revealed some minor inter-particle attractions as indicated by the slight incline of the scattering profiles in the 6 mg.mL^{-1} and 3 mg.mL^{-1} MtoD samples at the smallest scattering angles (low q). Lower signal/noise levels in the 1.6 mg.mL^{-1} sample at low q made it difficult to accurately determine whether these inter-particle effects were present at this MtoD-Strep concentration. Therefore, rather than merge low q data from the 1.6 mg.mL^{-1} sample with the 6 and 3 mg.mL^{-1} data, 0.021 Å^{-1} of intensities were cut from the lowest scattering angles of the 6 and 3 mg.mL^{-1} data to minimise the introduction of errors in the estimation of radius of gyration (R_g) and zero-angle intensity (I_0) for these samples. R_g and I_0 for each MtoD concentration were determined by Guinier analysis using the program AUTORG [41]. An R_g of 14.46 Å ± 0.06 was determined for the three concentrations of MtoD-Strep; plots of R_g and R_g/I_0 at each of the three MtoD concentrations (figure 3.10 B) revealed no concentration-dependence on the resulting estimation of R_g from the Guinier analysis.

Kratky analysis of scattering profiles produced bell-shaped plots with a gradually inclining tail at high q (figure 3.10 C), which is consistent with MtoD-Strep being a globular protein with some flexible behaviour. Small monoheme cytochromes c are not known to be inherently flexible proteins [1] and so it was

proposed this flexibility could be a result of the addition of an 8-amino acid Strep II tag to the C-terminus of MtoD.

A particle pair distance distribution was plotted for the 6 mg.mL^{-1} data using the program GNOM [20], which produced a bell-shaped distribution with a single peak of particle distances at 18.3 Å; the absence of further peaks supported MtoD being monomeric. The position of the peak of the distribution at ~D_{max}/2 (21 Å) supports MtoD being a globular shape, while the offset of the peak from D_{max}/2 and the tail in the $p(r)$ distribution from 35-42 Å suggests the presence of some prolate or oblate characteristics to the molecule's shape.
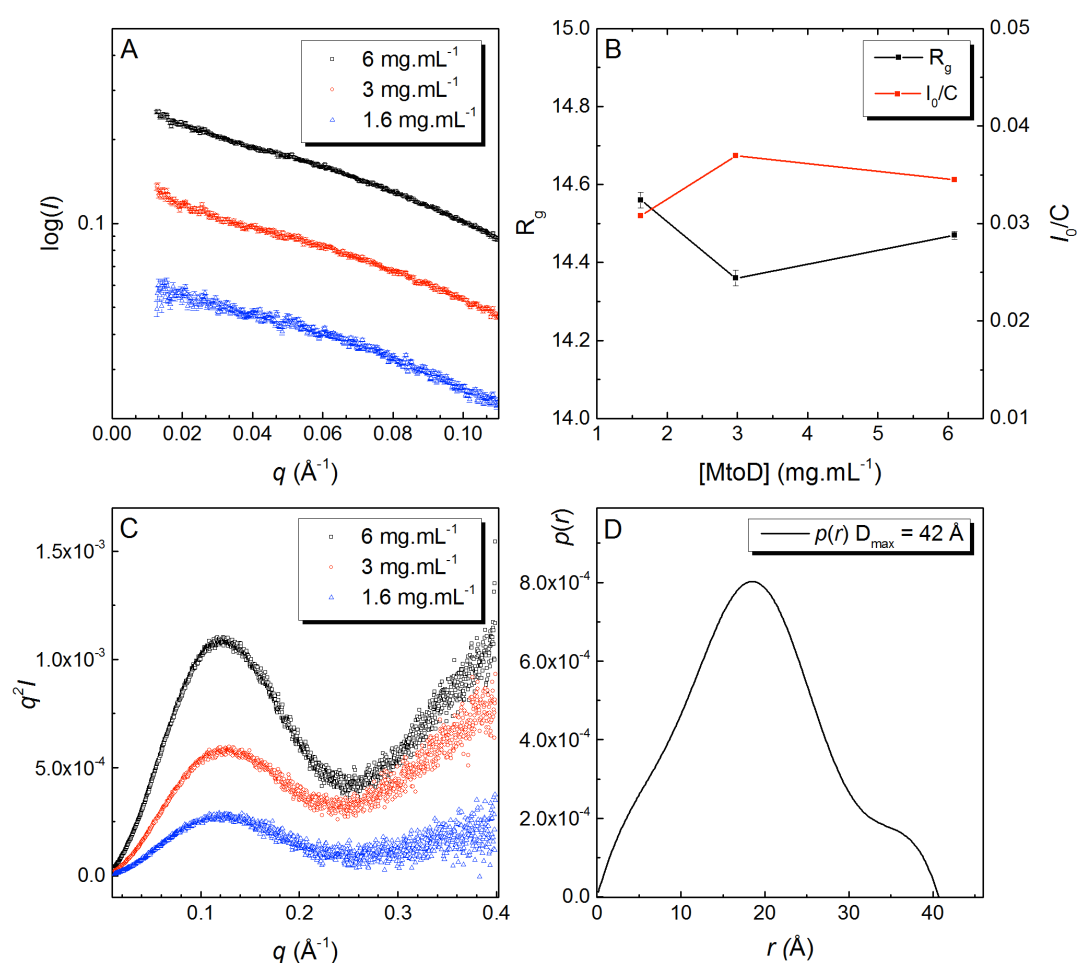
Figure 3.10 Analysis of SAXS data for 6, 3 & 1.6 mg.mL^{-1} MtoD suggests the protein is monomeric and globular with a small extension. A. Low q intensity vs. momentum transfer (q) revealed minor inter-particle interaction effects at 6 mg.mL^{-1} and 3 mg.mL^{-1}. **B.** R_g and I_0/C show concentration-independent behaviour. **C.** Kratky plots of data for each MtoD concentration produced line shapes typical of a globular protein with some flexible behaviour. **D.** Particle pair distance distribution $p(r)$ plot for 6 mg.mL^{-1} MtoD using a maximum inter-particle distance (D_{max}) of 42 Å.

Ab initio bead modelling based on the *p*(*r*) function determined by GNOM was performed in DAMMIF [42]. The program was run in 'slow' mode, which fitted the model to all points of the *p*(*r*) curve using dummy atoms with a radius of 1 Å. Ten batches of modelling performed in DAMMIF produced ten unique structure predictions, which were averaged in DAMAVER [43]. Further details of the DAMMIF settings can be found in Appendix table X3. Cross-comparison of the models in DAMSEL [44], after alignment by SUPCOMB [43], found one outlier model greater than two standard deviations from the mean normalised spatial discrepancy (NSD). This model was discarded and averaging of the remaining models produced an average structure containing 3,192 dummy atoms, shown as a mesh structure in figure 3.11 (A-C). Filtering of the averaged bead model by DAMFILT [44] removed low-occupancy dummy atoms, producing a final model containing 1,856 atoms with a total volume of 20,520 $Å^3$, shown as a surface envelope in figure 3.11 (A-C). Reported statistics from the DAMFILT job are detailed in Appendix table X3.

The dimensions of the filtered bead model were 40.7 x 30 x 27 Å, with the longest dimension given by the maximum particle-distance of 40.7 Å as determined by GNOM given a D_{max} of 42 Å. These dimensions agree well with the *f*/*f*$_0$ coefficient of 1.32 determined for MtoD by sedimentation velocity. As was apparent in Kratky plots and the *p*(*r*) distribution (figure 3.10 C & D), the averaged and filtered bead models have a globular structure with some oblate features. The greatest divergent distance between the averaged and the filtered bead models occur towards the rear and top of the overlaid models, most apparent in the 'side' view of the models as shown in figure 3.11 B. Large differences between averaged and filtered models are indicative of low-occupancy dummy atoms being present in this region of the averaged model, which in turn can result from the presence of flexible polypeptide regions. As a result, this region of the model was considered a candidate location for the C-terminal Strep II tag.

The theoretical scattering produced by the filtered MtoD model was calculated and compared to the experimental scattering for the 6 mg.mL^{-1} MtoD-Strep solution determined by SAXS using CRYSOL [55] (figure 3.11 D). The fit determined in CRYSOL [55] indicated the filtered MtoD surface envelope agreed well with the experimental X-ray scattering data, producing a χ^2 of 155.
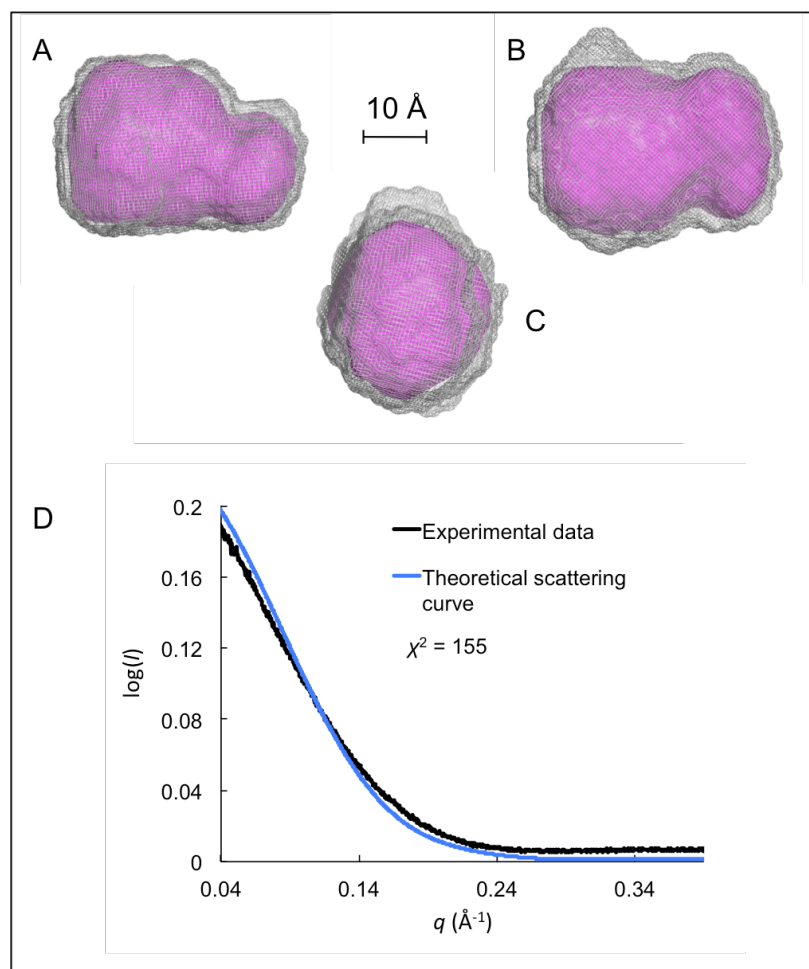
Figure 3.11 *Ab initio* **model of the molecular envolope of MtoD based on the particle pair distance distribution for 6 mg.mL^{-1} MtoD with a D$_{max}$ of 42 Å. A**, **B & C** show a top-view, side-view and view from the front of the surface structure respectively. The exterior mesh envelope is the average bead model produced by the program DAMAVER and the interior structure coloured magenta is the final filtered bead model produced in DAMFILT presented as a surface model. The dimensions of the filtered envelope are 40.7 x 30 x 27 Å. **D.** Experimentally determined X-ray scattering data for 6 mg.mL^{-1} MtoD overlaid with the theoretical scattering data for the filtered model of MtoD calculated using CRYSOL [55]. Pictures were produced in PyMOL [56].

To further validate the SAXS model for MtoD, a structural comparison was made between the filtered *ab initio* SAXS model for MtoD-Strep and characterised structures of cytochromes *c* most similar to MtoD. Cytochrome *c* structures were identified by performing a BLAST [57] search in the protein data bank (PDB) database using the mature MtoD sequence as a template. A multiple sequence alignment was performed on the resulting protein sequences with greatest similarity using Clustal Omega [9], the results of which are shown in table 3.1. The most apparent region of sequence similarity between MtoD and other cytochromes is around the 'CXXCH'

c-type heme-binding motif. MtoD lacks the 'PMPP' sequence commonly associated with the c_8 class of cytochromes. Superposition of these structures with the filtered SAXS model for MtoD-Strep was performed using SUPCOMB [43].

PDB	Organism	E-value	Sequence	
4XXL	*S. litho*		AVDVDAAKSLARENN**CFKCH**GVDKEKDGPSYKKVAEKYRGKADAEAKL	48
1A56	*N. europ*	2e-09	------DADLAKKNN**CIACH**QVETKVVGPALKDIAAKYADKDDAATYL	42
2PAC	*P. aerug*	5e-08	----EDPEVLFKNKG**CVACH**AIDTKMVGPAYKDVAAKFAGQAGAEAEL	44
2D0S	*H. therm*	1e-07	------DEALAKAKG**CMACH**AIDKKLVGPSYKDVAKKYTEAD--VPKL	40
1YNR	*H. therp*	2e-06	------NEQLAKQKG**CMACH**DLKAKKVGPAYADVAKKYAGRKDAVDYL	42
1COR	*P. stutz*	3e-06	----XDGEALFKSKP**CAACH**SIDAKLVGPAFKEVAAKYAGQDGAADLL	44
2ZXY	*A. aeoli*	4e-05	----ADGKAIFQQKG**CGSCH**QANVDTVGPSLKKIAQAYAGKEDQLIKF	44
			: : : * ** . . **: .:* : :	
4XXL	*S. litho*		IHHVTSGEKAKFP---DGHEEEHKNINGKASPEAIKNLVDWILSL-	90
1A56	*N. europ*	2e-09	AGKIKGGSSGVWG---QIP**PMPP**----NVNVSDADAKALADWILTLK	81
2PAC	*P. aerug*	5e-08	AQRIKNGSQGVWG---PIP**PMPP**----N-AVSDDEAQTLAKWVLSQK	82
2D0S	*H. therm*	1e-07	VEKVKKGGAGVWG---PVP**PMPP**----HPQVAEADIEKIVRWVLTLK	79
1YNR	*H. therp*	2e-06	AGKIKKGGSGVWG---SVP**PMPP**----Q-NVTDAEAKQLAQWILSIK	80
1COR	*P. Stutz*	3e-06	AGHIKNGSQGVWG---PIP**PMPP**----N-PVTEEEAKILAEWILSQK	82
2ZXY	*A. aeoli*	4e-05	L---KGEAPAIVDPAKEAIMKPQLTMLKGLSDAELKALADFILSHK	87
			. . : : :. ::*:	

Table 3.1 Sequence alignment of MtoD (PDB ID: 4XXL) against cytochromes *c* with solved structures from the PDB. The conserved CXXCH heme-binding motif is shown in green and the common PMPP sequence associated with c_8-type cytochrome *c* is shown in red. Full organism names in descending order: *Sideroxydans lithotrophicus* ES-1; *Nitrosomonas europaea*; *Pseudomonas aeruginosa*; *Hydrogenophilus thermoluteolus*; *Hydrogenobacter thermophilus*; *Pseudomonas stutzeri*; *Aquifex aeolicus*.

Superposition of cytochrome *c* structures from the PDB with the filtered SAXS model for MtoD-Strep revealed good overall fits in terms of size, which was expected due to the similar molecular weights of the cytochromes to MtoD. The best fit in terms of shape to the SAXS model for MtoD was provided by ferricytochrome *c*552 from *Nitrosomonas europaea* (1A56) as shown in figure 3.12 A, which also has the greatest sequence similarity to MtoD (37% E = 2e-09). This observation agrees well with CRYSOL [55] analysis in which each of the atomic models for the solved cytochrome *c* structures was fitted to the experimental SAXS data for MtoD. The quality of the fit was measured by magnitude of χ^2, as shown in figure 3.12. The $\chi^2 = 99.2$ for 1A56 compared to the greater values ranging between 107-130.8 for the other cytochromes confirmed this structure quantitatively provided the best fit to the experimentally determined SAXS structure of MtoD. 1A56 has a globular shape, slightly elongated along one axis, which allows the structure to fit into the narrowed surface around the 'front' of the MtoD SAXS model with few protrusions around

other regions of the surface. The N and C-terminal ends of 1A56 are present in the large globular section of the MtoD SAXS model, located on the left-hand side of the superposition shown in figure 3.12, and the heme cofactor is positioned at the opposite side of the protein, close to the narrow 'front' face of the MtoD envelope.

Based on the similarities observed after superposing the cytochrome *c* structures with the molecular envelope of MtoD-Strep, the overall shape and size of MtoD as determined by SAXS appeared to be consistent with other small monoheme cytochrome *c* structures. In particular 1A56, the NMR solution structure of ferricytochrome *c* from *Nitrosomonas europaea*, provided the greatest insight into the structural features expected to be present in MtoD prior to the solution of a high-resolution crystal structure for MtoD.
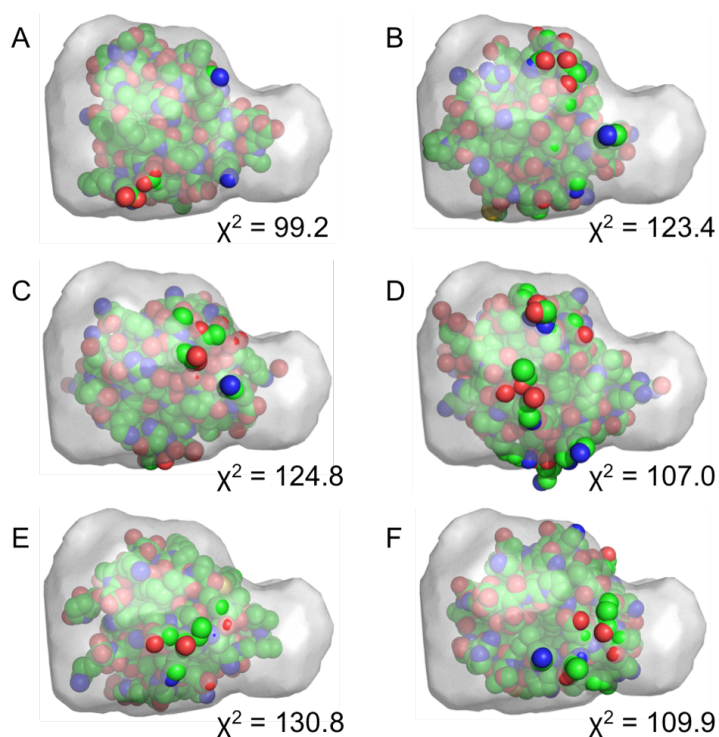
Figure 3.12 Superposition of the filtered SAXS model for MtoD with cytochrome *c* structures of greatest sequence similarity to MtoD. The SAXS model of MtoD is shown from the 'top' as in figure 3.11 A. **A.** Cytochrome *c*552 from *Nitrosomonas europaea* (1A56) [58]. **B.** Cytochrome *c*551 from *Pseudomonas aeruginosa* (2PAC) [59]. **C.** Cytochrome *c*552 from *Hydrogenophilus thermoluteolus* (2D0S) [60]. **D.** Cytochrome *c*552 from *Hydrogenobacter thermophiles* (1YNR) [61]. **E.** Cytochrome *c*551 from *Pseudomonas stutzeri* (1COR) [62]. **F.** Cytochrome *c*555 from *Aquifex aeolicus* (2ZXY) [63]. The quality of the fit between the atomic models of the cytochromes c and the experimental SAXS data for MtoD are given as χ^2, calculated using CRYSOL, with lower values indicating closer fits. The cytochrome *c* atomic models are shown as space-filling structures coloured by element.

3.4.3 X-ray crystallography

As detailed in section 3.3.3, a solution of MtoD-Strep was concentrated to a final protein concentration of 30 mg.mL^{-1}, as quantified spectroscopically and sitting drop vapour diffusion crystallisation was performed using two sparse matrix screens: JCSG-plus HT-96 (Molecular Dimensions) and Classics I (Qiagen). Red-coloured crystals were observed after 18 hours of incubation at 16°C in conditions containing 30% PEG 2000 MME and 0.1 M potassium thiocyanate (KCN) or 28% PEG 2000 MME and 0.1 M Bis-Tris pH 6.5. All MtoD-Strep crystals grew as plates with a maximum length of ~300 μm (figure 3.13 A). Optimisation of the crystallisation conditions from the sparse matrix screens was performed to create a range of each of the conditions' constituents. Optimisation and incubation under the same conditions yielded single plate crystals of MtoD-Strep (figure 3.13), which were harvested using 0.1-0.2 mm LithoLoops (Moleculr Dimensions) and cryoprotected by transferring the crystals into mother liquor containing 12% glycerol as a cryoprotectant before vitrifying in liquid nitrogen.
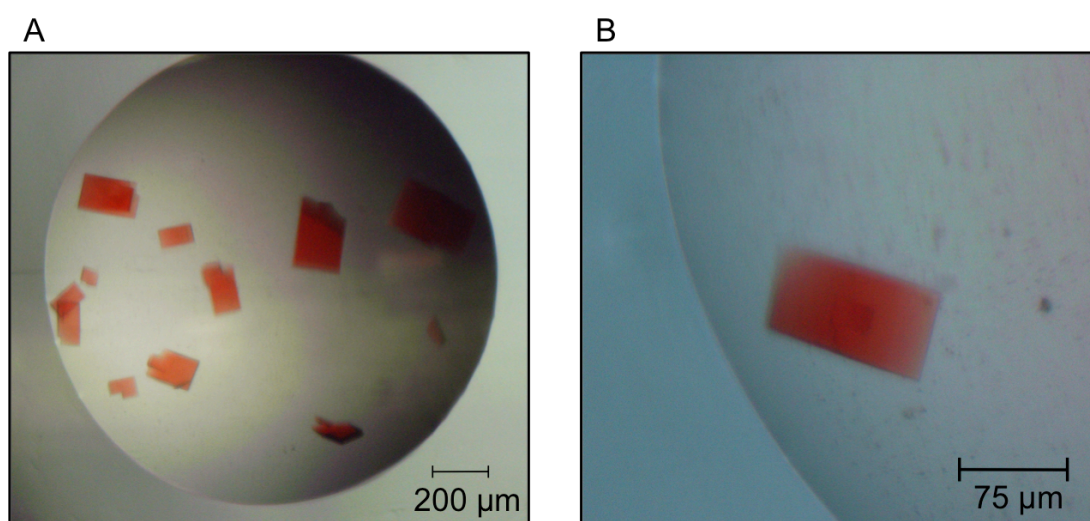
Figure 3.13 Crystals of Strep II-tagged MtoD grown at 16°C in optimised conditions containing 24% PEG 2000 MME & 50 mM potassium thiocyanate. All MtoD crystals were grown using the sitting drop vapour diffusion method. **A.** Typical MtoD-Strep crystals from a single drop. **B.** Enlarged picture of a single MtoD-Strep crystal.

X-ray diffraction by MtoD-Strep crystals at beamline I03 (Diamond Light Source) was first trialled by recording three test images at a wavelength of 1.72 Å

$(3.41 \times 10^{11} \text{ ph.s}^{-1})$, as previously described in the methods section for this chapter. These test images indicated the MtoD crystal diffracted to at least a resolution of 2.50 Å as indicated by the observation of Bragg spots at the edge and towards the corners of the detector in the test images (figure 3.14 C). Mosflm [64] predicted spacegroup P222 for the exposed crystal and the recommended strategy was adapted accordingly, initially continuing with wavelength of 1.72 Å required for anomalous scattering by iron. 360° of data were collected using 0.2° Ω oscillations and 0.05 s exposures to the unattenuated 20 x 20 μm beam. The SAD experiment produced 1,800 images of data, which were integrated and scaled using XIA2, which determined a maximum resolution of 2.29 Å.

After completing the SAD experiment, the wavelength of the X-ray beam was adjusted to 0.97 Å, allowing a native dataset to be collected from a different section of the same crystal (figure 3.14 B). The data collection strategy was altered, doubling the exposure time of the crystal to the same X-ray beam transmission, but the total Ω was halved (180° of data using 0.2° Ω oscillations and 0.1 s exposures). This strategy provided greater signal at high resolutions, allowing the detector to be moved for collection of data to 1.50 Å at the detector edge (figure 3.14 D). XIA2 identified Bragg spots to a maximum resolution of 1.47 Å.

The primitive orthorhombic space group $P2_12_12$ was determined by POINTLESS with average unit cell dimensions of a=42.26, b=92.29 and c=29.66 Å for the SAD data set and a=42.19, b=92.17 and c=29.69 Å for the native dataset. Full statistics from the scaling and averaging of data are shown in table 3.2. The half-dataset correlation coefficient ($CC_{1/2}$) of 0.989 for the SAD dataset showed an excellent level of internal consistency for the scaled and averaged data, although this diminished to 0.529 at higher resolutions. The minimum recommended $CC_{1/2}$ is 0.5 [26,65]. Nevertheless, the SAD data provided sufficient high-quality information at low resolutions to identify a single iron site and produce an initial model for MtoD using the polypeptide sequence for mature MtoD-Strep in AutoSol, after density modification by RESOLVE [33,47]. In addition to the iron sites, the initial model contained 22 water molecules and 41 residues built into three discrete fragments with an overall solvent content of 50.8% (R_{work} = 0.449; R_{free} = 0.453). The asymmetric unit contained one copy of the model. A second model was produced by AutoSol, which contained two copies of the model in the asymmetric unit, but had a solvent content of 1.6%. This was considered an unlikely solution and was not

pursued. Model building and refinement were performed on the first AutoSol solution using the AutoBuild wizard, which successfully built 80 residues in three fragments and 51 water molecules (R_{work} = 0.3069; R_{free} = 0.3595). This model was used for phasing the native dataset by molecular replacement in PHASER.
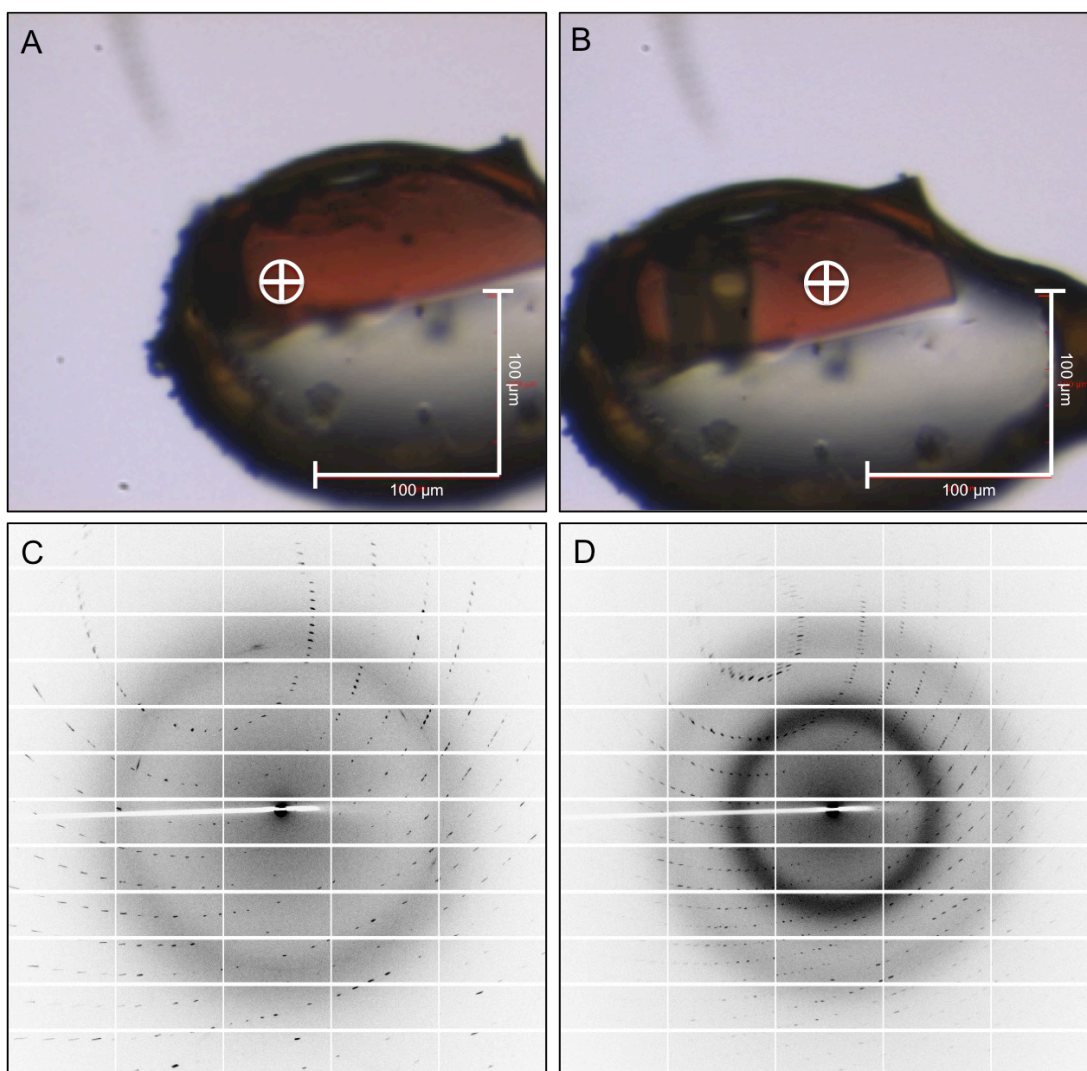
Figure 3.14 MtoD crystals initially tested and used to perform native and SAD X-ray diffraction experiments. A. SAD (λ = 1.72 Å) X-ray diffraction was tested to a resolution of 2.50 Å on an MtoD crystal grown in 24% PEG 2000 MME, 50 mM KCN and cryoprotected with 12% MPD. **B.** Native X-ray diffraction (λ = 0.97 Å) was tested to a resolution of 1.50 Å on the same MtoD crystal. **C.** Bragg spots were observed at a maximum resolution of 2.20 Å in the SAD test experiment (detector edge = 2.50 Å). **D.** X-ray diffraction in the native test experiment produced Bragg spots at a maximum resolution of 1.47 Å (detector edge = 1.50 Å), observed near the corners of the detector. Data were collected using a beam aperture of 20 x 20 μm and beam flux of 3.41×10^{11} ph.s^{-1} (SAD) and 3.73×10^{11} ph.s^{-1} (native).

The half-dataset correlation coefficients after scaling and averaging of intensities from the native dataset overall were $CC_{1/2} = 0.998$ and $CC_{1/2} = 0.776$ for the outer shell, showing a greater degree of internal consistency compared to the SAD dataset, particularly at high resolutions. The scaled and averaged intensities were inputted into PHASER [66,67] with the three-fragment model produced in AutoBuild [33] to provide prior information of the heme iron site and preliminary polypeptide structure to phase the native data. A near complete structure solution was achieved by Phenix AutoSol [47], as observed by visually interpreting the resulting electron density map with the AutoBuild model. Further model building and refinement was performed by repeating the AutoBuild procedure using the phased high-resolution native data.

Data collection	SAD	Native
Space group	P2$_1$2$_1$2	P2$_1$2$_1$2
Cell dimensions		
a, b, c (Å)	40.26, 92.29, 29.66	40.19, 92.17, 29.69
A, β, ϒ (°)	90, 90, 90	90, 90, 90
Wavelength (Å)	1.72	0.97
Resolution (Å)	2.29 - 36.90	1.47 - 92.17
$CC_{1/2}$	0.989 (0.529)	0.998 (0.776)
Rpim (%)	7.2 (40.6)	3.7 (30.3)
I/σI	14.29 (12.61)	13.6 (2.5)
Completeness (%)	96.1 (70.8)	99.4 (98.8)
Redundancy	10.8 (7.6)	6.0 (5.5)
Refinement		
Resolution (Å)		1.47
No. reflections used		18350
Rwork/Rfree		0.1943/0.2451
No. atoms		
Protein		718
Ligand		43
Water		128
B-factors		
Protein		17.556
Ligand		12.463
Water		30.509
RMSD		
Bond lengths (Å)		0.026
Bond angles (°)		2.27

Table 3.2 Data collection and refinement statistics associated with the crystallographic structure solution of MtoD. Data collection parameters and statistics from reduction of SAD and native data using XIA2 with final model refinement statistics from REFMAC5.

The final AutoBuild [33] run produced a model containing 87 residues in a single fragment with 121 water molecules (R_{work} = 0.2891; R_{free} = 0.3095). Manual model building in COOT [53] was used to build an alanine residue into density at the N-terminus of the model and a tryptophan and a serine residue from the Strep II tag into density at the C-terminus of the model, resulting in a final model containing 90 residues. Final refinement performed with REFMAC5 [54] yielded final R_{work} = 0.1943 and R_{free} = 0.2451.

Structure validation performed by MolProbity [68] produced a clashscore of 0, indicating no serious steric overlaps. No poor rotamers or Cβ deviations were identified and all residues in the MtoD model occupied allowed Ramachandran space; only one residue (Lys34) occupied unfavoured Ramachandran space (appendix, figure X5). Analysis of potential protein-protein interfaces for the MtoD-Strep model using PISA (Proteins, Interfaces, Structures and Assemblies) [69] revealed no specific interactions that could result in stable quaternary structures.

Like many other class I cytochromes *c*, MtoD has a significant α-helical component to its secondary structure. Helix *a,* at the N-terminus and helix *d* at the C-terminus form the majority of MtoDs globular structure furthest from the heme (figure 3.15 B). Helix *a*, formed by residues Val31-Asn41, holds the proceeding loop containing Cys43 and Cys46 close to the heme pocket, allowing the formation of thioether bonds between these cysteine residues and the porphyrin ring (figure 3.15 A). This loop also contains His47, which is held under the heme plane such that it is brought within 2 Å of the heme iron, allowing the formation of a coordinate bond.

Helices *b* and *c* form a hinge that brings the polypeptide chain above the heme plane. This chain loops in front of the heme cofactor, a common feature in class I cytochromes *c*, which limits the solvent exposure of the heme. Normally, this structural feature of class I cytochromes *c* forms a curved loop that shields the heme cofactor to solvent access from all but one side of the protein. In MtoD this is not the case; the polypeptide loop that shields the heme cofactor forms a β-hairpin motif, which does not enable the polypeptide to fold to either side of the heme. This results in the heme cofactor in MtoD being readily solvent accessible from two sides of the protein (figure 3.15 and 3.18). The β-hairpin motif allows the polypeptide chain to return above the heme plane, bringing His95 within 2 Å of the heme iron and allowing the formation of a second axial coordinate bond to the iron. The absence of methionine and the bis-His ligation of the heme iron make MtoD an atypical class I

cytochrome *c*. The histidine pair, which form the axial ligands to the heme iron, produce a dihedral angle of 46.3º, putting the pair almost exactly halfway between parallel perpendicular heme ligation (figure 3.15 C).
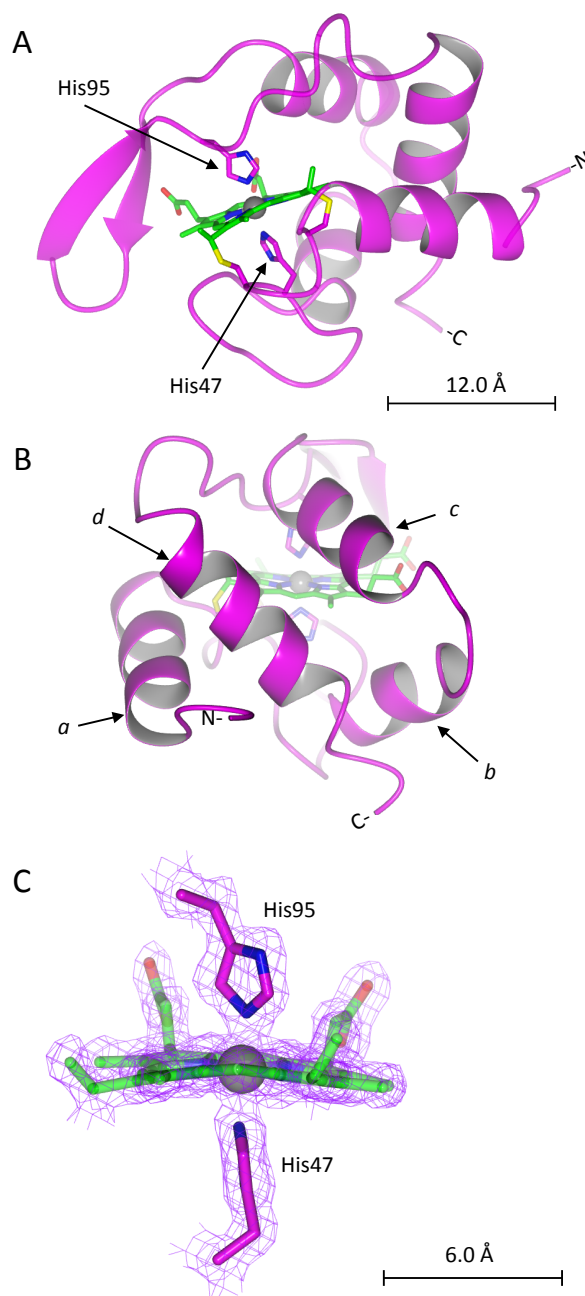
Figure 3.15 Crystal structure of MtoD showing the secondary structure heme-iron ligation. A. The secondary structure of MtoD is composed of 4 α helices joined by polypeptide loops and a β-hairpin motif, which shields the His47/His95-ligated heme c cofactor from solvent exposure. **B.** α helices *a-d* as shown from the posterior face (N-/C-termini) of MtoD. **C.** The histidine pair (His47 and His 95) that ligates the heme iron gave a dihedral angle of 46.3º, which is supported by the 2Fo-Fc electron density map (σ = 1.2).

The structural differences between MtoD-Strep and similar class I cytochrome *c* structures were analysed by performing secondary structure matching in the CCP4 program SUPERPOSE [70]. The overall deviations of the fixed model (MtoD) from the moving models were given as distance rmsd (Å). Cytochrome *c*552 from *Hydrogenobacter thermophilus* (1YNR) gave the lowest overall rmsd (2.589 Å) after superposition with MtoD; whilst other cytochrome *c* structures had greater sequence similarity to MtoD (table 3.1), 1YNR provided a closer superposition for the majority of the model; the superposition of 1YNR with MtoD-Strep can be seen in figure 3.16. Each superposition was inspected visually in addition to plotting the rmsd values for each main-chain atom. A pattern quickly began to emerge with overall rmsds being ~1-3 Å but increasing significantly in the main-chain atom region 200-300 (residues 80-95 in the MtoD structure).
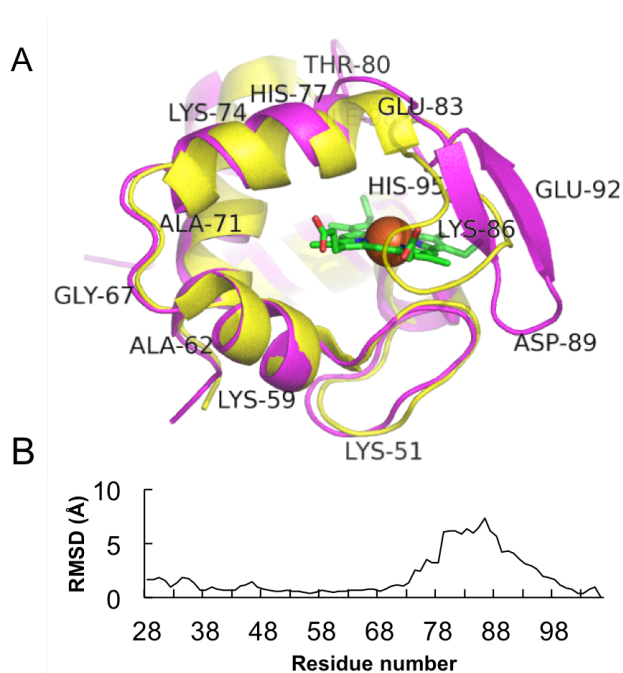
Figure 3.16 Superposition of MtoD with cytochrome c552 from *H. thermophilus* (1YNR) with similar sequence in SUPERPOSE [70] **revealed large rms differences around the heme cofactor. A**. Superposition of MtoD (magenta) and 1YNR (gold). **B.** Plot of rmsd (Å) as a function of residue number between the two structures. Cartoon structures were produced in PyMOL [56].

Crucially, this region of the polypeptide backbone includes the protein structure that normally shields the heme cofactor from solvent exposure. The large

rms differences in this region appear to occur as a result of MtoD containing a β-hairpin motif in this region.

The 1.47 Å crystal structure of MtoD almost certainly represents the reduced form of the protein due to cryoradiolytic reduction of the MtoD crystal in the X-ray beam (see section 3.2.5) [35]. This is also the case for each of the similar cytochrome structures to MtoD that were solved using X-ray crystallography. Several of the cytochrome structures that were identified as similar to MtoD were solved by NMR spectroscopy (2PAC, 1A56 and 1COR) and as a result these likely represent the oxidised states. While it is possible the reduced and oxidised states of these cytochromes *c* have slightly altered structures, this was not evident in consistent differences in superpositions of these structures.

Superposition of previously solved class I cytochrome *c* structures excluding MtoD (1YNR as the fixed model) in SUPERPOSE [70] using secondary structure matching produced overall rms differences ≤ 2.0 Å (figure 3.17), indicating a high degree of structural similarity. These superposed structures had a conserved arrangement of α-helices, polypeptide loops and protein fold around the propionate edge of the heme cofactor (figure 3.17 A and B), highlighting the unusual nature of the β-hairpin motif in MtoD. Overlaying the distance rmsd plot of 1YNR vs. MtoD with the same plot for the superposition of structurally similar cytochromes to MtoD also demonstrates the atypical nature of the protein fold in this region of the MtoD structure (figure 3.17 C). The heme cofactor in each of the superposed structures is accessible from the thiolated heme-edge but the propionate heme edge is shielded, unlike MtoD (figure 3.17 A and B).

To probe the solvent accessibility of the heme cofactor in MtoD relative to other similar cytochromes *c*, as listed in table 3.1, the program AREAIMOL [71] from the CCP4 suite was used to calculate the exposed heme surface area for each protein based on a probe solvent radius of 1.4 Å. The results of this analysis (Appendix table X4) showed MtoD had a significantly greater solvent-exposed heme surface area: 42.3 $Å^2$ compared to the average for the other structures of 16.5 ± 2.2 $Å^2$. This result is demonstrated visually in figure 3.18, in which MtoD and the structurally similar cytochrome *c*552 from *Hydrogenobacter thermophilus* (1YNR) are shown as surface structures, revealing the heme cofactor of MtoD is readily accessible from two faces of the protein structure whereas the more typical example demonstrated by 1YNR shows the heme can only be accessed from one side of the protein.
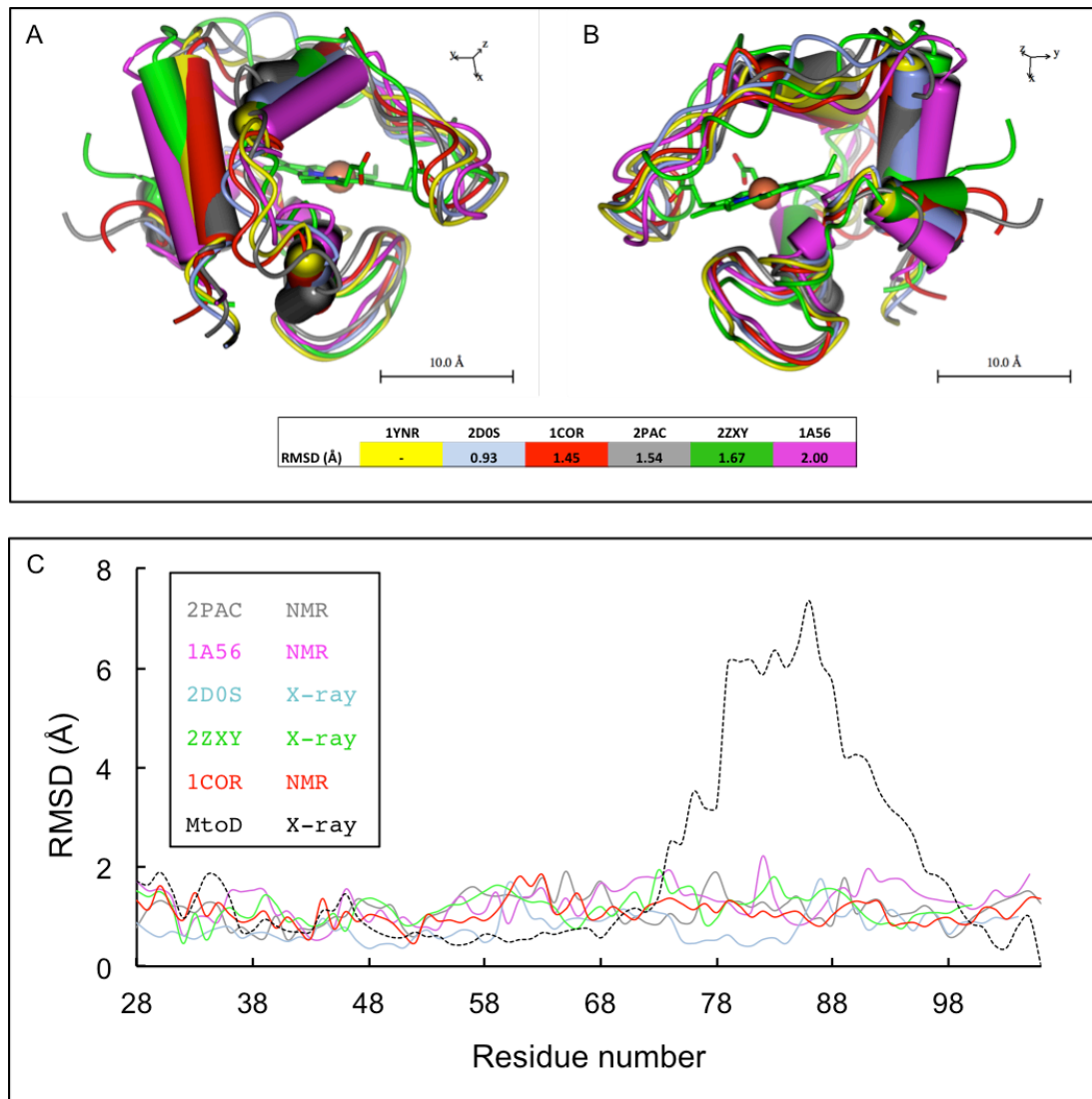
Figure 3.17 Superposition of class I cytochromes *c* with similar primary structures to MtoD. A. Superposed structures viewed from the propionate heme edge. **B.** Superposed structures viewed from the thiolated heme edge. Superposition was performed by secondary structure matching using SUPERPOSE with 1YNR used as the fixed model [70]. Overall RMSD values for each superposition are indicated below panel B. **C.** Plots of distance RMSD (Å) for each structure superposed with 1YNR. Residue numbers refer to the mature MtoD primary structure. The RMSD plot of MtoD superposed with 1YNR (from figure 3.16) is shown as a dashed line for reference. Organism of origin: **1A56:** *Nitrosomonas europaea*; **2PAC:** *Pseudomonas aeruginosa*; **2D0S:** *Hydrogenophilus thermoluteolus*; **1YNR:** *Hydrogenobacter thermophilus*; **1COR:** *Pseudomonas stutzeri*; **2ZXY:** *Aquifex aeolicus*. The method used for structure solution is also given (NMR = solution NMR structure; X-ray = X-ray crystallography).
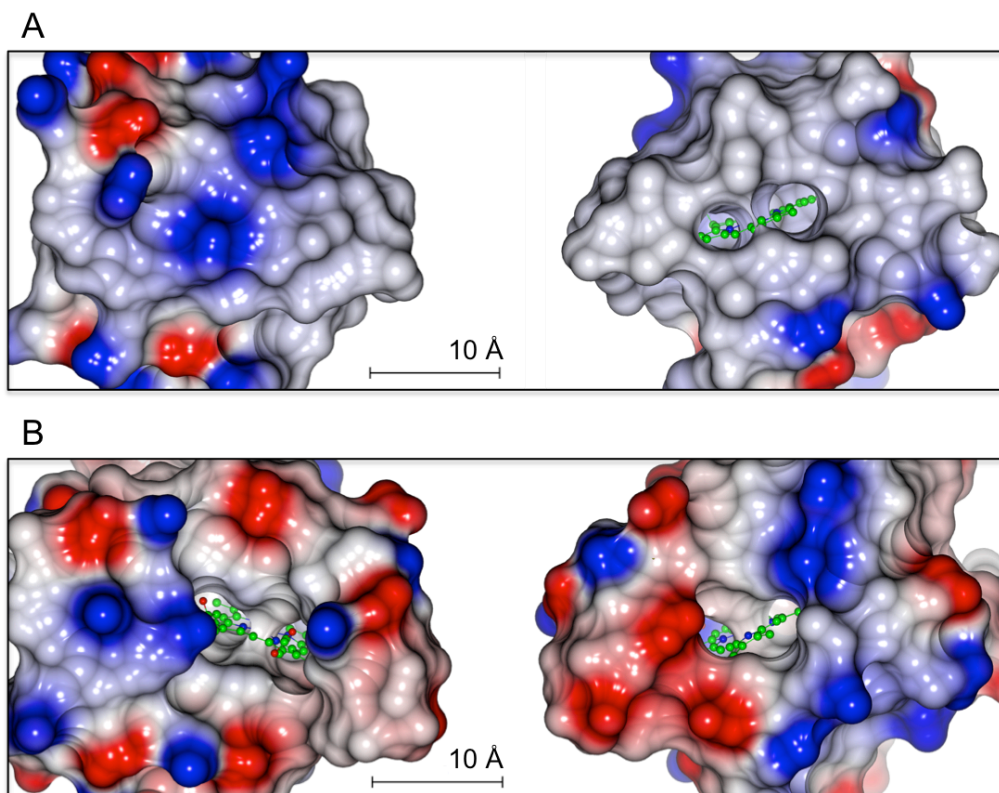
Figure 3.18 Surface representations of cytochrome *c*552 from *Hydrogenobacter thermophilus* (1YNR) and MtoD showing the relative exposure of the heme cofactors to solvent. Cytochrome *c*552 (panel **A**) and MtoD (panel **B**) are shown from the propionate edge of the heme cofactor in the left-hand image and from the opposite face of the protein on the right-hand side. MtoD and 1YNR are shown as surface structures coloured by electrostatic potential: blue = +0.4 V; white = 0 V; red = -0.4 V.

Further validation of the crystal and solution structures of MtoD was performed by superposing the crystal structure of MtoD-Strep with the filtered SAXS model of MtoD-Strep using SUPCOMB [43]. The result of the superposition showed the crystal structure of MtoD-Strep fitted well with the surface envelope provided by SAXS, providing a good match for both shape and size as demonstrated by the presentation of the crystal structure for MtoD-Strep as a secondary structure cartoon and space filling model (figure 3.19).
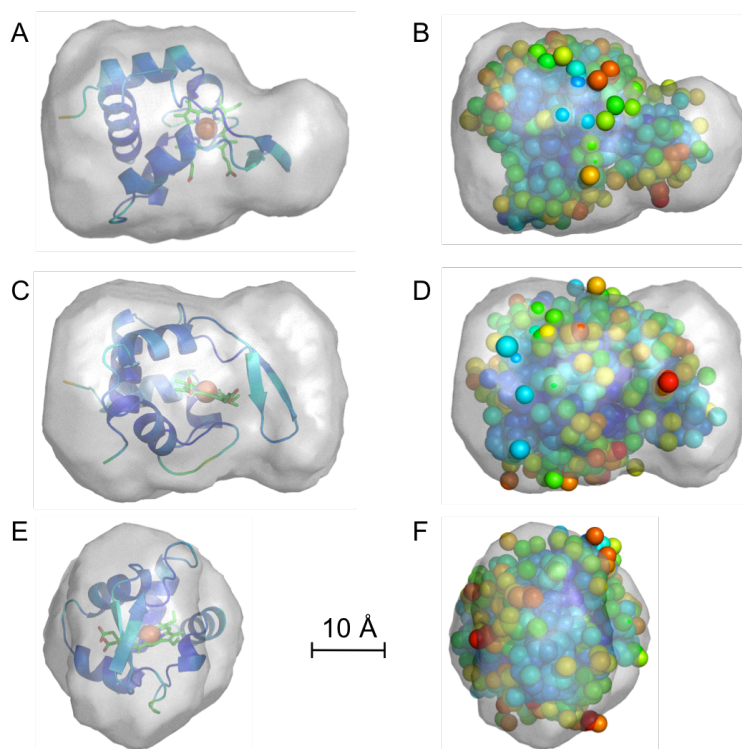
Figure 3.19 Filtered SAXS envelope of MtoD-Strep superimposed with the crystal structure of MtoD-Strep. A, **C** & **E** show the top, side and front view of MtoD respectively with the crystal structure's secondary structure shown. The crystal structure is coloured according to main-chain B-factors. **B**, **D** & **F** show identical views to **A**, **C** & **E**, but with the crystal structure represented as a space-filing model, demonstrating a good agreement between the solution structure of MtoD and the crystal structure (χ^2 of 53.5). The space-filling model is coloured according to atom-specific B-factor.

In addition to SUPCOMB [43] superposition, the program CRYSOL [55] was utilised as previously described to compare the SAXS data for MtoD-Strep to that predicted based on the atomic model of the protein (figure 3.19). As expected, the resulting χ^2 of 53.5 indicated the MtoD-Strep crystal structure provided a significantly better fit to the SAXS data than any of the other similar class I cytochromes *c*. Further comparison of the crystal structure of MtoD-Strep with the SAXS data were performed using SOMO [72], a solution modelling program in the UltraScan suite [73]. A pair distance distribution $p(r)$ function was determined for MtoD-Strep based on the atomic distances in the crystal structure. Some differences in the $p(r)$ distributions for the crystal structure and that determined by SAXS were expected, particularly D_{max} due to absence of six residues of the N-terminal Strep II tag from the model produced by X-ray crystallography due to these residues not

being resolved in electron density maps. SOMO produced a $p(r)$ function with a D_{max} of 39 Å for the crystal structure compared to the 42 Å expected based on the SAXS data (figure 3.20). This difference agrees well with the predicted difference in maximum distances expected given the N-terminal Strep II tag is located at the surface and on the long-axis of the crystal structure of MtoD. In addition, the shape of the $p(r)$ distribution at large pair distances was significantly different. This difference, as can be seen in figure 3.20, shows the $p(r)$ distribution produced by the SAXS data gives a greater distribution of large-distance particle pairs compared to the crystal structure. These differences in the $p(r)$ distributions manifest themselves in slightly different model shapes and sizes, particularly along the long axis of the SAXS model, as can be seen comparing the filtered SAXS model and the space-filling crystal structure model of MtoD (figure 3.19 B and D).
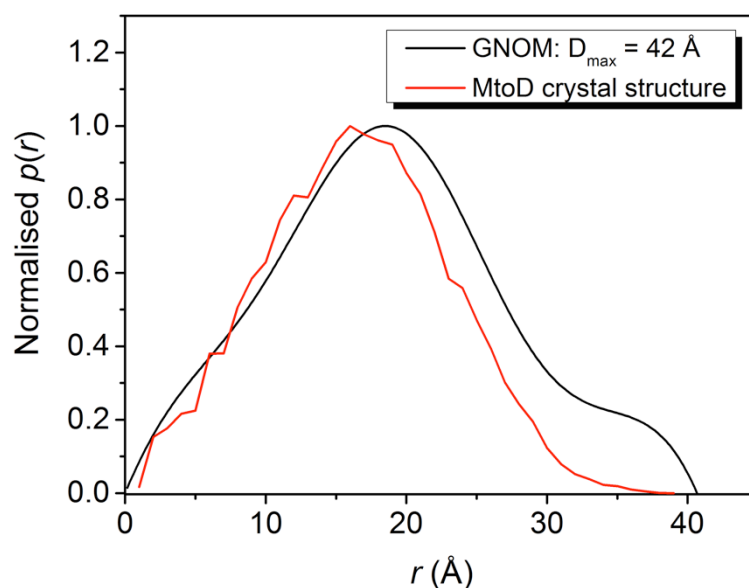
Figure 3.20 Particle pair distance $p(r)$ distributions for MtoD based on SAXS data (black) and the atomic model of the solved crystal structure determined by SOMO (red).

3.5 Discussion

Biophysical characterisation of MtoD-Strep by analytical ultracentrifugation and small angle X-ray scattering indicated the protein behaves as a globular monomer in solution with a molecular weight of ~11.8 kDa, typical of a class I cytochrome *c*. The narrow distribution of sedimentation coefficients determined for MtoD at three protein concentrations using sedimentation velocity gave clear evidence for MtoD-Strep behaving as a monomer across a concentration range, as did the higher protein concentration range used for SAXS, although scattering intensities at small momentum transfers indicated marginal aggregation of MtoD at the greatest protein concentrations. This experimental evidence for MtoD behaving as a monomer was further supported by PISA analysis of the MtoD-Strep crystal structure, which found no interfaces that could lead to stable oligomeric MtoD structures.

The shape and size of the solution surface model of MtoD-Strep determined by SAXS was consistent with other cytochromes of high sequence homology, with the NMR structure of ferricytochrome *c*552 from *Nitrosomonas europaea* (1A56) providing the closest match for the overall size and shape. The most significant difference between the SAXS structure of MtoD-Strep and the atomic structures of other small cytochromes *c* was observed around the site of heme coordination where the SAXS model suggested MtoD potentially had a more prominent structural feature in this region of the protein (figure 3.12). After the solution of the X-ray crystal structure of MtoD-Strep it became apparent MtoD contained a β-hairpin motif that extended in front of the heme cofactor in this region of the model where similar cytochromes *c* contained a more flexible polypeptide loop. The effect of this structural difference makes MtoD longer than other cytochromes *c* at 39 Å compared to the more conventional ~30 Å and significantly increases the solvent exposure of the heme cofactor (appendix – table X4).

The polypeptide loop referred to (as seen in figure 3.16) from other small cytochromes *c* forms a fold that shields the propionate edge of the heme cofactor from one side of the protein. This structural feature directs specificity for electron transfer through a single area of exposed protein surface (figure 3.17 A). By contrast, the formation of a β-hairpin in the same region of MtoD's protein structure

introduces structural inflexibility that prevents solvent shielding of the propionate edge of the heme cofactor. As a result, MtoD has an exposed heme surface area much greater than other cytochromes *c* and is solvent-accessible from two sides of the protein surface. This raises questions over the potential protein-protein interfaces that would allow specific electron transfer events to occur since it is apparent MtoD possesses two exposed faces that could allow heme-mediated electron transfer.

As previously reported, the presence of lysine residues around the binding site of class I cytochromes *c* is of great importance in their ability to form electrostatic interactions with suitably aligned carboxylate groups of interacting redox partners [74,5]. Lysine residues tend to be a prominent constituent of class I cytochromes *c*. The lysine content of small cytochromes *c* similar to MtoD with solved structures was 13.1 ± 1.2%, which is comparable to that of MtoD with a 15.6% lysine content. By contrast, other soluble cytochromes that are not redox partners of cytochrome *c* oxidases such as small tetraheme cytochrome (*S. oneidensis*), flavocytochrome *c* fumarate reductase (*S. putrefaciens*) and nitrite reductase NrfA (*E. coli*) have lysine contents of 7.7%, 8.0% and 8.6% respectively.
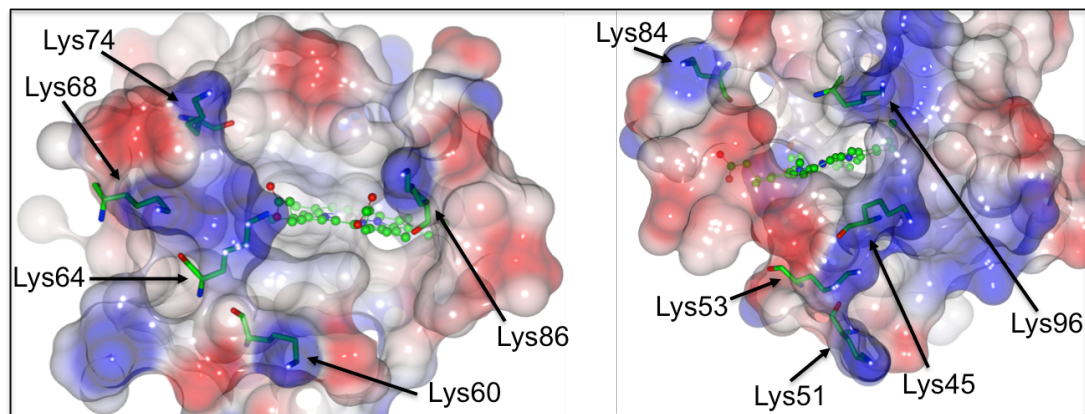
Figure 3.21 Lysine residues in MtoD cluster around the propionate edge (left) and thiolated edge (right) of the heme cofactor on either side of the protein. Lysine residues, shown as green cylinders, cluster around the heme on two sides of the protein around the solvent-exposed heme edges. Residues are shown as a surface model coloured by electrostatic potential: blue = +0.3 V; white = 0.0 V; red = −0.3 V.

Five of the MtoD lysine residues cluster around the propionate edge of the protein, giving a localised positive charge while a further five lysine residues can be found on the opposite side of the protein around the thiolated edge of the heme cofactor, as can be seen in figure 3.21. This localised clustering of lysine residues

around both edges of the heme cofactor potentially creates two unique binding sites for MtoD and provides evidence for MtoD perhaps having multiple interacting partners.

The sequence conservation of residues in MtoD was mapped onto the crystal structure using the ConSurf server [75]. A pairwise sequence alignment of MtoD with the 50 most similar protein sequences determined by BLAST analysis [57] indicated a number of conserved regions of the MtoD structure. Of particular interest was the conservation of lysine residues around the heme cofactor, which could be involved in an MtoD-cytochrome *c* oxidase interaction. Lysine residues around the propionate edge of the heme cofactor were not well conserved; only lysine-86 and lysine-64 were conserved on this side of the protein structure while other nearby lysine residues lysine-68, 74 and 84 were more variable (figure 3.22 A). On the other hand, lysine residues around the thiolated edge of the heme cofactor were highly conserved (figure 3.22 B). These included lysine-45, 53 and 96, all of which are positioned around the solvent accessible region of MtoDs heme cofactor. A greater degree of lysine conservation on this surface of MtoD should not be surprising since it is this region in which many other previously characterised class I cytochromes *c* are solvent accessible and bind to cytochrome *c* oxidase.
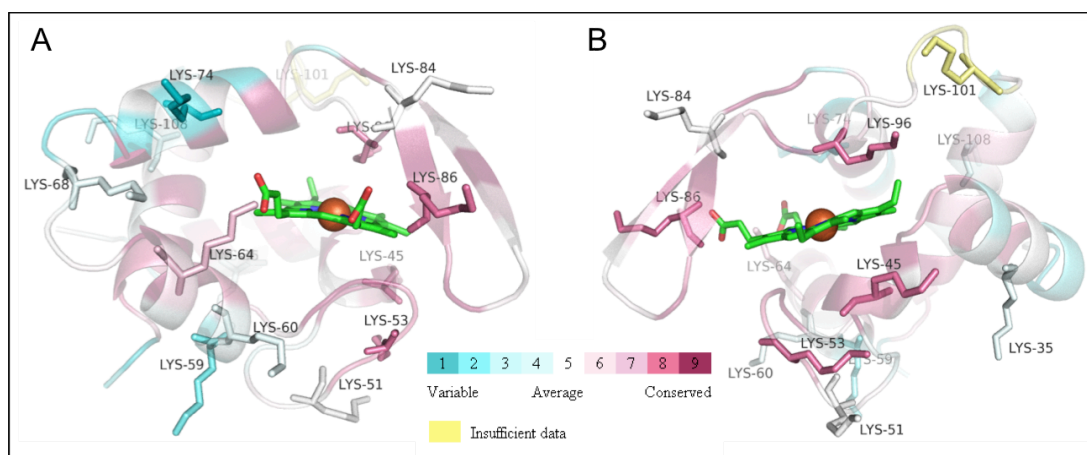
Figure 3.22 Analysis of sequence conservation in MtoD using the ConSurf server [75]. **A.** MtoD viewed from the propionate heme edge. **B.** MtoD viewed from the thiolated heme edge. Lysine residues are shown as cylinders coloured by degree of sequence conservation (see key). The heme cofactor is shown as green cylinders.

The less-well conserved lysine residues located around the propionate heme edge in MtoD could potentially be involved in a new binding interface with an alternate redox partner at the inner membrane in *S. lithotrophicus*.

In addition to the atypical secondary structure of MtoD around the heme, the bis-histidinyl ligation of the heme iron in MtoD is also unusual for a class I cytochrome *c*. While there are many examples of bis-His heme ligation in various classes of *c*-type cytochrome, class I cytochromes *c* are typically His/Met ligated in eukaryotes and prokaryotes. In general, the coordination of heme iron by nitrogen from histidine residues gives hemes more negative redox potentials compared to coordination by methionine sulphur atoms. As a result, His/Met ligated hemes tend to be more prevalent in class I cytochromes *c* due to their redox potential being closer to that of cytochrome *c* oxidase and the O_2/H_2O redox couple (+816 mV at pH 7). The bis-His ligation of iron in MtoD could give the heme cofactor a greater dynamic potential range, allowing transfer of electrons to partners with lower redox potentials than a His/Met-ligated heme cofactor could allow. Such dynamic redox behaviour could potentially make MtoD an important redox regulator in *Sideroxydans lithotrophicus* and conceptually further supports the hypothesis that MtoD could have multiple binding partners.

While there is currently insufficient evidence to confidently predict an electron transfer pathway involving MtoD, as was discussed in chapter 1, the findings of structural characterisation clearly show MtoD possesses atypical structural characteristics for a class I cytochrome *c* and suggest MtoD could be capable of electron transfer in multiple reaction complexes, potentially making MtoD a respiratory regulator for *Sideroxydans*.

Addressing these features and advancing current knowledge of the role MtoD plays in the respiratory chain of *Sideroxydans* requires the identification of potential interacting partners and characterisation of the protein interfaces in these complexes. This could be accomplished using MtoD-Strep as a molecular probe to pull out interacting partners from the cell lysate of *S. lithotrophicus* followed by techniques such as AUC or isothermal titration calorimetry (ITC) to biophysically characterise these interactions. Characterising the redox properties of MtoD and it's potential interacting partners will be critical to understanding the importance of the bis-histidinyl ligation of the heme iron. As such, the redox properties of MtoD were probed using electrochemical methods as described in chapter 4.

3.6   References

1.   Moore, G. & Pettigrew, G. *Cytochromes c: Evolutionary, Structural and Physicochemical Aspects*. (Springer-Verlag, 1990).

2.   Pettigrew, G. W. & Moore, G. R. *Cytochromes c: Biological Aspects*. (1987).

3.   Thöny-Meyer, L. Biogenesis of respiratory cytochromes in bacteria. *Microbiol. Mol. Biol. Rev.* **61,** 337–76 (1997).

4.   Nicholls, D. G. & Ferguson, S. J. *Bioenergetics*. (Academic Press, 2002).

5.   Döpner, S. *et al.* The structural and functional role of lysine residues in the binding domain of cytochrome c in the electron transfer to cytochrome c oxidase. *Eur. J. Biochem.* **261,** 379–91 (1999).

6.   Bushnell, G. W., Louie, G. V & Brayer, G. D. High-resolution three-dimensional structure of horse heart cytochrome c. *J. Mol. Biol.* **214,** 585–595 (1990).

7.   Banci, L. *et al.* Solution structure of oxidized horse heart cytochrome c. *Biochemistry* **36,** 9867–9877 (1997).

8.   Dickerson, R. E. & Mclain, G. The Structure of Paracoccus denitrificans Cytochrome. 4033–4046 (1976).

9.   Sievers, F. *et al.* Fast, scalable generation of high-quality protein multiple sequence alignments using Clustal Omega. *Mol. Syst. Biol.* **7,** (2011).

10.   Marcus, R. a. & Sutin, N. Electron transfers in chemistry and biology. *Biochim. Biophys. Acta - Rev. Bioenerg.* **811,** 265–322 (1985).

11.   Dolla, a, Blanchard, L., Guerlesquin, F. & Bruschi, M. The protein moiety modulates the redox potential in cytochromes c. *Biochimie* **76,** 471–479 (1994).

12.   Ambler, R. P. Sequence variability in bacterial cytochromes c. *Biochim. Biophys. Acta* **1058,** 42–47 (1991).

13.   Tezcan, F. a., Winkler, J. R. & Gray, H. B. Effects of ligation and folding on reduction potentials of heme proteins. *J. Am. Chem. Soc.* **120,** 13383–13388 (1998).

14.   Cole, J., Lary, J., Moody, T. & Laue, T. Analytical Ultracentrifugation: Sedimentation Velocity and Sedimentation Equilibrium. *Methods Cell Biol.* (2008). doi:10.1016/S0091-679X(07)84006-4.Analytical

15.   Lebowitz, J., Lewis, M. S. & Schuck, P. Modern analytical ultracentrifugation in protein science: a tutorial review. *Protein Sci.* **11,** 2067–2079 (2002).

16.   Mertens, H. D. T. & Svergun, D. I. Structural characterization of proteins and complexes using small-angle X-ray solution scattering. *J. Struct. Biol.* **172,** 128–141 (2010).

17.   Schnablegger, H. & Singh, Y. The SAXS Guide. *Ant. Paar* (2011).

18.   Glatter, O. A new method for the evaluation of small-angle scattering data. *J. Appl. Crystallogr.* **10,** 415–421 (1977).

19.   Liu, H. & Zwart, P. H. Determining pair distance distribution function from SAXS data using parametric functionals. *J. Struct. Biol.* **180,** 226–234 (2012).

20. Svergun, D. I. Determination of the regularization parameter in indirect-transform methods using perceptual criteria. *J. Appl. Crystallogr.* **25,** 495–503 (1992).

21. Svergun, D. I. Restoring low resolution structure of biological macromolecules from solution scattering using simulated annealing. *Biophys. J.* **76,** 2879–2886 (1999).

22. Westermeier, F. *et al.* Fast two-dimensional detection for X-ray photon correlation spectroscopy using the PILATUS detector. *J. Synchrotron Radiat.* **16,** 687–689 (2009).

23. Hahn, T. & Paufler, P. International tables for crystallography, Vol. A. space-group symmetry D. REIDEL Publ. Co., Dordrecht, Holland/Boston, U. S. A., 1983, 854 Seiten, Preis: Dfl. 385,–, US 165.00, ISBN 90-277-1445-2. *Cryst. Res. Technol.* **19,** 1306 (1984).

24. Kabsch, W. Xds. *Acta Crystallogr. Sect. D Biol. Crystallogr.* **66,** 125–132 (2010).

25. Evans, P. Scaling and assessment of data quality. in *Acta Crystallogr. Sect. D Biol. Crystallogr.* **62,** 72–82 (2006).

26. Evans, P. R. An introduction to data reduction: Space-group determination, scaling and intensity statistics. *Acta Crystallogr. Sect. D Biol. Crystallogr.* **67,** 282–292 (2011).

27. Grosse-Kunstleve, R. W. & Adams, P. D. Substructure search procedures for macromolecular structures. *Acta Crystallogr. - Sect. D Biol. Crystallogr.* **59,** 1966–1973 (2003).

28. Sheldrick, G. M. Experimental phasing with SHELXC/D/E: Combining chain tracing with density modification. *Acta Crystallogr. Sect. D Biol. Crystallogr.* **66,** 479–485 (2010).

29. Keegan, R. M. & Winn, M. D. Automated search-model discovery and preparation for structure solution by molecular replacement. *Acta Crystallogr. Sect. D Biol. Crystallogr.* **63,** 447–457 (2007).

30. Rohl, C. A., Strauss, C. E. M., Misura, K. M. S. & Baker, D. Protein Structure Prediction Using Rosetta. *Methods Enzymol.* **383,** 66–93 (2004).

31. Evans, P. & McCoy, A. An introduction to molecular replacement. *Acta Crystallogr. Sect. D Biol. Crystallogr.* **64,** 1–10 (2007).

32. Terwilliger, T. C. Maximum-likelihood density modification. *Acta Crystallogr. Sect. D Biol. Crystallogr.* **56,** 965–972 (2000).

33. Terwilliger, T. C. *et al.* Iterative model building, structure refinement and density modification with the PHENIX AutoBuild wizard. *Acta Crystallogr. Sect. D Biol. Crystallogr.* **64,** 61–69 (2007).

34. Afonine, P. V. *et al.* Towards automated crystallographic structure refinement with phenix.refine. *Acta Crystallogr. Sect. D Biol. Crystallogr.* **68,** 352–367 (2012).

35. Beitlich, T., Kühnel, K., Schulze-Briese, C., Shoeman, R. L. & Schlichting, I. Cryoradiolytic reduction of crystalline heme proteins: analysis by UV-Vis spectroscopy and X-ray crystallography. *J. Synchrotron Radiat.* **14,** 11–23 (2007).

36. Pompidor, G., Dworkowski, F. S. N., Thominet, V., Schulze-Briese, C. & Fuchs, M. R. A new on-axis micro-spectrophotometer for combining Raman, fluorescence and UV/Vis absorption spectroscopy with macromolecular crystallography at the Swiss Light Source. *J. Synchrotron Radiat.* **20,** 765–776 (2013).

37. Antonyuk, S. V. & Hough, M. a. Monitoring and validating active site redox states in protein crystals. *Biochim. Biophys. Acta - Proteins Proteomics* **1814,** 778–784 (2011).

38. Dworkowski, F. S. N., Hough, M. A., Pompidor, G. & Fuchs, M. R. Challenges and solutions for the analysis of *in situ* , *in crystallo* micro-spectrophotometric data. *Acta Crystallogr. Sect. D Biol. Crystallogr.* **71,** 27–35 (2015).

39. Harding, S. E. & Horton, J. C. *Analytical ultracentrifugation in biochemistry and polymer science*. (Royal Society of Chemistry, 1992). at <https://books.google.co.uk/books?id=bn0vAQAAIAAJ>

40. UltraScan II. (2013). at <http://www.ultrascan2.uthscsa.edu>

41. Petoukhov, M. V., Konarev, P. V., Kikhney, A. G. & Svergun, D. I. ATSAS 2.1 - Towards automated and web-supported small-angle scattering data analysis. *J. Appl. Crystallogr.* **40,** 223–228 (2007).

42. Franke, D. & Svergun, D. I. DAMMIF, a program for rapid ab-initio shape determination in small-angle scattering. *J. Appl. Crystallogr.* **42,** 342–346 (2009).

43. Kozin, M. B. & Svergun, D. I. Automated matching of high- and low-resolution structural models. *J. Appl. Crystallogr.* **34,** 33–41 (2001).

44. Volkov, V. V. & Svergun, D. I. Uniqueness of ab initio shape determination in small-angle scattering. in *J. Appl. Crystallogr.* **36,** 860–864 (2003).

45. Winter, G. Xia2: An expert system for macromolecular crystallography data reduction. *J. Appl. Crystallogr.* **43,** 186–190 (2010).

46. Winter, G., Lobley, C. M. C. & Prince, S. M. Decision making in xia2. *Acta Crystallogr. Sect. D Biol. Crystallogr.* **69,** 1260–1273 (2013).

47. Terwilliger, T. C. *et al.* Decision-making in structure solution using Bayesian estimates of map quality: The PHENIX AutoSol wizard. *Acta Crystallogr. Sect. D Biol. Crystallogr.* **65,** 582–601 (2009).

48. Terwilliger, T. C. Maximum-likelihood density modification. *Acta Crystallogr. Sect. D Biol. Crystallogr.* **56,** 965–972 (2000).

49. Terwilliger, T. C. Automated main-chain model building by template matching and iterative fragment extension. *Acta Crystallogr. - Sect. D Biol. Crystallogr.* **59,** 38–44 (2003).

50. ZWART, P. H., GROSSE-KUNSTLEVE, R. W., ADAMS, P. D. Xtriage and Fest: automatic assessment of X-ray data and substructure structure factor estimation. *CCP4 Newsl.* **43,** 27–35 (2005).

51. Headd, J. J. *et al.* Use of knowledge-based restraints in phenix.refine to improve macromolecular refinement at low resolution. *Acta Crystallogr. Sect. D Biol. Crystallogr.* **68,** 381–390 (2012).

52.   McCoy, A. J. *et al.* Phaser crystallographic software. *J. Appl. Crystallogr.* **40,** 658–674 (2007).

53.   Emsley, P., Lohkamp, B., Scott, W. G. & Cowtan, K. Features and development of Coot. *Acta Crystallogr. Sect. D Biol. Crystallogr.* **66,** 486–501 (2010).

54.   Murshudov, G. N. *et al.* REFMAC5 for the refinement of macromolecular crystal structures. *Acta Crystallogr. Sect. D Biol. Crystallogr.* **67,** 355–367 (2011).

55.   Svergun, D., Barberato, C. & Koch, M. H. CRYSOL - A program to evaluate X-ray solution scattering of biological macromolecules from atomic coordinates. *J. Appl. Crystallogr.* **28,** 768–773 (1995).

56.   DeLano, W. L. The PyMOL Molecular Graphics System. *Schrödinger LLC wwwpymolorg* **Version 1.,** http://www.pymol.org (2002).

57.   Madden, T. The BLAST sequence analysis tool. *BLAST Seq. Anal. Tool* 1–17 (2013). at <http://www.ncbi.nlm.nih.gov/books/NBK153387/>

58.   Timkovich, R., Bergmann, D., Arciero, D. M. & Hooper, a B. Primary sequence and solution conformation of ferrocytochrome c-552 from Nitrosomonas europaea. *Biophys. J.* **75,** 1964–72 (1998).

59.   Detlefsen, D. J., Thanabal, V., Pecoraro, V. L. & Wagner, G. Solution structure of Fe(II) cytochrome c551 from Pseudomonas aeruginosa as determined by two-dimensional 1H NMR. *Biochemistry* **30,** 9040–9046 (1991).

60.   Nakamura, S. *et al.* Structure of Cytochrome c552 from a Moderate Thermophilic Bacterium, Hydrogenophilus thermoluteolus: Comparative Study on the Thermostability of Cytochrome c‡. *Biochemistry* **45,** 6115–6123 (2006).

61.   Travaglini-Allocatelli, C. *et al.* An obligatory intermediate in the folding pathway of cytochrome c 552 from Hydrogenobacter thermophilus. *J. Biol. Chem.* **280,** 25729–25734 (2005).

62.   Cai, M., Bradford, E. G. & Timkovich, R. Investigation of the solution conformation of cytochrome c-551 from Pseudomonas stutzeri. *Biochemistry* **31,** 8603–8612 (1992).

63.   Obuchi, M. *et al.* Hyperstability and crystal structure of cytochrome c555 from hyperthermophilic Aquifex aeolicus. *Acta Crystallogr. Sect. D Biol. Crystallogr.* **65,** 804–813 (2009).

64.   Leslie, A. G. W. & Powell, H. R. *Processing diffraction data with MOSFLM. Evol. methods Macromol. Crystallogr.* (2007). doi:10.1007/978-1-4020-6316-9_4

65.   Diederichs, K. & Karplus, P. a. Better models by discarding data? *Acta Crystallogr. Sect. D Biol. Crystallogr.* **69,** 1215–1222 (2013).

66.   McCoy, A. J. Solving structures of protein complexes by molecular replacement with Phaser. *Acta Crystallogr. Sect. D Biol. Crystallogr.* **63,** 32–41 (2006).

67.   McCoy, A. J. *et al.* Phaser crystallographic software. *J. Appl. Crystallogr.* **40,** 658–674 (2007).

68.   Chen, V. B. *et al.* MolProbity: All-atom structure validation for macromolecular crystallography. *Acta Crystallogr. Sect. D Biol. Crystallogr.* **66,** 12–21 (2010).

69.   Krissinel, E. & Henrick, K. Inference of Macromolecular Assemblies from Crystalline State. *J. Mol. Biol.* **372,** 774–797 (2007).

70.   Krissinel, E. & Henrick, K. Secondary-structure matching (SSM), a new tool for fast protein structure alignment in three dimensions. *Acta Crystallogr. Sect. D Biol. Crystallogr.* **60,** 2256–2268 (2004).

71.   Lee, B. & Richards, F. M. The interpretation of protein structures: estimation of static accessibility. *J. Mol. Biol.* **55,** 379–400 (1971).

72.   Brookes, E., Demeler, B., Rosano, C. & Rocco, M. The implementation of SOMO (SOlution MOdeller) in the UltraScan analytical ultracentrifugation data analysis suite: Enhanced capabilities allow the reliable hydrodynamic modeling of virtually any kind of biomacromolecule. *Eur. Biophys. J.* **39,** 423–435 (2010).

73.   Demeler, B., Brookes, E., Wang, R., Schirf, V. & Kim, C. A. Characterization of reversible associations by sedimentation velocity with ultrascan. *Macromol. Biosci.* **10,** 775–782 (2010).

74.   Rieder, R. & Bosshard, H. R. Comparison of the binding sites on cytochrome c for cytochrome c oxidase, cytochrome bc1, and cytochrome c1. Differential acetylation of lysyl residues in free and complexed cytochrome c. *J. Biol. Chem.* **255,** 4732–4739 (1980).

75.   Ashkenazy, H., Erez, E., Martz, E., Pupko, T. & Ben-Tal, N. ConSurf 2010: Calculating evolutionary conservation in sequence and structure of proteins and nucleic acids. *Nucleic Acids Res.* **38,** (2010).

Chapter 4

Spectroscopic & electrochemical characterisation of MtoD.

Work presented in this chapter has been published in the following paper:

4.1   Abstract

MtoD from the lithotrophic bacterium *Sideroxydans lithotrophicus* is predicted to shuttle electrons from the outer membrane iron oxidising decaheme/β-porin complex MtoAB to the inner membrane. The electrons transported to the inner membrane are used to generate a proton motive force (PMF) for ATP synthesis and to generate NADH, which is used for lithotrophic growth. The unusual bis-His axial heme ligation was expected to give MtoD a lower redox potential than typically observed for class I cytochromes *c* (~+200 to +250 mV), which would enable electron transfer to the quinone pool (E_m +100 to -70 mV) and subsequent NAD^+ reduction (-320 mV). UV/Vis spectropotentiometric characterisation of MtoD solutions revealed a midpoint potential of +155 mV at pH 7 for the MtoD heme. Spectropotentiometric and voltammetric characterisation of MtoD protein films using optically transparent mesoporous nanocrystalline SnO_2 electrodes revealed two redox transformations with midpoint potentials of ~+50 mV and ~−220 mV at pH 7. A 1 nm red shift in the λ_{max} of the ~−220 mV (low potential) redox transformation was observed compared to λ_{max} of the ~+50 mV (high potential) redox transformation and MtoD in solution. This could be evidence of protein denaturation, or perhaps an interaction-induced conformational change around the heme, giving rise to altered midpoint potentials. The latter is of interest because the highly solvent-exposed MtoD heme is expected to be more susceptible to changes in its surrounding environment compared to other small monoheme cytochromes *c*. It is possible, given the accessibility of the heme cofactor from two sites, MtoD could interact with multiple redox partners and the interfaces formed could modulate the potential of the MtoD heme, allowing electron transfer to multiple inner membrane cytochromes.

4.2   Introduction

4.2.1 Spectral and redox properties of small monoheme cytochrome *c*

Small monoheme cytochromes have been classified based primarily on the structure and spectral properties of their heme cofactor(s), although other polypeptide sequence motifs and position of the heme-binding motif are characteristic of particular classes of cytochromes *c* [1]. *C*-type cytochromes contain heme *c*, which is covalently anchored to the protein by thioether bonds to cysteine residues that are commonly found in canonical CXXCH motifs, although other motifs are known in which more than two residues separate the cysteines [2]. Classification based on spectral properties is usually made on the basis of features in the visible region of the electromagnetic spectrum, specifically by the position of the α-band absorption peak for the reduced cytochrome, which is normally in the region of 549 to 555 nm [1].

The spectrum of a typical oxidised *c*-type cytochrome at visible wavelengths consists of a prominent absorption maximum at approximately 410 nm in addition to a broad absorption feature that peaks at ~530 nm. Reduction of the heme iron causes the 410 nm absorption maximum to shift to ~420 nm and splits the broad absorption feature into β/α absorption peaks, with maxima at ~520 nm and ~550 nm respectively. These absorption features in the visible region of the electromagnetic spectrum arise from π $\rightarrow$ π* electronic transitions associated with the porphyrin ring of the heme cofactor. The electronic state of the iron associated with the heme cofactor contributes to the transition energies required to promote electrons from π bonding orbitals to π* antibonding orbitals, resulting in different visible spectra for hemes containing oxidised and reduced iron [1].

Class I cytochromes *c* in the ferric state typically produce an additional absorption feature at ~650 nm, which arises as a result of a ligand to metal charge transfer between a methionine ligand and the heme iron. Cytochrome *c* class I are small monoheme proteins that typically display His/Met axial ligation of the *c*-type heme cofactor and are present in mitochondria and bacteria. The proximal histidine ligand is provided by the CXXCH heme binding motif and the distal methionine ligand is typically located closer to the C-terminal end of the primary structure. MtoD, a predicted class I cytochrome *c*, lacks methionine in its mature polypeptide

sequence and the 1.47 Å crystal structure (4XXL) clearly shows the MtoD heme is bis-His axially ligated (figure 3.15 C, chapter 3) [3].

The His/Met heme ligation commonly observed in mitochondrial and bacterial class I cytochromes c typically give heme midpoint potentials in the range +200 to +260 mV vs. SHE at pH 7 [4]. For example, the midpoint potential at pH 7 (E_{m7}) of mitochondrial cytochrome c from horse heart and *Saccharomyces cerevisiae* (+260 mV) is comparable to class I cytochromes c with His/Met heme ligation from *Pseudomonas aeruginosa* (+260 mV) and *Paracoccus denitrificans* (+250 mV). There are a number of exceptions to this trend observed for His/Met ligated monoheme cytochromes c isolated from bacteria. For example, cytochrome c551 from *Nitrosomonas europaea* has a midpoint potential of +25 mV [5]. The low potential exceptions still do not produce midpoint potentials as low as typically observed for bis-His ligated small monoheme cytochromes [4]. While there are relatively few examples of bis-His ligated monoheme cytochromes c, those that have been characterised typically have midpoint potentials in the range -250 to -280 mV at pH 7, as exemplified by cytochrome c550 from *Thermosynechococcus elongatus* and *Microcystis aeruginosa* (-250 mV and -260 mV respectively) [6,4] and cytochrome c549 from *Anacystis nidulans* (-280 mV) [7]. Consequently, the MtoD heme was expected to have a more negative midpoint potential compared to the previously observed values for His/Met cytochromes c.

Sideroxydans lithotrophicus is predicted to transfer electrons acquired from the oxidation of extracellular ferrous iron (Fe^{2+}) across the outer membrane into the periplasm via the outer membrane decaheme cytochrome/β-porin complex MtoAB [8]. MtoD is proposed to behave as an electron shuttle, transporting electrons from MtoA at the periplasmic face outer membrane to predicted quinone reductase $CymA_{ES-1}$ at the inner membrane [3,9]. The electron transfer mechanisms involved in growth and energy conservation in microaerophilic iron oxidising bacteria (FeOB) are poorly understood at present, primarily due to difficulties culturing large quantities of FeOB for protein expression and plating cultures to select for mutants [10,11]. Given the proposed electron transfer role of MtoD it is of interest to define the redox chemistry of MtoD to provide further insight into potential electron transfer pathways in *S. lithotrophicus*.

Three approaches were taken to define the redox chemistry of MtoD: (i) chemically-mediated spectropotentiometry of MtoD solutions (ii) electrode-based spectropotentiometry and (iii) cyclic voltammetry on MtoD protein films.

4.2.2 Defining redox properties of cytochromes *c*

(i) Mediated spectropotentiometry may be used in traditional solution-based titrations to characterise the redox chemistry of proteins containing redox active centres that produce a spectral change during redox transformations. This applies to the heme cofactor of cytochromes, since reduction of the heme produces a unique spectroscopic change accompanying the redox transition. As previously shown in figure 2.11 and 2.13 UV/Vis spectra of oxidised and reduced His-tagged and Strep-II tagged MtoD are distinct and characteristic of low spin heme in ferric and ferrous states. If the spectral properties of the fully oxidised and reduced heme are known, relating spectral changes to the reaction quotient ([ox]/[red]) for oxidised and reduced sample over a range of applied solution potentials (*E*) allows the midpoint potential of the heme (E°) to be determined using the Nernst equation (equation 1):

$$\text{Equation 1:} \qquad E = E^\circ + \frac{RT}{nF} ln\left(\frac{[\text{ox}]}{[\text{red}]}\right)$$

Where *n* is the number of electrons transferred and *R*, *T* and *F* are the gas constant (8.314 J K^{-1} mol), absolute temperature and Faraday constant (96,485 C.mol^{-1}) respectively.

Chemical titrants such as potassium ferricyanide and sodium dithionite are used to set the potential of the protein solution and chemical mediators are routinely used to facilitate rapid electron transfer between the reductant/oxidant compounds and the protein of interest. Mediator compounds with E_m values close the solution potentials to be investigated are chosen. However, care in selecting appropriate mediators for the spectroscopic method to be used is important since many redox mediators are coloured compounds that can interfere with the measurement of electronic absorption spectra. Such interference is often unavoidable, but does not preclude the accurate measurement of spectropotentiometric data so long as the

electronic absorption for the mediator(s) does not occur in the same region of the spectrum as the absorption signals to be measured from the protein of interest.

(ii) More recently methods have been developed to define the redox chemistry of protein films adsorbed to optically transparent electrodes [12–14]. These methods replace chemical titrants with a potentiostat, which is used to adjust potentials applied to the protein film via the electrode. The direct transfer of electrons to the electrode-adsorbed protein film removes the need for chemical mediators. The potentiostat is used to equilibrate the electrode-adsorbed protein sample at desired redox potentials and electronic absorption spectra are measured at each equilibrated potential and analysed as in (i).

(iii) It is also possible using electrode-based techniques to perform cyclic voltammetry. This allows the redox chemistry of protein solutions (solution voltammetry) or electrode-adsorbed protein films (protein film voltammetry) to be mapped using a change of current at applied potentials rather than relying on spectral changes from a chromophore.
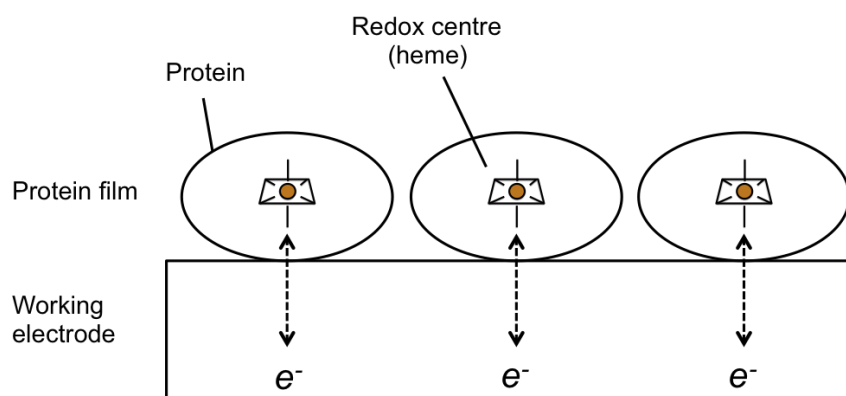
Figure 4.1 Protein film voltammetry (PFV) allows the direct measurement of electrodic response during reduction and oxidation of protein redox centres. The formation of protein films at the surface of a working electrode enables direct electron transfer to occur between the protein film and the electrode (dotted arrows). These electron transfer events occur as the potential applied to the protein film approaches the midpoint potential (E_m) of the redox centres present according to the Nernst equation.

While cyclic voltammetry can be performed on protein solutions and electrode-adsorbed protein films, if the protein of interest is susceptible to protein film formation at an electrode surface, protein film voltammetry (PFV) has the advantage of directly providing information about electron transfer between the

protein and the electrode without the added complication of diffusion of protein in solution to and from the electrode surface (figure 4.1).

Cyclic voltammetry utilises linear changes in applied potential, sweeping in a negative direction to drive reduction of redox centres and then returning in the positive direction to drive oxidation of redox centres. This process is repeated as a function of time to map the redox properties of the electrode-adsorbed protein film over the selected potential range (figure 4.2).
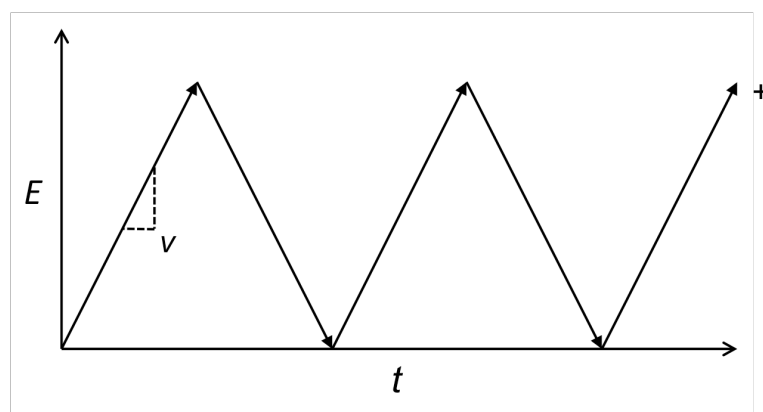
Figure 4.2 Scheme of potential change applied to the working electrode with time during a cyclic voltammetry experiment. The applied potential (E) is increased and decreased in a linear fashion with time (t) to drive oxidation and reduction respectively of redox centres present at the electrode surface. The gradient of the waveform gives the scan rate (v).

Reduction and oxidation of protein adsorbed on the electrode surface occurs when the applied electrode potential enters the electroactive potential range of the redox centres in the protein. Redox transformations are measured as a change in current at the working electrode as electrons are either transferred from the working electrode to the protein film (reduction), which is observed as a negative current, or from the protein film to the counter electrode (oxidation), which is observed as a positive current (figure 4.3).
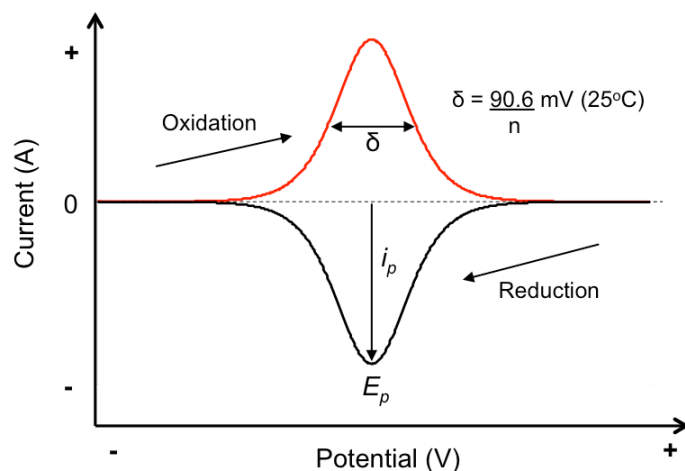
Figure 4.3 Analysis of cyclic voltammograms. Reduction of the protein film produces a negative peak (black line) and re-oxidation produces a positive peak (red line). Averaging the peak potentials (E_p) for the reducing and oxidising waves gives the midpoint potential. The peak height (i_p), and the width of the peak at half height (δ) provide the number of electrons involved in the redox transformation (n). For a one-electron redox transformation $n = 1$ at 25°C the width of peaks at half height is 90.6 mV. Measuring the peak areas for the reducing and oxidising scans gives insight into the reversibility of the reaction and the number of moles of electrons involved in each half reaction.

Analysis of the Faradaic peak shapes resolved using PFV (after subtracting buffer contributions) provides the number of electrons involved in the reduction/oxidation half reactions (n) using the width of Faradaic peaks at half-height (δ) in the following equation:

$$\text{Equation 2:} \qquad \delta = 3.53\frac{RT}{nF}$$

At 25°C the half-height peak width for a one-electron redox transformation is 90.6 mV (figure 4.3) [15]. The area under Faradaic peaks is related to the number of electrons transferred by (equation 3):

$$\text{Equation 3:} \qquad Q = \frac{\text{Peak area}}{v} = nFA\Gamma$$

Where v is the scan rate (V.s^{-1}), A is the electrode surface area (cm^2) and Γ is the electroactive coverage (mol.cm^{-2}). The peak area/scan rate may be given as charge or Q (coulombs).

Optically transparent SnO_2 electrodes were selected to characterise the redox properties of MtoD protein films due to their ability to provide simultaneous voltammetric and spectropotentiometric data. Spectropotentiometry was performed at visible wavelengths to characterise redox behaviour attributed to the MtoD heme whilst cyclic voltammetry was used corroborate spectropotentiometric data and to provide direct electrochemical evidence of other redox centres not identified in the MtoD crystal structure were present.

4.3   Methods

4.3.1 Optically monitored /dithionite titrations

Reduction and oxidation of 7.5 µM solutions of His-tagged and Strep II-tagged MtoD were performed by adding 1 mL MtoD in 20 mM HEPES pH 7, 100 mM NaCl to a glass cuvette in an anaerobic glovebox. The cuvette was sealed using a Suba-seal® septa before placing in a UV/Vis spectrophotometer (Jasco). Baseline measurements were made between wavelengths of 250 and 700 nm for the buffer solution in the same glass cuvette prior to adding protein. Spectroscopy of MtoD solutions was performed in the visible region of the electromagnetic spectrum between wavelengths of 350 and 700 nm due to significant interference in the measured spectra by sodium dithionite below 350 nm. Ascorbate (E_{m7} = +0.058 V [16]) and sodium dithionite (E_{m7} = -0.66 mV [17]) were used as chemical reductants. Solutions of ascorbate and dithionite were prepared in an anaerobic glovebox and sealed using a Suba-seal® septa. A +60 mM solution of sodium dithionite was prepared in water and a solution of 1 M ascorbate was prepared in 50 mM HEPES pH7. Reduction of MtoD solutions, monitored by increase in absorption at 549 nm (A_{549}), was performed by injecting ascorbate in 0.5 µL increments using a 10 µL capacity Hamilton syringe (figure 4.4) until no further change in A_{549} was observed. Optical spectra were recorded after incubating for 1 minute with solution mixing. Additions of sodium dithionite were made in increments of 0.5 µL and spectra were measured again, looking for a further increase in A_{549} that would suggest incomplete reduction of MtoD by ascorbate.
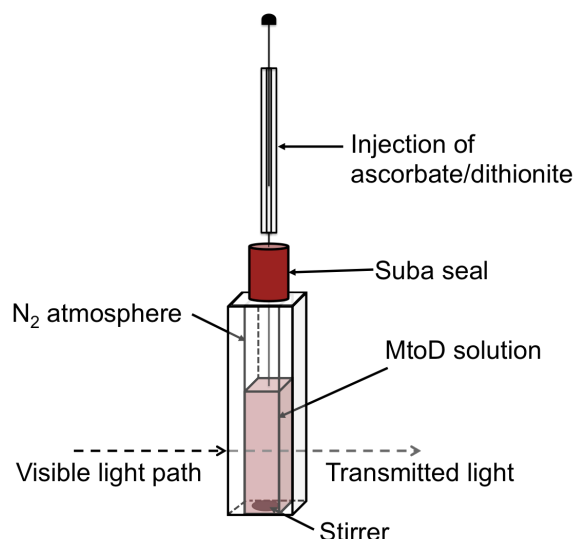
Figure 4.4 Experimental setup for optically monitored ascorbate reduction of MtoD. A 1 mL solution of 7.5 µM MtoD in 20 mM HEPES pH 7, 100 mM NaCl was prepared in an anaerobic glovebox in a glass cuvette with a magnetic stirrer to allow continuous mixing of the solution. The cuvette was sealed with a Suba® septa, which allowed injections of ascorbate and dithionite to be made through the seal. Reduction of MtoD was monitored by measuring electronic absorption between 700 and 350 nm and tracking change in absorbance at 549 nm.

4.3.2 Mediated solution spectropotentiometry

Mediated spectropotentiometry of Strep II-tagged MtoD in solution was carried out using previously described methods [18]. A 4 mL 5.5 µM solution of MtoD-Strep in 20 mM HEPES pH 7, 100 mM NaCl was prepared in a quartz electrochemical cell (Hellma) and made anaerobic by purging the cell with argon gas (figure 4.5). Continuous argon gas flow was used for the duration of the experiment to maintain an anaerobic atmosphere in the electrochemical cell. The solution potential inside the electrochemical cell was modulated by injection of the chemical reductant sodium dithionite or chemical oxidant potassium ferricyanide, which were prepared anaerobically as described in 4.3.1 at a concentration of 10 mg.mL^{-1}. Chemical reduction and oxidation processes were facilitated by a mixture of nine electrochemical mediators, with working concentrations of 5-10 µM, whose midpoint potentials ranged from +276 mV to -350 mV vs. SHE (table 4.1).

A combination Ag/AgCl|Pt reference|counter electrode (Metrohm) was calibrated using a saturated solution of quinhydrone dissolved in analytical grade water (Fisher) after continuous mixing for 30 minutes. The observed instrument

reading of +80 mV vs. Ag/AgCl was used to calculate a correction factor using the known literature reduction potential of +295 vs. SHE for quinhydrone [19].

The MtoD solution was initially adjusted to a potential of +0.4 V by addition of potassium ferricyanide before a reducing titre was performed using incremental additions of 0.5 µL sodium dithionite from a 25 µL gastight Hamilton syringe pre-filled with dithionite. The experimental solution containing MtoD was poised under continuous mixing until a steady potential was reached at potentials between +0.4 V and -0.36 V vs. SHE. UV/Vis spectra were measured at each poised potential and reduction of MtoD was monitored by increase in α-band absorption at 549 nm. A re-oxidising titre was performed to confirm the redox transformation was fully reversible by incremental additions of 0.5 µL potassium ferricyanide. Small changes to the experimental solution volume as a result of making chemical additions was corrected by adjusting the electronic absorbance data so that all spectra were equal at the known isosbestic point at 556 nm for MtoD.

Mediator	E_{m7} (mV)	M_r	Solvent	Working concentration (μM)
DAD (2,3,5,6-tetramethyl-*p*-phenylenediamine)	276	164.25	EtOH	10
PMS (phenazine methosulphate)	80	306.34	H_2O	10
PES (phenazine ethosulphate)	55	334.39	H_2O	10
Juglone (5-hydroxy-1,4-naphthoquinone)	30	174.16	EtOH	10
Duroquinone (2,3,5,6-tetramethyl-1,4-benzoquinone)	5	164.20	MeOH	10
Menadione (2-methyl-1,4-naphthoquinone)	-70	172.18	MeOH	10
AQDS (9,10-anthraquinone-2,6-disulphonic acid)	-185	412.31	EtOH (50%)	10
AQS (anthraquinone-2-sulphonic acid)	-225	328.30	EtOH (50%)	10
Benzyl viologen (1,1'-dibenzyl-4,4'-bipyridinium dichloride)	-350	409.40	H_2O	5

Table 4.1 Properties of electrochemical mediators used to facilitate redox poising during solution-based spectropotentiometric titrations. A stock solution of the mediator mixture was prepared with 10 mM mediator concentrations, except benzyl viologen, whose concentration was lowered to 5 mM to minimize interference with electronic absorption spectra. 4 μL of the stock mediator mix was added to 3.996 mL MtoD solution, giving a working mediator concentration range of 5-10 μM.

A protein-free spectropotentiometric titration was performed prior to spectropotentiometry on MtoD solutions under the same conditions and using the same mediator concentrations as used during spectropotentiometry on MtoD solutions. This experiment was used to determine regions of the UV/Visible spectra where absorption attributed to the mediator mixture were observed across the potential range to be used. Mediators included in the mixture were selected to minimise absorption near 550 nm, since the α-band region of the MtoD spectra (549 nm) was to be used to monitor the ferric/ferrous heme interconversion.
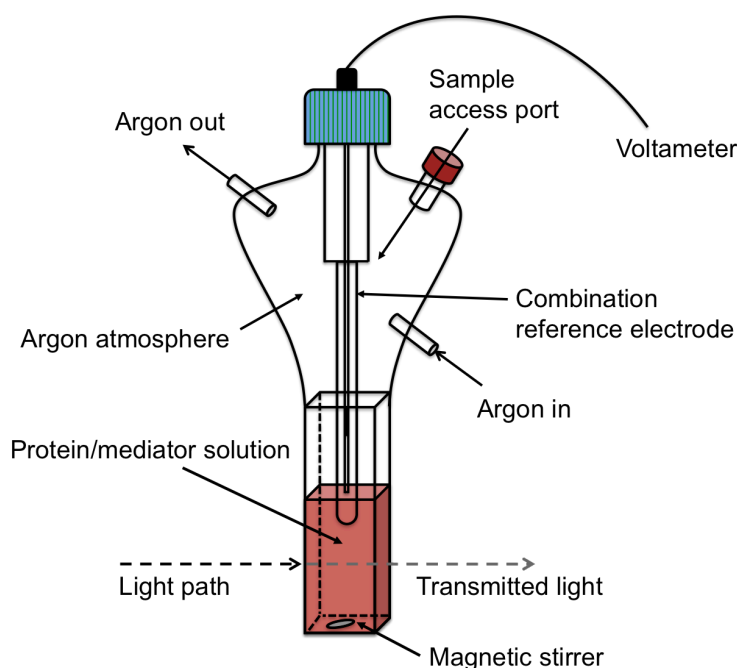
Figure 4.5 Experimental setup for solution-based mediated spectro-potentiometric titrations of MtoD solutions. 4 mL 5.5 µM MtoD-Strep solution and 10 µM mediators were mixed in a 1 cm path length quartz cuvette, and made anaerobic by purging the electrochemical cell with argon gas. The titre was performed under continuous argon gas flow. The solution potential was regulated by injection of the reductant sodium dithionite and oxidant potassium ferricyanide through the sample access port, which was sealed with a Suba® septa. The solution was continuously mixed by rotation of a magnetic stirrer and the potential of the solution was measured using a combination reference/counter electrode.

4.3.3 Optically transparent SnO$_2$ Spectroelectrochemistry

Spectroelectrochemistry was performed on SnO$_2$-adsorbed protein films as previously described [14]. The SnO$_2$ electrodes used consisted of a 4 μm layer of mesoporous nanocrystalline SnO$_2$ deposited on a conductive glass slide cut immediately prior to use to fit into a 1 cm path length glass cuvette, which was used as an electrochemical cell (figure 4.6). SnO$_2$ electrodes kindly provided by James Durrant (Imperial College London), which had an approximate SnO$_2$ surface area of 0.4 cm^2 to 0.5 cm^2, were prepared by heating in a furnace at a temperature of 450°C for 30 minutes before cooling to room temperature. In order to connect the SnO$_2$ working electrode to the potentiostat, a platinum connector wire was coupled to the conductive glass surface of the working electrode using heat-shrink tubing. The SnO$_2$ electrode was then incubated on ice and an ice-cold solution of 500 μM MtoD-Strep in 20 mM HEPES pH 7, 100 mM NaCl was applied to the electrode surface and incubated for 5 minutes. Excess protein solution was removed by washing the protein film with 20 mM HEPES pH 7, 100 mM NaCl.

The electrochemical cell used a three-electrode system with a platinum counter, Ag/AgCl reference and SnO$_2$ working electrodes. The Ag/AgCl wire reference electrode was calibrated in an anaerobic glovebox by performing solution-based cyclic voltammetry with a graphite edge working electrode on a 20 mM solution of potassium ferricyanide dissolved in 20 mM HEPES pH 7. The known E$_{m7}$ value of 430 mV for potassium ferricyanide [20] was used to calculate a correction factor for potentials observed using the Ag/AgCl wire electrode. The cuvette electrochemical cell was assembled in an anaerobic glovebox; a sufficient volume of anaerobic 20 mM HEPES pH 7, 100 mM NaCl buffer solution was added to the cell so that the reference and counter electrodes and the entire SnO$_2$-adsorbed MtoD film were immersed in buffer. The electrochemical cell was sealed using a Suba$^®$ septa and positioned in a UV/Vis spectrophotometer (Jasco) at a constant temperature of 278 K and the electrodes were connected to a potentiostat (AutoLab). A bare SnO$_2$ electrode was placed in the reference beam of the spectrophotometer to minimize spectral contributions from the nanocrystalline electrode material to the measured electronic absorbance data.

Redox characterisation of the MtoD-Strep film was performed using two methods. Spectropotentiometry, monitored in the visible region of the electromagnetic spectrum between wavelengths of 350 and 700 nm, was performed between poised potentials of 0.4 and -0.5 V vs. SHE to determine redox properties associated with the MtoD heme. Potentials were made more reducing until no further increase in A_{549} was observed before re-oxidising the MtoD film. The protein film was poised at selected potentials for 3 minutes prior to measuring optical spectra. Spectropotentiometry was complemented by the use of cyclic voltammetry, which was also performed on SnO_2-adsorbed MtoD films in the cuvette cell, to define the Faradaic response associated with the protein film, providing information about redox transformations associated with all potential redox centres in the protein film, including the heme.

Cyclic voltammetry was performed on the bare SnO_2 electrode to be used in the redox characterisation of MtoD-Strep to allow voltammograms of the non-Faradaic response associated with the 20 mM HEPES pH 7, 100 mM NaCl buffer and the specific SnO_2 electrode to be subtracted from voltammograms of SnO_2-adsorbed MtoD. Voltammograms for bare SnO_2 and SnO_2-adsorbed MtoD films were measured between potentials of 0.4 and -0.5 mV vs. SHE at a scan rate of 5 $mV.s^{-1}$.
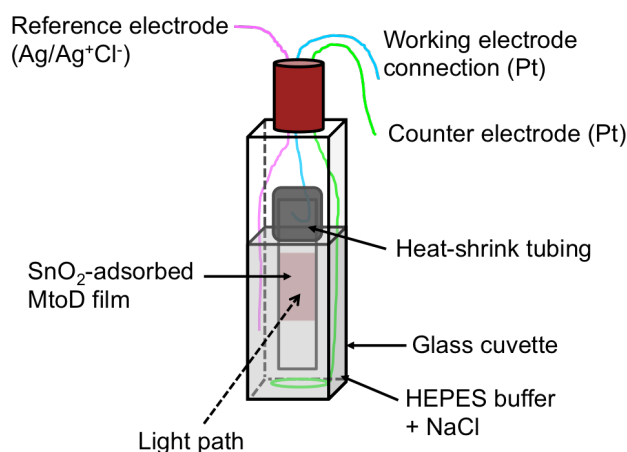
Figure 4.6 Electrochemical cell for spectroelectrochemical characterisation of SnO_2-adsorbed MtoD films. A SnO_2 working electrode was coupled to a platinum wire connector using heat-shrink tubing prior to applying an MtoD solution. Cell assembly was carried out in an anaerobic glovebox where the cell was filled with anaerobic 20 mM HEPES pH 7, 100 mM NaCl, allowing the MtoD film and electrodes to be immersed in buffer solution. The cell included a three-electrode system in which a platinum counter electrode and Ag/AgCl reference electrode were placed in the cell with the optically transparent SnO_2 working electrode.

4.4 Results

4.4.1 A comparison of the redox behaviours of MtoD-His and MtoD-Strep solutions

To quickly assess whether the difference of purification tag conferred a difference in redox behaviour for MtoD, anaerobic solutions of His-tagged and Strep II-tagged MtoD were each reduced with excess concentrated ascorbate (E_{m7} = +58 mV [16]) followed by sodium dithionite (E_{m7} = -660 mV [17]). This approach also provided insight into whether the MtoD heme reduction potential was as low as observed for other bis-His ligated small monoheme cytochromes, or whether the heme had a high potential commonly associated with His/Met ligated hemes. Given MtoD is predicted to accept electrons from MtoA, which is electroactive between potentials of -400 mV and +100 mV [8], the midpoint potential of the MtoD heme was expected to be more positive than ascorbate.

A 1 M ascorbate solution, prepared in an anaerobic glovebox with 50 mM HEPES pH 7, was added separately in 0.5 µL increments to a 1 mL solution of 7.5 µM His-tagged MtoD or 7.5 µM Strep II-tagged MtoD in 20 mM HEPES pH 7.0, 100 mM NaCl. Ascorbate was added to the protein solutions contained in a Suba®-sealed glass cuvette until no further increase in 549 nm absorbance was observed after several additions.

Only 27% heme reduction as determined by ΔA_{549} relative to the oxidised and dithionite-reduced spectra was observed for the His-tagged MtoD solution despite addition of excess ascorbate. The partial reduction is consistent with a partial shift of the Soret band to its known reduced maximum at 416 nm (figure 4.7 A). This behaviour indicated either the presence of at least two populations of heme in distinct environments, giving midpoint redox potentials more positive and more negative than ascorbate, or the presence of a heme with a redox potential similar to that of ascorbate. By contrast, addition of excess ascorbate to a solution of Strep II-tagged MtoD produced a fully reduced sample. Making additions of dithionite to the ascorbate-reduced Strep II-tagged MtoD sample increased A_{549} no further (figure 4.7 B). The redox behaviour of the Strep II-tagged MtoD sample is consistent with that predicted for the MtoD heme. The full reduction of Strep II-tagged MtoD by

ascorbate indicates the midpoint potential of the MtoD heme for this protein is more positive than ascorbate.
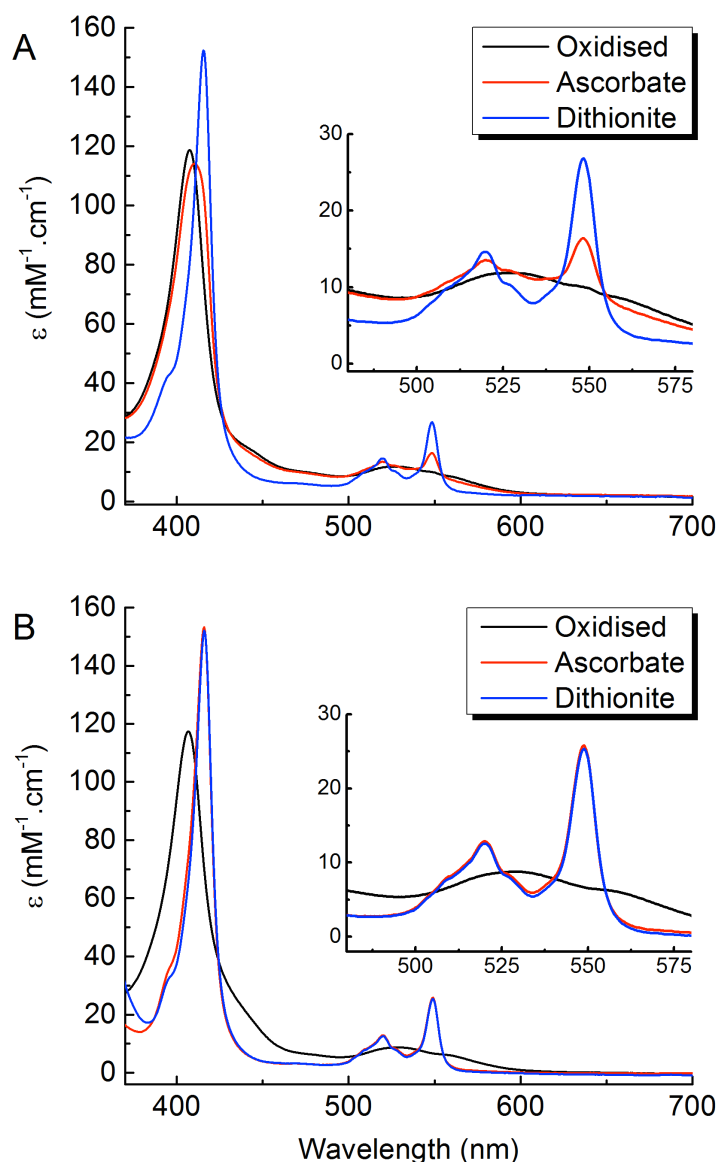
Figure 4.7 Preliminary optically monitored redox characterisation of His-tagged and Strep II-tagged MtoD. A. Addition of excess ascorbate to oxidised His-tagged MtoD in 20 mM HEPES pH 7, 100 mM NaCl (4°C) (black) was only able to partially reduce (27%) the sample (red). Additions of sodium dithionite produced a visible spectrum typical of a reduced cytochrome c (blue), with fully developed β/α absorption features and Soret shift to 416 nm, as previously seen for reduced MtoD. **B.** Adding ascorbate to an oxidised sample of Strep II-tagged MtoD in 20 mM HEPES pH 7, 100 mM NaCl (4°C) (black) fully reduced the sample (red). Additions of dithionite reduced the sample no further (blue).

The different redox properties of the His-tagged and Strep II tagged MtoD could have a number of causes. For example the histidine-rich protein regions are often associated with transition metal binding sites [21,22]. The presence of the 6xHis tag was important for purification of MtoD by immobilised metal affinity chromatography (IMAC), as described in chapter 2, however a potential consequence of the purification process could have been adventitious metal binding to the MtoD His-tag, which may have affected the potential of the heme cofactor. Coordination of the heme cofactor by one of the six histidine residues contained in the His tag and/or protein misfolding were also possibilities.

As a precaution, further redox characterisation was performed using the Strep II-tagged MtoD construct. This enabled a redox characterisation of the same construct used to solve the MtoD crystal structure.

4.4.2 Solution-based spectropotentiometric characterisation of MtoD-Strep

Spectropotentiometry was performed on a 5.5 μM Strep II-tagged MtoD sample in 20 mM HEPES pH 7, 100 mM NaCl to define the heme redox properties. The MtoD solution was prepared in a quartz electrochemical cell and made anaerobic by purging the cell with argon gas, which was under continuous flow for the duration of the experiment. The redox titre was mediated using a chemical mediator mixture with a midpoint potential range of +0.276 to -0.350 V vs. SHE at pH 7 (table 4.1). The solution potential inside the cell was adjusted by injection of 10 mg.mL^{-1} sodium dithionite or 10 mg.mL^{-1} potassium ferricyanide and monitored using a combination reference electrode (Metrohm). After addition of dithionite or ferricyanide the potential of the solution was allowed to equilibrate with continuous mixing before measuring UV/Vis spectra.

MtoD was first oxidised by addition of ferricyanide to measure a fully oxidised spectrum before the solution potential was made gradually more reducing by incremental additions of sodium dithionite to measure electronic absorption spectra for MtoD between solution potentials of 0.4 V and -0.36 V vs. the standard hydrogen electrode (SHE). UV/Vis spectra were recorded at numerous states of ferric/ferrous heme interconversion from the fully oxidised state to the fully reduced state based on

the development of β/α absorption bands and the shift of the Soret band from 406 nm to 416 nm (figure 4.8 B).
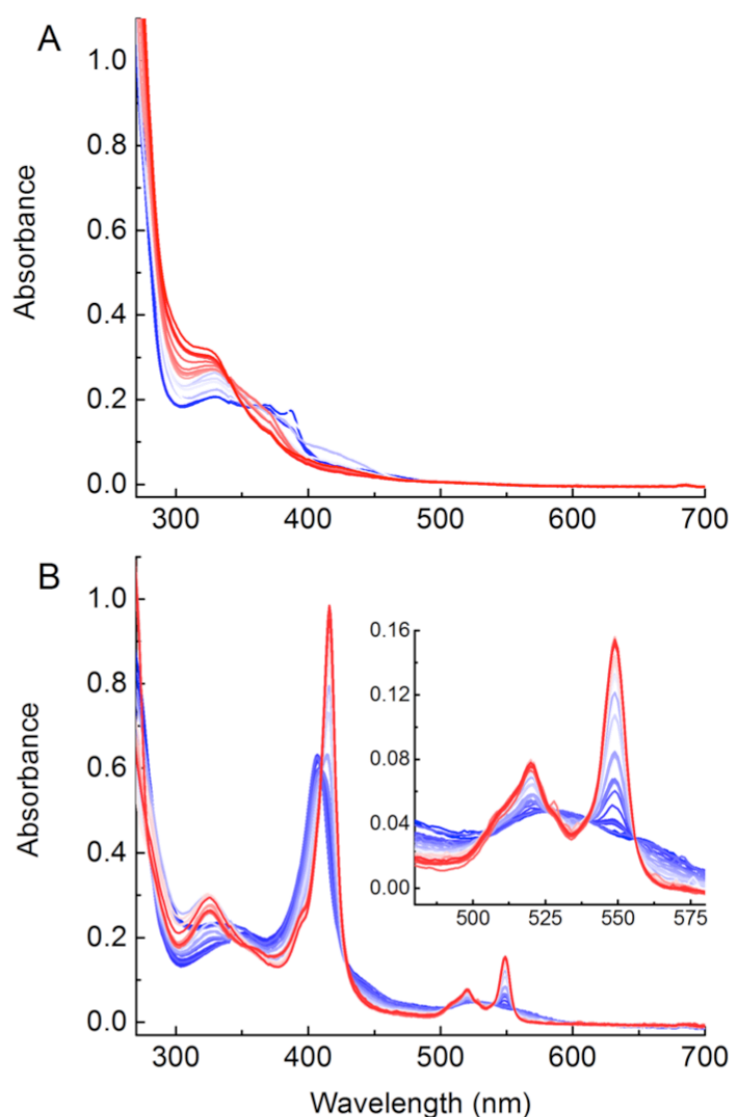
Figure 4.8 Electronic absorption spectra for solution-based spectro-potentiometric characterisation of MtoD. A. A spectropotentiometric titration performed between potentials of +0.4 and -0.4 V vs. SHE on an anaerobic solution of 20 mM HEPES pH 7, 100 mM NaCl + mediator mixture (table 4.1) at 4°C showed no significant changes in absorption above 500 nm. **B.** UV/Vis spectra were measured between 350 and 700 nm after poising a 5.5 μM MtoD solution in 20 mM HEPES pH 7, 100 mM NaCl + mediator mixture at 4°C between solution potentials of +0.4 and -0.36 V vs. SHE. Blue to red colour change indicates increasingly negative redox potentials, which also corresponds to increasingly reduced MtoD spectra.

The same titration was performed in the absence of MtoD to monitor the absorption changes attributed to ferricyanide, dithionite and mediator mix in the solution (figure 4.8 A). The protein-free titre revealed large absorption changes between 250 nm and 450 nm, which would also have affected the titre with MtoD. However, significant absorption changes in the 0.4 V to -0.36 V potential range, using the same concentrations of chemical mediators, were not observed between 500 nm and 600 nm, where the β/α bands of the MtoD spectrum appear. As a result, absorption change for the α band at 549 nm was selected to monitor reduction of the MtoD heme. Absorption changes at 549 nm, plotted as a function of solution potential showed the reduction of the MtoD heme was fully reversible and behaved as predicted by the Nernstian equation for a single redox centre undergoing a one-electron redox transformation with a mid-point potential (E_m) of 155 ± 10 mV vs. SHE (figure 4.8 B). This redox behaviour is in agreement with the results of preliminary optically monitored ascorbate reduction for Strep II-tagged MtoD, which indicated the MtoD heme had a redox potential >58 mV vs. SHE.
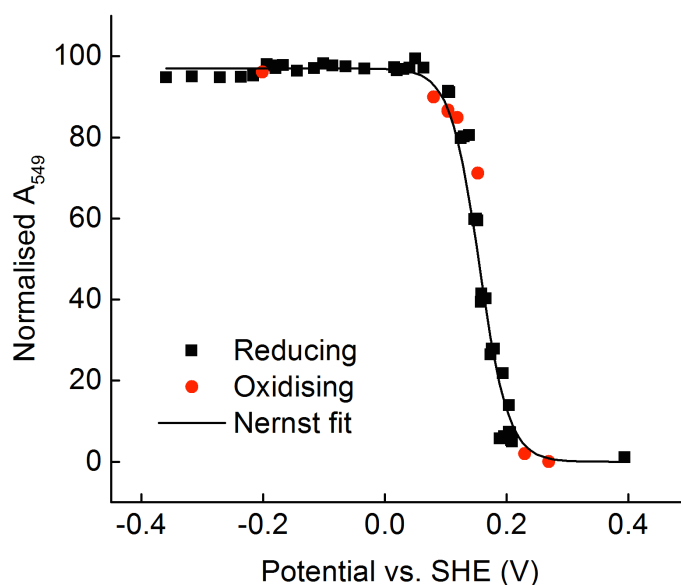
Figure 4.9 Solution-based spectropotentiometric characterisation of MtoD. Electronic absorption change at 549 nm (A_{549}) was used to monitor heme reduction with varying potential of a 5.5 μM solution of MtoD in 20 mM HEPES pH 7, 100 mM NaCl at 4°C. A_{549} data (points) fitted to the Nernst equation (line) for a single-redox centre undergoing a one-electron redox transformation with a midpoint potential (E_m) of 155 mV vs. Standard Hydrogen Electrode (SHE).

4.4.3 Spectroelectrochemical characterisation of MtoD-Strep adsorbed on optically transparent SnO₂ electrodes.

Spectroelectrochemical characterisation of Strep II-tagged MtoD was performed with optically transparent thin layer electrode cells using mesoporous nanocrystalline SnO_2 working electrodes. Clean SnO_2 electrodes were exposed to an ice-cold solution of 500 µM Strep II-tagged MtoD in 20 mM HEPES pH 7, 100 mM NaCl to form a protein film for 5 minutes before rinsing with 20 mM HEPES pH 7, 100 mM NaCl to remove excess protein. A visible red colour on the SnO_2 electrode surface indicated duccessful MtoD adsorption. Assembly of the three-electrode electrochemical cell was performed in an anaerobic glove box before positioning in a UV/Vis spectrophotometer with a bare SnO_2 electrode in the reference beam to minimise scattering contributions to the spectra of the MtoD-coated electrode. The three-electrode setup, which included the SnO_2 working electrode, Ag/AgCl reference electrode and platinum counter electrode, was connected to a potentiostat (AutoLab) to control the potential of the working electrode.

Spectropotentiometry, performed between potentials of 0.4 and -0.5 V vs. SHE at 4°C, revealed similar visible wavelength electronic absorption changes to solution spectropotentiometry of MtoD (figure 4.10 A). Background absorption attributed to scattering contributions from the SnO_2 electrode was present in all measured spectra, despite the presence of a bare SnO_2 electrode in the reference beam. This effect did not preclude the measurement or analysis of optical absorption data since the heme-associated absorption signals remained prominent features of all spectra. However, additional treatment of the spectra was required to recover the known isosbestic points for MtoD. Changes to the scattering contributions throughout the experiment were corrected by adjusting the electronic absorbance data so that all spectra were equal at the known isosbestic point at 556 nm for MtoD (figure 4.10 A inset) as previously used for spectropotentiometric data of MtoD solutions.
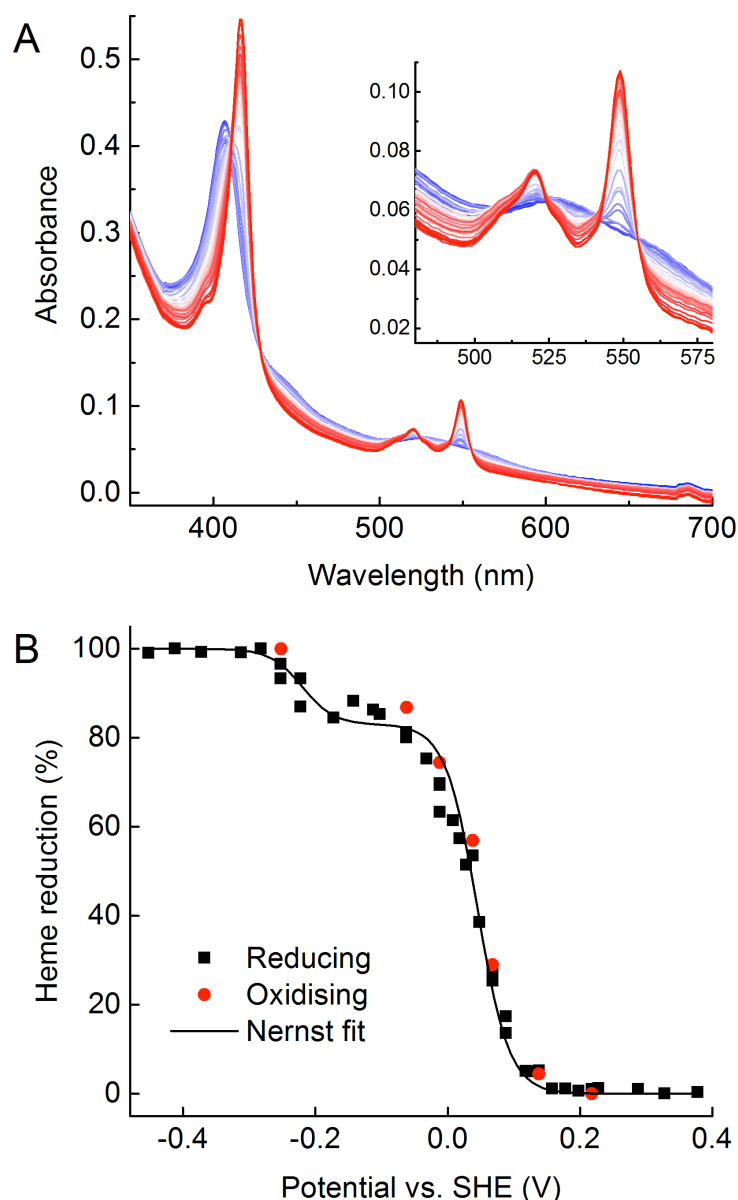
Figure 4.10 Spectropotentiometric characterisation of MtoD films adsorbed on optically transparent SnO₂. A. Visible spectra measured after poising the MtoD film between potentials of 0.4 and -0.5 V for 3 minutes in a solution of 20 mM HEPES pH 7, 100 mM NaCl at 4°C. Spectra were adjusted to be equal at the known isosbestic point for MtoD at 556 nm to allow accurate measurement of 549 nm absorption (A_{549}). Increasing MtoD heme reduction is indicated by a blue to red colour change. **B.** Absorption change at 549 nm plotted as a function of poised potential showed a fully reversible redox transformation, which best satisfied a Nernst equation for two redox centres undergoing one-electron transformations with midpoint potentials of 45 mV and -220 mV vs. Standard Hydrogen Electrode (SHE).

Change in absorption at 549 nm (A_{549}) plotted as a function of poised electrode potential revealed a fully reversible redox transformation of the MtoD protein film, which best fitted to the Nernst equation for two redox centres undergoing one-electron transformations with midpoint redox potentials of 45 mV and -220 mV vs.

SHE. It is unusual that both of these midpoint potentials are lower than that observed for the MtoD heme potential in solution since this likely represents a change to the heme environment as a result of protein film formation or the interaction of MtoD with the electrode surface. Assuming these heme environments gave equivalent changes in extinction coefficient for heme reduction ($\Delta\varepsilon \equiv \Delta$[reduced heme]), the 45 mV redox transformation accounted for 83% of the total heme reduction and the remaining 17% of reduction occurred at the more negative potential of -220 mV. The presence of a second redox potential is unusual for a class I cytochrome c and such a negative potential has only been observed previously in cytochromes c with bis-His axially ligated heme [6,7,20]. The 'low potential' redox feature gave a poorer fit to the Nernst equation compared to the 'high potential' feature. It is possible this behaviour was the result of absorption changes attributed to the SnO_2 electrode at these lower potentials. This behaviour is consistent with the poor quality of isosbestic points for MtoD around the β-band region of the spectrum (507 nm and 524 nm).

To assess reproducibility of this result, the spectropotentiometric characterisation of SnO_2-adsorbed MtoD films was repeated using a fresh aliquot of Strep II-tagged MtoD and a new SnO_2 electrode. The second experiment produced similar results, albeit with greater scattering contributions to the spectra of MtoD from the electrode, possibly due to less MtoD being adsorbed at the electrode surface. Electronic absorption spectra were adjusted to be equal at the 556 nm isosbestic point as previously. The isosbestic points around the β-band region of the spectra were poorly retained (figure 4.11 A inset) as observed in the first SnO_2-based spectropotentiometry experiment. The loss of isosbestic behaviour in this region of the optical spectra was more prominent compared to the first experiment and is consistent with greater absorbance contributions from the SnO_2 electrode to the protein spectra compared to the first experiment. It is plausible reduced adsorption of protein may have emphasised electrode-related effects on optical spectra.

The poor quality of the isosbestic points in this region of the electronic absorption spectra appears to have translated to a poor quality fit between the reduction of MtoD determined by ΔA_{549} and redox behaviour predicted by the Nernst equation (figure 4.11 B). Nevertheless, the dominant features of the analysis were present as seen in the first experiment, including the shift of the MtoD heme potential from its solution value of +155 mV to lower potentials on the electrode and the appearance of a second low potential redox transformation.
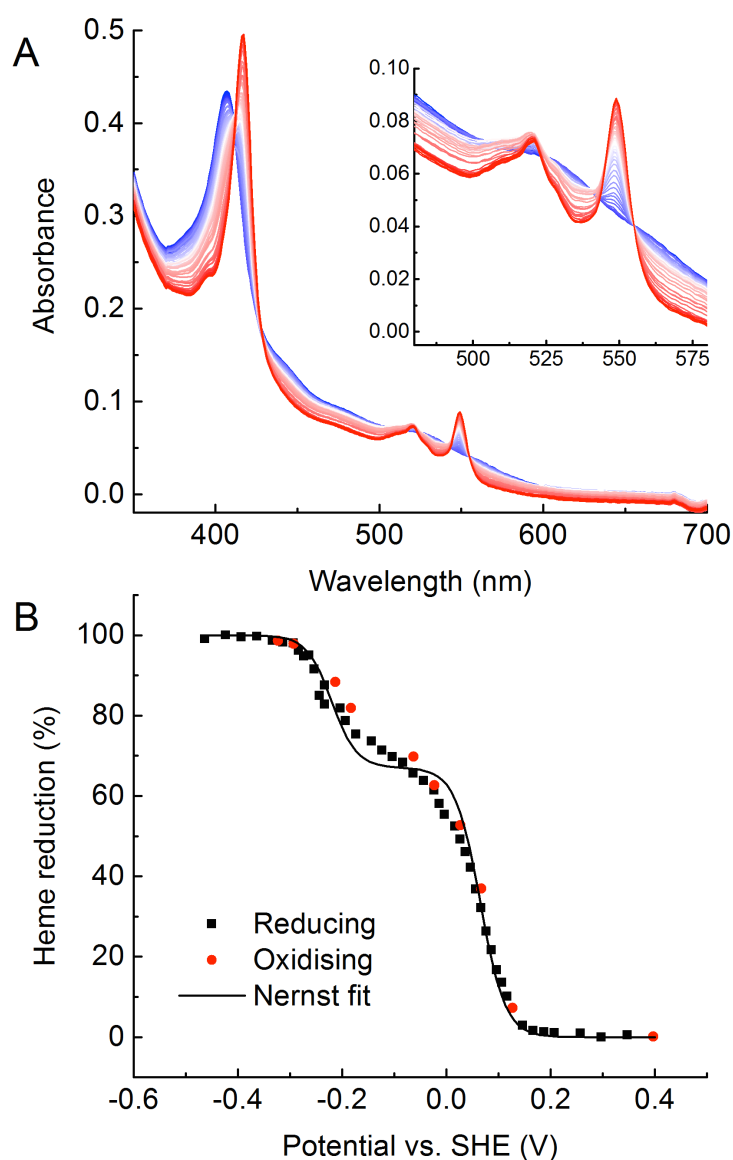
Figure 4.11 Repeated spectropotentiometric characterisation of a SnO₂-adsorbed MtoD film. A. Visible spectra were measured after poising the protein film between potentials of 0.4 and -0.5 V for 3 minutes at pH 7, 4°C. Spectra were adjusted to be equal at the known isosbestic point for MtoD at 556 nm (inset) to improve the accuracy of A_{549} measurements. Reduction of heme is shown as a blue to red colour change. **B.** A_{549} plotted as a function of poised potential indicated redox transformations were reversible. A_{549} measurements made between potentials of 0 mV and -0.3 mV fitted poorly to the Nernst equation; the best fit achieved predicted two redox centres undergoing one-electron transformations with midpoint potentials of +60 mV and -220 mV vs. (SHE), shown as 70% and 30% contributions to total reduction respectively.

The best Nernstian fit achieved for the redox transformation of the MtoD heme was for two redox centres undergoing one-electron transformations with midpoint potentials of +60 mV and -220 mV vs. SHE. The +60 mV 'high-potential' feature

produced by this MtoD film is comparable to the previously observed value of 45 mV on SnO_2 and the midpoint potential of -220 mV observed for the low potential redox transformation was consistent. However, the relative contributions of the high and low potential redox transformations differed slightly between the two experiments with the first experiment giving relative contributions of 83/17 for the high potential and low potential redox transformations and the second experiment giving approximate relative contributions of 70/30 (figure 4.11 B). These relative contributions are summarised in table 4.3.

A comparative analysis was performed using the spectropotentiometric data acquired from MtoD in solution and MtoD protein films adsorbed on SnO_2 electrodes. Reduced minus oxidised electronic absorption spectra were used to define the spectral changes associated with the MtoD heme over a given potential range. Spectra were normalised so that each reduced minus oxidised spectrum gave equal signal intensity. An 'oxidised' spectrum was selected from the start of the observed reduction and a 'reduced' spectrum was selected from the end of the observed heme reduction.

Solution-based spectropotentiometric characterisation of MtoD had revealed only one redox transformation. As a consequence, an oxidised spectrum, measured at a solution potential of +270 mV, was subtracted from the reduced spectrum measured at a potential of -30 mV (figure 4.12 A). The reduced minus oxidised spectrum for the redox transformation of the MtoD heme in solution at pH 7 gave Soret-band and α-band peak maxima at 416.5 nm and 549 nm respectively (blue line, figure 4.12 B).

Reduced minus oxidised spectra were produced for both the high potential and low potential redox transformations observed during spectropotentiometric characterisation of SnO_2-adsorbed MtoD films to define the spectral changes associated with each redox transformation. Oxidised and reduced spectra were selected from the beginning and end points of each redox transformation (indicated by magenta and black arrows in figure 4.12 A) for both SnO_2-based spectropotentiometric experiments.
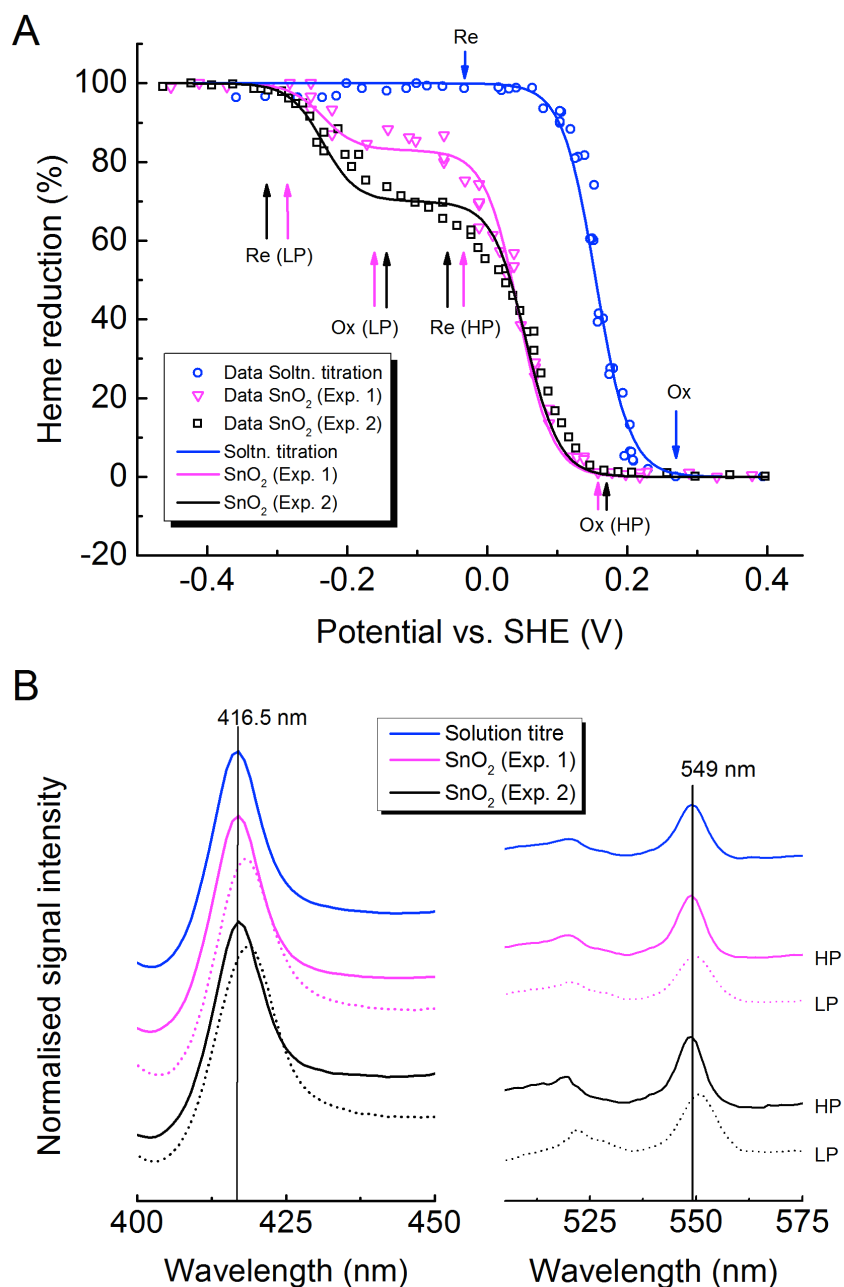
Figure 4.12 Comparative spectral analysis of redox transformations of MtoD in solution and as SnO₂-adsorbed protein films. A. Spectral properties associated with each redox event were determined using reduced (Re) – oxidised (Ox) spectra representing the start and end points of the redox transformation; selected spectra are indicated with coloured arrows. This was performed for high potential (HP) and low potential (LP) redox transformations for MtoD films from experiment 1 (Exp. 1) and experiment 2 (Exp. 2). **B.** Plots of reduced minus oxidised spectral data in the Soret-band and α/β-band regions show a 1 nm red shift of absorption maxima for the low potential spectra (dotted lines) for both MtoD films relative to the solution-based and MtoD film high potential spectra (solid lines).

The high potential redox transformation for both SnO_2-adsorbed MtoD films produced near identical spectral changes to those observed for MtoD in solution with Soret-band and α-band peak maxima at 416.5 nm and 549 nm respectively (shown as solid lines in figure 4.12 B). However, the low potential redox transformation for both SnO_2-adsorbed MtoD films produced reduced minus oxidised spectra in which the Soret-band and the α/β band absorption maxima were red-shifted by 1 nm (dotted lines, figure 4.12 B). The shift in peak maxima provides further evidence for a change in the MtoD heme environment, which could help explain the shift in heme potential.

4.4.4 Cyclic voltammetry of SnO_2-adsorbed MtoD-Strep films

Cyclic voltammetry (CV) on MtoD-Strep films was used to characterise the redox behaviour of MtoD at equilibrium using a scan rate of 5 $mV.s^{-1}$. Current flow between the MtoD-adsorbed SnO_2 electrode and the platinum counter electrode was monitored between potentials of 0.4 and -0.5 V vs. SHE at pH 7, 4°C. Prior to adsorbing MtoD onto the SnO_2 electrode, cyclic voltammetry was performed on the bare SnO_2 electrode in 20 mM HEPES pH 7, 100 mM NaCl to establish a voltammogram associated specifically with properties of the electrode and electrolytes in the buffer solution to be used, which could be subtracted from voltammetry experiments with MtoD films (figure 4.13). The 'protein free' voltammogram could not be directly subtracted from that produced by the MtoD-adsorbed electrode to give ideally baseline-subtracted data due to a poor fit in the initial re-oxidation phase of the voltammograms. This is a typical finding for this type of experiment and it may be a result of re-heating the electrode prior to adsorbing MtoD and repositioning electrode connections while reassembling the electrochemical cell.
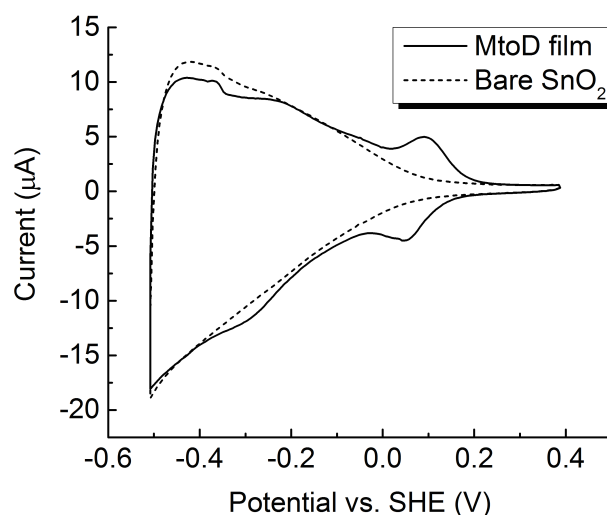
Figure 4.13 Overlaid bare-electrode response with CV data collected from the SnO₂ electrode after MtoD adsorption. The voltammogram of SnO$_2$-adsorbed MtoD (continuous line), measured at pH 7, 4°C differed from the bare SnO$_2$ electrodic response (broken line) in two regions, with negative and positive peaks in current indicating reduction and oxidation of the protein film at approximately +80 mV and -250 mV, respectively.   Measured in 20 mM HEPES pH 7 at a scan rate of 5 mV.s^{-1}.

Prior knowledge of the non-Faradaic envelope shape and features attributed to the electrode allowed a baseline to be created manually. This was performed using the peak analyser tool in OriginPro 9.1 (OriginLab, Northampton, MA) by adjusting the bare electrode response of the SnO$_2$ electrode so that the features of the bare electrode response were retained, but fitted ideally to the response of the SnO$_2$-adsorbed MtoD film (figure 4.14 A). A small peak in current at -370 mV was observed in all of the bare SnO$_2$ and MtoD-adsorbed SnO$_2$ voltammograms; this feature was included in the model baseline to remove it from the Faradaic response.

Subtracting the model non-Faradaic response (NFR) revealed two pairs of peaks for which the peak potentials were averaged to define redox potentials of +75 mV and -250 mV vs. SHE (figure 4.12 B). Peak separations (ΔE_p) of 45 mV and 65 mV for the high potential and low potential redox transformations respectively indicated quasi-reversible redox responses as ideally reversible redox processes of protein films give no peak separation.

The observation of two pairs of Faradaic peaks agrees well with the electrode-based spectropotentiometry of MtoD, which produced spectroscopic changes indicating redox events centred on +45 mV and -220 mV, and is consistent with the

MtoD heme cofactor contributing to both pairs of Faradaic features. The observed Faradaic peak areas were broad at ~0.1 V, which is most likely a result of using semiconductive SnO_2 electrodes, however the widths of peaks at half-height (δ) (table 4.2) were consistent with one-electron redox transformations. Integrating the reducing and oxidising Faradaic peaks gave equal peak areas associated with protein reduction and oxidation indicating reaction reversibility, which is consistent with the reversible reduction/oxidation observed during spectropotentiometric measurements. Taking into account the ca. 300x greater surface area of the mesoporous nanocrystalline SnO_2 electrodes compared to the geometric surface area [14,23] (0.5 cm^2 x 300 = 150 cm^2) an electroactive coverage (Γ) of Faradaic peaks was calculated as 5.23 $pmol.cm^{-2}$ and 1.97 $pmol.cm^{-2}$ for the high potential and low potential redox transformations respectively. The total electroactive coverage of 7.2 $pmol.cm^{-2}$ is consistent with previously observed coverages for small monoheme cytochromes c forming an electroactive monolayer [24,25]. These Γ values represent a 73/27 ratio of high/low potential redox activity, which compares to an 83/17 ratio determined spectroscopically for the same SnO_2-adsorbed MtoD film. It is possible some of this 10% difference could be accounted for by differences in the magnitude of the extinction coefficient change at 549 nm ($\Delta\varepsilon_{549}$) for the reduction of the MtoD heme in two distinct environments. There is also some error in the calculation of peak areas due to uncertainties in the position of baseline current.
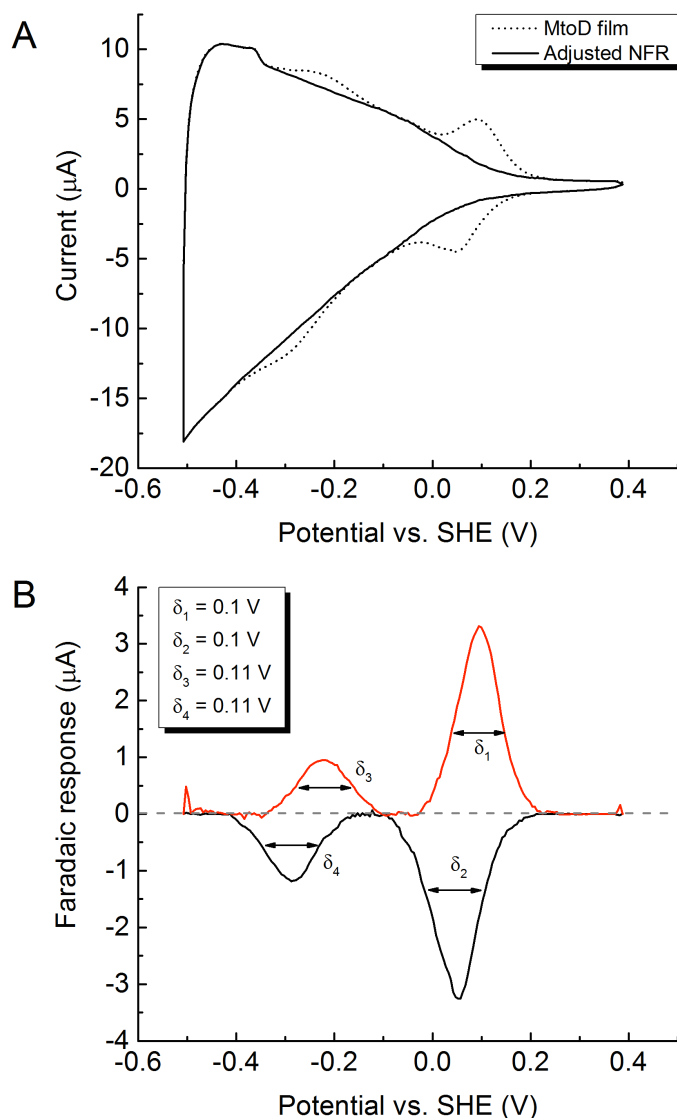
Figure 4.14 Resolution of the Faradaic features from SnO$_2$-adsorbed MtoD-Strep voltammograms. A. Overlay of a representative CV from MtoD (from Fig 4.19) (continuous line) with a current-potential profile generated to model the non-Faradaic response (NFR) (broken line). **B.** The Faradaic response arising from MtoD generated from CVs in panel A by subtraction of NFR from MtoD response. Red and black lines represent reducing and re-oxidising Faradaic response respectively. Two pairs of Faradaic peaks were observed with peak separations of 45 mV for the dominant high potential feature and 65 mV for the low potential feature. The averaging of Faradaic peak positions revealed midpoint potentials of +75 mV and -250 mV vs. SHE. Faradaic half peak-height widths (δ) were consistent with one-electron redox transformations.

Cyclic voltammetry was repeated under the same conditions using the second SnO$_2$-adsorbed MtoD film. A slightly different bare-electrode non-Faradaic voltammogram was observed and attributed to the use of a different electrode (figure 4.15 A). The SnO$_2$ electrodes used originated from the same batch, however some

differences were expected due to the electrodes not being prepared in parallel and their slightly different sizes (~0.4 cm^2 compared to 0.5 cm^2 electrode used previously). Cyclic voltammetry performed on the second SnO$_2$-adsorbed MtoD film produced near identical results to the first experiment with a dominant redox transformation apparent at ~80 mV and a second redox transformation visible at approximately -250 mV vs. SHE (figure 4.15 A).

Subtraction of non-Faradaic signal from the voltammograms was performed as before using a manually generated bare electrode response (figure 4.15 B). Subtraction of the adjusted bare electrode response from the MtoD CV data revealed two pairs of Faradaic peaks. Averaging the peak positions gave midpoint potentials of 85 mV and -230 mV vs. SHE. Peak widths at half height (δ) and separation of peak potentials for both redox transformations were consistent with quasi-reversible one-electron transfer events.

Electroactive coverages (Γ) of 3.5 pmol.cm^{-2} and 1.47 pmol.cm^{-2} were calculated for the high potential and low potential redox transformations respectively. The total Γ of 4.97 pmol.cm^{-2} is slightly lower than observed for the CV experiment performed on the first SnO$_2$-adsorbed MtoD film (table 4.2) and offers a reasonable explanation for the more prominent electrode-associated features observed in the optical spectra for the second spectropotentiometric experiment compared with the first (figures 4.10 A and 4.11 A). The proportion of electroactive coverage for the high potential and low potential redox transformations (70% and 30% respectively) compare well with the ~70/30 ratio of contributions made by the high and low potential redox transformations determined spectroscopically (table 4.3).
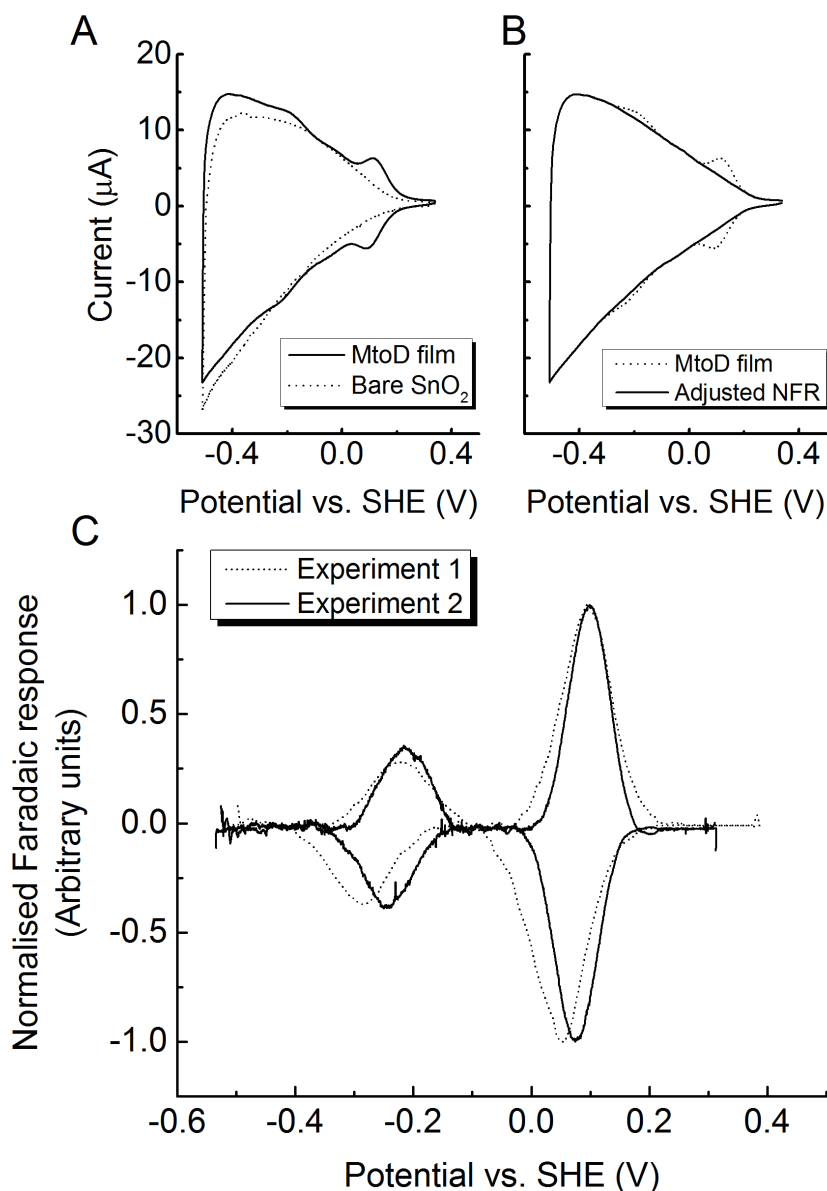
Figure 4.15 Repeating cyclic voltammetry on a second SnO₂-adsorbed MtoD-Strep film produced similar results to the first experiment. A. Voltammogram of SnO₂-adsorbed MtoD (continuous line), and bare SnO₂ electrodic response (broken line) measured at pH 7, 4°C. **B.** The bare electrode response was manually generated to produce an ideal non-Faradaic response (NFR). **C.** Subtraction of the adjusted NFR from the response of the SnO₂-adsorbed MtoD film revealed two pairs of Faradaic peaks (solid line). The peak positions were averaged to give midpoint potentials of 85 mV and -230 mV vs. SHE. The Faradaic response was normalised and overlaid with data from the first CV experiment (broken line) revealing similar redox behaviour between the two MtoD films.

Redox transformation	Experiment 1		Experiment 2	
	High potential	Low potential	High potential	Low potential
E_m (mV)	75	-250	85	-230
ΔE_p (mV)	45	65	25	29
δ Reducing (mV)	100	110	82	95
δ Oxidising (mV)	100	110	82	93
Q Reducing (C)	7.6×10^{-5}	2.9×10^{-5}	4.1×10^{-5}	1.7×10^{-5}
Q Oxidising (C)	7.1×10^{-5}	2.5×10^{-5}	4.0×10^{-5}	1.8×10^{-5}
Γ (pmol.cm^{-2})	5.23	1.97	3.50	1.47

Table 4.2 Faradaic peak characteristics for cyclic voltammetry (CV) experiments performed on SnO$_2$-adsorbed MtoD-Strep films. Two CV experiments were performed on different aliquots of Strep II-tagged MtoD using different SnO$_2$ working electrodes. Both SnO$_2$-adsorbed MtoD films produced two redox transformations, labelled 1 and 2. The midpoint potential of these redox transformations (E_m) was determined by averaging the oxidising and reducing peak potentials (E_p). The separation of peak potentials (ΔE_p) and the width of Faradaic peaks at half-height (δ) are consistent with one-electron quasi-reversible redox transformations. The charge (Q) associated with Faradaic peak areas, measured in Coulombs (C), was used to determine the electroactive coverage (Γ) for each of the redox transformations based on SnO$_2$ surface areas of 150 cm^2 and 120 cm^2 (geometric surface areas 0.5 cm^2 and 0.4 cm^2) for experiment 1 and 2 respectively.

The extent of change to the redox behaviour of MtoD on SnO$_2$ electrodes compared to in free solution is demonstrated in table 4.3, which summarises the midpoint potentials reported for each observed redox transformation for MtoD in solution and on SnO$_2$ electrodes using spectropotentiometric and voltammetric characterisation. The high potential and low potential redox transformations observed for SnO$_2$-adsorbed MtoD films were ~100 mV and ~380 mV lower than the MtoD heme in solution. The observation of a shift of heme potential to negative values on adsorption of protein , although unusual, has been reported previously for mitochondrial horse heart cytochrome *c* adsorbed on self-assembled monolayers (SAMs) and *Acidiphilium cryptum* cytochrome *c* adsorbed on indium-doped tin oxide (ITO) and hematite electrodes [25,26]. Chen *et al* (2002) concluded the use of a range of SAM compounds influenced the conformation and orientation of cytochrome *c* on the electrode, giving rise to a 500 mV range of orientation and conformation-dependent redox potentials for the monoheme cytochrome.

Method	Experiment	Midpoint potentials (mV vs. SHE) (contribution (%))	
		High potential	Low potential
Spectropotentiometry	Solution-based titration	155 (100)	-
	SnO$_2$ experiment 1	45 (83)	-220 (17)
	SnO$_2$ experiment 2	60 (70)	-220 (30)
Cyclic voltammetry	SnO$_2$ experiment 1	75 (73)	-250 (27)
	SnO$_2$ experiment 2	85 (70)	-230 (30)

Table 4.3 Comparison of midpoint potentials and relative contributions determined for MtoD by solution/electrode-based spectropotentiometry and cyclic voltammetry using optically transparent mesoporous nanocrystalline SnO$_2$. Solution-based spectropotentiometry revealed a midpoint potential of +155 mV for the MtoD heme based on ΔA_{549} at chemically poised potentials. By contrast, SnO$_2$-adsorbed MtoD films produced two redox features, both of which were cathode-shifted relative to MtoD solutions. The high potential redox transformation of the MtoD heme determined by spectropotentiometry and cyclic voltammetry was 70-110 mV lower than observed in solution. The low potential redox transformation was 375-405 lower than observed in solution. Figures in brackets represent the contribution of the high and low potential features to overall reduction and oxidation. These contributions were determined using the best fit of the Nernst equation to the spectral data for spectropotentiometry and by relative electroactive coverages for cyclic voltammetry. Potentials are accurate to ±10 mV.

4.5 Discussion

Spectropotentiometric characterisation of MtoDs redox properties in solution revealed a single redox transformation with a midpoint potential of +155 mV vs. SHE at pH 7, which is consistent with the presence of a single heme cofactor in MtoD. This heme potential is more negative than typically associated with class I cytochromes *c* with His/Met ligated hemes [27], but more positive than previously characterised small monoheme *c*-type cytochromes with bis-His axial heme ligation [7,20,27]. The redox characterisation of MtoD on optically transparent SnO$_2$ electrodes produced unexpected results, with a significant decrease in the midpoint potential of MtoD when compared to that determined in solution (table 4.3) and the appearance of a second low potential heme redox transformation previously not seen for MtoD in solution. The potential of the MtoD heme in solution and those observed for SnO$_2$-adsorbed MtoD films were all lower than typically observed for His/Met ligated monoheme cytochromes *c*.

The current evidence based on the primary structure and the crystal structure for MtoD, pyridine hemochrome analysis and solution-based spectropotentiometry

indicates MtoD is a monoheme *c*-type cytochrome. As a result, the appearance of a second heme redox transformation ~380 mV lower in potential compared to the midpoint potential of the MtoD heme in solution was puzzling. The redox behaviour of Strep II-tagged MtoD in solution experiments was consistent with the predicted response of a small monoheme cytochrome *c* and biophysical characterisation indicated MtoD solutions were homogenous. Consequently, the appearance of a second redox transformation is most likely to have occurred after the adsorption of MtoD to SnO_2 electrodes.

Previous work to characterise the redox properties of small monoheme cytochromes *c* using electrode-adsorbed protein films has produced several examples of negative shifts in heme midpoint potential relative to the heme potential determined in solution, as was observed for MtoD [25,26,28]. Chen *et al.* (2002) demonstrated monoheme mitochondrial cytochrome *c* from horse heart produces a ~ 0.5 V range of conformation and orientation-dependent midpoint redox potentials from +325 mV to -120 mV vs. SHE at the surface of a variety of self-assembled monolayers (SAMs). Similar negative shifts of the midpoint potential of horse heart cytochrome *c* were also reported using tin oxide and gold electrodes by Hinnen *et al.* (1983). In addition, Khare *et al.* (2006) revealed cytochrome *c* from the iron-reducer *Acidiphilium cryptum* gave a reproducible ~400 mV negative shift in its redox potential at indium-doped tin oxide (ITO) and hematite electrodes as a result of electrode interaction-induced conformational changes. The similarity between the redox behaviour of these small monoheme cytochromes *c* and that observed for MtoD at the surface of SnO_2 electrodes certainly makes orientation and conformation-dependent redox changes worth considering as an explanation for the redox behaviour of MtoD at the electrode surface.

Orientation dependency could offer an explanation for the appearance of two distinct heme redox transformations observed for SnO_2-adsorbed MtoD. The unusual dual accessibility of the MtoD heme cofactor, as seen in the 1.47 Å crystal structure [3] (figure 3.17, chapter 3) could allow the formation of two distinct protein-electrode interfaces. Orientation-dependent changes to the conformation of MtoD around the heme cofactor as a result of forming these interfaces might provide a heme environment which differs significantly enough to cause a ~380 mV change in heme potential.

The observation of a 1 nm redshift in Soret- and α-band peak maxima in the reduced minus oxidised difference spectra associated with the low potential redox transformation supports the formation of a different heme environment compared to the high potential redox transformation. These observations should be treated cautiously, since large negative shifts in heme midpoint potential have previously been linked with protein denaturation [29]. Ferri *et al.* (1996) reported a ~450 mV negative shift in potential of horse heart cytochrome *c* between the native protein and its denatured form, which is not greatly dissimilar from the potential change observed for the MtoD heme. Furthermore, similarly low potentials (~-200 mV vs. SHE) are observed for water-ligated heme at pH 7 [30], making it possible that the loss of a histidine ligand replaced by a water molecule might also cause a large negative shift in the MtoD heme midpoint potential.

The possibility of a ligand switch is also worth considering, given the close proximity of a second potential distal histidine ligand (His78) to the MtoD heme (figure 4.16). The 5.3 Å distance between His78 NE_2 nitrogen atom and the heme iron is much larger than the typical ~2 Å Fe−NE_2 bond distance, as observed for both Fe−His47 and Fe−His95 heme iron coordination distances in MtoD. This distance precludes His78 from coordinating the heme iron. However, it is possible a significant conformational change of MtoD around the heme cofactor could reposition His78 and His95 such that a ligand switch might occur. Given the propensity of presently characterised monoheme cytochromes *c* with bis-His ligated hemes to have low midpoint potentials (-250 mV to -280 mV [4,6,7]) it is possible a switch to His78 distal heme ligation could give the MtoD heme a similarly low potential, as observed using SnO_2 electrodes (table 4.3).

The possibility of a His → Lys ligand switch should also be considered since a significant conformational change might allow the sidechain of Lys96 to rotate towards the heme cofactor could potentially allow this residue to form the distal ligand to the heme iron (figure 4.16). Previous work by Barker *et al.* (1992) has indicated that a distal ligand switch from methionine to lysine under alkaline conditions is possible and is accompanied by a significant negative shift of the heme potential [31]. It is possible conformational changes at the electrode surface could induce similar changes in MtoD and might be responsible for the change in heme reduction potential in electrode-based electrochemical studies.
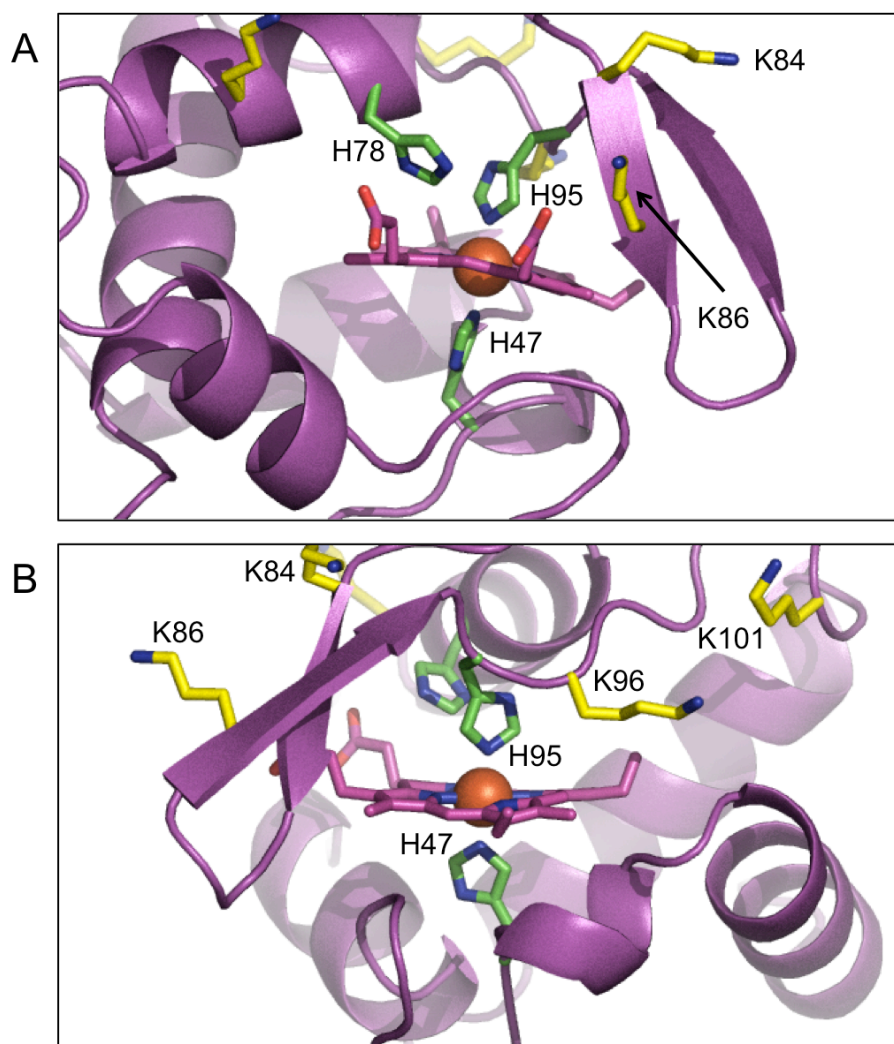
Figure 4.16 Positions of potential distal heme ligands viewed from the propionated (A) and thioloated (B) heme edges. The position of His78 in a α helix would be expected to make this residue inflexible, precluding its involvement as a potential heme ligand. However, a conformational change of great enough magnitude could potentially adjust the position of the heme cofactor to allow His78 to compete with His95 for heme iron ligation. His47 and His95 are the native axial heme ligands. Potential histidine and lysine ligands are coloured green and yellow respectively.

It is important to note the dominant redox features of MtoD in solution and as SnO_2-adsorbed protein films would theoretically allow a favourable transfer of electrons from the decaheme cytochrome MtoA to MtoD. Redox characterisation of MtoA by Shi *et al.* (2012) using PFV revealed a redox active potential window of -400 mV to +100 mV vs. SHE. The potential of +155 ±10 mV for the MtoD heme in solution is more positive than all of the redox active hemes in MtoA, while the high potential redox transformation observed for MtoD films of +75 ± 10 mV would also

favour electron transfer from MtoA to MtoD (figure 4.17). This supports the proposed role of MtoD in the periplasm of *Sideroxydans*.
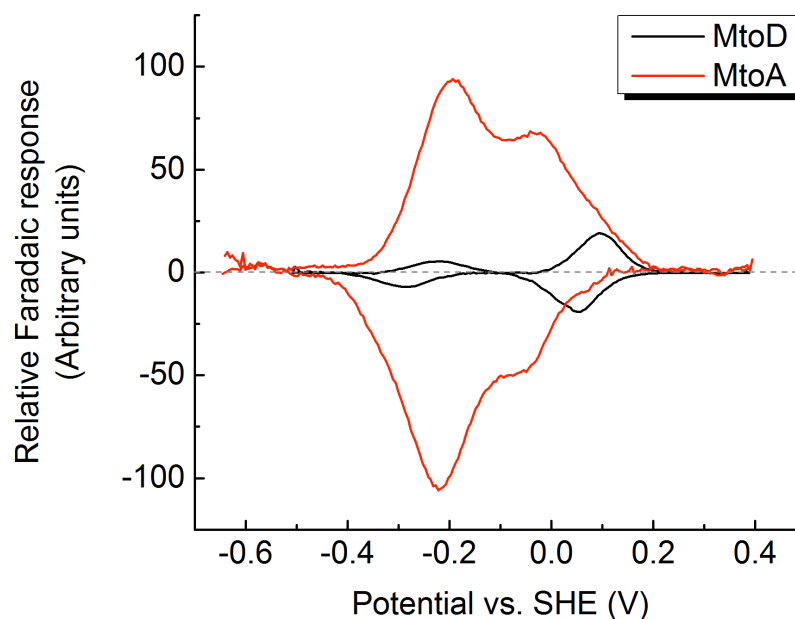
Figure 4.17 Faradaic response of MtoA (50 mV.s^{-1}) [8] **on a graphite electrode and MtoD (5 mV.s^{-1}) on a SnO$_2$ electrode in 20 mM HEPES pH 7 supports favourable electron transfer from MtoA to MtoD.** Faradaic peaks for MtoA and MtoD were normalised and the response of MtoD was scaled to account for its single heme compared to the decaheme MtoA. The high potential redox feature for MtoD is positive enough to support electron transfer from MtoA, whereas the low potential redox feature could support electron transfer from MtoD to inner membrane cytochromes.

Given the proposed role of MtoD as a periplasmic electron shuttle [3,9] the intriguing redox behaviour of SnO$_2$-adsorbed MtoD films is tantalising since the ability of MtoD to modulate the redox potential associated with its heme could allow electron transfer events previously considered to be unfavourable to take place at the inner membrane of *Sideroxydans*. The highly exposed heme surface of MtoD is likely to be sensitive to changes in the local environment, such as those caused by protein complex formation. This may allow lowering of the MtoD midpoint potential on association with inner membrane cytochromes, allowing the favourable transfer of electrons to facilitate the fixing of carbon for lithotrophic growth and generation of a proton motive force (PMF) for ATP generation. A more complete understanding of the nature of the redox behaviour of MtoD at the electrode surface is required to

provide further insight into the potentially complex role of MtoD in *Sideroxydans lithotrophicus*.

If modulation of the MtoD heme potential via interaction-induced changes occurs *in vivo*, discovering and characterising the potential interacting partners of MtoD in *Sideroxydans* could provide valuable insight to allow biophysical and redox characterisation of the interacting protein complexes. In particular, the effects of complex formation on the redox potential of the MtoD heme is an exciting prospect that could lead to a greater understanding of electron transfer pathways in *Sideroxydans*. The first stages of this work to further probe the role of MtoD in *Sideroxydans* are presented in chapter 5.

4.6   References

1.   Moore, G. & Pettigrew, G. *Cytochromes c: Evolutionary, Structural and Physicochemical Aspects*. (Springer-Verlag, 1990).

2.   Hartshorne, R. S. *et al.* A dedicated haem lyase is required for the maturation of a novel bacterial cytochrome c with unconventional covalent haem binding. *Mol. Microbiol.* **64,** 1049–60 (2007).

3.   Beckwith, C. R. *et al.* Characterization of MtoD from Sideroxydans lithotrophicus: a cytochrome c electron shuttle used in lithoautotrophic growth. *Front. Microbiol.* **6,** (2015).

4.   Dolla, a, Blanchard, L., Guerlesquin, F. & Bruschi, M. The protein moiety modulates the redox potential in cytochromes c. *Biochimie* **76,** 471–479 (1994).

5.   Miller, D. J. & Nicholas, D. J. N-terminal amino acid sequence of cytochrome c-552 from Nitrosomonas europaea. *Biochem. Int.* **12,** 167–172 (1986).

6.   Kerfeld, C. a. *et al.* Structural and EPR characterization of the soluble form of cytochrome c-550 and of the psbV2 gene product from the cyanobacterium Thermosynechococcus elongatus. *Plant Cell Physiol.* **44,** 697–706 (2003).

7.   Hoganson, C. W., Lagenfelt, G. & Andreasson, L. E. EPR and redox potentiometric studies of cytochrome c-549 of Anacystis nidulans. *Biochim. Biophys. Acta - Bioenerg.* **1016,** 203–206 (1990).

8.   Liu, J. *et al.* Identification and Characterization of MtoA: A Decaheme c-Type Cytochrome of the Neutrophilic Fe(II)-Oxidizing Bacterium Sideroxydans lithotrophicus ES-1. *Front. Microbiol.* **3,** 37 (2012).

9.   Shi, L., Rosso, K. M., Zachara, J. M. & Fredrickson, J. K. Mtr extracellular electron-transfer pathways in Fe(III)-reducing or Fe(II)-oxidizing bacteria: a genomic perspective. *Biochem. Soc. Trans.* **40,** 1261–7 (2012).

10.   Emerson, D. Biogeochemistry and microbiology of microaerobic Fe(II) oxidation. *Biochem. Soc. Trans.* **40,** 1211–6 (2012).

11.   Summers, Z. M., Gralnick, J. A. & Bond, D. R. Cultivation of an Obligate Fe (II)-Oxidizing Lithoautotrophic Bacterium Using Electrodes. *MBio* **4,** (2013).

12.   Topoglidis, E., Astuti, Y., Duriaux, F., Grätzel, M. & Durrant, J. R. Direct electrochemistry and nitric oxide interaction of heme proteins adsorbed on nanocrystalline tin oxide electrodes. *Langmuir* **19,** 6894–6900 (2003).

13.   Kemp, G. L. *et al.* Opportunities for mesoporous nanocrystalline SnO2 electrodes in kinetic and catalytic analyses of redox proteins. *Biochem. Soc. Trans.* **37,** 368–72 (2009).

14.   Marritt, S. J. *et al.* Spectroelectrochemical characterization of a pentaheme cytochrome in solution and as electrocatalytically active films on nanocrystalline metal-oxide electrodes. *J. Am. Chem. Soc.* **130,** 8588–8589 (2008).

15.   Compton, R. G. & Banks, C. E. *Understanding Voltammetry*. (Imperial College Press, 2011). at <https://books.google.co.uk/books?id=yil6gmSrLV8C>

16.   Lundblad, R. L. & Macdonald, F. *Handbook of Biochemistry and Molecular Biology, Fourth Edition*. (CRC Press, 2010). at <https://books.google.co.uk/books?id=sUDSBQAAQBAJ>

17.   Mayhew, S. G. The redox potential of dithionite and SO-2 from equilibrium reactions with flavodoxins, methyl viologen and hydrogen plus hydrogenase. *Eur.*

J. Biochem. **85,** 535–547 (1978).

18. Bamford, V. a *et al.* Structure and spectroscopy of the periplasmic cytochrome c nitrite reductase from Escherichia coli. *Biochemistry* **41,** 2921–31 (2002).

19. Roldán, M. D. *et al.* Spectroscopic characterization of a novel multiheme c-type cytochrome widely implicated in bacterial electron transport. *J. Biol. Chem.* **273,** 28785–28790 (1998).

20. Roncel, M. *et al.* Redox properties of the photosystem II cytochromes b559 and c550 in the cyanobacterium Thermosynechococcus elongatus. *J. Biol. Inorg. Chem.* **8,** 206–216 (2003).

21. Battistoni, A. *et al.* A histidine-rich metal binding domain at the N terminus of Cu, Zn-superoxide dismutases from pathogenic bacteria. A novel strategy for metal chaperoning. *J. Biol. Chem.* **276,** 30315–30325 (2001).

22. Hara, M., Fujinaga, M. & Kuboi, T. Metal binding by citrus dehydrin with histidine-rich domains. *J. Exp. Bot.* **56,** 2695–2703 (2005).

23. Astuti, Y. *et al.* Proton-Coupled Electron Transfer of Flavodoxin Immobilized on Nanostructured Tin Dioxide Electrodes : Thermodynamics versus Kinetics Control of Protein Redox Function. **108,** 13–21 (2004).

24. Collinson, M. & Bowden, E. F. UV-visible spectroscopy of adsorbed cytochrome c on tin oxide electrodes. *Anal. Chem.* **64,** 1470–1476 (1992).

25. Chen, X., Ferrigno, R., Yang, J. & Whitesides, G. M. Redox properties of cytochrome c adsorbed on self-assembled monlayers: a probe for protein confrmation and orientation. *Langmuir* **18,** 7009–7015 (2002).

26. Khare, N., Lovelace, D. M., Eggleston, C. M., Swenson, M. & Magnuson, T. S. Redox-linked conformation change and electron transfer between monoheme c-type cytochromes and oxides. *Geochim. Cosmochim. Acta* **70,** 4332–4342 (2006).

27. Zheng, Z. & Gunner, M. R. Analysis of the electrochemistry of hemes with E(m)s spanning 800 mV. *Proteins* **75,** 719–34 (2009).

28. Hinnen, C., Parsons, R. & Niki, K. Electrochemical and spectroreflectance studies of the adsorbed horse heart cytochrome c and cytochrome c3 from D. Vulgaris, miyazaki strain, at gold electrode. *J. Electroanal. Chem. Interfacial Electrochem.* **147,** 329–337 (1983).

29. Ferri, T., Poscia, A., Ascoli, F. & Santucci, R. Direct electrochemical evidence for an equilibrium intermediate in the guanidine-induced unfolding of cytochrome c. *Biochim. Biophys. Acta - Protein Struct. Mol. Enzymol.* **1298,** 102–108 (1996).

30. Pilloud, D. L., Chen, X., Dutton, P. L. & Moser, C. C. Electrochemistry of Self-Assembled Monolayers of Iron Protoporphyrin IX Attached to Modified Gold Electrodes through Thioether Linkage. *J. Phys. Chem. B* **104,** 2868–2877 (2000).

31. Barker, P. D. & Ma, A. G. pH-Linked Conformational Regulation of a Metalloprotein Oxidation-Reduction Equilibrium : Electrochemical Analysis of the Alkaline Form of Cytochrome c. *J. Am. Chem. Soc.* **114,** 3619–3624 (1992).

Chapter 5

Cultivation and bioinformatics analysis of *Sideroxydans lithotrophicus* ES-1: a preliminary insight into the cytochrome content of ES-1.

Work presented in this chapter has been published in the following paper:

5.1   Abstract

The isolation and *in vitro* cultivation of microaerophilic iron-oxidising bacteria (FeOB) has been challenging for many years due to difficulties growing FeOB on iron under aerobic conditions. This has precluded the physiological and biochemical characterisation of these bacteria [1,2]. Meanwhile their counterparts, the dissimilatory iron reducing bacteria (FeRB), which have been found to coexist with some FeOB in a groundwater iron seep [3] have been studied and characterised intensively in recent years, leading to a good overall understanding of their physiology and the electron transfer mechanisms involved in dissimilatory iron-reduction [4–6]. Several methods have recently been developed to cultivate FeOB on ferrous iron under microaerophilic conditions [1,2,7]. These include gradient plate and gradient tube methods, which replicate the opposing gradients of Fe^{2+} and O_2 that are found in the natural environment of these bacteria [1,7]. Using the gradient plate method with FeS as the source of ferrous iron, *Sideroxydans lithotrophicus* was cultivated under microaerophilic conditions producing an average final optical density at 600 nm (OD_{600}) of 0.0035 after 7-days of growth. Supplementing the growth medium with 0.1% glycerol produced an average final OD_{600} of 0.023. Cell densities were determined after using a new dithionite-based treatment for removing iron from cell samples. The increased cell densities in glycerol-supplemented cultures allowed genomic DNA to be isolated. Amplification and sequence analysis of the *mtoB* gene from genomic DNA confirmed the presence *S. lithotrophicus*. Probing the genome of *S. lithotrophicus* using the CXXCH heme *c* binding motif revealed 33 predicted *c*-type cytochromes. These included MtoA, MtoD and CymA$_{ES-1}$ contained in the *mto* gene cluster in addition to *c*-type cytochromes predicted to belong to *bc*$_1$ and *cbb*$_3$-type cytochrome complexes. This bioinformatics approach in addition to the redox properties of MtoA and MtoD have provided further insight into possible electron transfer mechanisms during lithotrophic growth of *S. lithotrophicus* on iron. MtoA and MtoD remain the most likely candidates as the iron oxidase and periplasmic electron shuttle respectively. An updated model for electron transfer pathways includes predicted quinone reductases cytochrome *bc*$_1$ and CymA$_{ES-1}$ in addition to a *cbb*$_3$-type cytochrome *c* oxidase as the most likely redox partners for MtoD at the inner membrane. Electron transfer pathways are suggested, which might allow *S. lithotrophicus* to generate NADH for CO_2 fixation and ATP for metabolic processes.

5.2 Introduction

The isolation and in vitro cultivation of lithotrophic iron oxidising bacteria (FeOB) has been a significant challenge for microbiologists for many decades. Iron oxidising bacteria were discovered as early as the nineteenth century [8], however the challenging task of cultivating FeOB has precluded research to characterise the biochemistry and physiology of these microorganisms [9,10]. Recent research has revealed the important role iron oxidising lithotrophic growth plays in the biogeochemical cycling of iron in sedimentary environments [11,3,12]. In addition, iron oxidising lithotrophs constitute a significant proportion of bacterial communities in iron-rich sediments, where they have been found to coexist with dissimilatory iron reducing bacteria (FeRB) [3]. While a number of FeRB, such as *Shewanella oneidensis* and *Geobacter sulfurreducens* have been intensely studied, leading to a growing understanding of their biochemistry and physiology, iron oxidising bacteria remain poorly understood. In particular the neutrophilic aerobic FeOB have been neglected due to the challenges involved with growing these organisms on Fe^{2+}, which is rapidly autooxidised under aerobic conditions [10]. Addressing this knowledge gap is essential to developing a more complete understanding of the microbial communities that thrive in iron-rich environments.

Gram-negative neutrophilic FeOB *Sideroxydans lithotrophicus*, which was discovered in iron-rich groundwater in Michigan [7] has been successfully isolated and cultivated in vitro using FeS as a source of Fe^{2+} [1,7]. Cultivation methods have included growth of *S. lithotrophicus* in bioreactors, on FeS gradient plates and in FeS gradient tubes [1]. Iron sulphide plate and tube cultivation methods utilise steep opposing gradients of Fe^{2+} and O_2, which provide *S. lithotrophicus* with a steady flux of Fe^{2+} under microaerobic conditions [1]. Both methods use modified Wolfe's mineral medium (MWMM) as a source of vitamins and minerals (figure 5.1). Using the gradient tube method, Emerson *et al.* (1997) discovered *S. lithotrophicus* has an approximate doubling time of 8-hours, producing a maximum cell density of 10^8 cells.mL^{-1}.
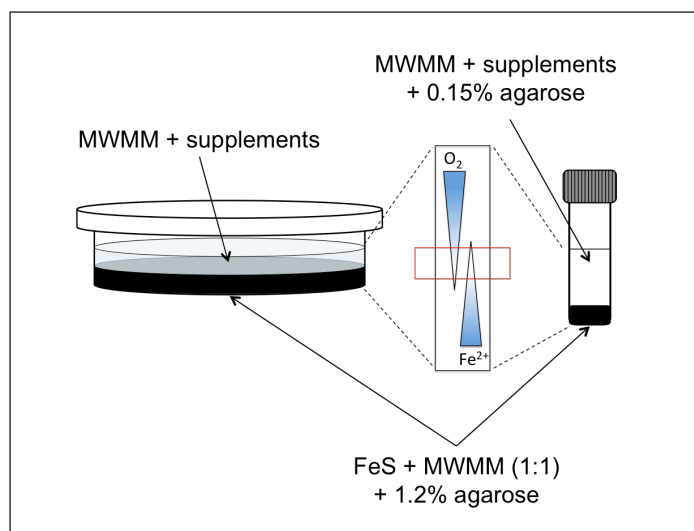
Figure 5.1 Gradient plate vs. gradient tube method for cultivating iron oxidising bacteria. The gradient plate method (left) utilises a solid bottom layer of FeS precipitate mixed 1:1 with modified Wolfe's mineral medium (MWMM) + 1.2% glycerol and a liquid top layer of MWMM with Wolfe's vitamin and mineral supplements. The gradient tube method (right) uses the same bottom layer composition as the gradient plate method, but the top layer is a semi-solid layer produced by adding 0.15% agarose to the MWMM solution used for the plate top layer. Opposing gradients of O_2 from the microaerobic atmosphere used to cultivate the bacteria and Fe^{2+} from the solid layer of FeS (opposing blue arrows) form a redox boundary at the interfacial region of the gradients (red box), where FeOB are able to grow.

Attempts have been made to replace Fe^{2+} as the sole source of energy for growth of *S. lithotrophicus* using various forms of complex media and organic substrates including acetate, pyruvate, succinate, glucose, galactose, ribose, glycerol, aspartate and glycine without success [13]. This evidence is consistent with *S. lithotrophicus* being incapable of heterotrophic growth. However, mixotrophic growth of *S. lithotrophicus* on FeS with organic substrates has not been extensively tested [7].

Despite the challenges involved in cultivating neutrophilic iron-oxidising bacteria, the genome of *S. lithotrophicus* has been sequenced by the Joint Genome Institute, which has allowed some insight into potential metabolic pathways used by this organism [13]. The acquisition of energy for growth from the oxidation of iron is expected to occur at the cell surface, since at circumneutral pH ferric iron reacts with water to precipitate ferric hydroxides, which would be lethal inside the cell. Consequently, the first attempts to probe the electron transfer pathways involved in

iron lithotrophy performed by *S. lithotrophicus* focussed on identifying potential outer membrane oxidases.

The gene pair *mtoAB* was discovered by Shi *et al*, who performed BLAST analysis to search the genome of *S. lithotrophicus* for open reading frames that produced predicted peptide products similar to MtrAB from *S. oneidensis* and PioAB from *R. palustris* TIE-1 [10]. MtrAB from *S. oneidensis* forms a trans-outermembrane complex (figure 1.6 A); MtrA is a decaheme cytochrome that allows electrons to traverse the outer membrane where outer membrane cytochromes on the cell surface perform dissimilatory mineral reduction [14]. MtrA is associated with β-porin MtrB, which holds the complex in the outer membrane. PioAB performs a similar function in the phototrophic iron-oxidising bacterium *R. palustris* TIE-1, except this complex allows electrons to traverse the outer membrane in the opposite direction compared to MtrAB, from ferrous iron into the periplasm (figure 1.6 D) [15]. Identification of a similar predicted protein complex in the genome of *S. lithotrophicus* has presented the most likely pathway by which electrons could enter the cell and allow lithotrophic growth on iron.

Two other predicted *c*-type cytochromes, *mtoD* and *cymA*$_{ES-1}$, were found flanking *mtoAB* with *mtoD* adjacent to and upstream of *mtoA* and *cymA*$_{ES-1}$ adjacent to and downstream of *mtoB* (figure 1.6 E). The conserved arrangement of *mtoAB* in iron-oxidising bacteria including *S. lithotrophicus*, *D. aromatic* and *G. capsiferriformans* ES-2 in addition to the arrangement of homologous *mtrAB* from iron-reducing bacteria such as *S. oneidensis* MR-1, *A hydrophila* and *R. ferrireducens* (figure 2.1) provides evidence of the essential conserved function of these genes in both iron-oxidising and iron-reducing bacteria. The presence of *mtoD* is also conserved in *S. lithotrophicus*, *D. aromatic* and *G. capsiferriformans* ES-2 and hints at a potentially important role for this class I cytochrome *c*.

Recent work performed by Shi *et al.* (2012) has provided an important redox characterisation of MtoA from *S. lithotrophicus*, revealing the first biochemical insights into this organism. MtoA, which was expressed in *S. oneidensis* MR-1, produced a complex voltammetric response typical of a protein with numerous redox-active cofactors, which is expected given MtoA is a predicted decaheme cytochrome [10]. Cyclic voltammetry on MtoA protein films at pH 7 indicate MtoA is redox active between potentials of -400 to +100 mV vs. SHE and is expected to be

more suited to oxidising Fe^{2+} compared to MtrA based on the more positive distribution of the MtoA Faradaic peak area [10] (figure 5.2).
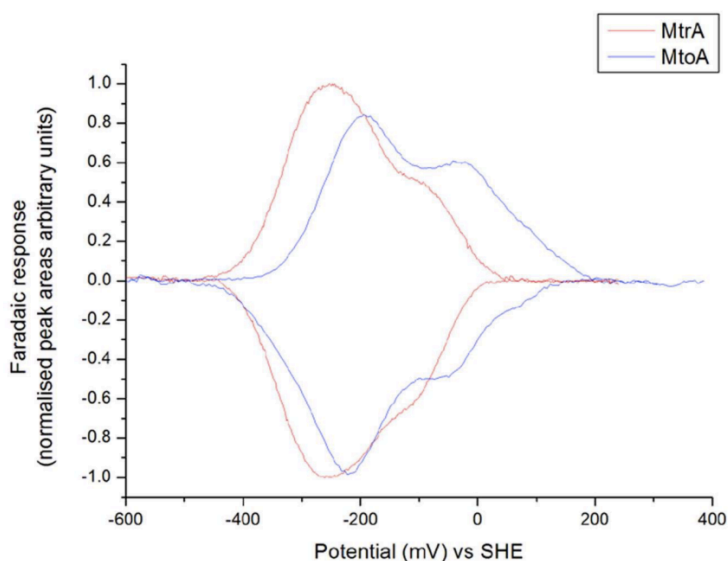
Figure 5.2 Cyclic voltammograms of MtrA and MtoA protein films at pH 7 reveal similar Faradaic responses for decaheme cytochrome MtrA and predicted decaheme cytochrome MtoA. The more positive distribution of the Faradaic response for MtoA (blue) indicates it may be better suited to oxidising the $Fe(OH)_3/Fe^{2+}$ redox couple (-236 mV) compared to MtrA (red) [10]. This figure is presented in Liu *et al.* 2012 and has been copied with written permission from the corresponding author, Dr Liang Shi.

The redox characterisation of MtoD (which was also expressed in *S. oneidensis*) using solution and electrode-based electrochemical methods (chapter 4) indicated electron transfer from MtoA to MtoD would be a favourable process [16]. This supports the current model of electron transfer during lithotrophic growth of *S. lithotrophicus* on iron (chapter 1, figure 1.8 A), which predicts MtoD behaves as an electron shuttle, transferring electrons from MtoA at the outer membrane to $CymA_{ES-1}$ at the inner membrane.

While these redox characterisations provide a useful insight into the potential functions of MtoA and MtoD, there is no experimental evidence yet to support their expression in *S. lithotrophicus*, their cellular localisation or their role in iron-oxidising lithotrophic growth.

Work presented in this chapter aimed to provide a preliminary analysis of the cytochromes expressed by *S. lithotrophicus* grown *in vitro* on FeS using the gradient plate method previously described by Emerson & Floyd (2005). The realistic

objective, given the previously reported low cell densities achieved during cultivation of *S. lithotrophicus*, was to provide an experimental basis for the proposed model of electron transfer in *S. lithotrophicus* during iron lithotrophy.

5.3 Methods

5.3.1 Making FeS gradient plates and culture of *S. lithotrophicus*

Iron sulphide was prepared according to instructions provided with ATCC medium 7266 (MWMM gradient plate medium). 2 x 300 mL volumes of RO-treated water were heated to 50°C in separate 500 mL beakers. 46.2 g $FeSO_4.7H_2O$ and 39.6 g $Na_2S.9H_2O$ were measured and added to one of the 300 mL volumes of water and stirred immediately until the NaS dissolved. This solution was transferred to a 500 mL Durran bottle and the second 300 mL volume of water at 50°C was used to rinse the first beaker and transfer remaining FeS precipitate to the Durran bottle. The bottle was filled to the brim with this water and sealed to avoid abiotic oxidation of FeS by air in the bottle. The FeS precipitate was allowed to settle. To remove traces of sulphur from the bottle, FeS precipitate was washed by pouring away the water and replacing with fresh RO water before allowing the FeS to settle once again. This was performed once per day for 5 days.

The bottom layer of FeS plates was made by aspirating FeS precipitate from the bottom of the Durran bottle and mixing with an equal volume of modified Wolfe's mineral medium (MWMM), which contained 1000 mg.L^{-1} NH_4Cl, 200 mg.L^{-1} $MgSO_4.7H_2O$, 100 mg.L^{-1} $CaCl_2.2H_2O$ and 50 mg.L^{-1} K_2HPO_4 (table 5.1). For the preparation of 10 FeS gradient plates 130 mL of the FeS/MWMM mixture was made and agarose added to a working concentration of 1.2% (w/v).

Media for the top layer of FeS gradient plates was made by adding $NaHCO_3$ to MWMM with a working concentration of 5 mM. For the preparation of 10 plates, 200 mL of top layer media was made. Glycerol supplemented FeS plates were made by adding glycerol to the top layer media at working concentration of 0.1% (v/v). After preparation, top and bottom media components were sterilised by autoclave treatment. The top layer media was immediately placed on ice until the solution was at approximately room temperature before adding 1 μL Wolfe's vitamin solution and Wolfe's mineral solution per 1 mL MWMM (table 5.1). This media was adjusted to

pH 6.0-6.4 by bubbling filter-sterilised CO_2 into the media using an autoclave-sterilised needle. The final pH of the media was tested using pH indicator paper. The bottom layer media was shaken gently to ensure an even distribution of FeS precipitate and pipetted into sterile petri dishes at 10 mL per dish inside a class II microbiological cabinet. After the bottom layer had set, 15 mL of top layer media was pipetted onto the bottom layer.

Plates to be used as negative controls were immediately sealed, while the culture of *Sideroxydans lithotrophicus* ES-1 was initiated by addition of 100 µL *S. lithotrophicus* inoculum into the top layer of plates. FeS plates were stored in petri dish culture jars, which contained a GasPak™ EZ Campy sachet (Becton Dickinson) generating a microaerobic atmosphere (6% ± 2% oxygen and 14% ± 2% CO_2 [17].). The sealed culture jars were stored in the dark to prevent advantageous growth of phototrophic bacteria at room temperature ($22^oC \pm 2^oC$) for 7 days.

Compound	Concentration (mg/L)	Compound	Concentration (mg/L)
Wolfe's mineral solution		*Modified Wolfe's mineral medium (MWMM)*	
Nitrilotriacetic acid	1500	NH_4Cl	1000
$MgSO_4.7H_2O$	3000	$MgSO_4.7H_2O$	200
$MnSO_4.H_2O$	500	$CaCl_2.2H_2O$	100
NaCl	1000	K_2HPO_4	50
$FeSO_4.7H_2O$	100	*Wolfe's vitamin solution*	
$Co(NO_3)_2.6H_2O$	100	Biotin	2
$CaCl_2$	100	Folic acid	2
$ZnSO_4.7H_2O$	100	Pyroxidine hydrochloride	10
$CuSO_4.5H_2O$	10	Thiamine.HCl	5
$AlK(SO_4)_2.12H_2O$	10	Riboflavin	5
H_3BO_3	10	Nicotinic acid	5
$Na_2MoO_4.2H_2O$	10	Calcium D-(+)-pantothenate	5
Na_2SeO_3	1	Vitamin B12	0.1
$Na_2WO_4.2H_2O$	10	p-Aminobenzoic acid	5
$NiCl_2.6H_2O$	20	Thioctic acid	5

Table 5.1 Composition of Modified Wolfe's mineral medium (MWMM), Wolfe's mineral supplement and Wolfe's vitamin solution. Stocks of MWMM, Wolfe's mineral supplement and Wolfe's vitamin solution were stored at 4^oC.

5.3.2 Harvesting cells from FeS gradient plates and removal of ferric precipitates

FeS gradient plates were removed from culture jars after seven days of growth. The 15 mL top layer media was aspirated using an electronic pipette and a sterile 25 mL pipette tip. To maximise the amount of cells collected from plates, the 15 mL of media was aspirated and dispensed 5-10 times to agitate bacteria from the surface of the solid bottom layer. The media was finally dispensed into separate 15 mL screw cap tubes for each plate culture. These tubes were stored vertically for 1 hour at 4°C to allow ferric precipitates to settle to the bottom of the tube.

For the measurement of culture cell density, 1 mL of culture was aspirated from each tube and moved to separate 1.5 mL microcentrifuge tubes. Centrifugation at 13,000 rpm for 1 minute in a microcentrifuge was used to pellet cells and remaining ferric precipitates. Pellets were resuspended in 1 mL solution of anaerobically prepared 50 mg.mL^{-1} sodium dithionite in 50 mM HEPES pH 7 by gently aspirating and dispensing the cell suspension using a 1 mL pipette until the brown coloured ferric precipitates were no longer visible. To wash sodium dithionite from samples, cell suspensions were pelleted by centrifugation at 13,000 rpm for one minute using a microcentrifuge and the pellets were resuspended in 1 mL 50 mM HEPES pH 7 with gentle mixing. Finally, cells were pelleted by centrifugation at 13,000 rpm for one minute then resuspended in 100 μL MWMM, creating an effective 10x concentration of the original cell density. This was required to increase the accuracy of optical density measurements from low original cell densities.

For the preparation of *S. lithotrophicus* inoculum, the remaining culture in the 15 mL tubes was transferred to fresh 15 mL tubes and cells were pelleted by centrifugation at 5,000 *g* for 8 minutes. This method caused remaining ferric precipitates to pellet with the cells. These cell/iron pellets were resuspended in 1 mL MWMM for use as inoculum for a new batch of FeS plates or 1 mL MWMM + 10% glycerol and flash-cooled in liquid nitrogen for storage at -80°C.

5.3.3 Measuring cell density

50 µL of the 100 µL volumes of dithionite-treated and washed cells were transferred to separate wells in a 90-well plate (Nunc®) for measurement of optical density at 600 nm (OD_{600}). Optical density of cell suspensions were measured using a BMG Labtech FLUROstar Omega plate reader.

5.3.4 PCR-amplification and analysis of *mtoB* from *S. lithotrophicus*

S. lithotrophicus culture from 20 FeS gradient plates supplemented with 0.1% glycerol were used for the isolation of genomic DNA. *Sideroxydans* cultures were combined in six 50 mL tubes and ferric precipitates were allowed to settle to the bottom of the tubes as described in 4.3.3. The cell suspensions were transferred to fresh 50 mL tubes and pelleted by centrifugation at 5,000 *g* for 8 minutes. Pellets were resuspended in 1 mL MWMM and the suspensions were transferred to a single 15 mL tube. Cells and ferric precipitates were pelleted by centrifugation at 5,000 *g* for 8 minutes. The pellet was resuspended in 2 mL 50 mg.mL^{-1} sodium dithionite in 50 mM HEPES pH 7 and gently agitated by aspirating and dispensing the suspension. The large amount of ferric precipitates present from combining twenty FeS plates of culture required 3-4 dithionite washes until the brown colour was no longer visible. Each wash was followed by centrifugation to pellet the cell suspension before resuspension in a fresh solution of 2 mL 50 mg.mL^{-1} sodium dithionite. The final wash was performed with 2 mL 20 mM HEPES pH 7 + 50 mM NaCl before pelleting cells by centrifugation at 13,000 rpm.

Genomic DNA was isolated from *S. lithotrophicus* cells using a genomic DNA preparation kit (PureLink®) according to the instructions provided for the isolation of genomic DNA from Gram-negative bacteria. Genomic DNA from *S. lithotrophicus* was quantified by nanodrop analysis. 100 ng of DNA was used as template DNA for the PCR-based amplification of *mtoB* from *S. lithotrophicus* genomic DNA. PCR-based amplification was performed using a 20 µL reaction volume containing 10 µL ES-1 genomic DNA, 4 µL 5x Phusion buffer GC, 0.2 µL Phusion polymerase, 0.4 µL 10 mM dNTPs, 1 µL forward primer, 1 µL reverse primer, 0.6 µL DMSO and 2.8 µL (ES-1) or 10.8 µL (MR-1) molecular biology grade water (table 5.2). Primers

used to amplify the *mtoB* gene fragment were designed using primer-BLAST (appendix, table X5) [18]. The forward and reverse primers for the amplification of *mtoB* had predicted T_M values of 69°C and the calculated gene fragment length expected using these primers was 500 base pairs.

Thirty cycles of PCR were performed using a 20-second, 95°C denaturing step followed by a 40-second annealing step at 64°C and extension at 72°C for 30-seconds (figure 5.3). Initial denaturation was performed at 95°C for 2 minutes and final extension was performed at 72°C for 5 minutes.

Component	Volume (μL)
Phusion buffer GC	4
dNTP mixture (10 mM)	0.4
ES-1 genomic DNA (11 ng/μL)	10
Forward Primer	1
Reverse Primer	1
Phusion polymerase	0.2
DMSO	0.6
H_2O	2.8
Total volume:	20

Table 5.2 Reaction components used in the PCR-based amplification of *mtoB* from the genome of *S. lithotrophicus.* Genomic DNA concentrations *S. lithotrophicus* were determined by nanodrop analysis.

Initial denaturation, 95°C
(2 minutes)

↓

30x
- 95°C (20 seconds)
- 64°C (40 seconds)
- 72°C (30 seconds)

↓

Final extension, 72°C
(5 minutes)
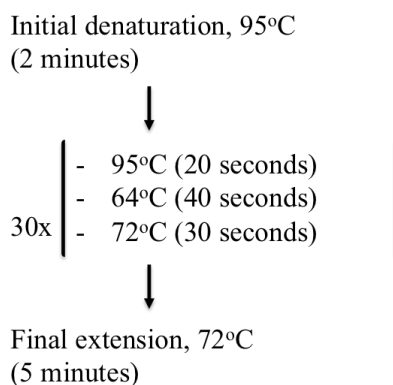
Figure 5.3 PCR program used for the amplification of *mtoB* from the genome of *S. lithotrophicus.*

The results of PCR amplification of *mtoB* was analysed by gel electrophoresis using 1% agarose gels as previously described in section 2.3.1.1. The result was visualised using a UV transilluminator.

5.4 Results

5.4.1 Culturing *Sideroxydans lithotrophicus* using an opposing Fe^{2+}/O$_2$ gradient

Sideroxydans lithotrophicus ES-1 was grown as previously described by Emerson *et al.* (2005) using FeS as a source of ferrous iron in modified Wolfe's mineral medium (MWMM). Creating an environment with low concentrations, but steady flux of dissolved O$_2$ and Fe^{2+} is essential for culturing *Sideroxydans in vitro*. To create an environment capable of supporting growth of *Sideroxydans*, petri dishes were used to create a 'gradient plate' system, which allowed *Sideroxydans* to grow in MWMM with a ferrous iron flux provided by a solid layer of FeS and a stable supply of oxygen available from a microaerobic environment created in a sealed petri dish container.

Gradient plates were composed of two layers: a solid bottom layer containing a 1:1 mixture of FeS and MWMM, which was set using 1.2% agarose (10 mL/petri dish) and a top layer containing a solution of MWMM + 5 mM NaHCO$_3$ (15 mL/petri dish). Wolfe's vitamin solution and trace minerals (ATCC) were added to the top layer MWMM media after autoclave-sterilisation of the stock solution. The solution was adjusted to pH 6.2 $\pm$ 0.5 by bubbling filter-sterilised CO$_2$ through the media to ensure the media would provide near-neutrophilic growth conditions for *S. lithotrophicus*. The approximate pH value was confirmed using pH indicator paper. The top layer of media for each plate was inoculated with 100 µL *Sideroxydans lithotrophicus* (ATCC® 700298™). Inoculum was not added to the '(+) FeS (-) ES-1' plates to be used as negative controls. A batch of gradient plates containing no FeS were inoculated with *Sideroxydans* in parallel and were used as a '(-) FeS (+) ES-1' negative control to confirm bacterial growth occurred as a result of iron oxidation. All gradient plates were stored in a sealed petri dish container with one GasPak™ EZ Campy sachet per ten plates. The GasPak™ EZ Campy sachets generated a microaerobic environment with an approximate atmospheric composition of 6% $\pm$ 2% oxygen and 14% $\pm$ 2% CO$_2$ [17]. Gradient plates were incubated at 22°C $\pm$ 2°C for seven days before harvesting *Sideroxydans* cells from the plate cultures.

Growth of *Sideroxydans* was accompanied by a characteristic flocculation of ferric hydroxides and the formation of an opalescent film on the surface of the top

layer of the plate (figure 5.4), which is consistent with observations made by Emerson *et al.* (2005) during growth of FeOB using this method. By contrast, the abiotic oxidation of ferrous iron in the negative control plates produced a more uniform distribution pattern of ferric hydroxides (figure 5.4).

− ES-1　　　　　　　　　　　　　+ ES-1
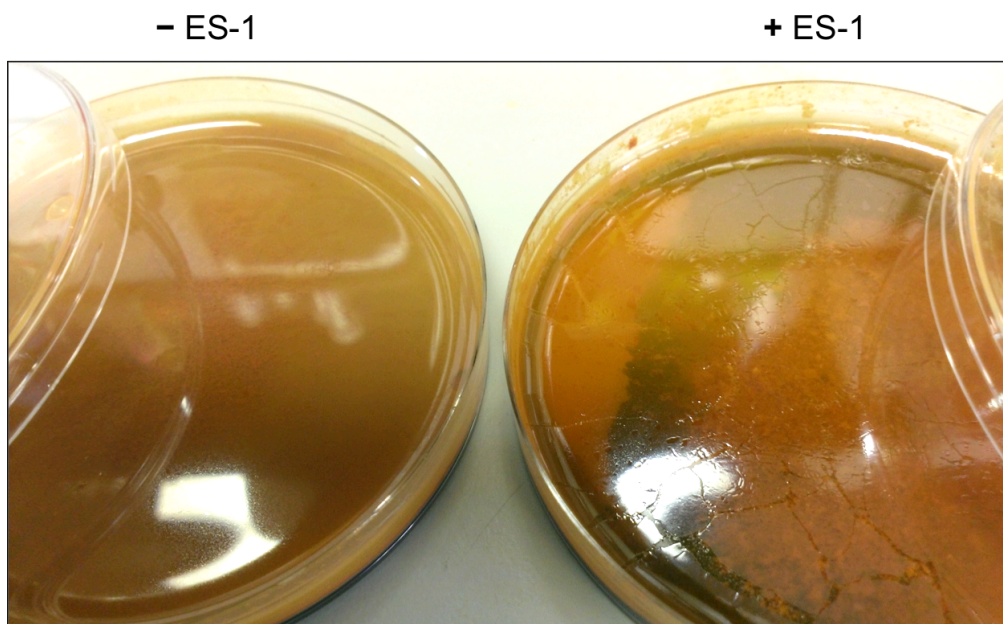
Figure 5.4. Appearance of *S. lithotrophicus* cultures on opposing Fe^{2+}/O_2 gradient plates. Abiotic oxidation of ferrous iron in negative control gradient plates, which were not inoculated with *Sideroxydans* (− ES-1) produced a uniformly distributed ferric iron hydroxide pattern (left). By Contrast, plates that were inoculated with *Sideroxydans* (+ ES-1) produced a characteristic floc of ferric iron hydroxides that was not uniformly distributed and accompanied by an opalescent film on the surface of the top layer (right).

The need to maintain a microaerobic atmosphere prevented the measurement of midpoint cell densities over the course of the seven-day incubation. Instead, an end-point measurement of total cell growth was performed on day seven. The measurement of cell growth was made challenging due to the presence of ferric precipitates in the top layer of the gradient plates. In order to accurately measure cell densities a sodium dithionite wash method was developed to chemically reduce the ferric oxyhydroxides, causing the iron precipitate to dissolve as ferrous iron.

Growth of *Sideroxydans* was performed in triplicate on FeS gradient plates and accompanied by negative controls in triplicate. The 15 mL top layer volume was aspirated and dispensed 5-10 times to agitate the exposed surface of the solid bottom

layer of media. This was performed to disturb *Sideroxydans* cells on the surface, allowing them to be collected. The same procedure was performed on negative controls. The 15 mL of aspirated cell cultures and controls were finally dispensed into separate sterile 15 mL screw-cap tubes. For the measurement of cell growth, 1 mL of the total 15 mL volume was moved to a 1.5 mL microcentrifuge tube. Cells were isolated from the media by centrifugation at 13,000 rpm for 1 minute in a microcentrifuge. To remove ferric precipitate from the cell pellets/controls, the brown-coloured pellets were washed with a 1 mL solution of anaerobically prepared 50 mg.mL^{-1} sodium dithionite in 50 mM HEPES pH 7 by resuspension and gentle mixing until the suspension was no longer a brown colour. Cell/control suspensions were pelleted again by centrifugation at 13,000 rpm using a microcentrifuge. Remaining sodium dithionite was washed from the cells by resuspending the pellets in 1 mL 50 mM HEPES pH 7 and gently mixing before pelleting as previously. Finally, cell pellets were resuspended in 100 µL MWMM. The resuspension volume was 10x smaller than the original volume. This was performed to increase the optical density of samples to improve the accuracy of optical measurements of cell density made by the plate reader (BMG Labtech – FLUROstar Omega).

50 µL of each culture and negative control triplicates were dispensed into a 96-well plate (Nunc®). In addition, three wells were filled with 50 µL MWMM to measure the baseline optical density expected from the 96-well plate and the media component of each sample. Optical density measured in triplicate for the MWMM was nearly identical to that produced by the '(+) FeS (-) ES-1' negative control samples (figure 5.5). The average difference in optical density at 600 nm (OD$_{600}$) of 0.0015 was within the expected instrument error. This suggested the sodium dithionite wash was an effective method for removing iron from samples. The optical measurements were made in aerobic conditions, so any iron present would be expected to precipitate in its oxidised form and produce greater absorption at 600 nm than was observed. Gradient plates containing no FeS produced a slightly higher average OD$_{600}$. The average difference of 0.003 OD units between the two negative controls is most likely a result of the *Sideroxydans* inoculum added to the '(-) FeS (+) ES-1' plates. By contrast, FeS plates inoculated with *Sideroxydans* produced an average OD$_{600}$ of 0.122, which were on average 0.035 OD units higher than observed for the '(+) FeS (-) ES-1' negative control. This difference is consistent with growth of *Sideroxydans*.
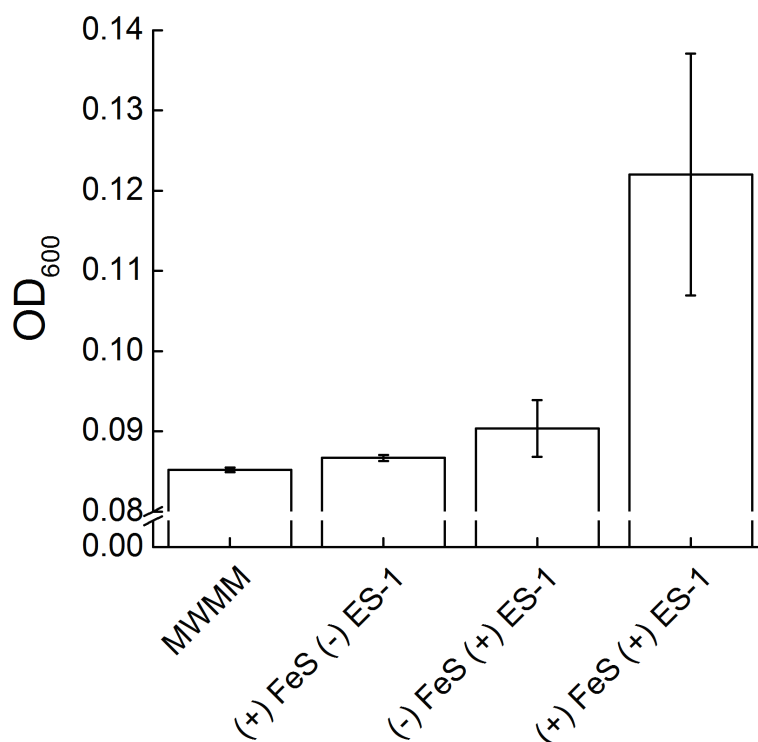
Figure 5.5. Growth of *Sideroxydans lithotrophicus* on FeS gradient plates. The 15 mL top layer of FeS plates was inoculated with 100 μL *Sideroxydans* stock culture and incubated under microaerobic conditions at 22°C ± 2°C for seven days. The measurement of cell growth was performed using optical density at 600 nm (OD_{600}) of 10x concentrated samples. Ferric precipitant was removed by washing cell/iron pellets with a 1 mL solution of 50 mg.mL^{-1} sodium dithionite. Near identical average OD_{600} measurements for MWMM and media aspirated from FeS plates not inoculated with *Sideroxydans* ((+) FeS (-) ES-1) indicated the dithionite wash provided an effective method for removing iron from samples. These controls compared closely with gradient plates lacking FeS that were inoculated with *Sideroxydans* ((-) FeS (+) ES-1), indicating *Sideroxydans* was unable to grow in the absence of FeS. By contrast, gradient plates containing FeS that were inoculated with *Sideroxydans* produced an increase in OD_{600} relative to the negatives controls consistent with growth of *Sideroxydans*.

Taking into account the 10x concentration of cells used to measure growth of *S. lithotrophicus*, the final OD_{600} on FeS gradient plates was on average 0.0035 after seven days of growth. Such low cell density is to be expected given previously reported doubling times of 8-15 hours for iron oxidising bacteria in gradient cultures [1,19]. Cell growth over this duration is consistent with previously reported cell densities of ~10^7 cells.mL^{-1} *Sideroxydans* in liquid culture after 7 days of growth [7]. Nevertheless, the low yield of cells made subsequent genomic or proteomic analysis impossible. To facilitate these goals, in order to confirm the presence of *S.*

lithotrophcius, the MWMM media was further supplemented by addition of 0.1% (v/v) glycerol. Studies of growth characteristics for *Sideroxydans* have revealed the bacterium is unable to oxidise organic substrates as a source of energy [20]. Previous attempts have been made to replace ferrous iron as the sole growth source of *S. lithotrophicus* with more complex media, such as glucose, acetate, glycerol, pyruvate, succinate, ribose or glycine and results indicated these substrates were unable to be the sole growth source [20]. Using sources of organic carbon to supplement the growth of *Sideroxydans* on ferrous iron has not been extensively tested.

5.4.2 Supplemented growth of *Sideroxydans* using FeS + glycerol

Supplementing FeS gradient plates was performed by adding 0.1% (v/v) glycerol to the top layer media. Growth of *Sideroxydans* was determined using nine separate FeS gradient plates for each condition: FeS with no organic supplements and FeS + glycerol. Three FeS plates not inoculated with *Sideroxydans* were used as a negative control; the average OD_{600} for these plates was subtracted from the OD_{600} for the inoculated plates to reveal optical density attributed only to cell biomass. Growth of *Sideroxydans* at room temperature for seven days, as before, yielded greater cell densities for glycerol-supplemented media (figure 5.6). The average optical density measured for glycerol-supplemented cultures was greater than the conventional FeS cultures by a factor of 12.5, indicating the plates with glycerol supplements achieved greater final biomass. While precautions were taken to prepare glycerol-supplemented FeS plates using sterile conditions, without antibiotic selection it is possible bacteria capable of growth on glycerol under microaerobic conditions might have contributed to this increase in observed cell density.
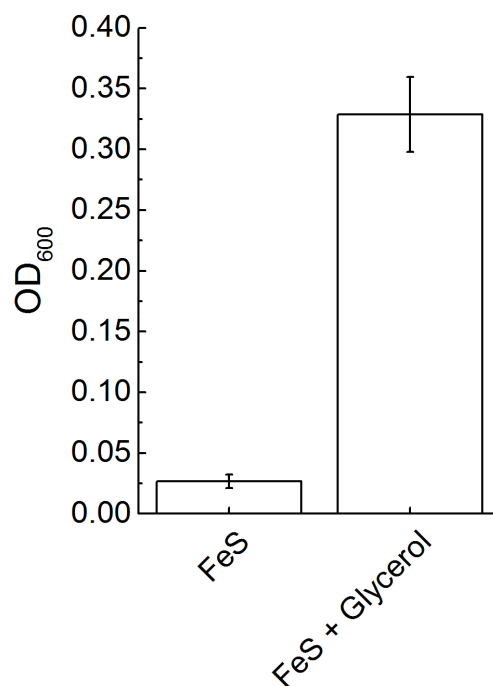
Figure 5.6. Final cell biomass measured for conventional FeS gradient plates compared with glycerol-supplemented plates. Glycerol-supplemented plates were made using MWMM containing 0.1% (v/v) glycerol. Results shown are the average (with standard error) of nine FeS plates made for each growth condition. Optical density measurements at 600 nm (OD_{600}) were performed after removing ferric precipitate by washing with sodium dithionite. Average OD_{600} measurements indicate FeS plates supplemented with glycerol were able to generate greater cell densities and indicates a greater biomass at the end of the 7-day growth period.

5.4.3 Confirming the presence of *S. lithotrophicus* in glycerol-supplemented cultures

To confirm the presence of *S. lithotrophicus* in FeS gradient plate cultures supplemented with glycerol a PCR-based method was used to amplify the *mtoB* gene (*Slit_2496*) from isolated *S. lithotrophicus* chromosomal DNA for gel electrophoresis and sequence analysis. Glycerol-supplemented cultures of *Sideroxydans* were grown at room temperature for seven days as described in section 5.4.2 and cultures were harvested and ferric precipitate removed using dithionite washes as described in section 5.4.1. Cells from five glycerol-supplemented FeS gradient plates were combined and pelleted by centrifugation at 13,000 rpm for 1 minute in a microcentrifuge. Cell lysis and genomic DNA extraction was performed using a genomic DNA preparation kit (PureLink) using cell lysis methods for Gram-negative bacteria. NanoDrop analysis of isolated genomic DNA determined a DNA

concentration of 11 ng.μL^{-1}. 100 ng genomic DNA was used as template for PCR amplification of *mtoB* from the *Sideroxydans* genomic DNA using a 20 μL reaction volume. Gel electrophoresis of PCR products on a 1% agarose gel revealed an approximate product size of 500 base pairs (figure 5.7), which is consistent with the expected product size of 500 base pairs for the *mtoB* gene fragment using *S. lithotrophicus* genomic DNA.
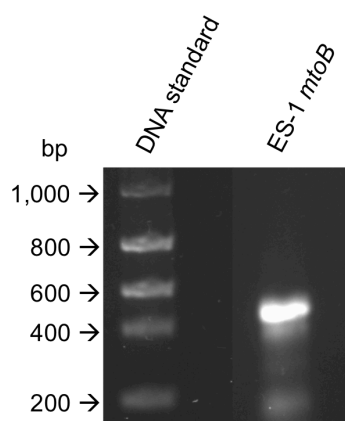
Figure 5.7. Analysis of PCR product sizes by gel electrophoresis indicated the *mtoB* (*Slit_2496*) gene fragment had been successfully amplified from the ES-1 chromosome. 5 μL PCR product was mixed with 1μL 6x loading dye (BioLabs) and gel electrophoresis was performed on a 1% agarose gel. The migration of PCR product on the agarose gel was consistent with the expected result of 500 bp *mtoB*.

Agarose gel electrophoresis was repeated using the same conditions and total PCR product. Product DNA was excised from the 1% agarose gel under UV illumination and extraction of DNA from the gel performed using a gel extraction kit (Qiagen). Sequencing results (Eurofins Genomics) of the extracted PCR product were analysed using BLAST [21] analysis against all non-redundant DNA sequences, which produced a single hit: *Slit_2496* (*mtoB*) from *Sideroxydans lithotrophicus* ES-1. *Slit_2496* gave a sequence identity of 99% over the PCR product region (alignment shown in figure 5.8). Non-identity at positions 1,2 and 3 are due to no nucleotide base being definitively assigned by sequence analysis, while the discrepancy at position 339 could be the result of an amplification error during PCR or a sequencing error. The positive identification of *mtoB*, and absence of sequence similarity with genes from other organisms, confirmed the presence of *S. lithotrophicus* in glycerol-supplemented FeS plate cultures, although it did not provide insight into the purity of the culture.

```
mtoB          tcctatccggcggggacgaattgtgtcgtcgcgcccaagagttatgacaacaagctgggc 1500
PCR_product   ------------------------------------nnganttatgacaacaagctgggc 24
                                                  **  *****************

mtoB          gccacctacaaggccagggcgagcgaggatctgaacctgaatgtgggttattccttcagc 1560
PCR_product   gccacctacaaggccagggcgagcgaggatctgaacctgaatgtgggttattccttcagc 84
              ************************************************************

mtoB          aagcgcgtaacaacctccgatccgaacgcagtcacctctcgcataggattgaacggtaac 1620
PCR_product   aagcgcgtaacaacctccgatccgaacgcagtcacctctcgcataggattgaacggtaac 144
              ************************************************************

mtoB          ctcaacccggctctggctgccgctaccctcatcgagggccagaatggcggggacttccgc 1680
PCR_product   ctcaacccggctctggctgccgctaccctcatcgagggccagaatggcggggacttccgc 204
              ************************************************************

mtoB          gggttctatccggtgttcgatgcttcgcgcaaggaacatatgttgaaggcaggtgcgaac 1740
PCR_product   gggttctatccggtgttcgatgcttcgcgcaaggaacatatgttgaaggcaggtgcgaac 264
              ************************************************************

mtoB          tggcagaccaccgagaaactgtccgtgagcatgggtgggaaatatacgttggacaagtac 1800
PCR_product   tggcagaccaccgagaaactgtccgtgagcatgggtgggaaatatacgttggacaagtac 324
              ************************************************************

mtoB          gactcgacctatggcgagcagaagggcaattcctggagtgtgaacctggatgcaagctac 1860
PCR_product   gactcgacctatggggagcagaagggcaattcctggagtgtgaac--------------- 369
              **************  ****************************
```

Figure 5.8. Alignment of *Slit_2496* (*mtoB*) with the sequencing result of ~500 bp PCR product produced using internal primers for *mtoB* with *Sideroxydans* genomic DNA template. *Slit_2496*, which encodes *mtoB* in *Sideroxydans lithotrophicus*, and the full result of sequence analysis of the predicted *mtoB* gene fragment amplified from *Sideroxydans* genomic DNA by PCR were aligned using Clustal Omega [22].

5.4.4 Probing the *c*-type cytochrome content of *S. lithotrophicus*

Analysis of the *S. lithotrophicus* ES-1 genome using the database search engine MOTIF (www.genome.jp/tools/motif) revealed 77 genes containing the CXXCH motif associated with the presence of a *c*-type heme cofactor. Of these only 33 appeared to be associated with a gene cluster and contained an N-terminal signal sequence that could allow secretion across the inner membrane (table 5.3) as determined by SignalP analysis [23]. The molecular weights of these 33 predicted protein products, including the weight of heme(s) equal to the number of CXXCH motifs identified, were calculated (table 5.3) and used to provide insight into the potential cytochrome content of *S. lithotrophicus*. The predicted cytochromes included *Slit_2495*, *Slit_2497* and *Slit_2498*, which are part of the '*mto*' gene cluster and encode CymA$_{ES-1}$, MtoA and MtoD respectively. Each of these proteins is implicated in electron transfer in the current model of lithotrophic growth of *S. lithotrophicus* on iron (chapter 1, figure 1.8 A).

The similar primary structure of predicted decaheme cytochrome MtoA to decaheme cytochrome MtrA (36% identity; E = 7e-68) from *S. oneidensis* MR-1 gives precedent for consideration of MtoA as an outer membrane electron transport protein. Not only do MtoA and MtrA share similarity, MtoB and MtrB from strain MR-1 share 22% sequence identity (E = 2e-23). The *mtoAB* and *mtrAB* genes can be found in a range of proteobacterial phyla, including the β, α and γ proteobacteria [14,24], where the predicted protein products are implicated in translocation of electrons across the outer membrane either in lithotrophic growth or dissimilatory mineral reduction [6]. The conserved arrangement of the *mtoAB* and *mtrAB* genes and the similar primary structures is consistent with conserved function and suggests MtoAB is the most likely candidate as the outer membrane iron oxidase in *S. lithotrophicus*. The voltammetric characterisation of MtoA by Liu *et al.* (2012), which indicated MtoA could theoretically oxidise the $Fe(OH)_3/Fe^{2+}$ redox couple at circumneutral pH (E = -236 mV) (figure 5.2) supports the role of MtoAB as an outer membrane iron oxidase complex.

At present, MtoD is predicted to shuttle electrons from the outer membrane to the inner membrane of *S. lithotrophicus*. The presence of *mtoD* in the *mto* gene cluster with $cymA_{ES-1}$, *mtoB* and *mtoA* (chapter 2, figure 2.1) makes it possible these genes could be co-expressed. If this is the case, MtoD would be expected to function in an electron transfer process linked to lithotrophic growth on iron. However, there are numerous other small, predicted *c*-type cytochromes that could theoretically perform similar functions. Some of these cytochromes are designated as 'cytochrome *c* class I', while others' have been designated as 'hypothetical proteins' (table 5.3).

Some of the hypothetical proteins contained domains that placed them in a family of cytochromes. For example *Slit_0645*, *Slit_1041* and *Slit_2649* contained domains characteristic of cbb_3-type cytochrome *c* oxidase subunit III. Others', such as *Slit_1015* and *Slit_1323*, which encode predicted small monoheme cytochromes do not possess domains of known function.

Discovering the cytochrome(s) involved in electron shuttling in the periplasm clearly requires an experimental approach to define the cytochrome content of *S. lithotrophicus* cell fractions and the use of knockout mutants to establish phenotypes associated with each cytochrome deletion mutant grown under iron-oxidising conditions. Attempts to investigate the cytochrome content of *S. lithotrophicus* cell lysates using heme-staining produced some promising results (Appendix, figure X3),

however without antibiotic selection or knowledge of the purity of the cell culture it was not possible to present this data as evidence of the cytochrome content of *S. lithotrophicus*.

The current model of electron transfer pathways during lithotrophic growth of *S. lithotrophicus* on iron shows electrons being transferred to $CymA_{ES-1}$ at the inner membrane [24]. $CymA_{ES-1}$ is a predicted tetraheme cytochrome belonging to the NapC/NirT family of quinol dehydrogenases (table 5.3). BLAST analysis of $CymA_{ES-1}$ against the genome of *S. oneidensis* MR-1 revealed the primary structure shares 34% sequence identity with CymA (E = 6e-24) and both contain four CXXCH heme *c* binding motifs. DAS-TMfilter [25] analysis of the $CymA_{ES-1}$ primary structure predicted residues 23-39 form a hydrophobic transmembrane structure (E =1.9e-05), suggesting this protein is anchored at the inner membrane like CymA from *S. oneidensis*. Quinol dehydrogenase CymA gives respiratory flexibility to *S. oneidensis*, where it acts as an electron transport hub, transferring electrons to one of several respiratory pathways depending on the available terminal electron acceptors [26]. It is possible during lithotrophic growth on iron $CymA_{ES-1}$ is able to perform the reverse reaction by reducing quinone at the inner membrane using electrons acquired from the oxidation of ferrous iron [6].

The genome of *S. lithotrophicus* also encodes cytochrome bc_1 (*Slit_0130 − Slit_0132*) and a *cbb3*-type cytochrome *c* oxidase complex (*Slit_0411 − Slit_0416*). Proteins from these complexes containing a *c*-type heme are shown in table 5.3. It is possible electrons carried by MtoD or another periplasmic electron shuttle could be transferred to $CymA_{ES-1}$, cytochrome bc_1 or directly to the *cbb3*-type cytochrome *c* oxidase at the inner membrane.

S. lithotrophicus contains genes encoding SoxA and SoxX (*Slit_1697 & Slit_1700* respectively) (table 5.3), which are present in the *soxXYZAB* gene cluster. This gene cluster shares significant homology with the *soxXYZAB* genes from *Thiobacillus denitrificans*, which are implicated in growth on sulphide or thiosulphate [13]. *S. lithotrophicus* has been previously shown to grow on 5 mM thiosulphate in a mineral salts medium [13], but grew with the same doubling time (8 hr) as observed for growth on $FeCl_2$. Emerson *et al.* (2013) concluded this is most likely because *S. lithotrophicus* is better adapted to growth on iron. Previous attempts to grow *S. lithotrophicus* on sulphide have been unsuccessful [7].

Gene ID	Hemes	Name	Signal	Mwt (Da)	Function
*Slit*_0132	1	Cytochrome c1	19	22,271	Cytochrome bc1
*Slit*_0412	1	Cytochrome c oxidase, cbb3-type, subunit II	TM	30,589	cbb$_3$ oxidase
*Slit*_0414	2	Cytochrome c oxidase, cbb3-type, subunit III	TM	33,629	cbb$_3$ oxidase
*Slit*_0640	5	Hypothetical protein	22	23,628	Unknown
*Slit*_0645	1	Hypothetical protein	19	17,973	Unknown
*Slit*_0868	17	Cytochrome c family protein	25	62,927	Unknown
*Slit*_1014	2	Cytochrome c	28	16,667	Unknown
*Slit*_1015	1	Hypothetical protein	25	13,188	Unknown
*Slit*_1041	1	Hypothetical protein	17	9,887	Unknown
*Slit*_1121	1	Cytochrome c class I	TM	16,731	NO reductase
*Slit*_1129	1	Nitrite reductase (NO-forming)	26	61,153	NO reductase
*Slit*_1323	1	Hypothetical protein	25	13,151	Unknown
*Slit*_1324	2	Diheme Cytochrome c	25	19,788	Unknown
*Slit*_1447	24	Cytochrome c family protein	29	80,476	Unknown
*Slit*_1448	28	Hypothetical protein	21	110,421	Unknown
*Slit*_1468	1	Fibronectin type III domain protein	53	37,543	Unknown
*Slit*_1469	1	Outer membrane autotransporter barrel domain protein	26	182,714	Unknown
*Slit*_1470	3	Hypothetical protein	37	68,462	Unknown
*Slit*_1677	3	Hypothetical protein	18	13,713	Unknown
*Slit*_1697	1	SoxA (sulphur oxidation)	22	29,382	Sulpher oxidation
*Slit*_1700	1	SoxX	24	10,569	Sulphur oxidation
*Slit*_1812	1	Hypothetical protein	19	57,655	Heme copper oxidase
*Slit*_1862	1	Hypothetical protein	26	10,926	Copper efflux
*Slit*_1877	2	Cytochrome C class I	18	21,636	Unknown
*Slit*_1878	2	Cytochrome C class I	22	31,843	Unknown
*Slit*_2495	4	NapC/NirT Cytochrome C domain protein	TM	25,456	CymA$_{ES-1}$
*Slit*_2497	10	Decaheme c-type cytochrome, DmsE family	25	41,522	MtoA
*Slit*_2498	1	Cytochrome C class I	27	10,543	MtoD
*Slit*_2649	1	Hypothetical protein	27	16,142	Unknown
*Slit*_2654	1	Cytochrome C oxidase mono-heme subunit/FixO	44	33,947	cbb$_3$ oxidase
*Slit*_2657	2	Cytochrome C class I	24	26,594	Unknown
*Slit*_2658	1	Hypothetical protein	TM	22,563	Unknown
*Slit*_2693	1	Cytochrome C class I	22	9,352	sulphur metabolism
*Slit*_2694	1	Cytochrome C class I	22	10,964	sulphur metabolism

Table 5.3. Analysis of the *Sideroxydans lithotrophicus* ES-1 genome using the database search engine MOTIF: www.genome.jp/tools/motif. The CXXCH heme-binding motif was used as a search query against all predicted protein products from *Sideroxydans*. 77 genes were identified that encoded polypeptide sequences containing at least one CXXCH motif. Of these, only 33 polypeptide products could be assigned as potential cytochromes contained in a gene cluster and containing either a transmembrane (TM) protein region (determined using DAS-TMfilter server [27]) or an N-terminal signal peptide that would allow entry into the *sec* pathway (determined by SignalP analysis [23]). The molecular weight of each predicted heme-containing protein was determined by subtracting the molecular weight of the signal peptide and adding the molecular weight of a heme cofactor (616.5 Da) multiplied by the number of CXXCH motifs present.

5.5   Discussion and future perspectives

Work presented in this chapter has provided a new method for measuring the growth of iron-oxidising bacteria involving dithionite washes to isolate bacteria from ferric hydroxide precipitates. The growth of *S. lithotrophicus* on FeS gradient plates in modified Wolfe's mineral medium produced cell growth comparable to that previously reported for *S. lithotrophicus* in gradient tubes for 7 days. Supplementing the growth of *S. lithotrophicus* using 0.1% glycerol produced greater cell densities, which allowed the isolation of genomic DNA.

Previous studies, which have attempted to replace ferrous iron with organic substrates for growth, suggest that *S. lithotrophicus* is an obligate lithotrophic organism. These studies were extended to investigate the growth of *S. lithotrophicus* on Fe^{2+} supplemented with acetate. However, no other organic supplements were tested [7]. The observed increase in cell density in *S. lithotrophicus* cultures grown on FeS + glycerol compared to FeS alone could be the first evidence *S. lithotrophicus* has the ability to co-metabolise glycerol when grown on FeS. However, the inability to select for *S. lithotrophicus* using antibiotics presently prevents any conclusive findings since the growth of contaminants with the ability to grow on glycerol under microaerobic conditions could theoretically have increased cell density in exactly the same way; *E. coli*, for example is capable of such growth [28].

The successful amplification of *mtoB* and sequence analysis confirmed *S. lithotrophicus* was present in glycerol-supplemented FeS cultures. However, it was not possible to establish the purity of cultures due to there being insufficient cells and chromosomal DNA to perform subsequent molecular biology experiments.

The next logical continuation of this project would use denaturing gradient gel electrophoresis of amplified 16s rDNA to provide a genetic fingerprint of the glycerol-supplemented FeS cultures. This would establish the purity of the cultures and enable further research to provide more robust conclusions, in particular whether *S. lithotrophicus* is able to utilise organic substrates as growth supplements. In the medium-to-long term future, work to develop a technique for producing recombinant *S. lithotrophicus* cells with antibiotic resistance is important for the scientific community investigating neutrophilic iron-oxidising bacteria as a whole. If *S. lithotrophicus* is capable of using organic substrates as growth supplements, the use

of antibiotics could allow supplemented growth methods to accelerate growth and increase achievable cell densities under selective conditions. The close genetic relationship between *S. lithotrophicus* ES-1 and *G. capsiferriformans* ES-2 [20] means a greater understanding of the biochemistry and physiology of *S. lithotrophicus* could concurrently provide useful insights into the lithotrophic metabolism of both of these and potentially other neutrophilic iron-oxidising bacteria.

At present, work to characterise the biochemistry of lithotrophic growth of *S. lithotrophicus* continues to be hindered by the slow growth and low achievable cell densities using FeS as an energy source under microaerobic conditions. Assuming MtoA and MtoD are expressed from the *mto* gene cluster under iron-oxidising growth conditions, insight provided by the redox characterisation of these proteins provides useful information with which to speculate electron transfer pathways during lithotrophic growth.

Redox characterisation of predicted decaheme cytochrome MtoA by Liu *et al.* (2012), shown in figure 5.2, indicates MtoA is redox-active over a potential range that would allow the MtoAB trans-outer membrane heterocomplex to oxidise iron at the cell surface. Unlike *S. oneidensis*, *S. lithotrophicus* lacks predicted outer membrane cytochromes to perform iron oxidation. Previous studies on MtrAB proteoliposomes have shown that the electron conduit from *S. oneidensis* is capable of reducing and oxidising iron substrates with MtrC absent, although reduction of insoluble iron minerals was not possible [29]. The outer membrane cytochrome modules from *Shewanella* species' (MtrC, MtrF, OmcA & UndA) are necessary for the reduction of ferric iron minerals, but not for the oxidation or reduction of soluble iron species'. Given the similarity between the primary structures of MtrAB and MtoAB, these previous observations indicate the MtoAB complex alone is capable of performing iron oxidation at the cell surface of *S. lithotrophicus*, as proposed in the current model of electron transfer in *S. lithotrophicus* (chapter 1, 1.8 A).

The MtoD heme redox potential in solution (+150 mV) and the dominant redox potential at the electrode surface (between +45 mV and +85 mV) indicate electron transfer from MtoA to MtoD would be a favourable process. However, the destination for electrons at the inner membrane is not clear. CymA$_{ES-1}$ is the proposed recipient of electrons during lithotrophic iron growth in the current model of electron transfer in *S. lithotrophicus* [10,24].

The best-studied example of electron transfer pathways during lithotrophic growth on iron is from *Acidothiobacillus ferroxydans* [30,31]. The electron transfer pathway determined for *A. ferroxydans*, similar to *S. lithotrophicus*, includes an outer membrane iron oxidase, which translocates electrons from ferrous iron at the cell surface to the periplasm. The periplasmic copper-containing protein rusticyanin (RcY) and cytochromes CYC 1 and CYC 42 are linked to two electron transfer pathways; CYC 1 performs the thermodynamically favourable reduction of cytochrome *c* oxidase, while CYC 42 performs the thermodynamically unfavourable reduction of the quinone pool via cytochrome bc_1 [31]. The second, thermodynamically unfavourable electron transfer pathway supplies NADH dehydrogenase with electrons from the Q-pool, enabling the protein to run in reverse to reduce NAD^+ to NADH, which is required for the fixation of CO_2 [32].

As a lithoautotrophic organism, *S. lithotrophicus* faces the same problem and must drive electron transfer in an 'uphill', thermodynamically unfavourable direction in order to generate NADH. Unlike *A. ferroxydans*, *S. lithotrophicus* does not contain genes encoding CYC 1 or CYC 42, which enables *A. ferroxydans* to supply electrons to two distinct electron transfer pathways at the inner membrane. Instead, *S. lithotrophicus* contains only MtoD as the predicted periplasmic electron transfer protein and three potential redox partners at the inner membrane: $CymA_{ES-1}$, cytochrome bc_1 and a *cbb*$_3$-type cytochrome *c* oxidase.

$CymA_{ES-1}$ is predicted to function as a quinone reductase; the homologous CymA from *Shewanella oneidensis* MR-1 has been shown to be specific for menaquinone (MQ) over ubiquinone (UQ) [33]., it seems unlikely MtoD heme, with a reduction potential of +155 mV in solution at pH 7, is low enough to provide electrons to the significantly more reducing MQ/MQH_2 redox couple ($E^o = -70$ mV) via $CymA_{ES-1}$. This makes the role of $CymA_{ES-1}$ in the current electron transfer model somewhat ambiguous. The presence of genes encoding cytochrome bc_1 in the genome of *S. lithotrophicus* makes electron transfer from MtoD to bc_1 a potential alternative route to supplying electrons to the quinol pool. Cytochrome bc_1, if run in reverse as in *A. ferroxydans* [31], would perform the reduction of ubiquinone to ubiquinol (UQH_2) ($E^o = +100$ mV). The potential of the UQ/UQH_2 redox couple is higher than that of MQ/MQH_2 and is only slightly lower than the reduction potential of the MtoD heme in solution (+155 mV). Electron transfer from MtoD to cytochrome bc_1 would therefore be a more thermodynamically favourable route to

supplying the quinol pool with electrons. Overall, electrons supplied by MtoD for the generation of NADH by a reverse-functioning NADH dehydrogenase represents an energetically 'uphill' process via both the CymA$_{ES-1}$ and bc_1 routes. The presence of *cymA$_{ES-1}$* immediately downstream of the conserved *mto* gene cluster (*mtoDAB* − chapter 2, figure 2.1) [24] makes co-expression of *cymA$_{ES-1}$* with the *mto* genes a possibility and would potentially involve CymA$_{ES-1}$ in NADH generation at the inner membrane of *S. lithotrophicus*. Without evidence of CymA$_{ES-1}$ or cytochrome bc_1 expression in *S. lithotrophicus* or redox properties of these proteins it is difficult to speculate whether or not electron transfer to these inner membrane cytochromes could provide a mechanism for modulating NADH production with the generation of ATP.

Modulating electron transfer to the energetically uphill and downhill pathways is likely to be important for regulation of ATP vs. NADH production using electrons acquired from the oxidation of extracellular iron. Roger *et al.* (2012) estimated 90% of electrons acquired from the oxidation of Fe^{2+} by *A. ferroxydans* are supplied via the downhill (CYC 1) pathway to cytochrome *c* oxidase, providing a small PMF for the generation of ATP, while 10% of electrons were supplied via the uphill (CYC 42) pathway to cytochrome bc_1 and UQ for the generation of NADH for anabolic processes [31]. While this modulation in *S. lithotrophicus* could be at the level of CymA$_{ES-1}$ vs. bc_1-mediated reduction of the quinol pool, it is also possible that modulation of the MtoD heme potential as a result of specific protein-protein interactions could provide a separate mechanism for regulating electron transfer at the inner membrane of *S. lithotrophicus*.

The nature of the negative midpoint potential shifts for MtoD-Strep films compared to the +155 mV reduction potential of the MtoD-Strep heme in solution (Chapter 4, figures 4.10, 4.11 & 4.21) is not known. If an interaction-induced conformational change were assumed to have been the cause for the unusual redox behaviour of MtoD films as has been observed previously [34], this would raise the question of whether the negative shift of the +155 mV reduction potential of MtoD-Strep in solution to +75 mV and −230 mV for MtoD-Strep films could be relevant in the context of protein-protein interactions in *S. lithotrophicus*. For example, changes to the MtoD heme environment upon interaction with CymA$_{ES-1}$ or cytochrome bc_1 might allow a negative shift of the heme potential, allowing a more thermodynamically favourable electron transfer to these proteins at the inner

membrane of *S. lithotrophicus*. Excluding the negative shift from +155 to −230 mV, since this low potential has previously been associated with protein denaturation using electrodes [34], the negative shift from +155 mV to +75 mV would theoretically allow favourable electron transfer to occur from MtoD to UQ via cytochrome bc_1.

Analysis of the crystal structure of MtoD-Strep (4XXL)[16] revealed the heme cofactor is highly exposed and appears to be accessible from two distinct sites (Chapter 3, figure 3.17). Such an exposed heme cofactor is likely to be sensitive to changes in its local environment, such as those caused by protein-protein interactions, making it possible MtoD might be able to reversibly alter its heme potential to allow a more thermodynamically favourable electron transfer to cytochrome bc_1 and possibly to CymA$_{ES-1}$. Such behaviour would be consistent with the physiological role of class I cytochromes *c*, which are involved in electron transfer between distinct redox partners. Mitochondrial cytochrome *c* for example shuttles electrons from cytochrome bc_1 to cytochrome *c* oxidase and there is evidence that interactions between mitochondrial cytochrome *c* and it's redox partners induces conformational changes that result in an altered cytochrome *c* heme redox potential [35–37].

While an interaction-induced conformational change is perhaps the most likely cause for the difference between the MtoD-Strep heme potential in solution vs. electrode-adsorbed protein films, the possibility of a ligand switch has not been ruled out. The 5.3 Å proximity of His78 to the iron-coordinating nitrogen atom of His95 (chapter 4, figure 4.22) makes it possible a conformational change to the heme pocket of MtoD might allow His95 to be displaced by His78. Despite the small distance between His95 and His78, a ligand switch would be expected to result from a significant change to the conformation of MtoD around the heme pocket and would equally be expected lead to significant changes to the heme environment, which might account for the large negative potential shift from the +155 mV solution potential to the -230 mV redox transformation observed for MtoD-Strep films. Further experiments would be required to investigate this.

Characterising the redox response of a H78F mutant of SnO$_2$-adsorbed MtoD films would theoretically provide an answer to this uncertainty, since unlike histidine, phenylalanine lacks the necessary nitrogen atom to form a coordinate bond to the heme iron, preventing a ligand switch to this residue. In addition, redox and spectroscopic characterisation of a H95F mutant of MtoD would provide insight into

whether His78 is able to replace His95 as the distal heme ligand and cause the potential of the MtoD heme to become significantly lower than its +150 mV solution potential. Failure of His78 to form a ligand to the heme iron in a H95F mutant would produce a pentacoordinate heme, which would be apparent in differences to UV/Vis spectra.

Electron transfer directly from MtoD (+150 mV) to the *cbb₃*-type cytochrome *c* oxidase complex, which reduces molecular oxygen to water (+816 mV), is a thermodynamically favourable process and would allow the cell to generate a small PMF to drive the generation of ATP (figure 5.9). The presence of two potential binding sites that allow access to the heme cofactor of MtoD (chapter 3, figure 3.17) might allow MtoD to form distinct binding interfaces with the *cbb₃*-type cytochrome *c* oxidase compared to its other predicted redox partners. The clustering of lysine residues around the putative MtoD binding sites (chapter 3, figure 3.20) supports an electrostatic interaction-based interface between MtoD and its redox partners. Electrostatic interactions involving lysine residues of class I cytochromes *c* and glutamate/aspartate residues of cytochrome *c* oxidases are widely recognised to be important for the interaction between these two redox partners [35,38–40]. It's possible the positioning of lysine residues might be a factor in creating specificity between the putative MtoD binding sites and its redox partners. The conservation of lysine residues positioned around the thiolated heme edge in MtoD (figure 3.21 B) for example hints at a conserved binding site.

Electron transfer to *cbb₃*-type cytochromes does not generate NADH, which is required for the fixation of CO_2 [30]. It is possible the uphill and downhill pathways are linked and the delicate balance of providing electrons for the generation of NADH via the endergonic $CymA_{ES-1}$/*bc₁* pathways is coupled the generation of a PMF via the exergonic electron transfer pathway from MtoD to the *cbb₃* complex (figure 5.9).

The exergonic electron transfer pathway to *cbb₃* generates a PMF of $4H^+$ per molecule of O_2 reduced to H_2O [41] (figure 5.9). However, this PMF alone is unlikely to be able to support the generation of ATP and provide the necessary energy to drive the uphill electron transfer and reduction of the quinol pool and NADH.
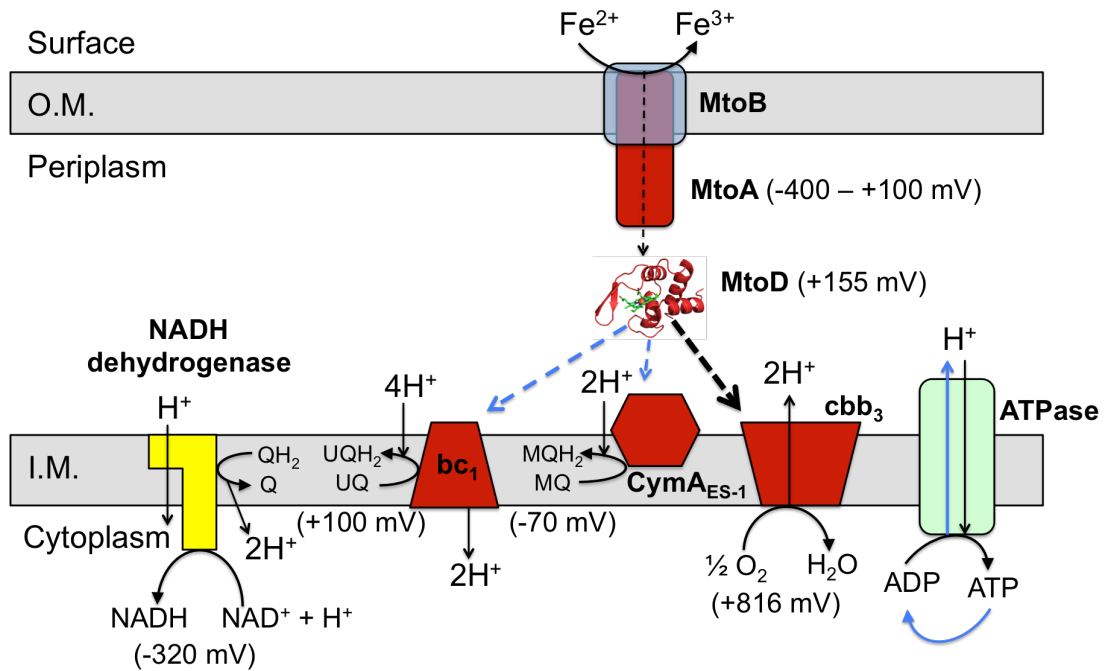
Figure 5.9 Revised model of electron transfer pathways during lithotrophic growth of *S. lithotrophicus* on iron. MtoAB functions as the iron oxidase in *S. lithotrophicus*, translocating electrons from the cell surface to the periplasm. MtoD is expected to shuttle electrons from MtoA to inner membrane redox partners. Direct electron transfer from MtoD (E^o = +155 mV) to the cbb_3-type cytochrome c oxidase for oxygen reduction (E^o = +816 mV) is thermodynamically favourable and theoretically produces a PMF of $4H^+/O_2$ [41]. However, electron transfer from MtoD to predicted quionone reductases $CymA_{ES-1}$ and cytochrome bc_1 presents an unfavourable (uphill) electron transfer. ATP hydrolysis could potentially contribute to the PMF as proposed by Elbehti *et al.* (2012). A combination of ATP hydrolysis and direct electron transfer to cbb_3 might produce a PMF sufficient to allow $CymA_{ES-1}$ and/or bc_1 to run in reverse to reduce the Q pool and facilitate the generation of NADH using endergonic electron transfer from MtoD (blue arrows).

In addition to the generation of a PMF via cytochrome c oxidase, Elbehti *et al.* (2000) proposed a second biochemical mechanism that might allow the generation of a greater PMF to support the reduction of reducing equivalents such as NADH in *A. ferroxydans*. This mechanism involves the hydrolysis of ATP to ADP and the reverse-functioning of the ATPase protein complex to pump electrons across the inner membrane into the periplasm [30]. The regulation of this putative mechanism was proposed to be at the level of ATP substrate concentrations [30,31].

It is possible a similar mechanism could function to regulate electron transfer for ATP/NADH generation during lithotrophic growth of *S. lithotrophicus* [16]. With a sufficient PMF to drive the reduction of quinones via $CymA_{ES-1}/bc_1$, NADH could be generated for the fixation of CO_2, providing carbon-based precursors for cellular

metabolism in *S. lithotrophicus*, for which ATP is required. However, as the PMF becomes depleted, the cell would be unable to fix carbon and consequently the requirement for ATP to drive metabolic processes would decrease. This would theoretically lead to ATP becoming available for hydrolysis by ATPase, which would replenish the PMF. The complex balance between ATP and NADH generation might allow *S. lithotrophicus* to utilise energy from iron oxidation efficiently, but could explain the slow growth of *S. lithotrophicus*.

It is possible MtoD could function as an important regulatory protein in electron transfer to inner membrane cytochromes during lithotrophic growth of *S. lithotrophicus* on iron. However, biochemical analyses of the proteins and protein complexes shown in figure 5.9 is required to provide insight into the true redox partners of MtoD. Assuming MtoD forms stable interactions with its partners, redox characterisation is required to verify whether or not the ~-230 mV redox transformation observed for MtoD-Strep films is physiologically relevant. Negative shifts in the midpoint potential of class I cytochrome *c* hemes adsorbed to electrodes has been reported previously [42,43]. Therefore it is important to establish whether similar behaviour accounts for the appearance of a low-potential redox transformation in MtoD films, or whether this low-potential redox feature occurs as a result of a physiologically relevant interaction-induced conformational change. Purifying the likely redox partners of MtoD and performing biophysical and redox characterisations of the potential partners and MtoD in complex with these partners could provide a clearer insight into electron transfer pathways involved in lithotrophic growth of *S. lithotrophicus* on iron. In turn, this could provide exciting new insights into the previously uncharacterised biochemical mechanisms that allow *S. lithotrophicus* and numerous other neutrophilic iron oxidising bacteria to grow.

5.6   References

1.   Emerson, D. & Floyd, M. M. Enrichment and isolation of iron-oxidizing bacteria at neutral pH. *Methods Enzymol.* **397,** 112–23 (2005).

2.   Summers, Z. M., Gralnick, J. A. & Bond, D. R. Cultivation of an Obligate Fe (II)-Oxidizing Lithoautotrophic Bacterium Using Electrodes. *MBio* **4,** (2013).

3.   Roden, E. E. *et al.* The microbial ferrous wheel in a neutral pH groundwater seep. *Front. Microbiol.* **3,** 1–18 (2012).

4.   Liu, Y. *et al.* A trans-outer membrane porin-cytochrome protein complex for extracellular electron transfer by G eobacter sulfurreducens PCA. *Environ. Microbiol. Rep.* **6,** 776–785 (2014).

5.   Shi, L. *et al.* The roles of outer membrane cytochromes of Shewanella and Geobacter in extracellular electron transfer. *Environ. Microbiol. Rep.* **1,** 220–227 (2009).

6.   Shi, L. *et al.* Molecular Underpinnings of Fe(III) Oxide Reduction by Shewanella Oneidensis MR-1. *Front. Microbiol.* **3,** 50 (2012).

7.   Emerson, D. & Moyer, C. Isolation and characterization of novel iron-oxidizing bacteria that grow at circumneutral pH. *Appl. Environ. Microbiol.* **63,** 4784–4792 (1997).

8.   Cullimore, D. & McCann, A. in *Aquat. Microbiol.* (Skinner, F. & Shewan, J.) 219–261 (London: Academic Press, 1978).

9.   Summers, Z. M., Gralnick, J. a. & Bond, D. R. Cultivation of an Obligate Fe (II) -Oxidizing Lithoautotrophic. *MBio* **4,** 1–5 (2013).

10.   Liu, J. *et al.* Identification and Characterization of MtoA: A Decaheme c-Type Cytochrome of the Neutrophilic Fe(II)-Oxidizing Bacterium Sideroxydans lithotrophicus ES-1. *Front. Microbiol.* **3,** 37 (2012).

11.   Blöthe, M. & Roden, E. E. Microbial iron redox cycling in a circumneutral-pH groundwater seep. *Appl. Environ. Microbiol.* **75,** 468–473 (2009).

12.   Roden, E. E., Sobolev, D., Glazer, B. & Luther, G. W. Potential for Microscale Bacterial Fe Redox Cycling at the Aerobic-Anaerobic Interface. *Geomicrobiol. J.* **21,** 379–391 (2004).

13.   Emerson, D. *et al.* Comparative genomics of freshwater Fe-oxidizing bacteria: implications for physiology, ecology, and systematics. *Front. Microbiol.* **4,** 254 (2013).

14.   Hartshorne, R. S. *et al.* Characterization of an electron conduit between bacteria and the extracellular environment. *Proc. Natl. Acad. Sci. U. S. A.* **106,** 22169–74 (2009).

15.   Jiao, Y. & Newman, D. K. The pio operon is essential for phototrophic Fe(II) oxidation in Rhodopseudomonas palustris TIE-1. *J. Bacteriol.* **189,** 1765–1773 (2007).

16.   Beckwith, C. R. *et al.* Characterization of MtoD from Sideroxydans lithotrophicus: a cytochrome c electron shuttle used in lithoautotrophic growth. *Front. Microbiol.* **6,** (2015).

17.   Van Horn, K. & Tóth, C. Evaluation of the AnaeroPack Campylo system for growth of microaerophilic bacteria. *J. Clin. Microbiol.* **37,** 2376–2377 (1999).

18.   Ye, J. *et al.* Primer-BLAST: A tool to design target-specific primers for polymerase chain reaction. *BMC Bioinformatics* **13,** 134 (2012).

19.   Emerson, D. *et al.* A novel lineage of proteobacteria involved in formation of marine Fe-oxidizing microbial mat communities. *PLoS One* **2,** (2007).

20.   Emerson, D. *et al.* Comparative genomics of freshwater Fe-oxidizing bacteria: implications for physiology, ecology, and systematics. *Front. Microbiol.* **4,** 254 (2013).

21.   Madden, T. The BLAST sequence analysis tool. *BLAST Seq. Anal. Tool* 1–17 (2013). at <http://www.ncbi.nlm.nih.gov/books/NBK153387/>

22.   Sievers, F. *et al.* Fast, scalable generation of high-quality protein multiple sequence alignments using Clustal Omega. *Mol. Syst. Biol.* **7,** (2011).

23.   Petersen, T. N., Brunak, S., von Heijne, G. & Nielsen, H. SignalP 4.0: discriminating signal peptides from transmembrane regions. *Nat. Methods* **8,** 785–786 (2011).

24.   Shi, L., Rosso, K. M., Zachara, J. M. & Fredrickson, J. K. Mtr extracellular electron-transfer pathways in Fe(III)-reducing or Fe(II)-oxidizing bacteria: a genomic perspective. *Biochem. Soc. Trans.* **40,** 1261–7 (2012).

25.   Cserzo, M., Eisenhaber, F., Eisenhaber, B. & Simon, I. TM or not TM: Transmembrane protein prediction with low false positive rate using DAS-TMfilter. *Bioinformatics* **20,** 136–137 (2004).

26.   Marritt, S. J. *et al.* A functional description of CymA, an electron-transfer hub supporting anaerobic respiratory flexibility in Shewanella. *Biochem. J.* **444,** 465–74 (2012).

27.   Cserzö, M., Eisenhaber, F., Eisenhaber, B. & Simon, I. On filtering false positive transmembrane protein predictions. *Protein Eng.* **15,** 745–752 (2002).

28.   Durnin, G. *et al.* Understanding and harnessing the microaerobic metabolism of glycerol in Escherichia coli. *Biotechnol. Bioeng.* **103,** 148–161 (2009).

29.   White, G. F. *et al.* Rapid electron exchange between surface-exposed bacterial cytochromes and Fe(III) minerals. *Proc. Natl. Acad. Sci. U. S. A.* **110,** 6346–51 (2013).

30.   Elbehti, A., Brasseur, G. & Lemesle-Meunier, D. First Evidence for Existence of an Uphill Electron Transfer through the bc1 and NADH-Q Oxidoreductase Complexes of the Acidophilic Obligate Chemolithotrophic Ferrous Ion-Oxidizing Bacterium Thiobacillus ferrooxidans. *J. Bacteriol.* **182,** 3602–3606 (2000).

31.   Roger, M. *et al.* Mineral respiration under extreme acidic conditions: from a supramolecular organization to a molecular adaptation in Acidithiobacillus ferrooxidans. *Biochem. Soc. Trans.* **40,** 1324–9 (2012).

32.   Shively, J. M., van Keulen, G. & Meijer, W. G. Something from almost nothing: carbon dioxide fixation in chemoautotrophs. *Annu. Rev. Microbiol.* **52,** 191–230 (1998).

33.   McMillan, D. G. G., Marritt, S. J., Butt, J. N. & Jeuken, L. J. C. Menaquinone-7 is specific cofactor in tetraheme quinol dehydrogenase CymA. *J. Biol. Chem.* **287,** 14215–14225 (2012).

34.   Khare, N., Lovelace, D. M., Eggleston, C. M., Swenson, M. & Magnuson, T. S. Redox-linked conformation change and electron transfer between monoheme c-type cytochromes and oxides. *Geochim. Cosmochim. Acta* **70,** 4332–4342 (2006).

35.   Witt, H., Malatesta, F., Nicoletti, F., Brunori, M. & Ludwig, B. Cytochrome-c-binding site on cytochrome oxidase in Paracoccus denitrificans. *Eur. J. Biochem.* **251,** 367–373 (1998).

36.   Cruciat, C. M., Brunner, S., Baumann, F., Neupert, W. & Stuart, R. a. The cytochrome bc1 and cytochrome c oxidase complexes associate to form a single supracomplex in yeast mitochondria. *J. Biol. Chem.* **275,** 18093–18098 (2000).

37.   Dick, L. a., Haes, A. J. & Van Duyne, R. P. Distance and Orientation Dependence of Heterogeneous Electron Transfer: A Surface-Enhanced Resonance Raman Scattering Study of Cytochrome c Bound to Carboxylic Acid Terminated Alkanethiols Adsorbed on Silver Electrodes. *J. Phys. Chem. B* **104,** 11752–11762 (2000).

38.   Sampson, V. & Alleyne, T. Cytochrome c/cytochrome c oxidase interaction. Direct structural evidence for conformational changes during enzyme turnover. *Eur. J. Biochem.* **268,** 6534–6544 (2001).

39.   Döpner, S. *et al.* The structural and functional role of lysine residues in the binding domain of cytochrome c in the electron transfer to cytochrome c oxidase. *Eur. J. Biochem.* **261,** 379–91 (1999).

40.   Rieder, R. & Bosshard, H. R. Comparison of the binding sites on cytochrome c for cytochrome c oxidase, cytochrome bc1, and cytochrome c1. Differential acetylation of lysyl residues in free and complexed cytochrome c. *J. Biol. Chem.* **255,** 4732–4739 (1980).

41.   Rauhamaki, V., Bloch, D. a. & Wikstrom, M. Mechanistic stoichiometry of proton translocation by cytochrome cbb3. *Proc. Natl. Acad. Sci.* **109,** 7286–7291 (2012).

42.   Hinnen, C., Parsons, R. & Niki, K. Electrochemical and spectroreflectance studies of the adsorbed horse heart cytochrome c and cytochrome c3 from D. Vulgaris, miyazaki strain, at gold electrode. *J. Electroanal. Chem. Interfacial Electrochem.* **147,** 329–337 (1983).

43.   Matsuda, N., Santos, J. H., Takatsu, A. & Kato, K. Spectroelectrochemical studies on surface immobilized cytochrome c on ITO electrode by slab optical waveguide spectroscopy. *Thin Solid Films* **438-439,** 403–406 (2003).

Appendix

Primer name	Primer sequence	T$_M$ (°C)
*mtoD*_1_F	ATG ACT CGT CAA GCT TAT TCC TCA ATG TTG	71
*mtoD*_R_6His	CTA GTG GTG GTG GTG GTG GTG GAG CGA AAG GAT C	82
*mtoD*_2_F	CAC CTA AGA AGG AGA TAT ACA TCC CAT GAC TCG TCA AGC TTA TTC	77
*mtoD*_SII_F	AAT TCG AGA AGT AGA AGG GCG AGC TCA AGC TTG AAG GTA	79
*mtoD*_SII_R	GTG GAT GAG ACC AGA GCG AAA GGA TCC AGT CCA CAG G	84
MJE_PBAD_F	GGT CAG TTG AAA GAG TTC CTC GAC GC	72

T$_M$ = melting temperature; T$_M$ values were estimated using the New England BioLabs T$_M$ calculator

Table X1. Primers used for PCR amplification, modification and sequencing of *mtoD*. Primer *mtoD*_1_F contains the 5' end sequence of *mtoD* and primer *mtoD*_R_6His contains reverse complementary sequence to the 3' end of *mtoD* with a 6x GTG repeat coding for a His tag. Forward primer *mtoD*_2_F contains a CACC 'overhang' which is required for TOPO cloning with pBAD202, immediately followed by a 'stop' codon then the ribosome binding sequence required for protein expression in *S. oneidensis* then the 5' end of *mtoD*. The forward primer *mtoD*_SII_F contains the second half of the sequence coding for a Strep II tag, followed by a TAG 'stop' codon then 25 bases of the pBAD202 vector at the 3' end of the *mtoD*-tag insert. Reverse primer *mtoD*_SII_R contains reverse complementary sequence to the first half of the Strep II tag followed by the 3' end of *mtoD*. Sequencing primer MJE_PBAD_F contains sequence that begins 15 bases upstream of the TrxFus forward priming site of the pBAD202 vector and allows the sequence downstream of this (including the inserted gene) to be sequenced.

```
MtoD    MTRQAYSSMLLSTAAALTLAFSLNASAAVDVDAAKSLARENNCFKCHGVDKE---KDGPS 57
HCYC    --------------------------MGDVEKGKK-IFVQKCAQCHTVEKGGKHKTGPN 32
                                  **: .*.    ::* :** *:*    * **.

MtoD    YKKVAEKYRGKADAE--------------AKLIHHVTSGEKAKFPDGHEEEHKNINGKA 102
HCYC    LHGLFGRKTGQAPGFSYTDANKNKGITWKEETLMEYLEN--PKKYIPGTKMIFAGIKKK- 89
             :  :   :  *:*  .                .*:.::  .   *:  *  :  .  *: *

MtoD    SPEAIKNLVDWILSL--- 117
HCYC    --TEREDLIAYLKKATNE 105
              ::*: :: .
```

Figure X1. Sequence alignment of MtoD with cytochrome *c* from horse heart (HCYC). The N-terminal signal sequence of MtoD is coloured grey. The conserved CXXCH *c*-type heme-binding motif is highlighted in bold text and conserved lysine residues are coloured blue. The distal ligand to the heme iron (His95 and Met80 in MtoD and HCYC respectively) are coloured green.
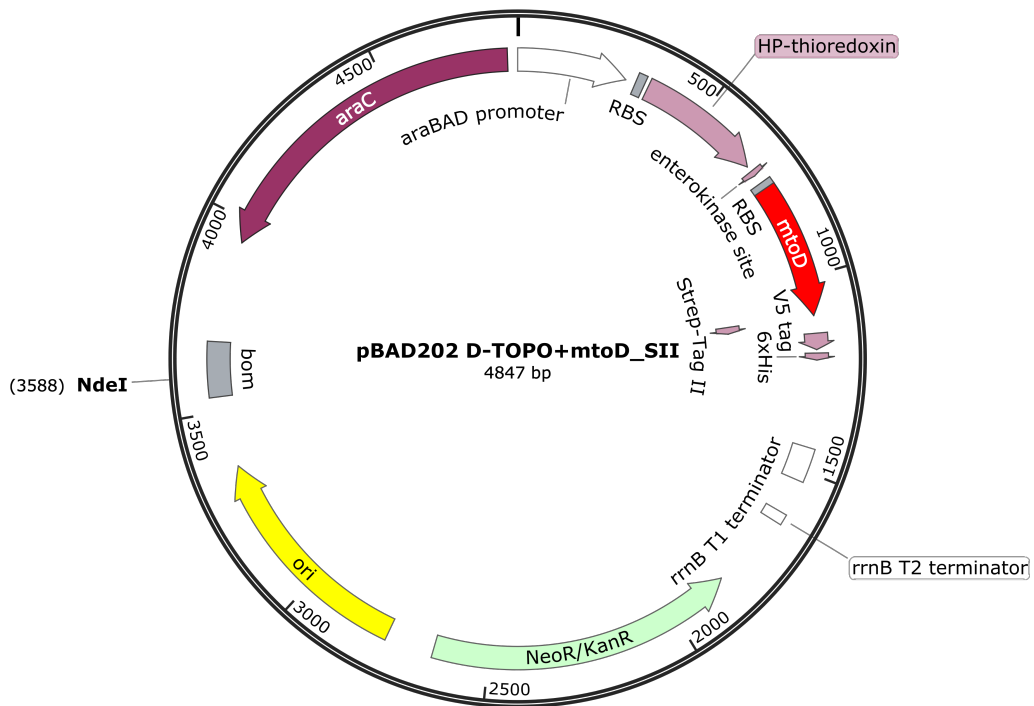
**Figure X2. Vector map of the pBAD202 D-TOPO plasmid used to express Strep II-tagged MtoD.** The *mtoD* gene, shown in red, was cloned into the pBAD expression vector with a 5'-ribosome binding sequence (RBS), which enabled the independent expression of *mtoD*. The *mtoD* gene was initially cloned into the pBAD vector with a 3'-6xHis tag. This was subsequently replaced with the Strep-tag II shown here. *NeoR/KanR* enabled selection of organisms containing the pBAD vector using the antibiotic kanamycin and the *araBAD* promoter enabled L-arabinose overexpression of *mtoD*.
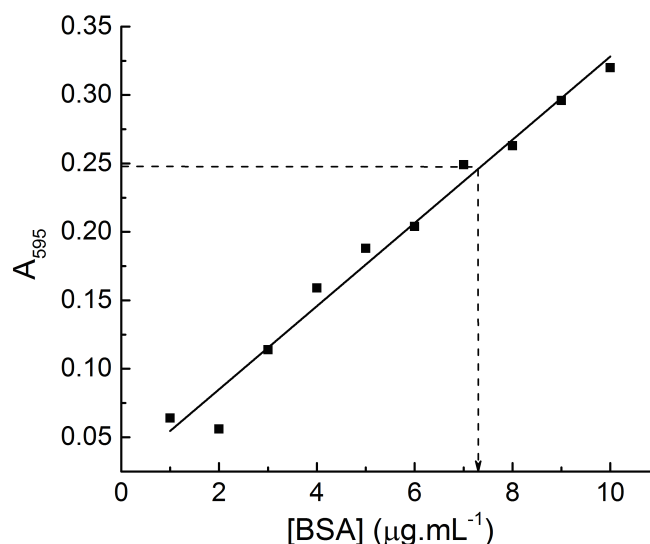
Figure X3. Quantifying protein concentration in MtoD samples using a BSA standard. The BSA standard was produced with a BioRad protein assay kit using the microassay approach. BSA concentrations from 1-10 $\mu g.mL^{-1}$ produced a linear change in absorbance at 595 nm, as shown using a standard linear fit function in OriginPro 9.1. A 1/1000 dilution of a stock solution of pure MtoD was prepared in the same way as the BSA samples and A_{595} for the MtoD sample (dotted line) indicated an approximate protein concentration of 7.4 $mg.mL^{-1}$ in the stock solution.
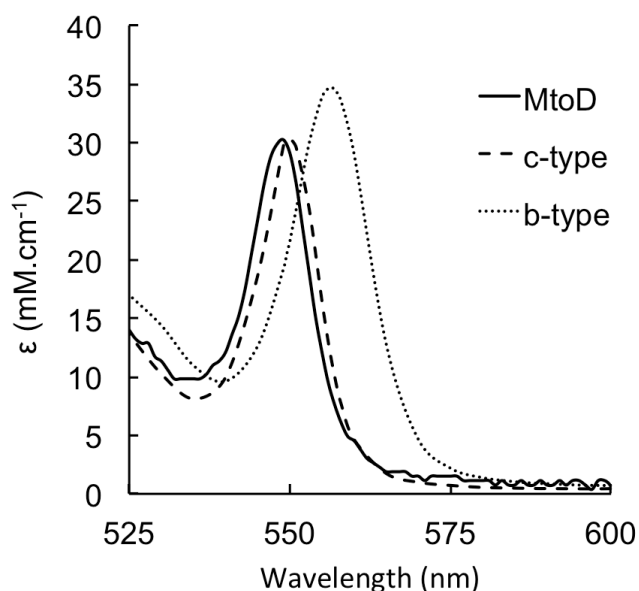
Figure X4. Electronic absorption spectrum of the pyridine hemochromagen derivative of MtoD-Strep. The MtoD pyridine hemochromagen spectrum in the visible region (solid line) was typical of a *c*-type cytochrome (dashed line) with the α-band maximum at 550 nm, in contrast to *b*-type cytochromes (dotted line), which produce a pyridine hemochromagen spectrum with an α-band peak maximum at 556 nm. The *c*-type and *b*-type pyridine hemochromagen spectra can be found in Berry and Trumpower, *Simultaneous Determination of Hemes a, b, and c from Pyridine Hemochrome Spectra* (1987).

Replicate	D (cm^2.s^{-1})	R (Å)	M_W (kDa)	Polydispersity (%)
1	1.23E-06	17.5	12.5	13.8
2	1.23E-06	17.5	12.5	13.5
3	9.24E-07	23.2	24.0	23.8
Average	3.37E-06 ± 1E-07	19.4 ± 1.9	16.3 ± 3.8	17.0 ± 3.4

Table X2. Summary of Dynamic Light Scattering (DLS) data for MtoD SAXS sample. Lights scattering by the 6 mg.mL^{-1} MtoD solutions was measured at 20°C using incident light with a wavelength of 824 nm. Three replicate experiments were performed, which revealed two MtoD protein solutions were homogenous, with minimal solution polydispersity. The third replicate experiment gave a greater predicted hydrodynamic radius (R) and corresponding molecular weight estimate (M_W) consistent with the presence of an MtoD dimer. However, increased sample polydispersity for this replicate suggests some sample aggregation may have been present, which could have produced a similar effect to an MtoD dimer. Overall, the hydrodynamic radii (R) and estimated molecular weights indicated MtoD behaved as a monomer at 6 mg.mL^{-1} concentrations.

DAMMIF parameters		DAMFILT report	
Max. particle diameter	40.7 (Å)	Atoms found	3,192
R_g	14.5 (Å)	Phases	1
Maximum q	0.399 (Å^{-1})	Minimum contacts	3
Dummy atom radius	1.0 (Å)	Maximum contacts	12
No. spherical harmonics	20	Contact threshold	5
Proportion of $p(r)$ fitted	1.0	Atomic radius	1.25 (Å)
Maximum steps	400	Excluded volume/atom	11.06 (Å^3)
Maximum iterations	100,000	Maximum radius	26.5 (Å)
Minimum successes	50	Cut-off volume	20,510 (Å^3)
Maximum successes	10,000	Final volume	20,520 (Å^3)
Temp. scheduling factor	0.95	Final No. atoms	1,856
R_g penalty weight	1x10^{-3}		
Center penalty weight	1x10^{-5}		
Looseness penalty weight	1x10^{-2}		
Anisometry penalty weight	0		

Table X3. *Ab initio* bead modelling parameters and report from DAMFILT. The maximum particle diameter, radius of gyration (R_g) and maximum momentum transfer (q) for bead modelling in DAMMIF were determined by the input $p(r)$ distribution produced by GNOM. Other parameters were determined automatically by running DAMMIF in 'slow' mode. DAMFILT found 3,192 atoms in the averaged bead model produced by DAMAVER and produced a filtered bead model with 1,856 remaining based on an input cut-off volume from DAMAVER.
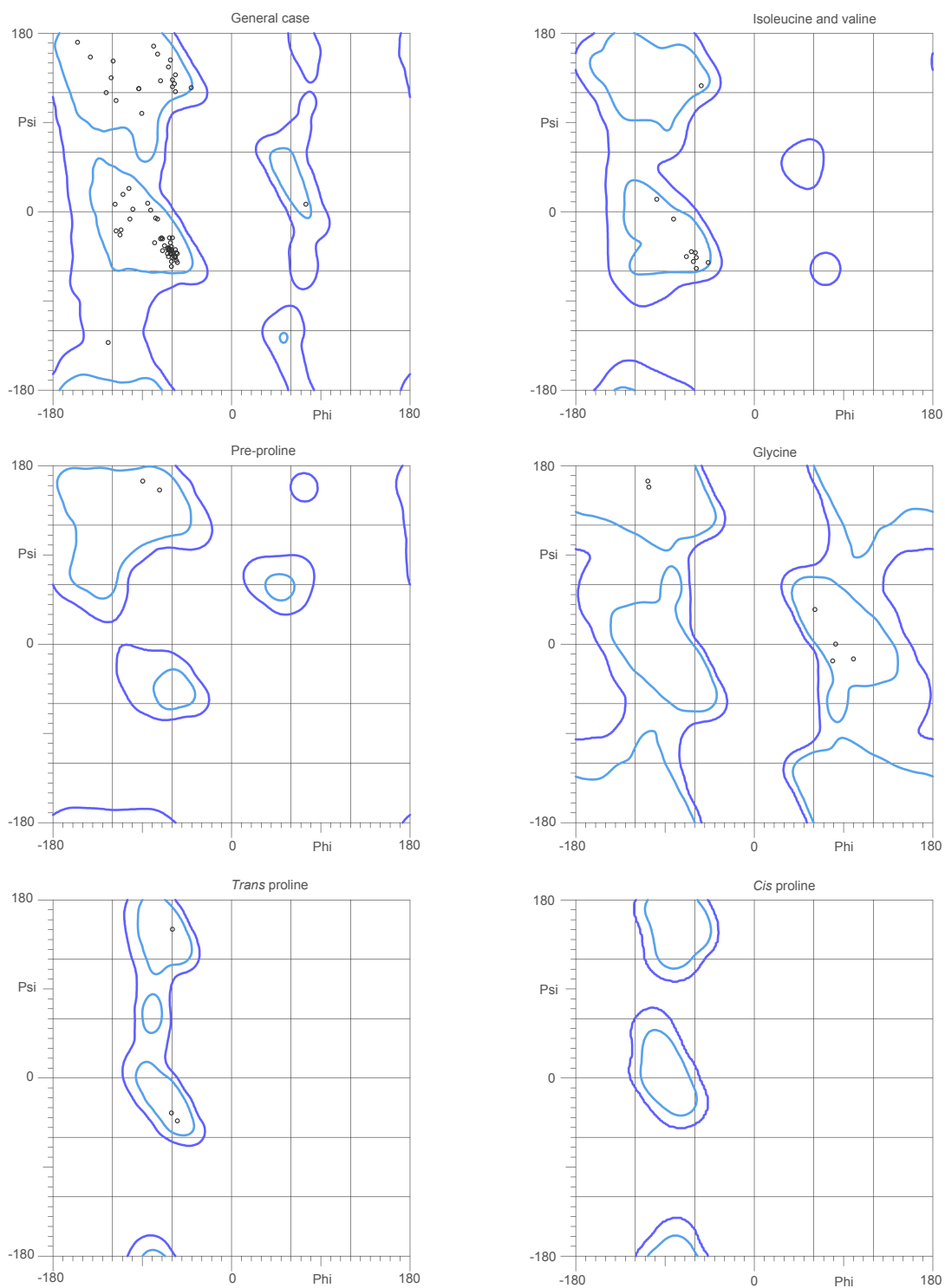
Figure X5. Ramachandran analysis for the final model of MtoD determined by X-ray crystallography. All Phi and Psi angles for residues in MtoD can be found in allowed Ramachandran space. Only Lys34 (general case panel) occupies unfavoured Ramachandran space.

| Organism	PDB ID	Ligation	Accessible heme area ($Å^2$)	SUPERPOSE RMSD (Å)
S. lithotrophicus	4XXL	His/His	42.3	-
N. eurpoaea	1A56	His/Met	16.7	3.227
P. aeruginosa	2PAC	His/Met	25.2	3.246
H. thermoluteolus	2D0S	His/Met	18.7	2.864
H. thermophilus	1YNR	His/Met	10.2	2.589
P. stutzeri	1COR	His/Met	17.0	3.079
A. aeolicus	2ZXY	His/Met	11.6	3.543

Radius of probe solvent = 1.4 Å

Table X4. Comparison of MtoD to similar cytochromes c. MtoD (4XXL) is an unusual class I cytochrome *c* with a bis-His ligated heme in the solved structure. Comparison of the solvent accessibility of each of the structures using AREAIMOL with a probe solvent radius of 1.4 Å showed MtoD has a significantly more solvent-exposed heme cofactor than any of the other cytochromes with similar structures. Performing structure superpositions of the cytochromes in SUPERPOSE indicated 1YNR provided the greatest structural similarity to MtoD with the lowest overall distance rms differences between the superposed models.

Primer name	Primer sequence	T_M (^{o}C)
*mtoB*_F	ACG ACG GGC ATC GTT TCC TA	69
*mtoB*_R	GTC ATT TCG CGT TGC CTG TG	69

T_M = melting temperature; T_M values were estimated using the New England BioLabs T_M calculator

Table X5. Primers used for the PCR-based amplification of *mtoB* from *S. lithotrophicus*.
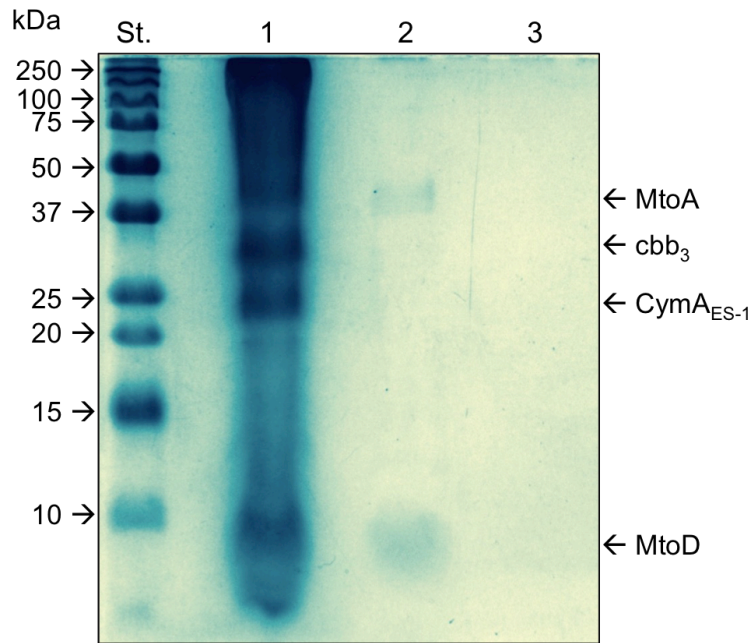
Figure X6. Heme stained SDS PAGE analysis of *Sideroxydans* cell fractions after polymyxin B sulphate treatment. *S. lithotrophicus* cells grown using the glycerol-supplemented FeS gradient plate method were suspended in a solution of 1 mL 10 mg.mL^{-1} polymyxin B sulphate in 20 mM HEPES pH 7 or 20 mM HEPES pH 7 with no polymyxin. Cell density in these solutions was approximately 25 mg.mL^{-1}. Cell suspensions were shaken horizontally at 220 rpm for 1 hour at 37°C. Samples were pelleted by centrifugation at 13,000 rpm using a microcentrifuge; the supernatant was retained and concentrated to a final volume of ~30 µL by centrifugal concentration using a 3 kDa MWCO membrane. SDS PAGE using a 17% polyacrylamide gel and heme stain analysis performed on the pelleted cells (lane 1) and the concentrate (lane 2) produced bands at 42, 32, 24 and 10 kDa for pelleted cells and 42 and 10 kDa for the concentrate of polymyxin-treated cells. No heme-staining signal was observed for cells washed in buffer with no polymyxin (lane 3). Based on predicted molecular weights, the most likely protein products are indicated (right).

Characterization of MtoD from *Sideroxydans lithotrophicus:* a cytochrome c electron shuttle used in lithoautotrophic growth

Christopher R. Beckwith[1], Marcus J. Edwards[1], Matthew Lawes[1], Liang Shi[2], Julea N. Butt[1], David J. Richardson[1] and Thomas A. Clarke[1]*

[1] Centre for Molecular and Structural Biochemistry, School of Biological Sciences and School of Chemistry, University of East Anglia, Norwich, UK, [2] Pacific Northwest National Laboratory, Richland, WA, USA

The autotrophic *Sideroxydans lithotrophicus* ES-1 can grow by coupling the oxidation of ferrous iron to the reduction of oxygen. Soluble ferrous iron is oxidized at the surface of the cell by an MtoAB porin-cytochrome complex that functions as an electron conduit through the outer membrane. Electrons are then transported to the cytoplasmic membrane where they are used to generate proton motive force (PMF) (for ATP synthesis) and NADH for autotrophic processes such as carbon fixation. As part of the *mtoAB* gene cluster, *S. lithotrophicus* also contains the gene *mtoD* that is proposed to encode a cytochrome c protein. We isolated *mtoD* from a *Shewanella oneidensis* expression system where the *mtoD* gene was expressed on a pBAD plasmid vector. Biochemical, biophysical, and crystallographic characterization of the purified MtoD revealed it as an 11 kDa monomeric protein containing a single heme. Sequence and structural alignment indicated that MtoD belonged to the class-1 cytochrome c family and had a similar fold to ferricytochrome c552 family, however the MtoD heme is bis-histidine coordinated and is substantially more exposed than the hemes of other family members. The reduction potential of the MtoD heme at pH 7 was +155 mV vs. Standard Hydrogen Electrode, which is approximately 100 mV lower than that of mitochondrial cytochrome *c*. Consideration of the properties of MtoD in the context of the potential respiratory partners identified from the genome suggests that MtoD could associate to multiple electron transfer partners as the primary periplasmic electron shuttle.

Keywords: class 1 cytochrome, MtoD, *Sideroxydans lithotrophicus* ES-1, iron oxidation

Introduction

The potential for bacteria to utilize iron as an energy source has been widely recognized in recent years (Bird et al., 2011; Konhauser et al., 2011). Several families of bacteria live at the microoxic/ferrous iron interface where they can survive by coupling the oxidation of ferrous iron to the reduction of oxygen (Hedrich et al., 2011). These bacteria are typically autotrophic and generate sufficient energy from this reaction to fix carbon dioxide and dinitrogen. Bacteria that are capable of this chemolithoautotrophic growth include acidophilic bacteria involved in acid mine drainage such as *Acidothiobacillus ferrooxidans* and *Leptospirillum ferrooxidans*

(Rawlings et al., 1999; Ferguson and Ingledew, 2008; Mishra and Rhee, 2014); the marine stalk-forming *Gallionella ferruginea* and the freshwater *Gallionella capsiferriformans* ES-2 and *Sideroxydans lithotrophicus* ES-1 (Hallbeck et al., 1993; Emerson and Moyer, 1997). The genomes of these organisms have been sequenced revealing a range of putative metabolic pathways (Emerson et al., 2013) and analysis of these pathways poses a range of interesting questions: how do the bacteria extract the electrons from the ferrous iron, and how are those electrons ultimately coupled to the generation of NADH and a proton motive force (PMF)?

The best studied of the iron oxidizing bacteria is the acidophilic *A. ferrooxidans,* where an outer membrane monoheme Cyc2 collects electrons from the oxidation of Fe(II) to Fe(III) and transfers them to a periplasmic rusticyanin which then transfers the electrons to two potential shuttles, the diheme cytochromes Cyc1 and CycA1. These diheme cytochromes then transfer the electrons down divergent routes, either to a cytochrome bc1 complex where electrons enter the quinol pool to ultimately generate NADH, or an aa3 oxidase where oxygen is reduced to water together with the transport of protons across the membrane (Bonnefoy and Holmes, 2012; Roger et al., 2012).

The neutrophilic *S. lithotrophicus* ES-1 does not contain any genes with significant homology for *cyc2*, but instead contains the genes *mtoA (Slit_2497)* and *mtoB (Slit_2496)* (Liu et al., 2012). These are homologs of *Shewanella oneidensis mtrA* and *mtrB*, which encode a decaheme cytochrome MtrA and transmembrane porin MtrB. These two proteins form a porin-cytochrome complex in the outer membrane of *S. oneidensis* that allows for efficient electron transport through the outer membrane via a chain of hemes (Hartshorne et al., 2009; White et al., 2013). It has been proposed that MtoA and MtoB fulfill a similar function in *S. lithotrophicus* ES-1, in forming an electron conduit that allows electrons to be collected from the oxidation of ferrous iron at the surface of the cell and transported through to the periplasm (Liu et al., 2012).

Both *mtoA* and *mtoB* are located in a gene cluster in the *S. lithotrophicus* ES-1 genome that also contains two other *c*-type cytochromes; *Slit_2498* that encodes MtoD, a small mono-heme cytochrome and *Slit_2495*, which encodes CymA$_{ES-1}$, a tetraheme quinol oxidoreductase. As part of the same cluster it is possible that all four of these genes are co-transcribed and expressed as part of an operon. This would provide a porin-cytochrome complex (MtoAB), a soluble periplasmic cytochrome (MtoD), and a quinol oxidoreductase in the cytoplasmic membrane (CymA$_{ES-1}$) (Emerson et al., 2013).

S. lithotrophicus ES-1 also contains the genes necessary to express two distinct oxygenases, a cytochrome bb3 oxidase (cbb$_3$), and a cytochrome bd1 oxidase (cbd$_1$). These have been characterized in other bacteria and shown to have low K_M-values for oxygen: typically cbd$_1$ operates in the micromolar range while cbb$_3$ operates in the sub-micromolar range. cbb$_3$ couples O$_2$ reduction to proton pumping and receives electrons from a cytochrome c, while cbd$_1$ has no proton pumping mechanism and receives electrons directly from the quinol pool (Pitcher and Watmough, 2004).

The bioenergetic and biochemical mechanism of precisely how iron oxidizing bacteria are able to couple Fe oxidation to O$_2$ reduction is still unclear. How do electrons from the MtoAB complex enter the cytochrome oxidase? It was previously suggested that CymA$_{ES-1}$ was the redox partner, however, this would result in the loss of protonmotive force. In order to better understand the possible roles of the periplasmic redox partners in *S. lithotrophicus* ES-1 the MtoD cytochrome was expressed in a recombinant form, purified and characterized using a range of biochemical, spectroscopic, and crystallographic techniques.

Materials and Methods

Expression and Isolation of Strep-II Tagged MtoD

The 354 bp sequence encoding *mtoD* was synthesized and cloned into a puc57 vector by GENScript. *mtoD* was amplified from pUC57 using the following primers: *mtoD_1_F*: 5′-ATG ACT CGT CAA GCT TAT TCC TCA ATG TTG and *mtoD_1_R*: 5′-GAG CGA AAG GAT CCA GTC CAC CAG. A second pair of primers were used to make modifications to *mtoD* including the addition of a 5′ CACC overhang, making the *mtoD* insert compatible with the desired pBAD202 D-TOPO cloning kit, followed by a ribosome binding sequence and a 3′ 6xCAC repeat coding for a C-terminal polyhistidine tag. *mtoD_2_F*: 5′-CAC CTA AGA AGG AGA TAT ACA TCC CAT GAC TCG TCA AGC TTA TTC. *mtoD_R_6xHis*: 5′-CTA GTG GTG GTG GTG GTG GTG GAG CGA AAG GAT C. A pBAD directional TOPO® expression kit was used clone *mtoD*-His into a pBAD202 expression vector. One Shot TOP10 *E. coli* cells were transformed with pBAD202_*mtoD*-His using methods described in the pBAD D-TOPO user guide. pBAD202_*mtoD*-His was conjugated from TOP10 to *S. oneidensis* MR-1 using *E. coli* helper strain DH5α pRK2013. Kanamycin and carbenicillin were used to select for successfully conjugated MR-1. DNA sequencing performed by Eurofins MWG operon using primers *mtoD_2_F* and *mtoD_R_6xHis* confirmed successful conjugation of pBAD202_*mtoD*-His into *S. oneidensis* MR-1. For the production of Strep II-tagged MtoD pBAD202_*mtoD*-His was isolated from *S. oneidensis* MR-1 using a miniprep kit and the whole plasmid was amplified using the primers *mtoD_SII_F*: 5′-AAT TCG AGA AGT AGA AGG GCG AGC TCA AGC TTG AAG GTA and *mtoD_SII_R*: 5′-GTG GAT GAG ACC AGA GCG AAA GGA TCC AGT CCA CAG G. The pBAD202_*mtoD*-His template was removed by DpnI digestion followed by PCR clean up. T4 polynucleotide kinase was used to phosphorylate the linear product and a blunt end ligation was performed using DNA ligase to circularize the pBAD202_*mtoD*-SII product. One Shot TOP10 *E. coli* were transformed with pBAD202_*mtoD*-SII and conjugation was used to produce recombinant *S. oneidensis* MR-1 as before.

Recombinant *S. oneidensis* MR-1_*mtoD*-SII was cultured aerobically at 30°C in 20 L batches in LB media. Expression of tagged protein was induced at mid-exponential phase (OD$_{600}$: 0.5) by addition of L-arabinose to a working concentration of 2 mM. Cultures were incubated for a further 5 h and harvested by centrifugation at 6000 *g* for 15 min. Recombinant MR-1 cell pellets were re-suspended in 20 mM HEPES pH 7 buffer and

three passes of French Press treatment at 1000 psi (6.89 MPa) were used to lyse the cells. The soluble cell fraction was isolated by ultracentrifugation of the lysate at 205,000 g for 2 h. The supernatant was retained for purification of tagged MtoD. MtoD was isolated using 5 mL Strep-Tactin affinity column (GE healthcare). The column was run with a 20 mM HEPES pH 7, 150 mM NaCl equilibration/wash buffer. Four cycles of loading and eluting were performed to isolate all of the expressed MtoD. SDS PAGE was used to analyze eluted fractions; MtoD fractions were dialysed with 20 mM HEPES pH 7, 150 mM NaCl overnight then concentrated in preparation for size exclusion chromatography. Gel filtration was performed using a Superdex S75 16/60 column. The column was equilibrated with 20 mM HEPES pH 7, 150 mM NaCl before loading MtoD and running at a flow rate of 0.5 mL.min^{-1}. Pure fractions of MtoD, determined by SDS PAGE analysis, were pooled, concentrated and dialysed with 20 mM HEPES pH 7, 100 mM NaCl overnight at 4°C.

Pyridine Hemochrome Analysis of MtoD

Oxidized spectra of horse heart cytochrome c and MtoD were prepared in 20 mM HEPES pH 7 buffer containing 2 mM CaCl$_2$ for cytochrome c, and 100 mM NaCl for MtoD. Each sample was fully oxidized with 10 μM K$_3$Fe(CN)$_6$ before measurement of UV/vis electronic absorption spectrum. The pyridine hemochrome method was used to quantify the concentration of heme in the purified MtoD sample and to determine the extinction coefficient of the Soret maxima of MtoD (Berry and Trumpower, 1987). Briefly cytochrome c and MtoD were mixed with pyridine and NaOH to give final concentrations of 3 and 75 mM, respectively. These samples were divided into two Suba-sealed quartz cuvettes. Samples were oxidized using 10 μM K$_3$Fe(CN)$_6$ and reduced with 3 mM Na$_2$S$_2$O$_4$ to give the oxidized and reduced spectra of heme bis-pyridine. A Bio-Rad protein assay kit was used to determine the total protein concentration.

Sedimentation Velocity

Four hundred and ten microliters of MtoD samples of 3.5 and 8.5 μM were measured into sample chambers of a two chamber cell assembly and 20 mM HEPES pH 7, 100 mM NaCl was measured into the reference chambers. A Beckman Optima XL-A analytical ultracentrifuge with an An50Ti rotor was used to optically measure sedimentation, monitoring absorbance at 406 nm with a rotational speed of 42,000 rpm. 300 radial scans were performed over a 20-h period at a constant temperature of 20°C. Analyses of the sedimentation velocity data were performed using SEDFIT (Brown and Schuck, 2006). The C(s) distribution model was applied to the data and non-linear fitting was performed. Buffer density and viscosity parameters (1.0039 g.mL^{-1} and 1.0264×10^{-2} ρ, respectively) in addition to predicted v-bar for MtoD (0.7282 mL.g^{-1}), were included in the C(s) model to solve Lamm equations.

MtoD Crystallization and Data Collection

A pure solution of MtoD was concentrated to 30 mg.mL^{-1} and sparse matrix screening, using the sitting drop method, was performed to explore potential crystallization conditions.

Crystals formed at 16°C in 0.6 μl drops at ratios of 1:1 or 2:1 mother liquor/protein. The mother liquor was 0.1 M KCN, 30% PEG 2000 MME. Crystals were cryo-protected by transferring to a solution of mother liquor containing 12% glycerol before being vitrified by plunging into liquid nitrogen. Data were collected on MtoD crystals in a gaseous stream of nitrogen at 100 K on beamlines I03 at the Diamond Light Source (UK). MtoD crystals were of space group P22$_1$2$_1$ with typical cell dimensions of $a = 29.70$, $b = 40.20$, $c = 92.180$ Å. A SAD dataset was collected at a wavelength of 1.72 Å to a final resolution of 2.5 Å. Further datasets from single crystals were collected using an x-ray wavelength of 0.97 Å.

MtoD Structure Determination and Refinement

MtoD datasets were processed using XIA2 (Winter, 2010). The SAD dataset of MtoD was analyzed using the autosol pipeline within the PHENIX software suite (Adams et al., 2010). The program HySS located one heavy atom site and the electron density maps calculated with PHASER/RESOLVE were sufficiently interpretable to manually place a single heme corresponding to a single MtoD molecule in the asymmetric unit. The model building program Phenix AutoBuild was used to build residues followed by alternating rounds of manual building and refinement using PHENIX (Adams et al., 2010) or REFMAC (Murshudov et al., 2011). The final model was refined to an Rcryst (Rfree) value of 19.4 (24.5)%. This model has no residues in the disallowed region of the Ramachadran plot. Coordinates have been deposited in the RCSB Protein Data bank under accession code 4XXL.
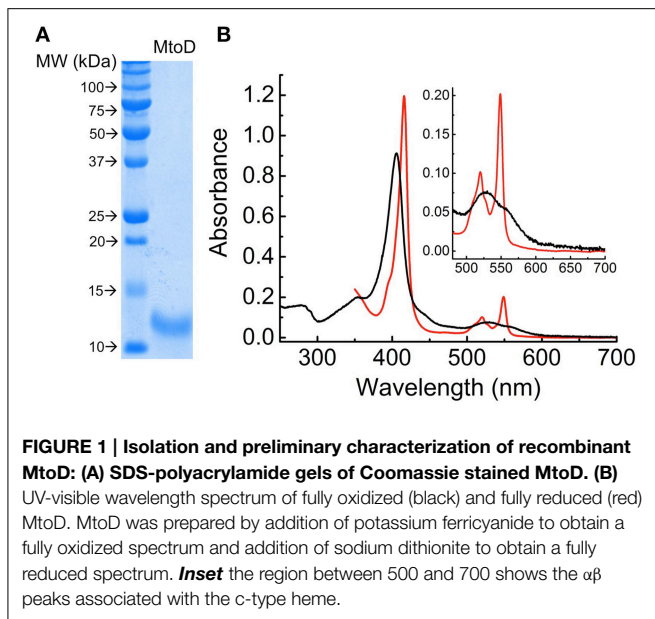
Electrochemistry

Mediated redox spectropotentiometry of a solution of MtoD was performed using methods described previously (Bamford et al., 2002). Experiments were performed under continuous argon gas flow with a solution of 5.5 μM MtoD in 20 mM HEPES pH 7, 100 mM NaCl containing 10 μM each of the following mediators: 2,3,5,6-tetramethyl-p-phenylenediamine (DAD), phenazine methosulphate (PMS), phenazine ethosulphate (PES), 5-hydroxy-1,4-napthoquinone, 2,3,5,6-tetramethyl-1,4-benzoquinone, 2-methyl-1,4-napthoquinone, 9,10-anthraquinone-2,6-disulphonic acid, anthraquinone-2-sulphonic acid and 1,1′-dibenzyl-4,4′-bipyridinium dichloride. The electrochemical potential was raised or lowered through the addition of aliquots of anaerobic solutions containing potassium ferricyanide or sodium dithionite, respectively.

Results

Expression, Purification, and Characterization of S. lithotrophicus MtoD

MtoD was purified to homogeneity from *S. oneidensis* as described in Methods. SDS-PAGE analysis revealed that MtoD ran as a single band with apparent molecular weight of 13 kDa, slightly larger than the predicted molecular weight of 11 kDa due to the c-terminal strep-II tag (**Figure 1A**). Edman degradation (PNAC facility, Cambridge UK) revealed the N-terminal sequence began AVDVD, matching the cleavage site

FIGURE 1 | Isolation and preliminary characterization of recombinant MtoD: (A) SDS-polyacrylamide gels of Coomassie stained MtoD. **(B)** UV-visible wavelength spectrum of fully oxidized (black) and fully reduced (red) MtoD. MtoD was prepared by addition of potassium ferricyanide to obtain a fully oxidized spectrum and addition of sodium dithionite to obtain a fully reduced spectrum. ***Inset*** the region between 500 and 700 shows the αβ peaks associated with the c-type heme.

FIGURE 2 | Redox characterization of MtoD. (A) Electronic absorbance of MtoD equilibrated at potentials between 0.4 and −0.4 V during a mediated potentiometric titration. Spectra are colored from blue to red corresponding to increasingly reduced protein. **(B)** Variation of absorbance at 549 nm (A_{549}) with solution potential (points) and best fit (line) to the Nernst equation for a one-electron transformation with a mid-point potential of +155 mV vs. SHE. Experiments performed in 20 mM HEPES pH 7, 100 mM NaCl at 21°C with a mediator range as listed in the methods.

predicted by SignalP (Petersen et al., 2011) and pyridine hemochrome assays revealed that the sample of MtoD contained approximately stoichiometric ratio of 0.85 heme: protein, giving an ε_{410} coefficient of 105.2 mM^{-1} cm^{-1}.
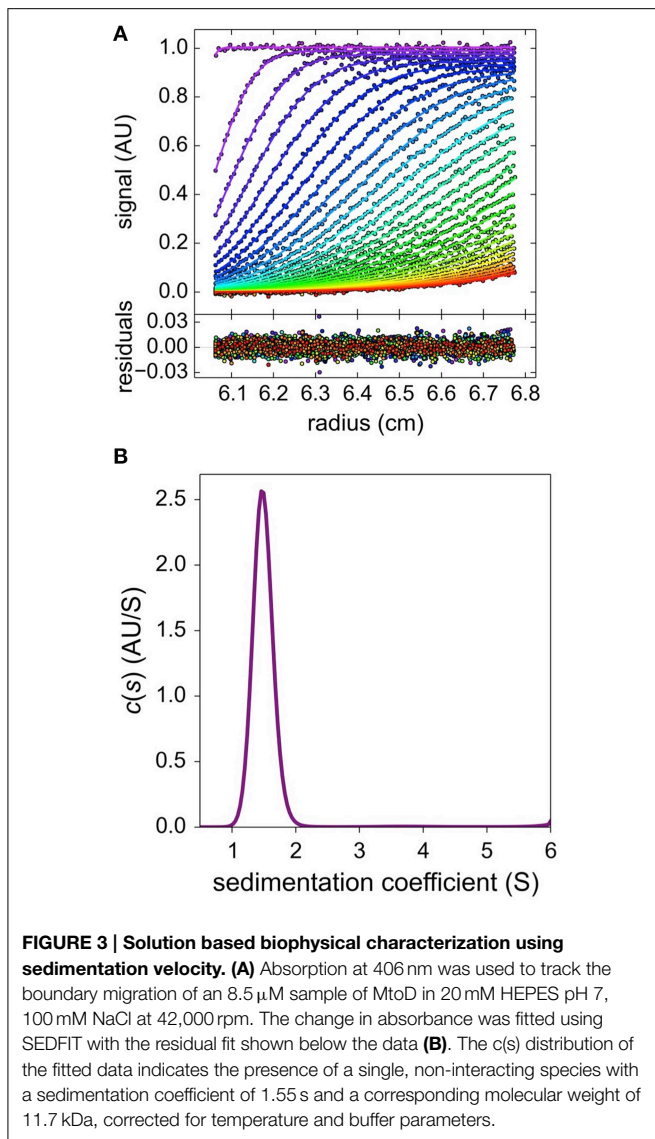
Solutions of MtoD display electronic absorbance spectra consistent with the presence of a low-spin c-type heme (**Figure 1B**). The characteristic Soret peak in the oxidized protein has a maximum at 406 nm, giving a 280/406 nm absorbance ratio of 0.19. The 406 nm maximum shifts to 416 nm on reduction of MtoD and α and β peaks appear with maxima at 549 and 520 nm, respectively. Spectral features above 600 nm would be indicative of high-spin ferric heme or low-spin ferric heme with His/Met axial heme ligation as is typically observed in other class-1 cytochrome-c family members (Bertini et al., 2006). However, MtoD displayed no detectable absorbance above 600 nm in agreement with the heme ligand set resolved by X-ray diffraction as described below. Mediated potentiometric titration of MtoD monitored by electronic absorbance spectroscopy defined the heme redox properties (**Figure 2A**). Changes in the absorbance at 549 nm due to the ferric/ferrous heme interconversion were fully reversible with change of solution potential (**Figure 2B**). The behavior was in excellent agreement with that predicted by the Nernst equation for a single redox center undergoing a one-electron redox transformation with a mid-point potential of 155 ± 10 mV vs. SHE.

The biophysical properties of MtoD in solution were examined using sedimentation velocity. MtoD samples at 3.5 and 8.5 μM were centrifuged as described in methods and the migration profile of MtoD at 406 nm was measured over 5 h (**Figure 3A**). The data was fitted using the software program SEDFIT which revealed a single species with a sedimentation coefficient of 1.55 s and a molecular mass of 11.7 kDa (**Figure 3B**). Further analysis of the sedimentation data gave a f/f_o coefficient of 1.24, indicating that MtoD behaved like a monomeric globular protein in solution.
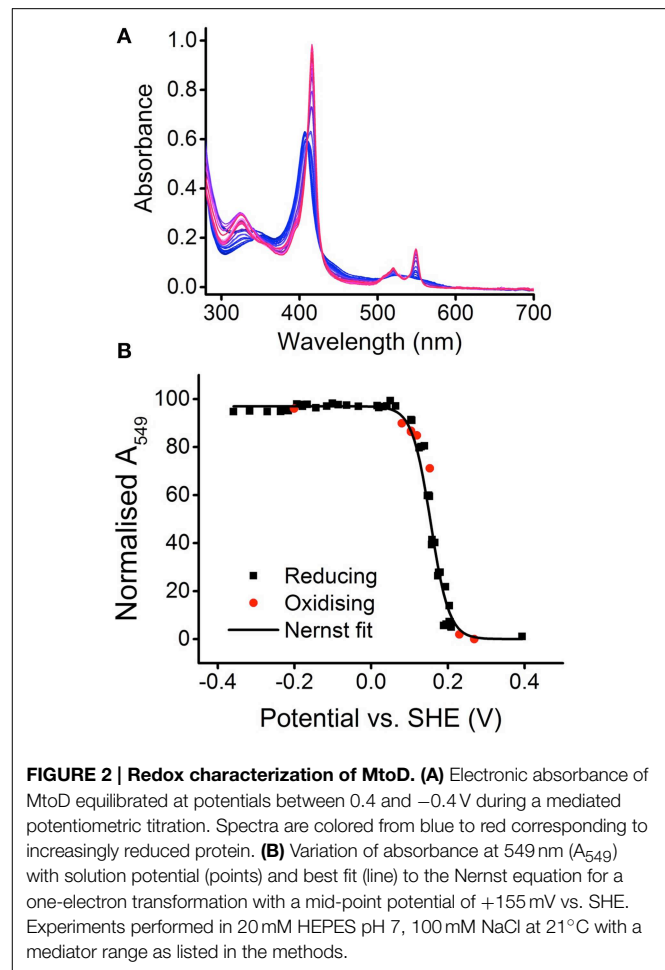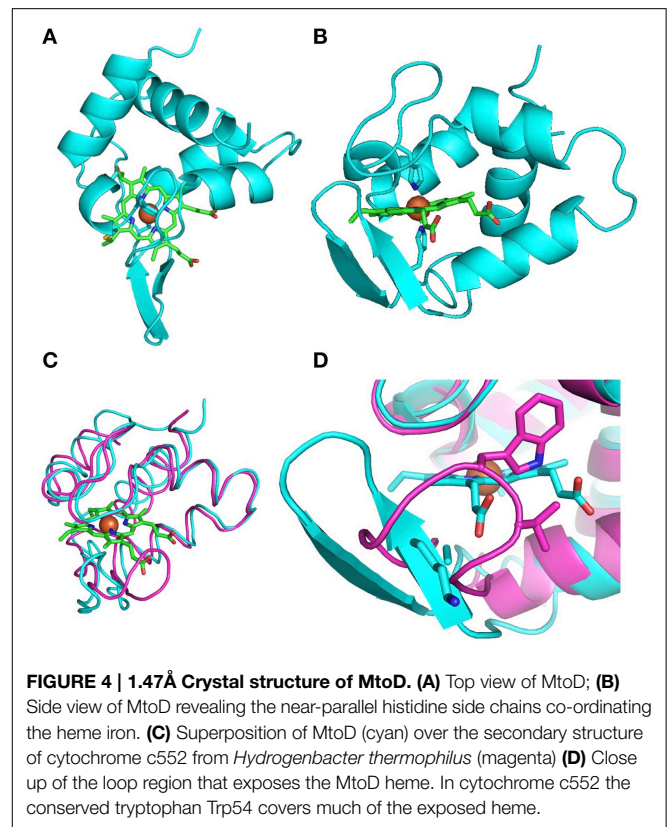
The crystal structure of MtoD was solved to an initial resolution of 2.29 Å by single wavelength anomalous dispersion (SAD) using the anomalous signal caused by the single iron atom contained within the heme group. The initial model was used as a template for molecular replacement to obtain a final resolution of 1.47 Å. The overall statistics obtained for data collection and structure refinement are given in Supplementary Table 1. The crystal structure contained residues 28–119 of the processed amino acid sequence and a single c-type heme covalently attached to Cys$_{43}$ and Cys$_{46}$ via thioether bonds (**Figure 4A**), consistent with the histidine ligands predicted from the sequence alignment. The iron atom of the heme group was coordinated by the imidazoles of the porin cofactor and His$_{47}$ and His$_{95}$ of the active site. The imidazole side chains of the two histidines coordinating the heme iron are arranged near-parallel relative to one another, at an angle of approximately 35° (**Figure 4B**).

The sequence alignment between MtoD and the other structurally resolved cytochromes revealed that cytochrome c552 from *Nitrosomas europea* had the highest amino acid sequence homology (Supplemental Figure 1). When the structure of MtoD was compared with the other available structures of bacterial monoheme c-type cytochromes, the closest structural homolog was cytochrome c552 from *Hydrogenobacter thermophilus* (PDB

FIGURE 3 | Solution based biophysical characterization using sedimentation velocity. (A) Absorption at 406 nm was used to track the boundary migration of an 8.5 μM sample of MtoD in 20 mM HEPES pH 7, 100 mM NaCl at 42,000 rpm. The change in absorbance was fitted using SEDFIT with the residual fit shown below the data (B). The c(s) distribution of the fitted data indicates the presence of a single, non-interacting species with a sedimentation coefficient of 1.55 s and a corresponding molecular weight of 11.7 kDa, corrected for temperature and buffer parameters.

FIGURE 4 | 1.47Å Crystal structure of MtoD. (A) Top view of MtoD; (B) Side view of MtoD revealing the near-parallel histidine side chains co-ordinating the heme iron. (C) Superposition of MtoD (cyan) over the secondary structure of cytochrome c552 from *Hydrogenbacter thermophilus* (magenta) (D) Close up of the loop region that exposes the MtoD heme. In cytochrome c552 the conserved tryptophan Trp54 covers much of the exposed heme.

TABLE 1 | Structural comparison of MtoD with similar monoheme c-type cytochromes.

Name	Class	PDB id	Axial ligands	Accesible Heme area ($Å^2$)	RMSD (Å)
S. lithotrophicus MtoD	–	4XXL	His/His	152.5	–
N. europea c552	c552	1A56	His/Met	54.2	3.23
P. aeruginosa c551	c551	451C	His/Met	52.6	3.25
H. thermoluteolus c552	c552	2D0S	His/Met	61.3	2.87
H. thermophilus c552	c552	1YNR	His/Met	57.4	2.59
P. stutzeri c551	c552	1COR	His/Met	55.2	3.08
A. aeolicus c555	c555	2ZXY	His/Met	37.5	3.54

Six cytochromes were identified through sequence similarity to MtoD using BLAST. Structures were downloaded from the RCSB protein data bank. The root mean square displacement (RMSD) was measured using SUPERPOSE (Krissinel and Henrick, 2004). Accesible heme area was measured using a 1.4 Å probe using AREAIMOL (Shrake and Rupley, 1973).

id. 1YNR). Superposition of the main chain of this cytochrome with MtoD gave an average root-mean-square-displacement of 2.59 Å (**Figure 4B**, **Table 1**). Despite the high level of secondary structure conservation there are notable structural differences between MtoD and the other known c-type cytochromes. One obvious difference is that the axial coordination of the MtoD heme is bis-Histidine, while other crystallized cytochromes have Histidine/Methionine coordination (**Table 1**). The class 1 cytochromes typically contain a flexible loop that covers the front of the heme, however in MtoD this region is restrained by a hydrogen bonding network that causes the formation of a β-loop and prevents the peptide sidechains from interacting with the heme propionate groups (**Figures 4C,D**). This causes an increase in the overall surface exposure of the MtoD heme, giving an overall exposed heme of 152 $Å^2$ compared to 30–61 $Å^2$ for other class 1 cytochromes. Typically the hemes of these class 1 cytochromes are exposed on one side, next to the thiolated cysteine residues, with the propionate edge being completely covered. To date the heme group of MtoD is significantly more

exposed to solvent than the heme of any other structurally resolved monoheme cytochrome, suggesting that the properties of the heme are likely to be extremely susceptible to changes within the local environment.
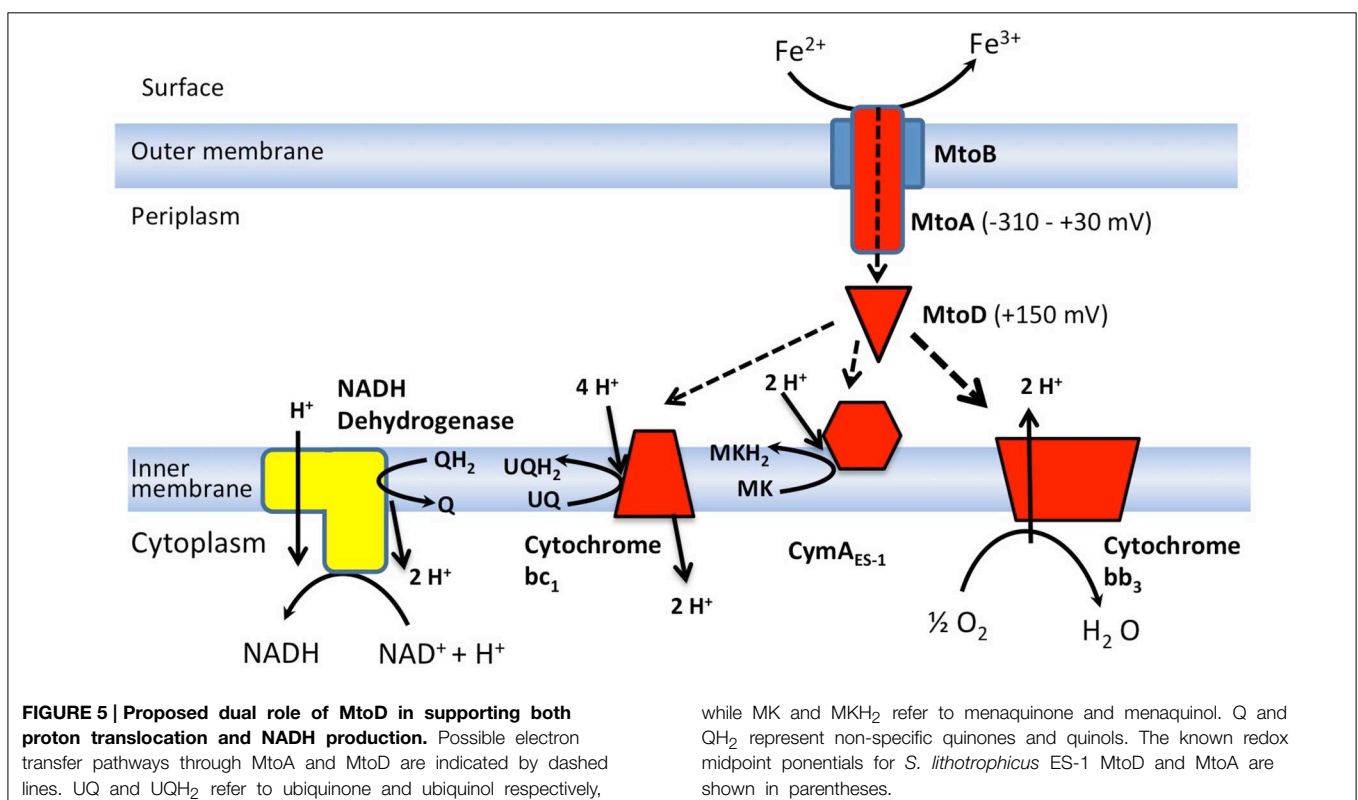
Discussion

Autotrophic iron oxidizing bacteria face a significant bioenergetic challenge in generating both the reducing equivalents (NADH) and chemical energy (ATP) required

for carbon fixation and other anabolic reactions essential for cell survival. The energy source for both NADH and ATP production is generated from the liberation of electrons obtained from the oxidation of iron at the cell surface. At pH 7.0 the redox potential of this iron couple $Fe(OH)_3/Fe^{2+}$ is -236 mV vs. SHE, which is low enough to allow electron transfer across the outer membrane through the MtoAB complex (Widdel et al., 1993; Liu et al., 2012). The electrons obtained from iron oxidation are required both for PMF-coupled oxygen reduction, and the reduction of NADH at the cytoplasmic membrane. At an initial potential around -236 mV the energy associated with these electrons would be sufficient to catalyze the reduction of oxygen ($+816$ mV), but they would not be able to reduce NAD^+ to NADH (-320 mV). As a consequence electrons destined for NADH formation will have to be pumped "uphill" through different carriers before reducing NADH. The energy source for this uphill electron transfer is most likely to be obtained from the proton gradient. In *A. ferrooxidans* two periplasmic diheme cytochromes Cyc1 and CycA1 take electrons to either the cytochrome oxidase or the cytochrome bc_1 complex, which then runs in reverse to reduce ubiquinone. These cytochromes are located in two separate operons; the *rus* operon contains *cyc1* as well as *cyc2*, *rusA* and the genes for a cytochrome c oxidase, while the *petI* operon contains *cycA1* and the genes for a cytochrome bc_1 complex (Roger et al., 2012). In contrast the *mto* gene cluster of *S. lithotrophicus* contains the gene for only one monoheme cytochrome: *mtoD*, while the gene clusters that contain the genes of cytochrome bc_1 and cytochrome bb_3 do not contain any soluble monoheme cytochromes.

The MtoD cytochrome has a number of unusual features. Comparative analysis of the MtoD amino acid sequence with the sequences of other structurally defined class-1 cytochromes revealed that MtoD is unusual in having bis-His coordination instead of His/Met, and that the sequence around the distal ligand is not proline rich as observed for other cytochromes (**Table 1** and Supplemental Figure 1). The measured redox potential of $+155$ mV for the MtoD heme is high for a bis-His coordinated heme and the heme group is significantly more solvent exposed than in monoheme cytochromes. It is possible that these unusual features of the MtoD heme group allow it to function as an electron donor to cytochrome bb_3, cytochrome bc_1 and/or $CymA_{ES-1}$ (**Figure 5**).

Previous studies on the potentials of the heme groups of MtoA indicate that they span a mid-point potential range between $+30$ and -350 mV (Liu et al., 2012), which is lower than the potential of MtoD and indicates that electron transfer from MtoA to MtoD would be thermodynamically favorable. This supports the hypothesis that MtoD could be the electron transfer shuttle between the outer membrane MtoAB complex and the cytochrome bb_3 oxidase on the cytoplasmic membrane, allowing the efficient generation of a PMF.

A membrane bound NADH dehydrogenase is proposed to reduce NAD^+ to NADH using electrons provided by the quinol pool and energy generated by the PMF (Emerson et al., 2013). Either the cytochrome bc1 complex or $CymA_{ES-1}$ could generate quinol, using electrons supplied by MtoD (**Figure 5**). At $+155$ mV, the potential of MtoD is only slightly higher than the midpoint potential of ubiquinol ($+100$ mV vs. SHE)

FIGURE 5 | Proposed dual role of MtoD in supporting both proton translocation and NADH production. Possible electron transfer pathways through MtoA and MtoD are indicated by dashed lines. UQ and UQH$_2$ refer to ubiquinone and ubiquinol respectively, while MK and MKH$_2$ refer to menaquinone and menaquinol. Q and QH$_2$ represent non-specific quinones and quinols. The known redox midpoint ponentials for *S. lithotrophicus* ES-1 MtoD and MtoA are shown in parentheses.

and consequently electron transfer from MtoD to cytochrome bc_1 could occur in order to drive NADH production. The generation of reduced ubiquinol from cytochrome bc1 has been observed in other iron oxidizing bacteria, notably *A. ferrooxidans* (Elbehti et al., 2000). In this system, the two half reactions of the cytochrome bc1 complex run in reverse, causing the net transport of two protons across the cytoplasmic membrane for every ubiquinone reduced.

The role of $CymA_{ES-1}$ is less clear. The homologous CymA cytochrome from *S. oneidensis* MR-1 was shown to be specific for menaquinone, that has a midpoint potential of -70 mV vs. SHE (McMillan et al., 2012). This suggests that the measured potential of MtoD would not allow thermodynamically favorable electron transfer to $CymA_{ES-1}$. However, the highly exposed heme surface of MtoD is likely to be sensitive to changes in the local environment, such as those caused by protein complex formation. This may allow lowering of the MtoD midpoint potential on association with $CymA_{ES-1}$, facilitating electron exchange and menaquinone reduction.

In summary, the structure and electrochemical properties of MtoD are consistent with its possible role as an electron shuttle between MtoAB on the outer membrane and a range of potential electron acceptors on the inner membrane. However, a full biochemical analysis will be required to verify the true redox partners and confirm the pathway of electron transfer through this iron oxidizing bacterium.

Supplementary Material

The Supplementary Material for this article can be found online at: http://journal.frontiersin.org/article/10.3389/fmicb.2015.00332/abstract

References

Adams, P. D., Afonine, P. V., Bunkoczi, G., Chen, V. B., Davis, I. W., Echols, N., et al. (2010). PHENIX: a comprehensive Python-based system for macromolecular structure solution. *Acta Crystallogr. D Biol. Crystallogr.* 66, 213–221. doi: 10.1107/S0907444909052925

Bamford, V. A., Angove, H. C., Seward, H. E., Thomson, A. J., Cole, J. A., Butt, J. N., et al. (2002). Structure and spectroscopy of the periplasmic cytochrome c nitrite reductase from *Escherichia coli*. *Biochemistry* 41, 2921–2931. doi: 10.1021/bi015765d

Berry, E. A., and Trumpower, B. L. (1987). Simultaneous determination of Hemes-a, Hemes-B, and Hemes-C from pyridine hemochrome spectra. *Anal. Biochem.* 161, 1–15. doi: 10.1016/0003-2697(87)90643-9

Bertini, I., Cavallaro, G., and Rosato, A. (2006). Cytochrome c: occurrence and functions. *Chem. Rev.* 106, 90–115. doi: 10.1021/cr050241v

Bird, L. J., Bonnefoy, V., and Newman, D. K. (2011). Bioenergetic challenges of microbial iron metabolisms. *Trends Microbiol.* 19, 330–340. doi: 10.1016/j.tim.2011.05.001

Bonnefoy, V., and Holmes, D. S. (2012). Genomic insights into microbial iron oxidation and iron uptake strategies in extremely acidic environments. *Environ. Microbiol.* 14, 1597–1611. doi: 10.1111/j.1462-2920.2011.02626.x

Brown, P. H., and Schuck, P. (2006). Macromolecular size-and-shape distributions by sedimentation velocity analytical ultracentrifugation. *Biophys. J.* 90, 4651–4661. doi: 10.1529/biophysj.106.081372

Elbehti, A., Brasseur, G., and Lemesle-Meunier, D. (2000). First evidence for existence of an uphill electron transfer through the bc(1) and NADH-Q oxidoreductase complexes of the acidophilic obligate chemolithotrophic ferrous ion-oxidizing bacterium *Thiobacillus ferrooxidans*. *J. Bacteriol.* 182, 3602–3606. doi: 10.1128/JB.182.12.3602-3606.2000

Emerson, D., Field, E. K., Chertkov, O., Davenport, K. W., Goodwin, L., Munk, C., et al. (2013). Comparative genomics of freshwater Fe-oxidizing bacteria: implications for physiology, ecology, and systematics. *Front. Microbiol.* 4:254. doi: 10.3389/fmicb.2013.00254

Emerson, D., and Moyer, C. (1997). Isolation and characterization of novel iron-oxidizing bacteria that grow at circumneutral pH. *Appl. Environ. Microbiol.* 63, 4784–4792.

Ferguson, S. J., and Ingledew, W. J. (2008). Energetic problems faced by micro-organisms growing or surviving on parsimonious energy sources and at acidic pH: I. *Acidithiobacillus ferrooxidans* as a paradigm. *Biochim. Biophys. Acta Bioenerg.* 1777, 1471–1479. doi: 10.3389/fmicb.2012.00037

Hallbeck, L., Stahl, F., and Pedersen, K. (1993). Phylogeny and phenotypic characterization of the stalk-forming and iron-oxidizing bacterium *Gallionella-ferruginea*. *J. Gen. Microbiol.* 139, 1531–1535. doi: 10.1099/00221287-139-7-1531

Hartshorne, R. S., Reardon, C. L., Ross, D., Nuester, J., Clarke, T. A., Gates, A. J., et al. (2009). Characterization of an electron conduit between bacteria and the extracellular environment. *Proc. Natl. Acad. Sci. U.S.A.* 106, 22169–22174. doi: 10.1073/pnas.0900086106

Hedrich, S., Schlomann, M., and Johnson, D. B. (2011). The iron-oxidizing proteobacteria. *Microbiology* 157, 1551–1564. doi: 10.1099/mic.0.045344-0

Konhauser, K. O., Kappler, A., and Roden, E. E. (2011). Iron in microbial metabolisms. *Elements* 7, 89–93. doi: 10.2113/gselements.7.2.89

Krissinel, E., and Henrick, K. (2004). Secondary-structure matching (SSM), a new tool for fast protein structure alignment in three dimensions. *Acta Crystallogr. D Biol. Crystallogr.* 60, 2256–2268. doi: 10.1107/S0907444904026460

Liu, J., Wang, Z. M., Belchik, S. M., Edwards, M. J., Liu, C. X., Kennedy, D. W., et al. (2012). Identification and characterization of MtoA: a decaheme c-type cytochrome of the neutrophilic Fe(II)-oxidizing bacterium *Sideroxydans lithotrophicus* ES-1. *Front. Microbiol.* 3:37. doi: 10.3389/fmicb.2012.00037

McMillan, D. G., Marritt, S. J., Butt, J. N., and Jeuken, L. J. (2012). Menaquinone-7 is specific cofactor in tetraheme quinol dehydrogenase CymA. *J. Biol. Chem.* 287, 14215–14225. doi: 10.1074/jbc.M112.348813

Mishra, D., and Rhee, Y. H. (2014). Microbial leaching of metals from solid industrial wastes. *J. Microbiol.* 52, 1–7. doi: 10.1007/s12275-014-3532-3

Murshudov, G. N., Skubak, P., Lebedev, A. A., Pannu, N. S., Steiner, R. A., Nicholls, R. A., et al. (2011). REFMAC5 for the refinement of macromolecular

crystal structures. *Acta Crystallogr. D Biol. Crystallogr.* 67, 355–367. doi: 10.1107/S0907444911001314

Petersen, T. N., Brunak, S., von Heijne, G., and Nielsen, H. (2011). SignalP 4.0: discriminating signal peptides from transmembrane regions. *Nat. Methods* 8, 785–786. doi: 10.1038/nmeth.1701

Pitcher, R. S., and Watmough, N. J. (2004). The bacterial cytochrome cbb(3) oxidases. *Biochim. Biophys. Acta Bioenerg.* 1655, 388–399. doi: 10.1016/j.bbabio.2003.09.017

Rawlings, D. E., Tributsch, H., and Hansford, G. S. (1999). Reasons why 'Leptospirillum'-like species rather than *Thiobacillus ferrooxidans* are the dominant iron-oxidizing bacteria in many commercial processes for the biooxidation of pyrite and related ores. *Microbiology* 145, 5–13. doi: 10.1099/13500872-145-1-5

Roger, M., Castelle, C., Guiral, M., Infossi, P., Lojou, E., Giudici-Orticoni, M. T., et al. (2012). Mineral respiration under extreme acidic conditions: from a supramolecular organization to a molecular adaptation in *Acidithiobacillus ferrooxidans. Biochem. Soc. Trans.* 40, 1324–1329. doi: 10.1042/BST201 20141

Shrake, A., and Rupley, J. A. (1973). Environment and exposure to solvent of protein atoms - lysozyme and insulin. *J. Mol. Biol.* 79, 351–371. doi: 10.1016/0022-2836(73)90011-9

White, G. F., Shi, Z., Shi, L., Wang, Z. M., Dohnalkova, A. C., Marshall, M. J., et al. (2013). Rapid electron exchange between surface-exposed bacterial cytochromes and Fe(III) minerals. *Proc. Natl. Acad. Sci. U.S.A.* 110, 6346–6351. doi: 10.1073/pnas.1220074110

Widdel, F., Schnell, S., Heising, S., Ehrenreich, A., Assmus, B., and Schink, B. (1993). Ferrous iron oxidation by anoxygenic phototrophic bacteria. *Nature* 362, 834–836. doi: 10.1038/362834a0

Winter, G. (2010). xia2: an expert system for macromolecular crystallography data reduction. *J. Appl. Crystallogr.* 43, 186–190. doi: 10.1107/S0021889809045701